

Modelling of Sediment Dynamics in the Dithmarschen Bight, German North Sea Coast

Dissertation
zur Erlangung des Doktorgrades
der Mathematisch-Naturwissenschaftlichen Fakultät
der Christian-Albrechts-Universität zu
Kiel

vorgelegt von
Carlos Alejandro Escobar Sierra

Kiel
May 2007

Referent: Prof. Dr. Roberto Mayerle
Korreferent: Prof. Dr. Franciscus Colijn
Tag der mündlichen Prüfung: 18. Juli 2007
Zum Druck genehmigt

Der Dekan
gez. ...

To Gloria Isabel

Acknowledgments

This investigation received explicit and implicit support from many people and institutes concerned in the successful evolvment of this project. I thank God for gather all these contributions in benefit of this work.

I would like to thank my supervisor Prof. Roberto Mayerle. He gave me the opportunity to join the Coastal Research Laboratory and involved me into several important projects from which I have obtained valuable experience. I thank him for his support and willingness to listen and discuss throughout this investigation.

Also, I would like to thank the Eafit University Medellín Campus from which I received a leave and support to carry out the doctoral program. Special thanks to Dr. Alberto Rodriguez, Dr. Angela Echeverry, Dr. Felix Londoño and Mr. Carlos Mario Betancourt.

Special thanks go to Dr. Mauricio Toro, for his readiness and kindness to look over the thesis. I greatly appreciate his corrections and suggestions.

I also appreciate the collaboration of Dr. Poerbandono for sharing his experience with sediment models in coastal areas and also for provide me valuable field data.

Furthermore, I thank Dr. Kalle Runte and Dr. Klaus Ricklefs for sharing their knowledge, field data and also for their valuable comments on this work.

I would like to express my thanks to the former and current coordinators of the Coastal Research Laboratory, Markus Reckermann and Peter Weppen for their help in solving any kind of difficulties during my stay in Kiel.

Special thanks go to Katharina Roisin for the translation of the thesis abstract and to Leslie Malick for reviewing the English text.

I am also very grateful to all my colleagues from the Coastal Research Laboratory. Special thanks for Jose Fernandez, Nestor Jimenez, Huang Tsheng, Talal Etri, Gerd Bruss, Wiwin Windupranata, Gatot Pramono, Jort Wilkens, Jorge Echeverry, Dirk Schulz, Maryam Rahbani, and Ilgar Özgürel for being so nice, helpful and good humoured.

Finally, special thanks go to my beloved family. My mother Dora, my wife Gloria Isabel, my brothers Jaime and Juan, and also to my friend Jorge Ivan for their valuable support throughout this investigation.

Abstract

The main concern throughout this thesis is the development of a numerical sediment transport model for an area in the German North Sea coast exhibiting a complex-bathymetry which is subject to a prevailing semi-diurnal tidal forcing (mean tidal range of about 3.2m) in the tidal channels and a combined wave-current influence on the shallower tidal flats and sand banks.

The construction of the sediment model evolved from an initial condition based on the formulae for the sediment dynamics of non-cohesive particles in which sediment and morphological input parameters were set constant in space and time. Subsequently, in order to improve the performance of this model a combined analysis of cohesive and non-cohesive sediment dynamics is carried out.

The improved sediment model is further enriched by means of spatial and temporal refinement of relevant input parameters, namely:

- a) Spatial distribution of grain sizes. A functional relationship between grain sizes, orbital velocities and relative wave height is proposed and successfully validated in the study area by means of comparisons between predicted and observed grain sizes.
- b) Spatial and temporal variation of bedforms and equivalent roughness sizes. An existent methodology extensively used and validated for uniform, steady flows [Van Rijn, 1993] is adapted for unsteady tidal flows. Measurements of bedform heights and lengths along the main tidal channels of the study area corroborate the validity of this approach.
- c) Sediment availability. Areas in the deepest parts of the tidal channels, where layers of highly consolidated materials have outcropped, are included into the model through the reduction of the sediment supply at the bed-flow interface.
- d) Seasonal variation of cohesive sediment properties. The non-stationary character of the driving gravitational force affects the temporal behavior of several parameters through the neap-spring cycle. Interpolation and extrapolation techniques based on two well calibrated conditions at neap and spring stages are used to define some parameters such as: critical shear stress (erosion-deposition), settling velocity, fraction of cohesive content and erosion rate coefficient at any flow stage under calm weather conditions.

The final sediment transport model including all aspects mentioned above, rendered an overall improvement in the model performance of about 50%. Comparisons between predicted and observed suspended sediment concentrations for five independent datasets at different stages in the neap-spring cycle resulted in RMAE values ranging from 0.42 to 0.53. The difficulty in measuring suspended concentrations in the field as stated by several authors, underlines the accuracy of the results obtained through this sediment transport model.

Kurzfassung

Das Hauptanliegen dieser Arbeit ist die Entwicklung eines numerischen Sedimenttransportmodells im Bereich der Deutschen Nordseeküste. Es besitzt eine komplexe Bathymetrie und unterliegt in den Prielen überwiegend halbtägigen Gezeiten (mittlerer Tidenhub von etwa 3,2m). Die flachen Wattbereiche sind durch eine Kombination von Wellen- und Strömungseinfluss gekennzeichnet.

Die Ausgangsbedingungen des Sedimentmodells basieren auf der Sedimentdynamik nicht-kohäsiver Partikel und nehmen räumlich und zeitlich konstante sedimentologische und morphologische Eingabeparameter an.

Zur Verbesserung der Leistungsfähigkeit des Modells wird eine Kombinationsanalyse unter Berücksichtigung von kohäsiven und nicht-kohäsiven Sedimentdynamiken durchgeführt.

Das optimierte Sedimentmodell wird weiterhin durch die räumliche und zeitliche Verfeinerung relevanter Eingabeparameter verbessert, und zwar:

- a) Räumliche Verteilung von Korngrößen. Es wird eine funktionale Beziehung zwischen Korngrößen, Orbitalgeschwindigkeiten und relativen Wellenhöhen angenommen und erfolgreich validiert, indem prognostizierte und beobachtete Korngrößen verglichen werden.
- b) Räumliche und zeitliche Variationen von Bodenformen und äquivalenten Rauheiten. Eine bereits bestehende Methode, welche weitgehende Anwendung findet und für gleichförmige und stationäre Strömung validiert ist [Van Rijn, 1993], wird für instationäre Gezeitenströmungen angepasst. Messungen von Bodenformhöhen und -längen entlang der Hauptpriele im Untersuchungsgebiet bestätigen die Validität dieses Ansatzes.
- c) Sedimentverfügbarkeit. Flächen in den tiefsten Bereichen der Priele, in denen Lagen von stark konsolidiertem Material freiliegen, werden durch eine Verminderung der Sedimentverfügbarkeit an der Boden-Wassersäule Grenze in dem Modell berücksichtigt.
- d) Saisonale Variationen von Kohäsionseigenschaften. Der ortsveränderliche Charakter der Schwerkraft als Antriebskraft beeinflusst das zeitliche Verhalten einiger Parameter während des Nipp-Springtide Zykluses. Für zwei gut kalibrierte Bedingungen während des Nipp-Springtide Zykluses werden Interpolations- und Extrapolationstechniken angewendet, um diese

Parameter zu definieren. Hierzu gehören: die kritische Schubspannung (Erosion, Deposition), die Sinkgeschwindigkeit, der Anteil an kohäsivem Material und die Erosionsrate unter jeglichem Fließstadium bei ruhigen Wetterbedingungen.

Das endgültige Sedimenttransportmodell, welches alle der oben genannten Aspekte einbezieht, erreichte eine Gesamtverbesserung der Modelleistung um etwa 50%. Vergleiche zwischen prognostizierten und beobachteten suspendierten Sedimentkonzentrationen für fünf unabhängige Datensätze zu verschiedenen Zeitpunkten im Nipp-Springtide Zyklus, ergaben RMAE-Werte von 0,42 bis 0,53. Die Ergebnisse des Sedimenttransportmodells können, in Anbetracht der Schwierigkeiten, die von vielen Autoren bei der Feldmessung von suspendierten Sedimentkonzentrationen beschrieben wurden, als relativ genau bezeichnet werden.

Contents

Acknowledgments	i
Abstract	iii
Kurzfassung	v
Contents	vii
List of Figures	x
List of Tables	xv
Notations	xvi
Introduction	1
1.1 General.....	1
1.2 Objectives.....	3
1.3 Basics of sediment transport models	3
1.4 Outline	4
1.5 Study area.....	4
Literature review	6
2.1 Introduction.....	6
2.2 General.....	6
2.2.1 Physical properties of individual non-cohesive particles	7
2.2.2 Physical properties of cohesive particles.....	16
2.2.3 Bedforms on non-cohesive sediments	18
2.2.4 Bedforms on cohesive sediments	27
2.2.5 Flow Resistance.....	28
2.3 Incipient motion	31
2.3.1 General	31
2.3.2 Estimation of the incipient motion state.....	32
2.4 Modes of sediment transport.....	36
2.4.1 Rolling, sliding and saltation motion.....	37
2.4.2 Suspended motion.....	38

2.5	Sediment settling	39
2.5.1	General	39
2.5.2	Factors affecting fall velocity	39
2.6	Summary of existent sediment transport models	41
2.6.1	Bed load	41
2.6.2	Suspended load.....	42
Spatial distribution of grain sizes		46
3.1	Introduction.....	46
3.2	Surficial sea bed characteristics	47
3.3	Flow and wave patterns	50
3.3.1	Flow patterns.....	50
3.3.2	Wave patterns	52
3.4	Grain size sorting and representative flow conditions	57
3.5	Grain size sorting and representative wave conditions.....	60
3.6	Summary	66
Spatial and temporal variation of bedforms and roughness.....		68
4.1	Introduction.....	68
4.2	Bedform measurements.....	69
4.2.1	Side scan sonar SSS.....	70
4.2.2	Echo sounder.....	73
4.3	Prediction of bedform dimensions and roughness in tidal environments... 80	
4.3.1	Methodology	80
4.3.2	Representative flow condition.....	84
4.3.3	Bedforms in tidal flats and sand banks	86
4.4	Performance assessment of bedform predictions	88
4.4.1	Bedform Lengths	88
4.4.2	Bedform heights.....	89
4.5	Seasonal variation of bedform dimensions.....	91
4.5.1	Excess bed-shear stress parameter	92
4.5.2	Bedform types	93
4.5.3	Bedform lengths.....	94
4.5.4	Bedform heights.....	95
4.5.5	Bedform roughness	96
4.6	Summary	98
Sediment transport model		99
5.1	Introduction.....	99
5.2	Model input.....	100
5.2.1	Morphology input	100

5.2.2	Hydrodynamic input	102
5.2.3	Sedimentological input	106
5.3	Sediment dynamics	107
5.3.1	Boundary conditions for sediment transport	107
5.3.2	Sediment transfer functions at the flow-bed interface	108
5.3.3	Sediment transport	110
5.3.4	Interaction of several sediment fractions	112
5.4	Sensitivity analysis of the sediment transport model	113
5.4.1	Numerical parameters	114
5.4.2	Physical parameters	117
5.5	Summary	118
Prediction of sediment transport		120
6.1	Introduction.....	120
6.2	Measurement of suspended sediment concentrations.....	121
6.2.1	Measuring techniques.....	121
6.2.2	Field campaign.....	123
6.2.3	Sediment concentration profiles.....	125
6.3	Calibration of the sediment transport model	126
6.3.1	Calibration at spring tide.....	127
6.3.2	Calibration at neap tide	131
6.4	Validation of the sediment transport model.....	139
6.5	Evolution of the sediment transport model.....	141
6.6	Modelling applications.....	148
6.7	Summary	160
Conclusions		162
References.....		166
Erklärung.....		183
Curriculum Vitae.....		185

List of Figures

Figure 1.1 Coastal erosion case - Happisburgh.....	2
Figure 1.2 Coastal sedimentation case - Dog River.....	2
Figure 1.3 Study area.....	5
Figure 2.1 Shape characteristics of gravels from different environments [Reineck and Singh, 1980].....	8
Figure 2.2 Concept of sediment roundness [Wadell, 1932]	8
Figure 2.3 Visual determination of roundness [Powers, 1953].....	9
Figure 2.4 Form classification of particles [Zingg, 1935].....	10
Figure 2.5 Sphericity and form classification [Lees, 1964; Janoo,1998]	10
Figure 2.6 Relationship between fall velocity and nominal diameter [Interagency Report No. 12, 1957]	11
Figure 2.7 Sediment distribution on the tidal flats of the Dithmarschen Bight [Reimers, 2003].....	13
Figure 2.8 Hjulström’s diagram [Hjulström, 1939]	14
Figure 2.9 Side view of a typical bedform.....	18
Figure 2.10 Classification of bedforms [van Rijn, 1993]	20
Figure 2.11 Flow instability due to a surface of discontinuity [Prandtl, 1952; Rouse, 1947].....	23
Figure 2.12 Flow pattern over a bed discontinuity [Reineck and Singh, 1980].....	24
Figure 2.13 Criterion of ripple formation [Liu,1957]	25
Figure 2.14 Bedforms effect on bed shear stress. [Fredsoe, 1992]	27
Figure 2.15 Shields’ curve as a function of the particle parameter [Van Rijn, 1989] ..	32
Figure 2.16 Critical shear stress criterions [Van Rijn, 1989].....	33
Figure 2.17 Relationship between dimensionless critical velocity and Reynolds number [Yang, 1973]	36
Figure 2.18 Different modes of sediment transport.....	37
Figure 2.19 Criterions for the occurrence of suspended load [van Rijn, 1993].....	38
Figure 3.1 Thickness of the potentially mobile sediments [Asp, 2004]	48
Figure 3.2 Surficial seabed sediment distribution in the main tidal channels [Vela-Diez, 2001].....	48
Figure 3.3: Location and results of the bed sediments sampling during 1999 and 2000. Adapted after Reimers [2003]	49

Figure 3.4 Time-averaged velocities during a spring tidal cycle	50
Figure 3.5 Time-averaged velocities during a neap tidal cycle	51
Figure 3.6 Time-averaged shear stresses during a spring tidal cycle.....	51
Figure 3.7 Time-averaged shear stresses during a neap tidal cycle	51
Figure 3.8 Wave buoy locations - September 1996 campaign [Niemeyer et al., 1995]	53
Figure 3.9 Significant wave heights at the five wave buoy locations [Wilkens, 2004]	53
Figure 3.10 Wave rose at Pos 2 (left) and Sylt Island (right).....	54
Figure 3.11 Local wind measurements at the Büsum station.....	54
Figure 3.12 Wind rose for the Dithmarschen Bight [Luthardt, 1987]	55
Figure 3.13 Averaged wave height at the Dithmarschen Bight during the TTC.....	56
Figure 3.14 Averaged wave period at the Dithmarschen Bight during the TTC.....	56
Figure 3.15 Averaged wave length at the Dithmarschen Bight during the TTC.....	56
Figure 3.16 Maximum orbital velocities at the Dithmarschen Bight during the TTC.	57
Figure 3.17 Variation of d_{50} with flow conditions in the Dithmarschen Bight.....	58
Figure 3.18 Variation of d_{90} with flow conditions in the Dithmarschen Bight.....	58
Figure 3.19 Variation of mud content with flow conditions in the Dithmarschen Bight	59
Figure 3.20 Variation of d_{50} with maximum velocities computed in a TTC	59
Figure 3.21 Grain size dataset from the Dithmarschen Bight superimposed on Hjulström diagram	60
Figure 3.22 Classification of tidal areas. Hayes [1979]	61
Figure 3.23 Spatial variation of the tidal range at the intertidal zone	61
Figure 3.24 Variation of d_{50} with typical wave parameters averaged over the TTC...	62
Figure 3.25 Variation of d_{50} with maximum wave parameters computed for a TTC..	63
Figure 3.26 Wave effect on the equilibrium grain sizes	64
Figure 3.27 Relationship for the equilibrium grain sizes on the tidal flats.....	64
Figure 3.28 Assessment of performance for grain size predictions on the tidal flats .	65
Figure 3.29 Predicted (background) and measured (circles) grain sizes in the study area	66
Figure 4.1 Field measurements of bedforms in the tidal channels [Mayerle et al., 2005]	70
Figure 4.2 Klein 595 side scan sonar	70
Figure 4.3 Typical SSS images [Mayerle et al. 2005]	71
Figure 4.4 Estimation of ripple heights by side scan sonar	72
Figure 4.5 Spatial variation of bedforms [Mayerle et al., 2002].....	73
Figure 4.6 Frequency distribution of bedform lengths in the Dithmarschen channels	73
Figure 4.7 Seafloor profiles from a Fahrentholz Echo sounder, [Razakafoniaina, 2001]	74
Figure 4.8 Frequency distribution of bedform heights.....	75

Figure 4.9 Seafloor profiles from a Lowrance echo sounder [Pramono, 2005]	76
Figure 4.10 Temporal variation of bedform dimensions during a spring tidal cycle. Modified after Pramono [2005].....	78
Figure 4.11 Migration of bedforms during a spring tidal cycle [Mayerle et al., 2005]	79
Figure 4.12 Seafloor profiles in muddy areas of the tidal channels [Pramono, 2005].	79
Figure 4.13 Bedform size behavior under unsteady cyclic flow (Low hydraulic regime)	81
Figure 4.14 Similitude of bedform size behavior under unsteady and steady flows..	81
Figure 4.15 Proposed methodology for defining bedform dimensions and roughness	84
Figure 4.16 Bedform size behavior under cyclic flow conditions	85
Figure 4.17 Determination of the RFC on a semi-diurnal tidal flow	86
Figure 4.18 Bedform regimes in oscillatory flow [Allen, 1982]	87
Figure 4.19 Ratio \bar{u}'_c/\bar{u}'_w in the Dithmarschen Bight.....	88
Figure 4.20 Frequency distribution of λ/h in the tidal channels.....	88
Figure 4.21 Comparison of the bulk of bedform lengths	89
Figure 4.22 Prediction of bedform heights in the Dithmarschen Bight.....	89
Figure 4.23 Comparison of the bulk of bedform heights	90
Figure 4.24 Seafloor topography at the surveyed area [Pramono, 2005]	90
Figure 4.25 Bedform predictions on April 17, 2003.....	91
Figure 4.26 Excess bed-shear stress predictions at the RFC in the Dithmarschen Bight	93
Figure 4.27 Bedform type predictions at the RFC in the Dithmarschen Bight.....	94
Figure 4.28 Bedform length predictions in the Dithmarschen Bight.....	95
Figure 4.29 Bedform height predictions in the Dithmarschen Bight.....	96
Figure 4.30 Bedform roughness predictions in the Dithmarschen Bight.....	97
Figure 5.1 Model bathymetry.....	101
Figure 5.2 The curvilinear model grid	103
Figure 5.3 Open sea boundaries for the study area	105
Figure 5.4 Nesting sequence for the generation of open sea boundary conditions for the Dithmarschen Bight [Winter, 2003]	106
Figure 5.5 Lag phase between current velocities and sediment load [Van Rijn, 1989]	111
Figure 5.6 Monitoring stations in the Dithmarschen Bight	114
Figure 5.7 Time step sensitivity	115
Figure 5.8 Definition of the warming-up period – Tertius station	116
Figure 5.9 Sensitivity of suspended sediment concentrations due to critical shear erosion (left) and erosion rate (right) variations at the Tertius station	118
Figure 6.1 Sampler mounted with CTD equipment	122

Figure 6.2 Optical beam transmissometer.....	123
Figure 6.3 Measuring transects in the tidal channels of the Dithmarschen Bight [Poerbandono, 2003].....	124
Figure 6.4 Cross-sectional variations of measured concentration [Poerbandono, 2005]	126
Figure 6.5 Suspended concentrations at spring tidal cycle (Transect T1, March 22)	134
Figure 6.6 Suspended concentrations at spring tidal cycle (Transect T2, March 21)	134
Figure 6.7 Suspended concentrations at spring tidal cycle (Transect T3, March 23)	135
Figure 6.8 Suspended concentrations at neap tidal cycle (Transect T1, December 5)	136
Figure 6.9 Suspended concentrations at neap tidal cycle (Transect T2, December 5)	136
Figure 6.10 Suspended concentrations at neap tidal cycle (Transect T3, December 6)	137
Figure 6.11 Water level lag-phases at spring tidal cycle (Büsum station)	138
Figure 6.12 Water level lag-phases at neap tidal cycle (Büsum station)	138
Figure 6.13 Definition of non-stationary physical parameters.....	140
Figure 6.14 Depth-integrated suspended sediment concentrations at cross section T1 for the five cases considered on the evolution of the sediment transport model	143
Figure 6.15 Depth-integrated suspended sediment concentrations at cross section T2 for the five cases considered on the evolution of the sediment transport model	144
Figure 6.16 Depth-integrated suspended sediment concentrations at cross section T3 for the five cases considered on the evolution of the sediment transport model	145
Figure 6.17 Bed load transport at cross section T1.....	146
Figure 6.18 Bed load transport at cross section T2.....	147
Figure 6.19 Bed load transport at cross section T3.....	147
Figure 6.20 Depth-averaged suspended sediment concentration for high currents during a spring tide.....	149
Figure 6.21 Depth-averaged suspended sediment concentration for slack water during a spring tide.....	150
Figure 6.22 Depth-averaged suspended sediment concentration for high currents during a neap tide	151
Figure 6.23 Depth-averaged suspended sediment concentration for slack water during a neap tide	152
Figure 6.24 Suspended load transport during a spring tide.....	153
Figure 6.25 Suspended load transport during a neap tide	154
Figure 6.26 Cumulative volume of sediment through cross sections T1, T2 and T3 during spring phase	155

Figure 6.27 Cumulative volume of suspended sediment through cross sections T1, T2 and T3 during neap phase.....	156
Figure 6.28 Cumulative volume of sediment through cross section T2' extending through the entire width of the domain.....	158
Figure 6.29 Cumulative volume of bed load through cross sections T1, T2 and T3 .	159
Figure 6.30 Cumulative volume of bed load through cross section T2'	160

List of Tables

Table 2.1: Plasticity classification	16
Table 2.2: Summary of bedform classification [Van Rijn, 1993].....	21
Table 2.3: Estimation of bedform dimensions at lower flow regime [Van Rijn, 1993]	26
Table 2.4 Hydraulic regimes and resistance coefficients.....	30
Table 2.5 Factors influencing the critical erosion shear stress of cohesive soils. Adapted after Briaud [1999].....	34
Table 2.6 Representative diameter of the suspended sediment.....	40
Table 3.1: Monthly averages of wind speed at Büsum station.....	55
Table 3.2: Typical wave forcing at the Dithmarschen Bight	55
Table 4.1: Tidal ranges during SSS campaigns	72
Table 4.2: Bedform heights and lengths at the inner Piep channel [Pramono, 2005]..	77
Table 4.3: Grain and form roughness [van Rijn, 1993]	82
Table 4.4: Summary of grain and form roughness equations.....	83
Table 5.1: Non-cohesive sediment constituents used in the sediment transport model	113
Table 5.2: Set of additional numerical parameters.....	116
Table 5.3: Sensitivity analysis of physical parameters (non-cohesive materials)	117
Table 5.4: Sensitivity analysis of physical parameters (cohesive materials).....	117
Table 5.5: Set of physical parameters without sensitivity analysis.....	118
Table 6.1: Datasets of suspended sediment concentration [Poerbandono, 2003]	124
Table 6.2: Calibration of physical parameters at spring tide	129
Table 6.3: Performance assessment of numerical model after first calibration round	130
Table 6.4: Best parameter settings at spring tidal cycle.....	131
Table 6.5: Best calibration settings at neap and spring tidal cycles	132
Table 6.6: Variation range of calibrated input parameters	133
Table 6.7: Parameter settings for the validation study	141
Table 6.8: Performance assessment of sediment model	141

Notations

a	Longest particle axis, Van Rijn's reference height
A	Wave amplitude
\hat{A}_s	Orbital excursion
$AKSFAC$	Multiplication factor for Van Rijn's reference height
b	Intermediate particle axis, flow width
c	Shortest particle axis, suspended sediment concentration, soil cohesion
c_a	Mass concentration at reference height a .
c_o	Maximum concentration
C	Chezy resistance coefficient
C'	Grain related Chezy coefficient
C_D	Drag coefficient
C_s	Du Boys' coefficient
C_{se}	Local equilibrium concentration
d	Particle size
d_s	Representative diameter of suspended sediment
d_{50}	Medium particle diameter of bed material
d_{90}	Sediment grain diameter in which 90% of sample by mass is smaller
D	Sediment deposition rate
D_*	Dimensionless particle parameter
e_b	Efficiency factor
E	Sediment erosion rate
f	Friction factor
f'_c	Current-related friction factor
f'_w	Wave-related friction factor
F_f	Resistance force
g	Acceleration of gravity
$G_{\xi\xi} G_{\eta\eta}$	Coefficients used to transform curvilinear to rectangular coordinates
h	Water depth
H_f	Towfish height
i	Energy gradient
K	Factor relating sediment discharge to flow velocity

k_s	Equivalent roughness size
k'_s	Grain roughness
k''_s	Form roughness
L_s	Slant range of the shadow
M	Erosion rate coefficient
n	Manning resistance coefficient
N	Number of data
P	Roundness
q_B	Volume rate of bed load discharge per unit width
q_S	Volume rate of suspended load discharge per unit width
Q	Discharge source or sink per unit area
$R-r$	Radius, hydraulic radius, slant range
Re	Reynolds number
rt	Response time of bedforms to new flow conditions
s	Specific density
S_f	Slope of energy grade line
SF	Shape factor
S_o	Bed slope
SUS	Multiplication factor for suspended sediment reference concentration
t	Temporal coordinate
T	Excess bed-shear stress parameter, wave period
T_s	Dimensionless adaptation time
u	Depth integrated velocity in x, ξ direction
u_*	Bed shear velocity
$u_{*,c}$	Current-related effective bed-shear velocity
$u_{*,w}$	Wave-related effective bed-shear velocity
u_o	Flow velocity near bed
\hat{U}_δ	Peak orbital velocity
v	Depth integrated velocity in y, η direction
v'	Velocity fluctuation in y direction
w	Velocity in z direction
w_l	Water content limit
w_s	Settling velocity in a suspension
W	Particle weight
x, y, z	Spatial coordinate axes
Z, Z'	Suspension numbers
β	Angle of bottom slope, Rouse number, ratio of sediment and fluid mixing
δ	Viscous sublayer thickness
Δ	Height of bedforms

\mathcal{E}	Empirical floc erosion rate
\mathcal{E}_s	Sediment transfer or mixing coefficient
ϕ	Angle of repose
\mathcal{N}	Dune presence factor
\mathcal{R}	Ripple presence factor
η	Bed elevation
K	Constant of Von Karman
λ	Length of bedforms
λ_1	Horizontal projection of stoss side
λ_2	Horizontal projection of lee side
ν	Kinematic viscosity coefficient
θ	Particle mobility parameter
θ_{cr}	Critical Shields parameter
ρ	Density of fluid
ρ_s	Density of solids
σ	Normal pressure on the rupture plane
τ	Shear strength
τ_b	Bed shear stress
$\tau_{b,cr,s}$	Critical bed-shear stress on a sloping bottom (non-cohesive sediments)
$\tau_{b,cr}$	Critical bed-shear stress on a horizontal bottom (non-cohesive sediments)
$\tau_{cr,e}$	Critical erosion shear stress (cohesive sediments)
$\tau_{cr,s}$	Critical deposition shear stress (cohesive sediments)
$\tau_{b,max}$	Local maximum shear stress during a tidal cycle
$\tau_{b'}$	Bed-shear stress related to grains
Ψ	Correction factor related to turbulence damping and hindered settling
ζ	Free surface elevation above reference (datum)

Chapter 1

Introduction

1.1 General

This research continues a series of investigations developed in the coastal zone of the Dithmarschen Bight at the German North Sea coast. Human settlement, land reclamation and continued sea-level rise have brought concerns about their influence on the morphological evolution of the study area and the possibility that natural features of the Wadden Sea could be lost. The Dithmarschen coastal region was completely surveyed for the first time in 1838 by standard hydrographic techniques, which resulted in the publication of the first reliable chart of the area in 1846. Recently, over the period 2000 to 2002 the project PROMORPH developed, calibrated, validated and applied process-based models for the simulation of medium-scale morphodynamics in the central Dithmarschen Bight.

The main concern in this investigation has been the study of sediment dynamics given their relevance to morphological developments. The study of sediment dynamics is strongly tied to hydrodynamics and morphodynamics through feedback and complex non-linear interactions. This process is normally modeled in a single temporal step-by-step mode, where each module (hydrodynamics, sediment dynamics and morphodynamics) is treated separately and linked afterwards into the system through input or output data. However, the actual phenomenon shows a simultaneous interaction between these three modules.

In spite of the lack of tools to model this simultaneous process that represents a complex multi-phase phenomenon, some reliable approaches are available for stand-alone description of sediment dynamics. These approaches have been based on equilibrium transport formulae and the advection-diffusion equation, which have led to reasonably good predictions that can handle most of the practical applications in the engineering fields.

Engineering applications regarding sediment dynamics might be roughly summarized by erosional or depositional developments. In near shore areas, changes

due to erosional processes could lead to a loss of waterfront property and aesthetic value, as well as an increase in flooding vulnerability during storms. On the other hand, changes due to sedimentation processes might imply immense expenses on maintenance of navigation channels, harbors and shipping installations.

Erosion and sedimentation are key processes determining the coastline evolution. Their pace can be altered by human interference (e.g. dikes, land reclamation, coastal structures) and natural factors such as climate change and sea level rise. Figures 1.1 and 1.2 depict both cases in coastal areas.



Figure 1.1 Coastal erosion case - Happisburgh



Figure 1.2 Coastal sedimentation case - Dog River

1.2 Objectives

The main part of this research is aimed to improve the numerical prediction of sediment transport in a selected tidal dominated area of the German North Sea coast. Therefore, the development of a robust sediment transport model is intended. The model will be based on a detailed description (spatial-temporal) of relevant hydrodynamic, morphological and sedimentological parameters to enable its application under a wider range of conditions.

A comprehensive dataset of field measurements as well as a set of process-based models are used to design some methodologies to predict sediment properties, seafloor morphology and sediment transport rates in the study area.

Particularly, this research will focus on the following aspects and their relevance in sediment dynamics:

- Non-uniform distribution of sediment grain sizes over the study area;
- Spatial and temporal variation of bedforms and equivalent roughness sizes;
- Sediment availability;
- Dynamics of cohesive and non-cohesive sediments;
- Seasonal variation of sediment properties (cohesive materials) through the neap-spring cycle, such as critical erosion shear stress, critical deposition shear stress, settling velocity, fraction of cohesive content and erosion rate coefficient.

Each of these aspects has been intended to improve the predictive ability of the sediment transport model. Their individual effect in the model accuracy is assessed in order to define its relevance and priority on future investigations regarding sediment dynamics in tidal areas.

1.3 Basics of sediment transport models

Available methodologies to predict sediment transport rates have been derived from analytical or semi-empirical studies, which have largely used laboratory and river observations for validation purposes. These methods are supported by the physical concept that sediment transport is a phenomenon with a threshold of motion and a maximum capacity load that can be restricted through the actual sediment supply. Under these general concepts a large set of methodologies are available, from which the most suitable one should fit particular characteristics of the interest area in terms of flow conditions, sediment properties and geological features; but even so, none of them are ready to be used at any place before validation tests.

Sediment transport models have included functions to describe physical processes concerning each stage in the sediment motion cycle: entrainment, transport and deposition. The entrainment process considers the incipient motion stage and the breaking of inertial forces (cohesion and friction) by shear stresses due to currents and waves. Sediment transport regards the motion of grains and its classification into bed or suspended load, where gravity and turbulence are, respectively, the governing factors. The deposition process involves the settling of particles on the bed surface. Its analysis considers different aspects like hindered settling effect, turbulence, sediments heterogeneity and grain shape.

Recent models have implemented routines to simulate the behavior of sediment mixtures that consider entrainment-deposition rates of individual fractions and their mutual interactions. These are improvements to former models that only sum up the results for independent fractions. There are also additional efforts regarding feedback processes between sediment and flow models such as the effect of sediment on fluid density, which can create density currents and affect the vertical turbulent mixing.

1.4 Outline

This research work is presented in seven chapters. In chapter 1, general notes containing the basics of sediment models, objectives and the study area are given. Chapter 2 describes some physical concepts involved in flow and sediment dynamics. Sediment properties, morphological features and flow aspects are regarded briefly before consideration of the incipient motion, modes of sediment transport and sediment settling concepts. Chapter 3 presents the methodology to predict the spatial distribution of grain sizes in the Dithmarschen Bight. Chapter 4 presents a methodology to define the spatial and temporal variation of bedforms and roughness in a tidal environment. Throughout Chapter 5 the sediment transport model is set up. Chapter 6 deals with the calibration and validation of the sediment model, the sediment dynamics in the study area and the relevance of the proposed methodologies in terms of the transport model accuracy. Finally, Chapter 7 is devoted to stating the main conclusions drawn through this research.

1.5 Study area

Investigations were carried out between the Eider and Elbe estuaries in the southwestern area of the German North Sea coast. The morphology of the study area is dominated by tidal flats, tidal channels and sandbanks over the outer region. The

intertidal channels, i.e. Norderpiep located in the northwest part of the domain and Süderpiep in the southwest, unite inside the study area to form the Piep channel (Fig. 1.3). Maximum water depths in the channels are in the order of 23m, and approximately 50% of the area is intertidal. The hydrodynamics and sediment dynamics are driven by the combined effects of tides, waves and wind-induced currents. Under normal conditions the tidal influence prevails. The semi-diurnal tide has a mean range of 3.2m, which varies temporally (between 2.4m at neap tides and 4.2m at spring tides) and spatially. Westerly winds (SW-W) prevail. Maximum wave heights in the outer western region are up to 3.5m with a mean value about 0.8m, though waves break along the outer margins of the area of interest. Maximum current velocities of 2m/s have been observed in the channels. The spatial and temporal variations of the currents are strongly influenced by the complex bathymetry and gravitational forces respectively. Storm surges can result in water level set-ups of up to 5m, favouring wave propagation into normally shallow regions. The surficial seabed sediment in the tidal flats and channels consists mainly of fine sands with varying proportions of silt and clay. The grain sizes range from 60 to 230 μm . Coarser sediments are located in the outer wave exposed areas while finer particles occupy sheltered regions close to the high water line. Relative large bedforms such as megaripples are mainly observed along the tidal channels with lengths varying between 3m to 22m. In the deeper areas, outcropping of consolidated cohesive sediments hinders erosion and formation of bedforms.

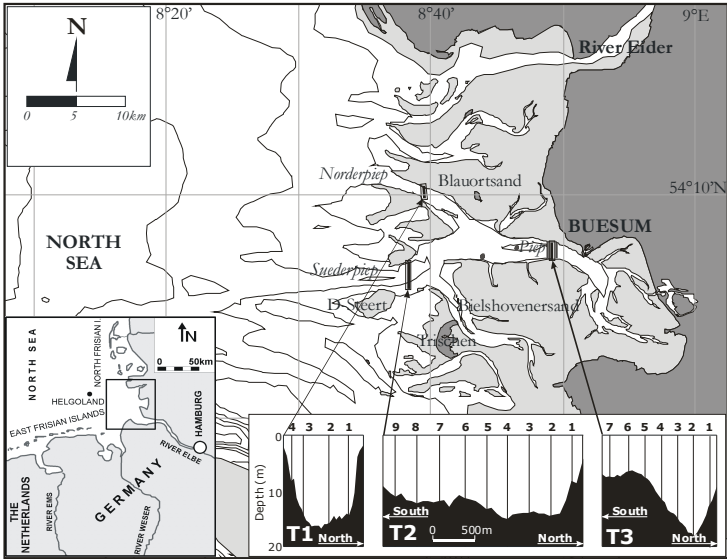


Figure 1.3 Study area

Chapter 2

Literature review

2.1 Introduction

The motion of sediment particles occurs in a wide range of phenomena, where its distinctive character is defined by the following essential features [Bagnold, 1966]:

- The motion is a shearing motion wherein successive layers of solids are sheared over one another.
- An impelling or tractive force, applied in the direction of motion, is necessary to maintain the motion.
- The array of solids is immersed in some pervading fluid, either a liquid or a gas, and this fluid also is under shear.
- The solids are heavier than the fluid, and are therefore pulled downward toward a lower boundary or bed.

The above features suggest that higher sediment concentrations under current or wave forcings do mainly occur in the near-bed region, where bed shear stresses resulting from the fluid flow are required to start and maintain the particles motion. Bed shear stress becomes a key element in this study and therefore it is discussed in more detail on the next sections. As bed shear stresses depend on the local grain sizes, bedforms and flow hydraulic regime, this chapter will start with a brief description of these topics.

Later, the emphasis is headed to the three main processes steering sediment motion i.e. entrainment, transportation and deposition. Finally, a selection of existent sediment transport models is presented.

2.2 General

Movement of non-cohesive sediment depends on the physical properties of individual particles, such as size, shape and density. These properties play an

important role in all the stages of sediment transport e.g. entrainment, transportation and deposition, which will be subsequently explained in this chapter.

This section presents non-cohesive sediments as individual particles whose properties and classifications are considered. However, it is pointed out that current sediment models consider bulk properties instead of individual grain characteristics. Therefore, models generally appeal to medium continuum's principles rather than implementing the properties of every single grain into the main governing equations of sediment transport.

Fine sediments or sediment mixtures with a clay content of about 10% or higher present internal electrostatic forces that become comparable to or exceed the gravity force [Van Rijn, 1989]. The cohesive particles tend to stick together and behave as aggregates instead of individual particles. Cohesion, plasticity and flocculation are some representative properties posing great effects on the motion of cohesive sediments.

2.2.1 Physical properties of individual non-cohesive particles

2.2.1.1 Size

The grain size parameter defines the characteristic length of sediment grains. It is essential on the mobility classification of sediment particles under currents or waves. The grain size is also a measure of the energy of the basin of deposition [Reineck and Singh, 1980]. The grain size is fundamental in sediment transport studies. It directly affects all sediment motion stages. Moreover, it might indirectly affect sediment dynamics through the effect on flow resistance (skin friction) and bedforms (classification and dimensions).

Grain sizes range from very large boulders to very fine clays, which can be hardly entrained or settled respectively. Given the irregular or non-spherical shape of sediment particles, it is important to define a characteristic length for each grain. A typical grain-size classification is shown in Raudkivi [1976]. Some common definitions for the characteristic length are:

- **Sieve diameter:** match the mesh size of the sieve where the grain is retained. It is used for sand and fine gravel.
- **Equivalent or sedimentation diameter:** diameter of a sphere with the same density and terminal settling velocity in a standard fluid. Method used for clays, silts and fine sands.
- **Nominal diameter:** diameter of a sphere of equal volume. Used for larger particles.
- **Tri-axial dimensions:** cubic root of three perpendicular grain sizes' product.

2.2.1.2 Shape

Grain shape comprises the overall external morphology or the particle geometry including surface texture, roundness and form. Although grains' shapes are mostly determined by their composition, internal structure and original form of minerals; they can also be affected by the environment energy, the length of the transport path and the available time to wear and tear the grains [Reineck and Singh, 1980]. Figure 2.1 presents the characteristic shape of grains on different environments: a) Aeolian environment (ventifacts); b) High energy sea coast (more or less spherical gravels); c) Low-energy sea coasts (flat gravels); d) Rivers (rod-shaped gravels); e) Glacial moraines (tabular with pentagonal outline); f) Glacial and/or frost areas (unworked frosted pieces).

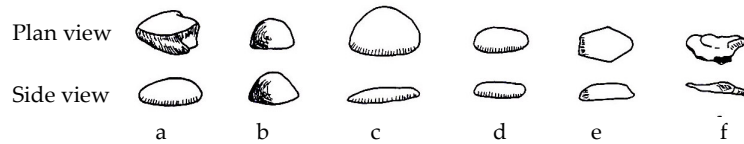


Figure 2.1 Shape characteristics of gravels from different environments [Reineck and Singh, 1980]

Methods to studying sediment shapes vary with coarse or fine grains and 2-D and 3-D analyses are available for support. Some criteria used for shape classifications are roundness, sphericity and rollability.

Roundness (P) is defined as the ratio of the average of the corners and the edges of a particle to the radius of a circle inscribed in the maximum projected area of the particle (see Figure 2.2). Therefore, roundness of grains is a measure of sharpness of edges and corners [Reineck and Singh, 1980]. P is computed through Wadell's [1932] approach as follows:

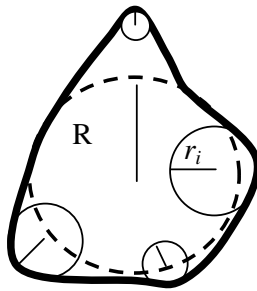


Figure 2.2 Concept of sediment roundness [Wadell, 1932]

$$P = \frac{\sum_{i=1}^N \left(\frac{r_i}{R} \right)}{N} \quad (2.1)$$

The better-rounded sediments indicate a prolonged mechanical wear and tear and therefore a long transport path. The roundness of sediments also shows a strong relationship to grain sizes. Generally, coarser grains possess a better roundness than finer ones under similar wear-tear conditions and primary anisotropy.

As defined by equation 2.1 roundness measurements could become highly inconvenient in practice, especially for fine grains. Hence, the most common method of defining grain roundness is based on a visual classification, leading to six classes (see Fig. 2.3): a) Very angular; b) Angular; c) Subangular; d) Subrounded; e) Rounded; f) Well rounded.

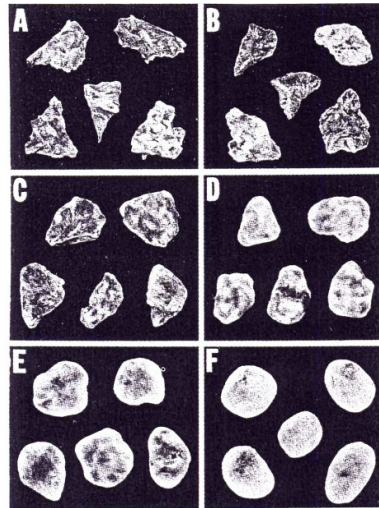


Figure 2.3 Visual determination of roundness [Powers, 1953]

Sphericity (Ψ) is another measurement of grain shape and it is defined as the ratio of surface area of the particle to that of a sphere of the same volume. It is independent from roundness. However, as in the previous case the practical difficulty to measure the sphericity led to an alternative methodology. The following expression by Uthus et al. [2005] defines this attribute in terms of the mutually perpendicular grain axes (a, b, c).

$$\Psi = \frac{12.8 \left(\sqrt[3]{\frac{c^2}{ab}} \right)}{1 + \frac{c}{b} \left(1 + \frac{b}{a} \right) + 6 \sqrt{1 + \frac{c^2}{b^2} \left(1 + \frac{b^2}{a^2} \right)}} \quad (2.2)$$

with: a : longest particle axis.

b : intermediate axis.

c : shortest axis.

The variation in proportion of the three particle axes leads to the following classification onto disc-shaped, spherical, blade-like, or rod-like particles (see Fig. 2.4).

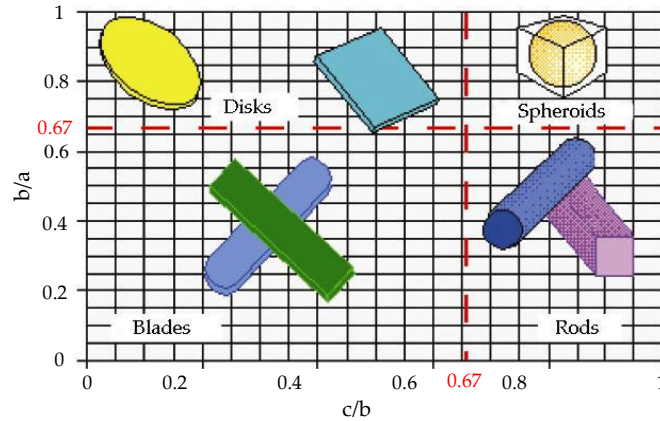


Figure 2.4 Form classification of particles [Zingg, 1935]

However, the sphericity factor has little application on sediment dynamics as it was defined above. Therefore, other related parameters such as the shape factors, SF and F , by McNown [1951] and Zingg [1935] respectively, are used.

$$SF = \frac{c}{\sqrt{ab}} \quad (2.3)$$

$$F = ca/b^2 \quad (2.4)$$

The particle shape factors can also be correlated to sphericity values, as shown in Figure 2.5. Generally, sphericity tends to increase with increasing particle size as the roundness attribute does, but it is only slightly affected by the wearing away of the sharp edges.

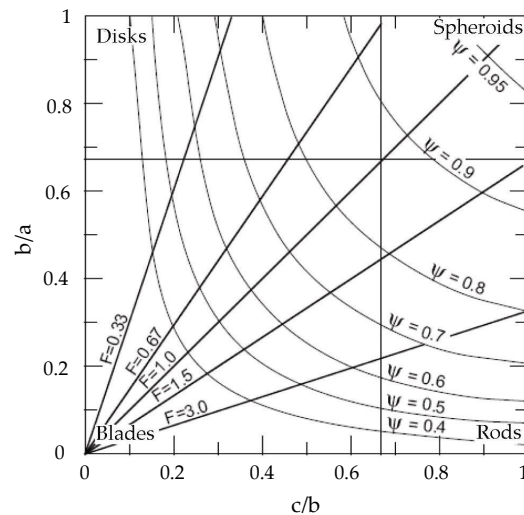


Figure 2.5 Sphericity and form classification [Lees, 1964; Janoo, 1998]

Rollability is a concept introduced by Winkelnoten [1971]. It measures the ease with which a sediment rolls after the initial pivot. Hence, rollability has a direct bearing on the dynamic behavior of the grains during transport processes. It shows a positive correlation with settling velocity and a negative correlation with transportability. It was found, in general, that receiving environments and lag deposits are characterized by low and high rollabilities respectively.

Grain shape effects on sediment dynamics, major effects of grain shape on sediment dynamics refer to the fall velocity and the critical shear stress on sloping bottoms. Efforts to quantify the shape effect into these parameters that affect both entrainment and sedimentation processes are outlined as follows.

Shape effect on fall velocity has been determined by different empirical works, as displayed in the example of Figure 2.6. This figure shows a minor or even negligible effect for very fine sand or smaller particles. However, bigger sized particles present discrepancies in fall velocities larger than 30% for the range of shape factors *SF* between 0.5 and 0.9. In this figure a positive correlation between shape factor and fall velocity is also observed.

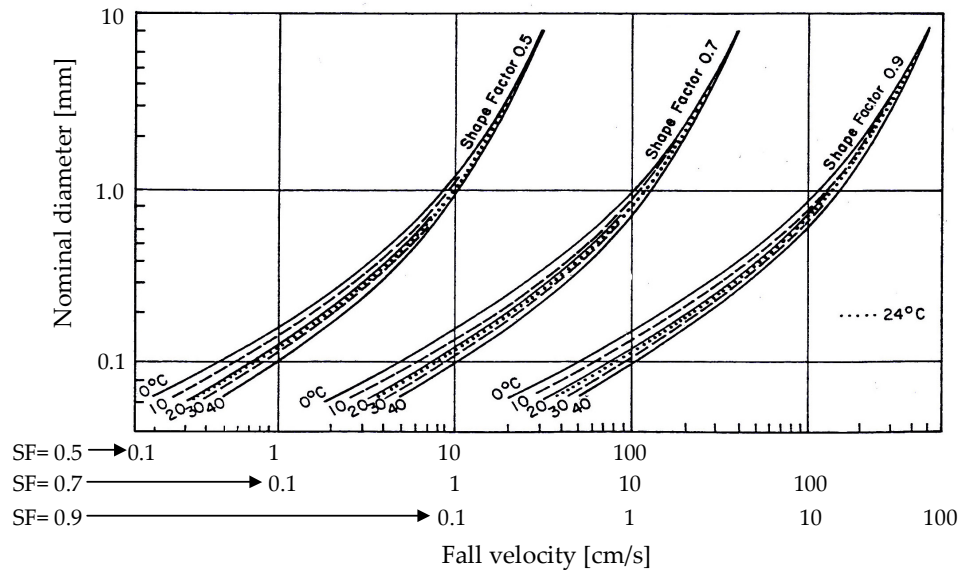


Figure 2.6 Relationship between fall velocity and nominal diameter [Interagency Report No. 12, 1957]

The particle shape affects critical shear stresses only on sloping bottoms. The critical shear stress depends on the angle of repose, as shown in eq. 2.5 by Van Rijn [1989], which is affected in turn by the sediment shape.

$$\tau_{b,cr,s} = \tau_{b,cr} \frac{\sin(\phi - \beta)}{\sin \phi} \tag{2.5}$$

with: $\tau_{b,cr,s}$: critical bed-shear stress on a sloping bottom

$\tau_{b,cr}$:	critical bed-shear stress on a horizontal bottom
ϕ :	angle of repose
β :	angle of bottom slope

Unfortunately, there is not yet a quantitative way to determine the relationship between particle shape and the angle of repose. General patterns show that flatter particles can present a high angle of repose, which is more notorious when grains are stacked like bricks with flat sides touching and nearly level. The opposite happens, however, with round grains, where the angle of repose decreases.

2.2.1.3 Spatial and temporal variability of sediment sizes

Temporal variability of marine shallow sediments is mainly caused by variations in the hydrodynamic conditions along the littoral zone or in the sediment characteristics of the source areas [Guillén et al. 2004]. Temporal changes of sediment sizes have a lower magnitude than spatial ones [Medina et al., 1994]. Therefore, their assessment is rarely considered on sediment transport predictions. However, their effects should be verified under medium and long-term morphological simulations where the growing accumulation of little inaccuracies might become significant.

General aspects that can imply temporal variability of grain-sizes over the study area are described as follows: (1) Tidal forcing, which involves daily and weekly hydrodynamic variations through the semi-diurnal and the neap-spring cycles respectively. Expected variations on shear stresses along these cycles could evolve on changes of sediment characteristics (at least theoretically); (2) On a larger time scale the effect of storms on grain sizes can be considered. Since nearshore areas buffer the unleashed wave energy, they can consequently undergo changes in morphology and sediment features; (3) The proximity to river mouths also implies seasonal variability of sediment grain-sizes due to deposition of ephemeral sediment layers during floods. The ephemeral layers can be subsequently reworked by means of currents, waves or bioturbation and therefore a continuous process of surficial bed variability is started; (4) Biological activity of benthic fauna or flora also suggests bed sediment changes (bioturbation processes) either on muddy or sandy environments; (5) Fishing activities could become also a chief element in the analysis of the temporal variability of sediment characteristics over unprotected regions exposed to highly-intensive trawling practices.

The second part of this section deals with the study of the spatial variability of grain sizes in nearshore areas. Spatial variability of geological features, morphology and hydrodynamic forcing in a specific area tend to produce a heterogeneous spatial distribution of grain sizes, which has a remarkable influence on the sediment transport rates. However, the common shortage of data required to define the spatial distribution of grain sizes is still a drawback on the setup of any sediment model.

To overcome this drawback, different approaches have been presented by several authors. In the beginning, qualitative approximations of grain size distributions were published, which, in general, stated that offshore of breakers the particle size decreases with increasing depth and onshore of breakers grain size decreases or increases for sand and shingle beaches respectively [Raudkivi, 1976].

In tidal flats, according with Reineck and Singh [1980], the grain size distribution exhibits a characteristic pattern. Near the high-water line and watershed, sediments are muddy. The intertidal region near the low-water line is sandy. The muddy zone grades gradually into sandy intertidal flats. The transition part is known as mixed intertidal flats. The reasons for this characteristic distribution of sediment on tidal flats are because of the energy and partly the transport mechanism. Near the low-water line the wave activity is strongest and active for the longest time as compared to higher parts of the intertidal zone. Thus, the sand is enriched near the low-water line. This pattern can be observed in several regions e.g. the Jade Bay [Gadow, 1970], the Jiangsu coast [Wang and Ke, 1997], the Dithmarschen Bight [Ricklefs and Asp, 2005]. Figure 2.7 shows the spatial distribution of sediments on the tidal flats of the Dithmarschen Bight.

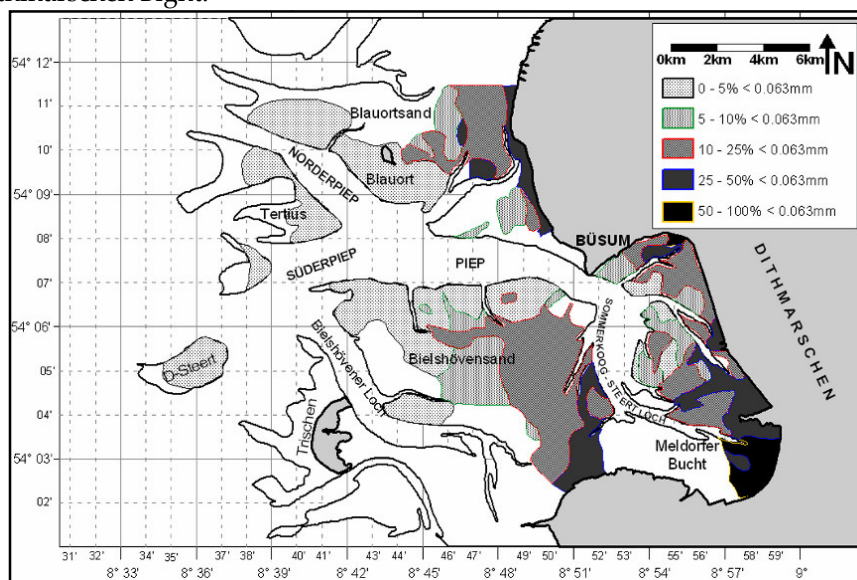


Figure 2.7 Sediment distribution on the tidal flats of the Dithmarschen Bight [Reimers, 2003]

Later on quantitative and rather successful methodologies predicted the grain size sorting by means of the relationship between critical particle size and critical velocities or shear stresses. These relationships are still largely used through the Hjulström (see Fig. 2.8) or Shield diagrams (see Fig. 2.15).

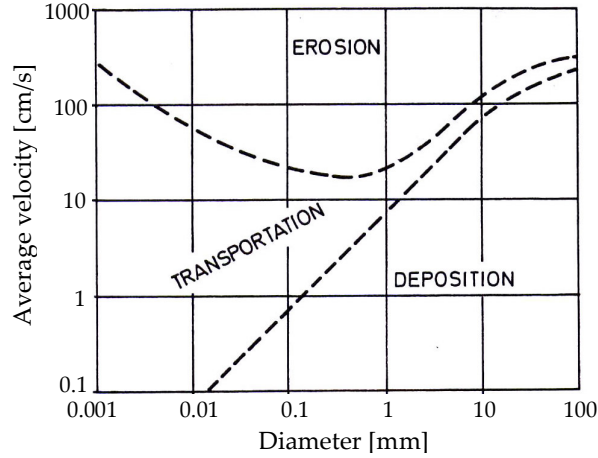


Figure 2.8 Hjulström's diagram [Hjulström, 1939]

Application of the Hjulström diagram on the determination of the initial particle size distribution in tidal areas was reported by Hirschhäuser et al. [1998]. A description of the non-cohesive part of the Hjulström curve [Zanke, 1995] is defined as:

$$V_{mcr} = 2.8(g\rho'd)^{0.5} \quad (2.6)$$

Where:

V_{mcr} : characteristic velocity (max. velocity occurring during one tidal cycle)

d : characteristic diameter; d_{90} was found the most suitable for the tidal channels of the North-Frisian-Wadden-Sea [Hirschhäuser, 1997]

A different quantitative approach based on waves rather than current energy is also available, but applicable on sand or shingle beaches with slopes ranging from 1:5 to 1:90. The coarser the material the greater is the required wave asymmetry and slope. The spatial distribution of grain sizes along the beach profile is given according with the equation 2.7 [Bascom, 1951]:

$$d \approx 1.9\sqrt{S_o} \quad (2.7)$$

With: d : particle size [mm]

S_o : bed slope

This grading is caused by the energy difference in flow up and down the beach. As waves run up a slope they become asymmetric in shape, so that the forces up the slope are greater than during the seaward motion under the trough. Therefore, on the equilibrium profile the differences of wave force balance the grains' weight component, where the coarser the material the greater the wave force difference and the slope.

It seems that the two major theories presented in the past to explain the selective shore-normal sorting of grain sizes are the hypothesis of asymmetrical threshold

under waves and the null point hypothesis [Horn, 1992], both hypotheses being grounded on asymmetric wave behavior.

The asymmetrical threshold hypothesis is applicable to shallow areas where waves start to be affected due to lower depths. A number of authors have recognised the significance of wave-induced asymmetrical orbital velocities and suggested the hypothesis of asymmetrical sediment thresholds under waves [Cornish, 1898; Bagnold, 1940; Inman, 1949; King, 1972; Carter, 1988]. Observations under waves show an onshore motion with a high velocity and short duration, and an offshore motion with a lower velocity but a longer duration. This fact indicates that higher onshore velocities would produce a shear stress large enough to initiate motion for both large and small sediment particles, while the lower offshore velocities would only exceed the threshold shear stress for the smaller particles. Thus, this mechanism would act selectively to drive larger particles onshore, with a net offshore transport of finer particles.

The null-point hypothesis includes the effects of bed sloping in the asymmetrical threshold theory. It was first proposed by Cornaglia [1889], and further developed by several authors [Ippen et al., 1955; Eagleson et al., 1959-1961-1963; Miller et al., 1958-1964]. The null-point hypothesis combines flow asymmetry due to waves running up the slope with the gravitational field acting on grains. This hypothesis suggests that for every grain size exists a unique depth at which the wave-induced onshore flows exactly balance the offshore force of gravity. The position of zero net transport is called the null-point and should be located further onshore for large grains than for smaller ones.

To test the hypothesis of asymmetrical thresholds under waves, Horn [1991] put this hypothesis into a quantitative form. The threshold grain size is calculated using the expression of Komar and Miller [1975] for both the onshore and offshore peak flows (see eq. 2.8). Hence, the two threshold grain diameters predicted can be used as the limits of the grain size distribution at any particular water depth or location on the beach profile.

$$U_{w,crit}^2 = \left[(\rho_s - \rho) g d a'' (d_{w,crit} / d)^{1/2} \right] / \rho \quad (2.8)$$

where:

- $U_{w,crit}$: critical wave orbital velocity
- d : median grain size of the bed sediment
- a'' : empirical constant (0.21)
- $d_{w,crit} = \frac{U_{w,crit} T_w}{2\pi}$: near bottom wave orbital semi-excursion
- T_w : wave period

2.2.2 Physical properties of cohesive particles

2.2.2.1 Cohesion

Cohesion is defined as the internal force acting between sediment particles. Cohesion in sediments becomes relevant for clay content larger than 10%. Electrochemical factors explain largely the cohesive internal forces [Van Rijn, 1989]. The critical erosion shear stress parameter in the sediment transport model is largely affected by the cohesion property, which can be estimated by the Coulomb's law [Coulomb, 1773] as:

$$\tau = c + \sigma \tan \phi \quad (2.9)$$

Where:

τ : shear strength

σ : normal pressure on the rupture plane

ϕ : angle of internal friction

c : soil cohesion

2.2.2.2 Plasticity

Plasticity is the property through which substantial permanent deformations can occur without breaking [van Rijn, 1993]. This property can indicate the degree of consolidation of fine deposits, which can affect the critical bed-shear stress for erosion in sediment transport models. Soil plasticity is classified in five subclasses according to the water content as illustrated in Table 2.1.

Table 2.1: Plasticity classification

Class name	Range of water content limit
Low plasticity	$w_l \leq 35\%$
Intermediate plasticity	$35\% < w_l < 50\%$
High plasticity	$50\% < w_l < 70\%$
Very high plasticity	$70\% < w_l < 90\%$
Extremely high plasticity	$w_l \geq 90\%$

w_l : is the limit of water content in which a soil start to behave as a liquid.

2.2.2.3 Flocculation

Clay particles are flaky. Their thickness is very small relative to their length and breadth. In some cases they are as thin as 1/100th of the length. Clay sediments therefore have high to very high specific surface values. Particle surfaces carry a

small negative electrical charge that will attract the positive end of water molecules, that leads to the formation of a cloud of cations (positive charged ions) around the clay particles (double layer theory). Further details about the double layer theory can be found in van Olphen [1963].

The resulting attractive or repulsive force between the particles will depend on the number of cations and their mutual distance. Flocculation is much more efficient in saline water than in fresh water suspensions due to the abundant presence of positive sodium-ions that enhance the Van der Waals attractive forces. Besides the salinity factor, other elements affecting flocculation are: size, concentration of particles, temperature, organic material content and particle collisions [Van Rijn, 1993]. The flocculation property is considered in sediment transport models because its large influence on the settling velocities.

2.2.2.4 Erosion rate

It is defined as the amount of material eroded per time and area for a given bed shear stress. Two main types of erosion have been noted in the description of cohesive sediment transport: surface and mass erosion [Mehta et al. 1982]. These have been recently described as Type I and Type II and also as “benign” and “chronic” erosion [Amos, 1995]. Type I erosion takes place when the critical erosion shear stress $\tau_{cr,e}$ increases with sediment depth due to consolidation and limits the extent of erosion. On the contrary, Type II erosion occurs when $\tau_{cr,e}$ does not change with depth into the sediments [Sanford and Maa, 2001]. The erosion rate can be determined through the following formulations for Type I [Gularte et al., 1980] and Type II [Ariathurai, 1974] erosion respectively.

$$E = \varepsilon_f e^{\left\{ \alpha [\tau_b - \tau_{cr,e}(z)]^\beta \right\}} \quad (2.10)$$

$$E = M (\tau_b - \tau_{cr,e}) \quad (2.11)$$

Where:

E : erosion rate

M : erosion rate coefficient

τ_b : bed shear stress

$\tau_{cr,e}$: critical erosion shear stress

ε_f : empirical floc erosion rate

α, β : empirical constants

ε_f : empirical floc erosion rate

2.2.3 Bedforms on non-cohesive sediments

All kind of irregularities present on the seabed are called bedforms. Bedforms are strongly related to sediment properties and hydrodynamic conditions, both affecting their spatial distribution and geometry. Classification of bedforms is given basically through their mode of origin, size or shape. Bedforms are considered in this research as 2D entities, defined by their profile features: height " Δ " and length " λ " as shown in Figure 2.9.

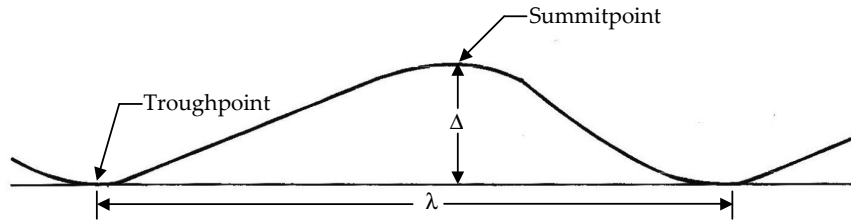


Figure 2.9 Side view of a typical bedform

The length of the bedform (λ) is defined as the horizontal distance between two consecutive troughpoints (minimum elevations in vertical profile) and Δ is the height of the bedform, which is determined by the vertical distance between the troughpoint and the summitpoint (maximum elevation in vertical profile).

2.2.3.1 Bedforms classification

Literature presents an outstanding amount of information about bedforms and their classification [Engelund, 1970; Liu, 1957; Simons and Richardson, 1966; Van Rijn, 1984c; Van den Berg et al., 1989]. Given the broad range of data sources, some terms used to determine specific types of bedforms have not yet a worldwide consensus. Therefore a rather big confusion might arise when different terms seem to define the same type of bedform. Thus, the classification herein adopted may have discrepancies with some previous works although generality was the main concern. Characteristic types of bedforms sorted out from low to high shear stresses are defined as follows:

A **Flat bed** is a very particular bed configuration, since it can occur with and without sediment movement, under the upper and lower flow regimes respectively. Flat beds are geometrically defined by the absence of irregularities (elevations or depressions) larger than the maximum size of the bed material.

Miniripples spring up after flow velocities or shear stresses just exceed their critical values, then a sort of undulation over the bed with an asymmetric profile (see Fig. 2.9) is formed. The ripple stoss side located upstream has a gentle slope, which differs from the steep lee side downstream that defines its asymmetric shape.

Miniripples are common over fine-grained beds with particle sizes smaller than 0.7 mm and are rarely seen in grain sizes coarser than 0.9 mm. Miniripples are sized smaller than 60 cm in length and 6 cm in height and usually form in lower flow regimes.

Megaripples are bedforms common over fine-grained beds and similar to miniripples in shape, but larger in size as they are created under higher bed shear stresses. Megaripples' lengths range from 60 cm to several meters (up to 30 m) and heights between 6 cm to 1.5 m.

Dunes, in general, are features much larger than the above mentioned ripples. They originate when ripples (on fine materials) or flat beds (on coarser materials) are subjected to higher shear stresses. Dune lengths range from 3 to a maximum of 15 times the water depth while their heights are about 10-20% of this dimension. Under exceptional cases, heights and lengths reach values of 7m and 500m respectively, as those observed in the Parana river [van Rijn, 1989]. Dunes are also the last bedforms observed under the lower flow regime.

Transition includes all the bedforms between dunes to flat beds, which occur between lower and upper flow regimes. Hence, after the lower flow regime further increases of the shear stresses will wash out existing dunes. This process is carried out by an increase of the bedform length and a simultaneous decrease of the bedform height. Flume observations describe this transitional condition as low amplitude dunes covering part of the channel length with a flat bed over the remainder.

Antidunes appear after the establishment of the upper flow regime by means of gradual increases in shear stresses. Antidune lengths may vary from 1 cm to 6m (about 10 times water depth), whereas their height ranges from 1 mm to 45 cm. Their longitudinal profile has a sinusoidal shape in phase with the water surface and can distinctly move either upstream or downstream.

From the numerous attempts to determine bedform classifications in terms of sediment properties and flow conditions, the approaches of Simons and Richardson [1966], Allen [1968], Athallah [1968], Bogardi [1974], Znamenskaya [1969], van Rijn [1993] are representative. Van Rijn's approach is shown in Figure 2.10 below.

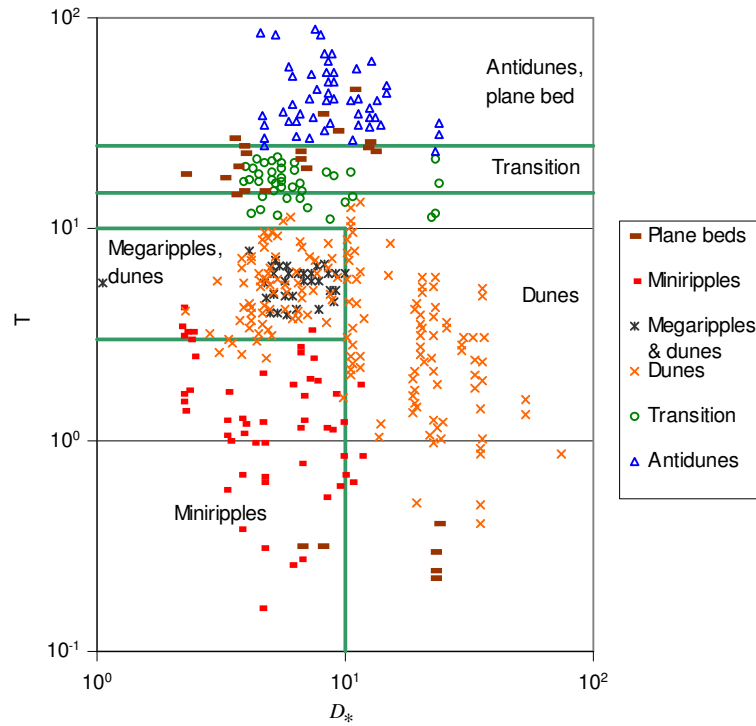


Figure 2.10 Classification of bedforms [van Rijn, 1993]

Where D_* is the dimensionless particle parameter, which is defined as:

$$D_* = d_{50} \left(\frac{(s-1)g}{\nu^2} \right)^{1/3} \quad (2.12)$$

In which:

d_{50} : medium particle diameter of bed material

$s = \frac{\rho_s}{\rho}$: specific density

ν : kinematic viscosity coefficient

g : acceleration of gravity

In Figure 2.10 T is the excess bed-shear stress parameter, which is defined as follows:

$$T = \frac{\tau_b' - \tau_{b,cr}}{\tau_{b,cr}} \quad (2.13)$$

Where:

$\tau_{b,cr} = \theta_{cr} [(\rho_s - \rho)gd_{50}]$: critical bed shear stress according to Shields

$\tau_b' = \rho g \left[\frac{u}{C'} \right]^2$: grain related bed shear stress

$C' = 18 \log \left(\frac{12h}{3d_{90}} \right)$: grain related Chezy coefficient

u : depth integrated velocity

h :	water depth
θ_{cr} :	critical Shields parameter
d_{90} :	sediment grain diameter in which 90% of sample by mass is smaller

The critical Shields parameter θ_{cr} , developed by Shields [1936] and still widely used for the determination of the initiation of motion, can be expressed in terms of the particle parameter D_* as shown by Yalin [1972]:

$$\begin{aligned}
 \theta_{cr} &= 0.24D_*^{-1} \rightarrow 1 < D_* \leq 4 \\
 \theta_{cr} &= 0.14D_*^{-0.64} \rightarrow 4 < D_* \leq 10 \\
 \theta_{cr} &= 0.04D_*^{-0.1} \rightarrow 10 < D_* \leq 20 \\
 \theta_{cr} &= 0.013D_*^{0.29} \rightarrow 20 < D_* \leq 150 \\
 \theta_{cr} &= 0.055 \rightarrow D_* > 150
 \end{aligned}
 \tag{2.14}$$

Classification of bedforms in the Dithmarschen Bight was carried out by using van Rijn [1993] methodology, which is characterized by the extensive number of flume and field data used for its development, the further differentiation of ripples into miniripples and megaripples and also its favorable reception in the scientific community. This methodology shown in Figure 2.10 can also be summarized as presented in Table 2.2.

Table 2.2: Summary of bedform classification [Van Rijn, 1993]

Transport regime	Particle size		
	$1 \leq D_* \leq 10$	$D_* > 10$	
Lower	$0 \leq T \leq 3$	Miniripples	Dunes
	$3 < T \leq 10$	Megaripples and dunes	Dunes
	$10 < T \leq 15$	Dunes	Dunes
Transition	$15 < T < 25$	Washed-out dunes, sandwaves	
Upper	$T \geq 25, Fr < 0.8$	(symmetrical) sandwaves	
	$T \geq 25, Fr \geq 0.8$	Plane bed and/or antidunes	

2.2.3.2 Bedform origin and models

Bedform origin. The sudden apparition of irregularities or bedforms as they are currently observed during flume or field experiments, has been explained by several approaches and authors [Exner, 1925; Anderson, 1953; Velikanov, 1936; Tison, 1949; Liu, 1957; Raudkivi, 1976; Inglis, 1949; Kennedy, 1961-1963-1969; Yalin, 1964; Allen, 1968; Van Rijn, 1993], although there is not yet convergence or total agreement around one unique theory. Among the different theories presented for the formation of bedforms, only a few of them will be briefly described in the next paragraphs.

1) Exner [1925] established a differential erosion equation for two-dimensional flow:

$$\frac{\partial \eta}{\partial t} + K \frac{\partial u_o}{\partial x} = 0 \quad (2.15)$$

Where:

η : bed elevation

t : time

K : factor relating sediment discharge to flow velocity

u_o : flow velocity near bed

x : distance in the downstream direction

This equation relates changes in bed elevation due to longitudinal variation of bottom velocity. This principle is sound, however, it cannot explain properly the origin of bedforms after an initial plane bottom, where velocity changes are not expected.

2) Anderson [1953] complemented the above approach reasoning that in case of shallow flow, the surface waves may affect the alluvial bottom and cause sand waves over it. Hence, an initially smooth bed requires at least a source of momentum coming from somewhere other than the bedform itself to start the formation of ripples, which can be reflected in the surface waves.

Then, the prior drawback from Exner theory is solved by means of the surface waves. However, some doubts rise about this hypothesis, since it cannot explain the origin of bedforms in closed conduit flows, sandwaves in very deep flows or desert dunes where surface waves have no effect.

3) Turbulence has also been considered as the possible cause for bedform origin. This hypothesis is supported by Velikanov [1936], whose studies showed that turbulence could cause erosion and deposition along the bottom. Tison [1949] also found that bedforms are only present under turbulent flow.

However, the turbulence theory leaves the following questions unexplained according to Liu[1957]: " a) Since turbulence is non-periodic, how can it produce regular sand wave patterns? b) What is the relation between the scale of turbulence and sand wave form, especially for the case of ripples formed on the upstream faces of large sand waves? c) What is the effect of turbulence on sand ripples in case the laminar sublayer exists along the bottom? d) Since sediment ripples and waves can create turbulence, how can it be proved that turbulence causes ripples and not vice versa?"

4) Instability theory by Helmholtz [1888] was applied on bedforms formation. This theory stated that a surface of discontinuity can occur between two fluids flowing parallel to each other but with different densities or velocities. A physical explanation of the breaking up of the surface of discontinuity was given by Prandtl [1952] and Rouse [1947] for two fluids with equal density and different velocities as is shown in Figure 2.11.

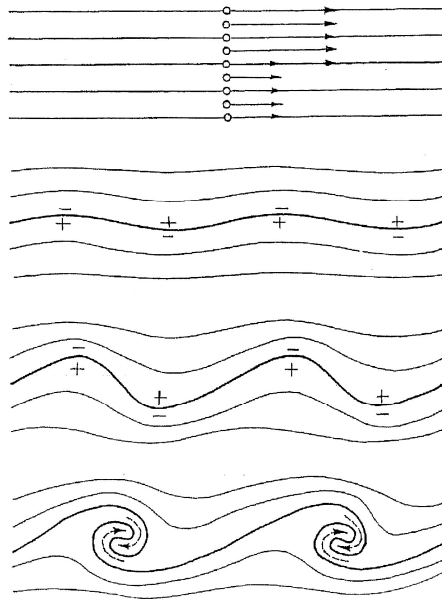


Figure 2.11 Flow instability due to a surface of discontinuity [Prandtl, 1952; Rouse, 1947]

Based on Figure 2.11 Bernoulli's theorem is applied to reproduce the fluctuations and wavy characteristics along the surface of discontinuity by means of the transformation of kinetic into potential energy or vice versa. Lower velocity is compensated by higher pressure (+ sign in Figure 2.11) along a streamline. Therefore periodic variations of velocity are generated at the interface of both fluids.

Equation 2.15 from Exner [1925] requires a longitudinal variation of near bed velocities to explain bedforms origin. The instability principle provides an explanation for velocity fluctuations even under initial plane beds. However, the assumption that a viscoelastic material like the sediment layer can be considered as a fluid and also the difficulties in obtaining a mathematical solution for the instability problem remain as the main drawbacks for this theory.

5) Ripple formation is explained by Raudkivi [1976] in the following way:

"When a discontinuity forms in the bed surface, whether by scouring and subsequent deposition, by an extreme eddy, or by piling up of some lighter grains on larger ones, or whatever action, a wake is created in the lee of the discontinuity. The flow separates at the crest and reattaches about five to six step heights downstream. Since the velocity gradients across this surface of separation are steep, this interface is also the location of intense production of turbulence. Hence, the flow which meets the boundary at the point of reattachment has a higher than average level of turbulence and can excavate more material than the flow further downstream is able to transport. This leads to the next mount, etc."

Raudkivi's theory is very similar to the approach presented by Inglis [1949] who explained the initial discontinuity on a plane bed surface by the effect of a turbulent

flow acting over a given mixture of particles varying in size and shape, which then might generate a particle collection and therefore a bed disturbance promoting the next ones downstream. However, as it was mentioned before, all available theories do not fulfill all expectations about bedforms origin. Hence, under this latter case, it has been pointed out that an initial discontinuity as above illustrated generally results in a minor bed elevation change of the magnitude of the particle size, which is too small compared to bedforms found in nature.

Figure 2.12 shows a typical vertical velocity profile across a bed discontinuity, where can be clearly observed the longitudinal variation of the near bed velocities along a bed trough and three characteristic flow zones. These are defined as the zone of no diffusion (unaffected region), the zone of mixing (high turbulence) and the zone of backflow.

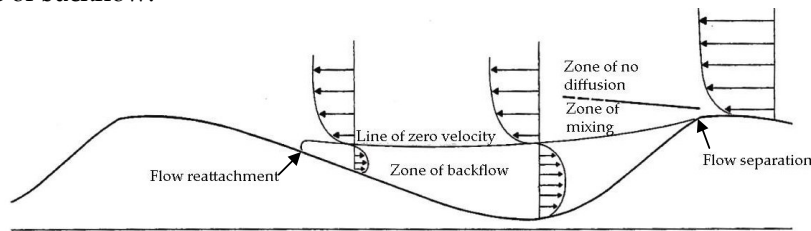


Figure 2.12 Flow pattern over a bed discontinuity [Reineck and Singh, 1980]

Bedform models. Different methodologies have faced the determination of bedforms geometry. They are typically subdivided into four types [Raudkivi, 1976]:

(1) Classical mechanics. It involves a relation between near bed velocities and bed changes induced by erosion or deposition. This relation can be obtained from coupling equation 2.15 by Exner [1925] to the solid mass conservation equation. An initial bed configuration should be provided. Flat beds are avoided as initial conditions given the difficulties in modelling the origin of bedforms.

2) Instability models. These types of models are based on the 2D parallel flow of two fluids (see Fig. 2.11) with different velocities and densities. Theoretical analysis of this flow leads to periodical variations of velocities and pressures along the fluids' interface, which can result in an unstable surface. This phenomenon might present certain similitude with bedform disturbances if the lower fluid is assumed to be a granular bed with infinite viscosity like a density current.

Investigations developed by Liu [1957] define an instability index $u_* d / \nu$ and a movability number of the sediment u_* / w in which u_* is the shear velocity and w is the sediment settling velocity. Both parameters can predict the beginning of the sediment-ripple formation as is shown in Figure 2.13, however, difficulties remain on the definition of bedforms geometry given the earlier mentioned complexity of the mathematical approach.

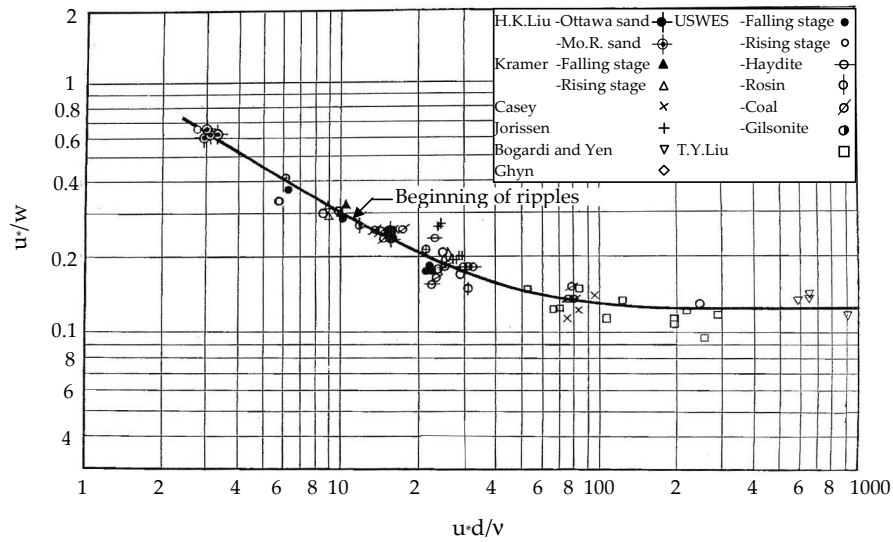


Figure 2.13 Criterion of ripple formation [Liu,1957]

3) Statistical models. Even under the most uniform pattern of bedforms features found in nature or the laboratory, a strict regularity of wavelengths or heights has never been observed. Moreover, in spite of forcing similar flow and sediment conditions, there would be low possibilities to obtain identical results on bed disturbances. Consequently, a deterministic model cannot, by itself, describe successfully this peculiarity that should be only accounted by statistical or probabilistic models. However, as was stated by Raudkivi [1976], the final solution may have to be a combination of both types of models.

Probabilistic models consider bed elevation as a random variable that can be represented by equation 2.16.

$$\eta = f(x) \quad (2.16)$$

The main random function $f(x)$ is defined according to a non-inertial reference system that moves along the x axis with the bed features' celerity. Statistical parameters computed from real observations such as mean values, variance, autovariance and autocorrelation parameters, should be met by the statistically generated function $f(x)$.

4) Kinematic models. The kinematic instability models are the most extensively developed. They are based on proposed potential flows. The major contribution is due to Kennedy [1961, 1963, 1969], who reported a two dimensional potential flow with an erodible boundary that gives a sinusoidal perturbation on the boundary. From his analysis the bedform length λ can be determined by equation 2.17.

$$Fr^2 = \frac{\cosh^2 kh}{kh(\sinh 2kh + kh)}; \quad \delta = \alpha\lambda$$

$$Fr^2 = \frac{1 + kh \tanh kh + jkh \cot jkh}{(kh)^2 + (2 + jkh \cot jkh)kh \tanh kh}; \quad \delta \neq \alpha\lambda$$
(2.17)

Where:

Fr : Froude number

α : positive integer value

$k = 2\pi/\lambda$

λ : bedform length

δ : distance by which the local sediment transport rate lags behind the local velocity at the mean bed level

$j = \delta/h$, being h the water depth

5) Semi-empirical models. This additional group of models involving a combination of dimensional analysis with extensive measurements in laboratory or nature has provided some functional relationships between bedform dimensions, flow and sediment properties. Some well known works published by Yalin [1964], Allen [1968] and van Rijn [1993] are among these models.

Herein on Table 2.3 is summarized the van Rijn's approach to define bedform dimensions for miniripples, megaripples and dunes, which are the types of bedform features currently observed in the study area.

Table 2.3: Estimation of bedform dimensions at lower flow regime [Van Rijn, 1993]

	Type of Bedforms		
	Miniripples	Megaripples	Dunes
Length	$\lambda = 500 \text{ to } 1000 d_{50}$	$\lambda = 0.5b$	$\lambda = 7.3b$
Height	$\Delta = 50 \text{ to } 200 d_{50}$	$\frac{\Delta}{b} = 0.02(1 - e^{-0.1T})(10 - T)$	$\frac{\Delta}{b} = 0.11\left(\frac{d_{50}}{b}\right)^{0.5}(1 - e^{-0.5T})(25 - T)$

Where:

λ : length of bedforms

Δ : height of bedforms

h : water depth

T : excess bed-shear stress parameter

2.2.3.3 Bedforms significance on sediment transport

Bedforms are characteristic features distinguishing an open flow over a movable bed from one over a fixed boundary. An underlying difference between these two

cases is their flow resistance, which can be determined by the skin friction on fixed beds [Nikuradse, 1933] or the skin friction plus the form roughness on movable beds.

Therefore, flow over bedforms are subject to higher shear stresses as is indicated by Figure 2.14.

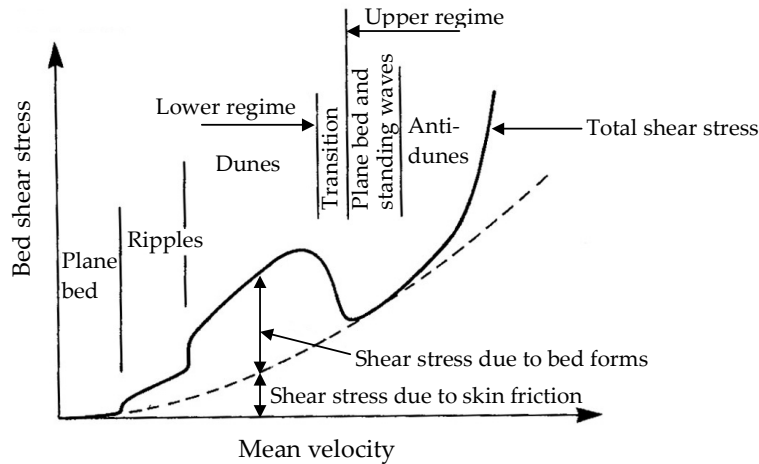


Figure 2.14 Bedforms effect on bed shear stress. [Fredsoe, 1992]

Bed resistance has two opposite effects on sediment transport. First, an increase of shear stress leads to the initial motion of grains according to Shields' [1936] experiments and also to increased erosional fluxes as is shown by van Rijn [1993] and Partheniades [1965] for non-cohesive and cohesive materials respectively. Hence, a positive correlation between shear stress and sediment movement is apparent. Second, any shear stress increase will reduce flow energy due to the higher friction force. The flow slows down according to the momentum law, and therefore, it might decrease the capacity to transport sediments.

2.2.4 Bedforms on cohesive sediments

Although, this study focuses on bedforms developing over non-cohesive soils, a brief summary of cohesive bedforms is given next. Further details can be found in Reineck and Singh [1980]. Regions with muddy sediments do not show the typical bedforms usually observed over non-cohesive soils. What has been observed is that moving fluids create two broad classes of bedforms over a cohesive substrate:

1) erosional bedforms created by the fluid itself (flutes and gutters): Flute marks are erosive structures which are spoon shaped depressions in the bed surface. They are probably produced when eddies touch the bed surface (i.e. the viscous boundary layer breaks down due to excessive turbulence). Flutes typically have an elongated tapered shape with a higher relieved upstream "head" and a downstream "tail" that has less of a relief. The characteristic shape of a flute is caused by flow separation at

the upstream lip of the flute and flow reattachment downstream at the lowest point in the flute. Flutes come in a very wide variety of shapes, probably because they typically form from erosional modification of some "imperfection" on the substrate. In their deepest part they may range from few millimeters to few centimeters, and in length they are few centimeters to several decimeters [Reineck and Singh, 1980]. Gutters are created by the interaction of a fluid vortex along the substrate and are typically associated with highly turbulent flow during storm events. Gutters are very elongated "gutter-shaped" features that, unlike flutes, are not usually strongly asymmetric and do not have the well-defined up-stream scour.

2) Tool Marks: These bedforms include a wide class of erosional features that involve the interaction with some object (a "tool") on the substrate. Allen [1971] provides detailed information on the erosional marks. Tools may include sticks, clasts, skeletal material, etc. Tool marks may include skip or bounce marks (formed by an object coming into repeated contact with the substrate), groove marks (formed by an object carving out an elongated groove from the bottom), and prod marks (formed by an object prodding the substrate). In many instances, tool marks are further modified by erosion of the moving fluid.

It is pointed out that various benthonic animals inhabit muddy beds in great numbers. Hence, the micro topography may also be controlled by biological activity especially in low-energy regions [van Rijn, 1993].

2.2.5 Flow Resistance

Resistance forces hinder free water movement in open channels and closed conduits. This force is included into the flow analysis by means of the law of momentum conservation. A steady or unsteady flow defines its resistance according to the slope of the energy grade line, as presented on equation 2.18 [du Boys, 1879].

$$\tau_b = \rho ghS_f \quad (2.18)$$

Where:

τ_b : bed shear stress

h : water depth

ρ : fluid density

S_f : Slope of the energy grade line

Equation 2.18 assumes a flow over a wide channel where the hydraulic radius approaches the water depth. The resistance in a steady uniform flow is a particular case that can be easily defined, since the slope of the energy grade line coincides with the bed slope. For unsteady flow the solution is otherwise more complex, since S_f differs from the bed slope due to the unbalanced external forces.

2.2.5.1 Bed shear stress

The methodologies used to define the bed shear stress for unsteady flow are generally based on the assumption that flow resistance approximates that of a steady uniform flow at the same depth. Therefore, a set of different well-known formulations for steady conditions becomes applicable under unsteady cases.

Equations 2.19 to 2.21 represent the mathematical description of the flow resistance principles based on global or depth-averaged flow characteristics. Hence, phenomena taking place in the internal flow structure (as inside the boundary layer) are roughly considered under these relationships by means of the Chezy's coefficient [Herschel, 1897], Manning's coefficient [Manning, 1895] and Darcy's friction factor [Darcy, 1854].

$$u = C\sqrt{RS_f} \quad (2.19)$$

$$u = \frac{1}{n}R^{2/3}S_f^{1/2} \quad (2.20)$$

$$f = \frac{8gRS_f}{u^2} \quad (2.21)$$

Where:

C : Chezy's resistance coefficient

n : Manning's resistance coefficient

f : Darcy's friction factor

R : hydraulic radius

u : depth integrated velocity

Combination of the equation 2.18 with equations 2.19 to 2.21 leads to the definition of the bed shear stress according to Chezy, Manning and Darcy-Weisbach respectively. Equations 2.22 to 2.24 define the shear stress under these formulations where the hydraulic radius R was replaced by the water depth h .

$$\tau_b = \rho g \left(\frac{u}{C} \right)^2 \quad (2.22)$$

$$\tau_b = \frac{\rho g n^2 u^2}{h^{1/3}} \quad (2.23)$$

$$\tau_b = \frac{\rho u^2 f}{8} \quad (2.24)$$

The above formulations define the shear stress for any flow condition through the current velocity u and the water depth h . The resistance coefficients C , n and f should be defined according to the flow hydraulic regime. These coefficients can be related among themselves by manipulating relations 2.22 to 2.24.

2.2.5.2 Hydraulic regimes

Hydraulic regimes can be classified according to the instability level of the internal flow structure. The beginning of the internal flow instability is determined through the Reynolds number. If inertial forces overcome the viscous forces by a certain length, the turbulent or chaotic movement of particles appear. Then, a combined effect of viscosity and turbulence factors determine the flow resistance.

Nature generally exhibits turbulent flows, however the low velocities present near the bottom or walls allow the existence of laminar flow in a small region close to the solid boundary. This region is called the viscous or laminar sublayer. The viscous sublayer thickness decreases when the turbulence intensity increases (equation 2.25). High turbulence levels speed up water movement near the boundaries through momentum exchange, therefore the laminar sublayer is reduced and might not completely cover surface irregularities.

$$\delta = 11.6 \frac{\nu}{u_*} \quad (2.25)$$

Where:

δ : viscous sublayer thickness

u_* : bed shear velocity

Surface irregularities or equivalent roughness (k_s) as defined by Nikuradse [1933] are compared to the laminar sublayer thickness. If the laminar sublayer is thick enough to cover the surface roughness, a hydraulically smooth flow develops. Otherwise, a hydraulically rough flow takes place and turbulence becomes a dominant factor on flow resistance. Between these two characteristic conditions, a hydraulically transitional flow might exist. Depending on the actual flow; viscosity, turbulence or both define water dynamics and bed resistance. Table 2.4 summarizes the different friction coefficients accordingly to the hydraulic regimes.

Table 2.4 Hydraulic regimes and resistance coefficients

Coefficients	Hydraulic regimes		
	Smooth turbulent flow	Rough turbulent flow	Transitional flow
Chezy	$C = 18 \log \left(\frac{12h}{3.3\nu/u_*} \right)$	$C = 18 \log \left(\frac{12h}{k_s} \right)$	$C = 18 \log \left(\frac{12h}{k_s + 3.3\nu/u_*} \right)$
Darcy Weisbach	$\left(\frac{f}{8} \right)^{-0.5} = 3 + 2.5 \ln \left(\frac{u_* h}{\nu} \right)$	$f = 0.24 \log^{-2} \left(\frac{12h}{k_s} \right)$	$\left(\frac{f}{8} \right)^{-0.5} = 6 + 2.5 \ln \left(\frac{h}{k_s + 3.3\nu/u_*} \right)$

k_s is the equivalent roughness size

2.3 Incipient motion

2.3.1 General

The initial motion of bed grains represents one key element in the study of sediment dynamics. Transfer of sediments from the bed to the flow might only start when this incipient condition is reached. Hence, this is the criterion to differentiate a single phase fluid flow from a complex two-phase phenomenon involving fluid and sediment motion. The inclusion of incipient motion into the analysis of sediment dynamics is given by means of a so-called critical velocity or critical shear stress concept. These concepts were first introduced by Brahm [1754] as shown by equation 2.26. Since then many newer approaches have been proposed to date, where the extensively applied Shield's diagram (Fig. 2.15) and Hjulström's curve are the most representative (Fig. 2.8).

$$V_{critical} = kW^{1/6} \quad (2.26)$$

Where:

k : empirical constant

W : particle weight

From the physical point of view, the momentum imbalance of the forces acting at a sediment particle will unleash the initial motion. The main forces to be considered are the particle weight (divided into its normal and tangential components), fluid forces (lift, surface and form drag) and constraining forces due to neighboring grains. Thus, the driving forces over the particle are the tangential component of the weight and the fluid forces with the last ones changing dramatically from laminar to turbulent flow (e.g. from smooth to rough turbulent flow).

Under laminar flow or turbulent conditions with a laminar sublayer entirely covering the bed grains, the surface drag due to viscous skin friction becomes the main driving force. This force is exerted indistinctly over all particles on the bed surface. On the other hand, when flow velocity increases and a rough turbulent regime is reached, some surficial grains are exposed to turbulence, implying a higher drag force on exposed grains than on grains still covered by the laminar sublayer. Exposed grains shed eddies and create a wake downstream favoring pressure differences between the front and backside of the particle. This phenomenon results in an additional force acting on the grain that is denoted as the form drag, which affects the momentum balance and therefore the particle's stability.

2.3.2 Estimation of the incipient motion state

2.3.2.1 Critical shear stress on non-cohesive sediments

Figure 2.15 below presents the Shields' diagram, used to define the average shear stress exerted by the fluid when bed particles begin to move. It is expressed in terms of the dimensionless particle parameter, D^* , and the mobility parameter θ_{cr} [Yalin, 1972].

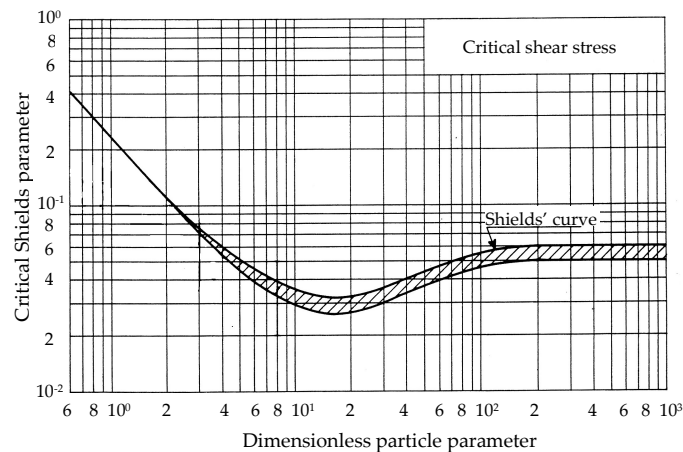


Figure 2.15 Shields' curve as a function of the particle parameter [Van Rijn, 1989]

The straightforward application of this curve and the relative agreement with a great variety of independent data from other sources have made this approach a classical methodology for the study of sediment transport processes, although some drawbacks have been pointed out.

Grass [1970] reported a considerable scatter when data from Casey [1935], Gilbert [1914] and Tison [1953] is plotted on Shields' diagram. Some reasons explaining this scatter are given next:

(a) Difficulty encountered in consistently defining critical flow conditions. Given the stochastic character of turbulent flow there will always be a bed shear stress large enough to move a particle. Thus, particle movement can occur at appreciably smaller critical values than those defined on Shields' curve. Experiments performed at Delft Hydraulics (see Fig. 2.16) distinguish seven different criteria relative to critical flow, namely:

1. Occasional particle movement at some locations;
2. Frequent particle movement at some locations;
3. Frequent particle movement at many locations;
4. Frequent particle movement at nearly all locations;
5. Frequent particle movement at all locations;

6. Permanent particle movement at all locations;
7. General transport (initiation of ripples);

From all the above criteria, condition 6 seems to best fit Shield's criterion.

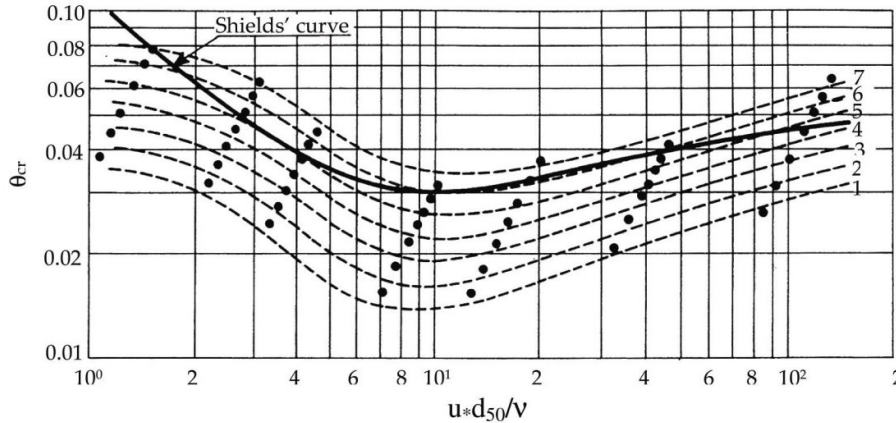


Figure 2.16 Critical shear stress criteria [Van Rijn, 1989]

b) Effect of bed slope. Shields' curve has been developed on experiments carried out in laboratory flumes with flat beds. Therefore, the driving forces due to tangential components of the grains weight on sloping beds are not included in Shields' diagram. Van Rijn [1989] presented a methodology relating critical shear stresses on flat and sloping beds (see eq. 2.5).

c) Some other factors affecting critical shear stresses and not explicitly considered on Shields' diagram are: grain shape, gradation, proportion of cohesive materials, turbulence structure, etc. Hence, the further these factors lay from the specific conditions used on Shields' experiments the more scatter with respect to his diagram is expected.

2.3.2.2 Critical shear stress on cohesive sediments

Critical erosion shear stress, it is an erosion threshold used to quantify sediment surface erodibility. Therefore, there is a critical shear stress $\tau_{cr,e}$ below which no erosion occurs and above which erosion starts. The critical shear stress of cohesive soils is not tied to the particle size (as in non-cohesive substrates) but rather to a number of factors as listed in Table 2.5 [Briaud et al., 1999] implying the existing difficulties on the determination of a reliable and practical methodology to estimate this parameter. According to Briaud [2004] the critical erosion shear stress of cohesive soils varies within the same range as cohesionless soils (0.1 N/m² to 5 N/m² for the most common cases).

In the intertidal zone the critical erosion shear stress of soft fine-grained sediment when diatom biofilms are absent varies typically in the order of 0.2 to 0.5 N/m²

[Andersen, 2001]. However, when biofilms are present this critical shear stress may increase to more than 3 N/m² [Riethmüller et al., 2000; Austen et al., 1999; Tolhurst et al., 1999]. An extensive research considering the spatial and temporal patterns of erodibility of an intertidal flat in the East Frisian Wadden Sea (Germany) remarks the relevance of biological factors on the estimation of critical erosion shear stresses [Mahatma, 2004]. The previous investigation shows critical erosion shear stresses ranging from 0.27 to 2.67 N/m² where the small and large-scale variations of this parameter are mainly governed by biostabilization (tube building worms, concentration of extracellular polymeric substance, Chlorophyll a concentration) and biodestabilization.

Table 2.5 Factors influencing the critical erosion shear stress of cohesive soils. Adapted after Briaud [1999]

When this parameter increases	Critical erosion shear stress
Soil water content	*
Soil unit weight	Increases
Soil plasticity index	Increases
Soil undrained shear strength	Decreases
Soil void ratio	Decreases
Soil swell	Decreases
Soil mean grain size	*
Soil percent passing sieve #200	Increases
Soil clay minerals	*
Soil dispersion ration	Decreases
Soil cation exchange capacity	*
Soil sodium absorption ration	Decreases
Soil pH	*
Soil temperature	Decreases
Water temperature	Decreases
Water chemical composition	*

* unknown

Critical deposition shear stress, deposition of cohesive sediments is dominating when the bed shear stress τ_b falls below a critical value for deposition $\tau_{cr,s}$, as shown by Krone [1962]. Therefore, to determine when deposition flux is applicable, the understanding and acquisition of this critical shear stress is essential [Chan et al., 2006]. However, the critical shear stress for deposition $\tau_{cr,s}$ is not obvious at first glance. High shear near the bed breaks up large flocs before they can settle. Then, the resulting smaller flocs and individual particles are resuspended. Hence, the critical shear for deposition $\tau_{cr,s}$ is that through which large flocs can pass without being

broken up or the shear stress in the bottom boundary layer which cannot overcome cohesion in the settling flocs.

Experimental results show that the critical bed-shear stress for erosion is significantly larger than that for deposition $\tau_{cr,e} > \tau_{cr,s}$ [van Rijn, 1989]. Moreover, in the CERC [2002] it is indicated that $\tau_{cr,s}$ is generally on the order of one fourth of $\tau_{cr,e}$. This implies that deposition and erosion are mutually exclusive, i.e., the classical cohesive sediment paradigm. This paradigm has been disputed by Sanford and Halka [1993] and very recently by Winterwerp [2003]. In situ observations [Sanford and Halka, 1993; Chan et al. 2006] have shown that the total resuspended sediment load increases in conjunction with increasing bottom shear stress, but deposition is initiated soon after the shear stress begins to decrease and long before the stress falls below the value at which erosion had previously begun.

2.3.2.3 Critical velocity

Hjulström [1939] plotted grain sizes versus critical tractive velocities when grain movement begins (see Fig. 2.8). From the Hjulström diagram two different behaviors can be observed. Considering coarse and fine grains, the correlation between critical velocity and grain size is positive and negative respectively. The latter confirms an increase of cohesive forces on smaller particles, which require higher flow velocities to entrain them in flow as their sizes decrease.

Figure 2.17 shows a different diagram by Yang [1973] determining the critical velocity in terms of the settling velocity and the shear velocity Reynolds number. This author derived the relation from basic concepts in fluid mechanics and boundary layer theory, which was supported by 153 datasets independently collected by eight other investigators. The performance assessment of this approach shows a correlation coefficient of 0.955 and a standard error of 0.513 between observations and the functional relation proposed. It is worth mentioning that data from Casey [1935], Gilbert [1914] and Tison [1953] earlier referenced, due to their high scatter on Shields' diagram are also included in this study.

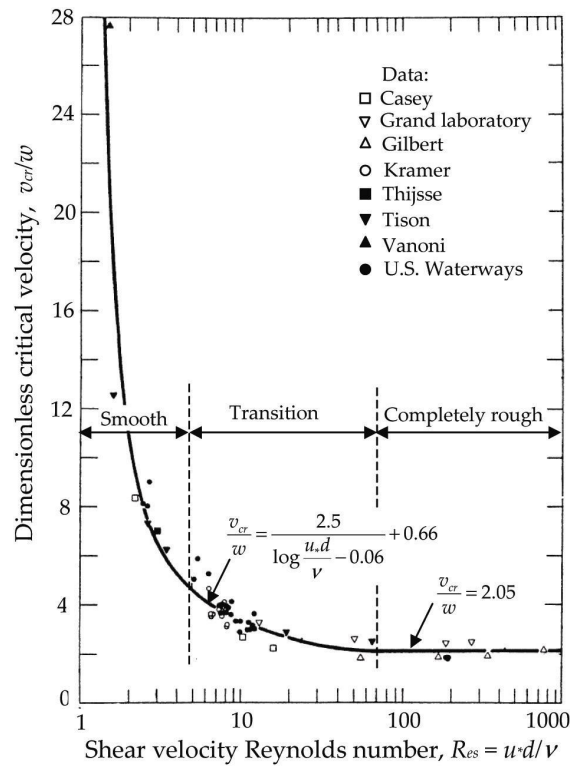


Figure 2.17 Relationship between dimensionless critical velocity and Reynolds number
[Yang, 1973]

2.4 Modes of sediment transport

After the initial destabilization of particles by driving forces, grains start their movement downstream. This motion is made in different ways, namely: rolling or sliding, saltation or hopping and suspension.

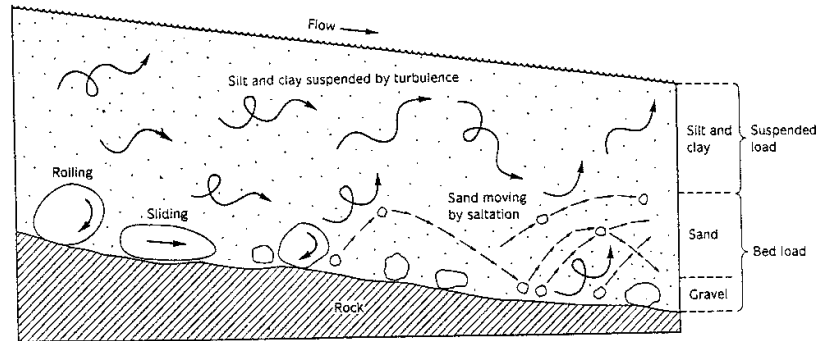


Figure 2.18 Different modes of sediment transport

2.4.1 Rolling, sliding and saltation motion

Grain motion follows the particle incipient state when critical shear stresses are exceeded. Particles will be rolling, sliding and jumping in a quasi-continuous contact with the bed. This motion is strictly limited by the effect of gravity [Bagnold, 1956], which differs from suspended motion where turbulence is also involved. Therefore, characteristics of grain movement and physical principles differentiate the modes of sediment transport.

The latter condition drives modelers to divide the total sediment transport load into bed-load (rolling, sliding and saltation) and suspended load. Although in natural conditions there is not such a sharp division between these modes of transport. Bed-load is generally small in comparison to suspended load, even so, it is very important in morphological processes and determination of bed roughness. Du Boys [1879] presented the earliest analytical formula determining bed-load rates as a function of bed shear excess:

$$q_B = C_s \tau_b (\tau_b - \tau_{b,cr}) \quad (2.27)$$

Where:

q_B : volume rate of bed load discharge per unit width

And C_s was defined by Straub [1940] as a function of the particle diameter:

$$C_s = \frac{0.17}{d^{3/4}} \quad (2.28)$$

Many subsequent relationships have been defined since then:

Meyer-Peter and Müller [1948] first empirical equation;

Einstein [1950] concept of probabilistic particle movement;

Bagnold [1966] concept of energy balance; and

van Rijn [1984a] concept of particle saltations.

2.4.2 Suspended motion

As flow shear stress increases, grains that are moving by jumps can be caught and drifted in suspension by the main current. Hence, sediment particles will lose their continuous bed-contact during a significant part of their movement. This phenomenon, where a particle denser than the pervading fluid remains in suspension against the gravity forces was explained by Bagnold [1966], who concluded: "It is reasonable to suppose that no solid can remain suspended unless at least some of the turbulent eddies have upward velocity components v' exceeding the fall velocity w of the solid". Figure 2.19 presents the criteria by Engelund [1965], Bagnold [1966], and Van Rijn [1984b] for the occurrence of suspended load.

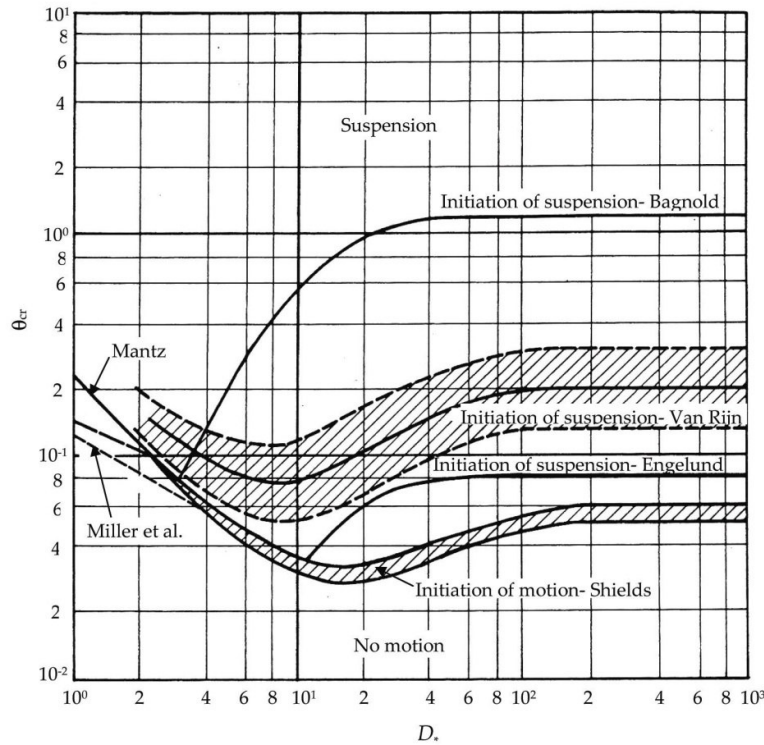


Figure 2.19 Criteria for the occurrence of suspended load [van Rijn, 1993]

Suspended sediment concentrations can be estimated according to the diffusion approach which considers the particle spreading due to random molecular action and turbulent mixing. This analysis is carried out through the Fick's law [Fick, 1855] and the mass-balance equation, which for steady vertical diffusion is expressed as:

$$cw + \varepsilon_s \frac{dc}{dy} = 0 \quad (2.29)$$

Where:

c : sediment concentration at height y above bed

ε_s : sediment transfer or mixing coefficient

w : settling velocity

2.5 Sediment settling

2.5.1 General

Particle deposition is another component of the sediment motion cycle. Increasing shear stress entrains sediments off the bed and the opposite decreasing condition will settle them back. Therefore, the evaluation of sediment settling is also a key element on the study of sediment transport, which as seen on equation 2.29 defines the depth-integrated suspended concentration.

The settling or fall velocity for individual spherical particles in laminar flows is fairly well understood and defined by Stokes' law (valid for R_e numbers lower than 1) [Stokes, 1851]:

$$w = \left[\frac{4}{3} \frac{1}{C_D} g d \left(\frac{\rho_s - \rho}{\rho} \right) \right]^{1/2} \quad (2.30)$$

$$C_D = \frac{24}{R_e} \quad (2.31)$$

Where:

C_D : drag coefficient

ρ_s : density of solids

However, fall velocities in most real cases can differ quite a lot from the results obtained by this approach due to several factors as can be seen next.

2.5.2 Factors affecting fall velocity

Fall velocity is affected greatly under the action of different factors that are frequently present in field conditions. These factors are not included in Stoke's law and therefore the following corrections should be regarded:

1) Turbulence effect. The drag coefficient depends strongly on the level of free stream turbulence, which for $R_e < 800$ is defined by Schiller and Naumann [1933] as:

$$C_D = \frac{24}{R_e} (1 + 0.150 R_e^{0.687}) \quad (2.32)$$

2) Grains' shape effect. Non-spherical particles experience both an increase in the fluid lift force and in the length of their settling path resulting in a slower fall velocity. As shape effect is larger on greater particles, van Rijn [1989] proposed the following formulae to define the fall velocity for three different ranges of particle size. The formulation used depends on the diameter of the sediment in suspension d_s :

$$w = \frac{(s-1)gd_s^2}{18\nu} \quad \text{for } 1 < d_s < 100 \mu\text{m} \quad (2.33)$$

$$w = \frac{10\nu}{d_s} \left[\left(1 + \frac{0.01(s-1)gd_s^3}{\nu^2} \right)^{0.5} - 1 \right] \quad \text{for } 100 < d_s < 1000 \mu\text{m} \quad (2.34)$$

$$w = 1.1[(s-1)gd_s]^{0.5} \quad \text{for } d_s > 1000 \mu\text{m} \quad (2.35)$$

Table 2.6 shows van Rijn's methodology to estimate the representative diameter of the suspended sediment d_s according with the sediment diameter d_{50} of the bed material. When the bed material is well sorted, the use of several sediment fractions is recommended to model its behavior more accurately.

Table 2.6 Representative diameter of the suspended sediment

Transport regime		Particle size
Lower	$0 \leq T \leq 1$	$d_s = 0.064d_{50}$
	$1 < T \leq 15$	$d_s = d_{50}[1+0.015(T-25)]$
Transition	$15 < T < 25$	$d_s = d_{50}[1+0.015(T-25)]$
Upper	$T \geq 25$	$d_s = d_{50}$

3) Hindered settling effect. Observations show a strong reduction in the fall velocity under large sediment concentrations. This phenomenon is mainly caused by the upward return flow induced by the sediment deposition. According to Oliver [1961] the settling velocity in a fluid-sediment suspension can be determined as:

$$w_s = (1 - 2.15c)(1 - 0.75c^{0.33})w \quad (2.36)$$

where:

w_s : particle fall velocity in a suspension

w : fall velocity in clear water

c : suspended sediment concentration

4) Effect of heterogeneous sediments. The effective mean fall velocity of a heterogeneous suspension should be defined according to the work rate required to maintain the particles in suspension [Bagnold, 1966], which may be much larger than the fall velocity of a solid of size d_{50} on the conventional cumulative diagram.

The work required to suspend such a mixture is the sum of component contributions for each range of sizes. Therefore, the effective fall velocity is defined in terms of the arithmetic mean:

$$w = \frac{\sum p_i w_i}{\sum p_i} \quad (2.37)$$

where p_i and w_i are the weight and fall velocity of the size range i .

2.6 Summary of existent sediment transport models

2.6.1 Bed load

Various formulae are available to predict the bed load rates. Herein, the approaches of Meyer-Peter and Müller [1948], Frijlink [1952], Bagnold [1966], and Van Rijn [1984, 2000] are briefly described. These methodologies were defined for steady flow, however, their application to non-steady cases is also valid due to the swift response of near bed particles to new hydraulic conditions.

Meyer-Peter and Müller [1948]:

$$q_B = 8[(s-1)g]^{0.5} d_{50}^{1.5} (\mu\theta - 0.047)^{1.5} \quad (2.38)$$

In which:

q_B : bed load transport

s : specific density

$\mu = \left(\frac{C}{C'}\right)^{1.5}$: bed form factor

$C = 18 \log\left(\frac{12h}{k_s}\right)$: overall Chézy-coefficient

$C' = 18 \log\left(\frac{12h}{d_{90}}\right)$: grain-related Chézy coefficient

$\theta = \frac{\tau_b}{(\rho_s - \rho)gd_{50}}$: particle mobility parameter

$\tau_b = \rho g h i$: bed shear stress

h : water depth

i : energy gradient

k_s : equivalent roughness size

d_{50}, d_{90} : particle diameters

Frijlink [1952]:

$$q_B = 5\mu^{0.5} u_* d_{50} e^{-0.27/(\mu\theta)} \quad (2.39)$$

Where u_* is the bed shear velocity.

Bagnold [1966]:

$$q_B = \frac{e_b}{(\rho_s - \rho)g(\tan\phi - \tan\beta)} \tau_b u \quad (2.40)$$

In which:

q_B : bed load transport

e_b : efficiency factor (≈ 0.1)

τ_b : bed shear stress

- u : depth averaged velocity
 ϕ : angle of repose of bed material
 β : local bed slope

Van Rijn [1984]:

$$q_B = 0.053[(s-1)g]^{0.5} d_{50}^{1.5} D_*^{-0.3} T^{2.1} \quad (2.41)$$

In which:

- q_B : bed load transport
 D_* : dimensionless particle parameter
 T : bed shear stress parameter

Van Rijn [2000]

$$q_B = 0.5\eta\rho_s d_{50} u_{*c}' D_*^{-0.3} T \quad (2.42)$$

In which:

- $u_{*c}' = \left(\frac{1}{8} f'\right)^{0.5} u$: effective bed shear velocity
 $f' = 0.24 \log^{-2}(12h/k_s)$: grain related friction factor ($k_s = 3d_{90}$)
 η : relative availability of the sediment fraction in a mixed layer

2.6.2 Suspended load

Suspended sediment transport does not adjust rapidly to variations in hydraulic conditions, since it takes time to transport the particles upward and downward over the depth. Therefore, suspended sediment models under stationary and non-stationary flows present different characteristics.

2.6.2.1 Stationary models

A summary of several approaches used to model suspended sediment transport under stationary or quasi-stationary conditions is presented hereafter.

Einstein [1950]

$$q_s = 11.6 u_{*c}' c_a a \left[I_2 + I_1 \ln \left(\frac{30.2eh}{d_{65}} \right) \right] \quad (2.43)$$

$$I_1 = 0.216 \frac{A^{Z-1}}{(1-A)^Z} \int_A^1 \left(\frac{1-z'}{z'} \right)^Z dz' \quad (2.44)$$

$$I_2 = 0.216 \frac{A^{Z-1}}{(1-A)^Z} \int_A^1 \left(\frac{1-z'}{z'} \right)^Z \ln(z') dz' \quad (2.45)$$

In which:

q_s :	suspended load transport
$c_a = \frac{q_B}{11.6u_{*c}a}$:	reference concentration
$a=2d$:	reference level
h :	water depth
u_{*c} :	effective bed shear velocity
d :	particle diameter
$A=a/h$:	dimensionless reference level
$z'=z/h$:	dimensionless vertical coordinate
$Z = \frac{w_s}{(\kappa u_*)}$:	suspension number
e :	correction factor

Bagnold [1966]

$$q_s = \frac{e_s(1-e_b)}{(\rho_s - \rho)g\left(\frac{w_s}{u} - \tan\beta\right)} \tau_b u \quad (2.46)$$

In which:

q_s :	suspended load transport
e_s :	efficiency factor (≈ 0.02)
e_b :	efficiency factor (≈ 0.1)
τ_b :	bed shear stress
u :	depth averaged velocity
w_s :	particle fall velocity
β :	angle of local bottom slope

Bijker [1971]

$$q_s = 1.83q_B \left[I_2 + I_1 \ln \left(33 \frac{h}{k_s} \right) \right] \quad (2.47)$$

In which:

q_s :	suspended load transport
$q_B = bu_* d_{50} e^{-0.27/(\mu\theta)}$:	bed load transport
I_1, I_2 :	Einstein's integrals
$a=ks$:	reference level
u_* :	bed shear velocity
μ :	bed form factor
θ :	particle mobility factor
b :	coefficient (≈ 5)

Van Rijn [1984]

$$q_s = Fuhc_a \quad (2.48)$$

In which:

q_s :	suspended load transport
$F = \frac{(a/h)^{Z'} - (a/h)^{1.2}}{[1 - (a/h)]^{Z'} (1.2 - Z')}$:	shape factor
a :	reference level ($a=0.5\Delta$ or $a=k_s$)
Δ :	bedform height
$Z' = Z + \psi$:	suspension number
$Z = \frac{w_s}{\beta\kappa u_*}$:	suspension number
$\psi = 2.5 \left(\frac{w_s}{u_*} \right)^{0.8} \left(\frac{c_a}{c_o} \right)^{0.4}$:	correction factor related to turbulence damping and hindered settling
$c_a = 0.015 \frac{d_{50} T^{1.5}}{a D_*^{0.3}}$:	reference concentration
c_o :	maximum concentration =0.65
$\beta = 1 + 2 \left(\frac{w_s}{u_*} \right)^2$	ratio of sediment and fluid mixing coefficient ($\beta_{max}=2$)
D_* :	dimensionless particle parameter
T :	bed shear stress parameter
κ :	constant of Von Karman =0.4

2.6.2.2 Non-stationary models

A summary of several approaches used to model suspended sediment transport under non-stationary conditions is presented hereafter. The models are based in advection-diffusion process suitable for two-dimensional vertical (2DV), two-dimensional horizontal (2DH) and three-dimensional (3D) situations.

Three-dimensional models (3D) [O'Connor, 1986]

$$\begin{aligned} \frac{\partial c}{\partial t} + \frac{\partial}{\partial x}(uc) + \frac{\partial}{\partial y}(vc) + \frac{\partial}{\partial z}[(w - w_s)c] - \frac{\partial}{\partial x} \left(\epsilon_{s,x} \frac{\partial c}{\partial x} \right) + \\ - \frac{\partial}{\partial y} \left(\epsilon_{s,y} \frac{\partial c}{\partial y} \right) - \frac{\partial}{\partial z} \left(\epsilon_{s,z} \frac{\partial c}{\partial z} \right) = 0 \end{aligned} \quad (2.49)$$

where:

c :	sediment concentration
u, v, w :	fluid velocity components in x, y, z directions
ϵ_s :	sediment mixing coefficient
w_s :	particle fall velocity

Two-dimensional vertical models (2DV) [Kerssens et al, 1979]

$$\frac{1}{b} \frac{\partial}{\partial x} (buc) + \frac{\partial}{\partial z} (w - w_s)c - \frac{\partial}{\partial z} \left(\varepsilon_s \frac{\partial c}{\partial z} \right) = 0 \quad (2.50)$$

where:

- c : sediment concentration
- b : flow width
- u, w : fluid velocity components in x, z directions
- ε_s : sediment mixing coefficient
- w_s : particle fall velocity

Two-dimensional horizontal models (2DH) [Galapatti and Vreugdenhil, 1985]

$$c = \alpha c + \beta \frac{h}{w_s} \frac{\partial c}{\partial t} + \gamma \frac{uh}{w_s} \frac{\partial c}{\partial x} \quad (2.51)$$

where:

- c : sediment concentration
- u : fluid velocity in x direction
- h : water depth
- w_s : particle fall velocity
- α, β, γ : coefficients representing the vertical distribution effects (profile functions)

Chapter 3

Spatial distribution of grain sizes

3.1 Introduction

The well-known advantages of process-based numerical models capable of managing a particular phenomenon over extensive areas, force modellers to put additional efforts into representing accurately the spatial heterogeneous input parameters involved in the model domain. This chapter deals with the spatial variability of sediment grain sizes, a generally heterogeneous scalar field under natural conditions, which have major importance on the estimation of all constituents of the sediment motion cycle (e.g. sediment entrainment, transport and fall velocity). Even so, the information on grain-size distribution in the field is normally not available, and it represents one of the greatest obstacles in the accurate prediction of sediment transport and morphological developments. Field measurements offer valuable means for describing spatially heterogeneous input parameters, although the cost of field surveys increases with increasing demand on accuracy.

To overcome this drawback several hypotheses suggesting a spatial distribution of grain sizes due to flow energy have been proposed [Hjulström, 1939 and Shields, 1936] and applied in morphodynamic modelling in tidal areas as in Hirschhäuser et al. [1998]. Other approaches are based on wave characteristics and among them two major theories have been proposed to explain the selective shore-normal sorting of grain sizes: the hypothesis of asymmetrical thresholds under waves and the null-point hypothesis [Horn, 1992]. Both hypotheses are founded on asymmetric wave behavior, suggesting that under a wave environment the higher onshore velocities would produce a shear stress large enough to initiate motion for both large and small sediment particles, while the lower offshore velocities would only exceed the threshold shear stress for the smaller particles. Thus, this mechanism would act selectively to drive larger particles onshore, with a net offshore transport of finer sediment.

The fact that these hypotheses and interpretations of sediment sorting are mostly stated in qualitative form means that there is still a shortage of applicable tools for predicting grain-size distribution over a specific coastal area. On this basis, Dean [1991] outlined the need for research designed to predict and interpret sediment sorting. Therefore, the major objective of the current chapter is to determine a functional relationship between flow-wave characteristics and grain sizes that may be easily applied in the study area and perhaps also in similar near-shore regions.

About 200 surficial sediment samples gathered in the Dithmarschen Bight for a range of flow-wave conditions were considered in the analysis. The temporal variation of grain sizes was neglected. The resulting grain-size dataset was correlated with local flow and wave parameters. Maximum and time-averaged values of hydrodynamic parameters were obtained from 2-D flow-wave simulations performed during a Typical Tidal Cycle (TTC), as characterized by a mean tidal range and mean wave forcing.

The topics contained in this chapter are presented in six sections. In section 1, the problem definition and objectives of the study are given. Section 2 comprises the materials and datasets used in the study. Section 3 presents the methodology used to determine stationary flow-wave characteristics in the study area. Sections 4 and 5 present the results of the correlations between grain sizes vs. flow-wave characteristics and the proposed relationship to define equilibrium grain sizes. Section 6 summarizes the main aspects dealt in this chapter and proposes some topics on which future investigations should focus.

3.2 Surficial sea bed characteristics

The composition of the sediment deposits in the study area corresponds extensively to recent tidal flat sediments [Ricklefs et al., 2005]. The thickness of the recent deposits is about 20m, excluding areas where the Dithmarscher Klei or Early Holocene Layer EHL outcrops. Fig. 3.1 shows the thickness of the potentially mobile sediment above the EHL [Asp, 2004]. The EHL (Dithmarscher klei) consists of consolidated cohesive sediments forming a natural base that hinders erosion in the tidal channels [Ricklefs et al., 2005]. The EHL appears in the central part of the channels, where shear stresses are high and non-cohesive deposits have been entirely removed. Therefore, the thickness of the potentially mobile sediment layer increases towards the northern and southern banks of the main tidal channels.

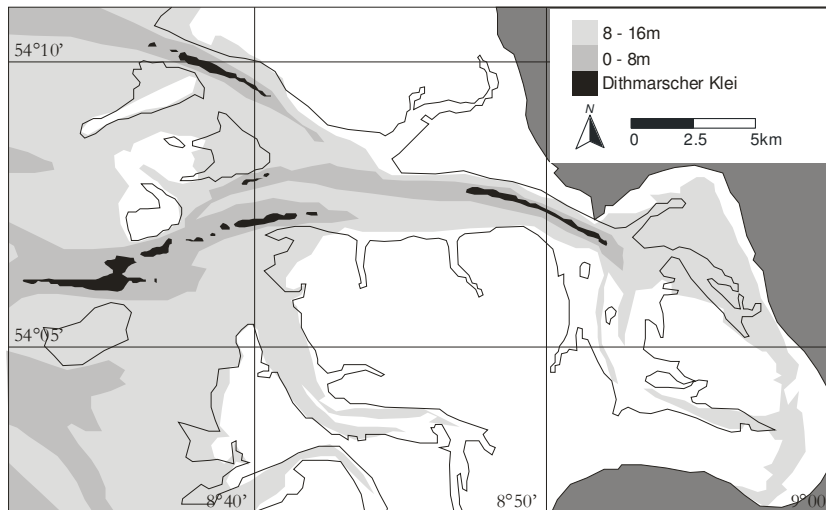


Figure 3.1 Thickness of the potentially mobile sediments [Asp, 2004]

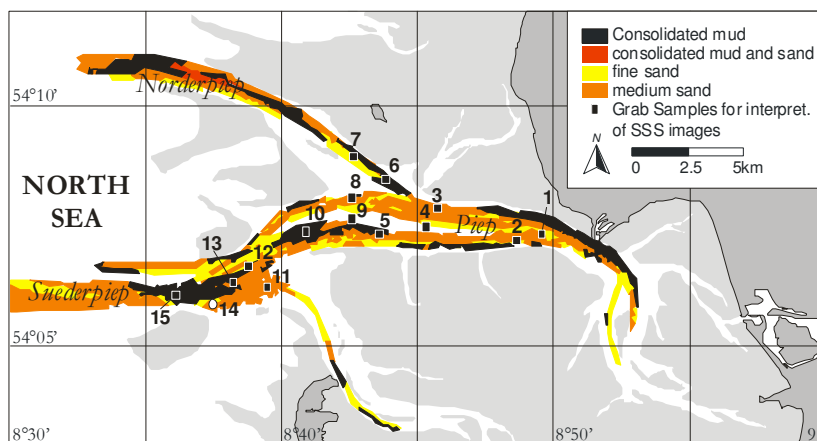


Figure 3.2 Surficial seabed sediment distribution in the main tidal channels [Vela-Diez, 2001]

Fig. 3.2 shows the different sediment types present in the Dithmarschen tidal channels. They were derived from side-scan sonar images (SSS) calibrated with grab samples [Vela-Diez, 2001]. The spatial distribution of surficial seabed sediments is quite variable, where sand, mud and consolidated deposits prevail. Sands are mainly very fine to fine sands with some isolated patches of medium sands. The grab samples for interpretation of SSS images showed very well sorted sand with d_{50} values varying between $80\mu\text{m}$ and $230\mu\text{m}$. Consolidated fine sediments occurred mostly at deeper locations in the channels. An analysis of the mud content ($\% < 0.063\mu\text{m}$) in the less-exposed areas confirmed mud presence in all samples. Laboratory analysis indicated that silt and clay content of the sediment samples were generally

greater than 5%, attaining maximum values of 75%-80%. Moreover, values exceeding 10% were found in about 50% of the samples [Poerbandono and Mayerle, 2005].

Fig. 3.3 presents the sample locations and the mean grain sizes of surficial sediments at the Dithmarschen tidal flats. They are mostly constituted of sandy sediments with diameters higher than $63\ \mu\text{m}$. From the western wave dominated tidal flat region to the eastern sheltered areas, an increase of fine materials can be observed. Broadly speaking, the grain-size distribution exhibits the typical pattern for a tidal flat bay: coarser sediments in the more wave-exposed areas and fine-grained muddy deposits in sheltered zones close to the high water line [Reineck and Singh, 1980].

Three sediment classes were defined at the tidal flats according to the methodology presented by Mcmanus [1988]: (a) Fine to medium sand, which is characteristic for sediments of the exposed western shoals. Samples of such type were exclusively found within the wave dominated D-Steert, Tertius and Blauort sand banks; (b) Fine sand and mixed sediments are representative of the huge areas of the open tidal flats. This type of deposit is widely spread on the higher parts of the sand banks of Bielshövensand and Helmsandsteert; and (c) Clay and silt become more predominant in the sheltered areas close to the high water line, at the backside of supratidal morphologic units, in tidal gully head regions and for many inner banks. This class of sediment indicates a calm hydrodynamic condition.

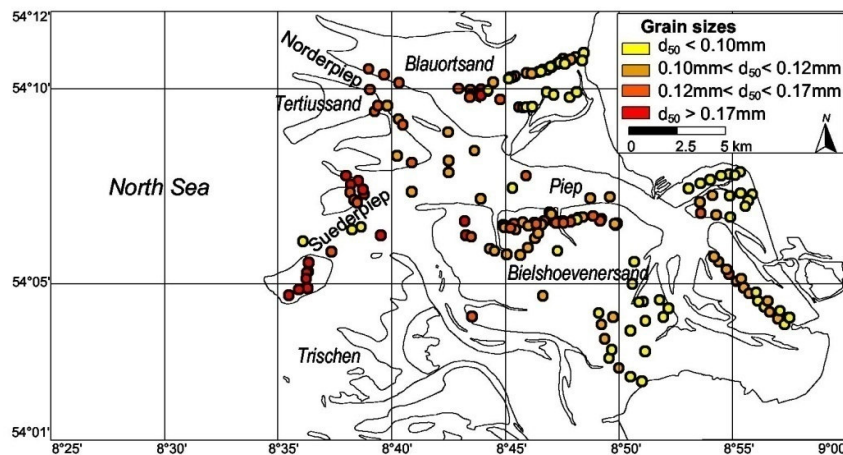


Figure 3.3: Location and results of the bed sediments sampling during 1999 and 2000.

Adapted after Reimers [2003]

3.3 Flow and wave patterns

As grain sizes are assumed stationary, their prediction should not be affected by temporal variations on flow or wave conditions. Therefore, the definition of representative stationary flow-wave fields at the study area is the main concern in this section. The representative flow-wave conditions will enable subsequent correlations with the available grain size dataset collected during 1999-2000, in order to define possible reciprocal relationships of stationary character.

3.3.1 Flow patterns

The typical flow condition is defined by time-averaged or maximum hydrodynamic variables including shear stress, flow velocity and water depths occurring during the Typical Tidal Cycle (TTC). The TTC is characterized by a mean tidal range of 3.2m and a mean wave forcing (described in the next section). Figures 3.4 to 3.7 show the results of time-averaged modeled velocities and shear stresses during neap and spring tidal cycles, which indicate the high temporal variability of these variables. Flow simulations are performed by means of the WL | Delft Hydraulics computer software. Definition of the flow model settings is carried out in agreement to the model proposed by Palacio [2002].

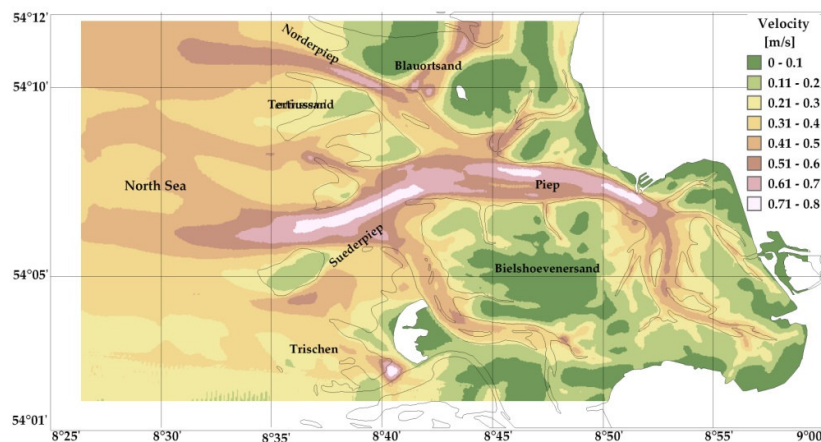


Figure 3.4 Time-averaged velocities during a spring tidal cycle

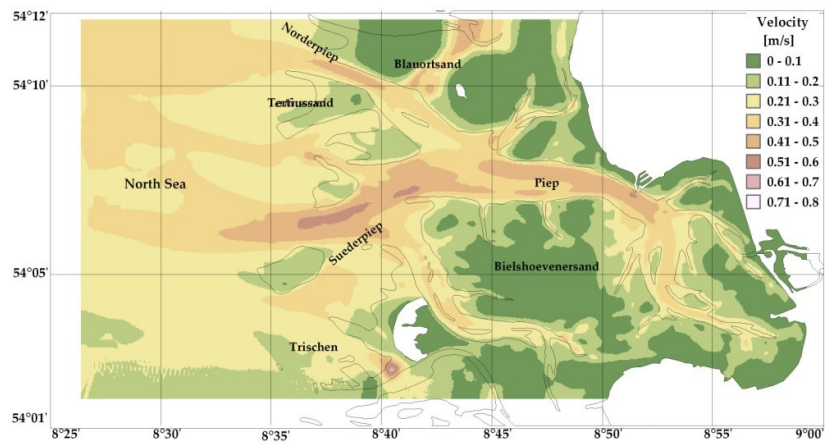


Figure 3.5 Time-averaged velocities during a neap tidal cycle

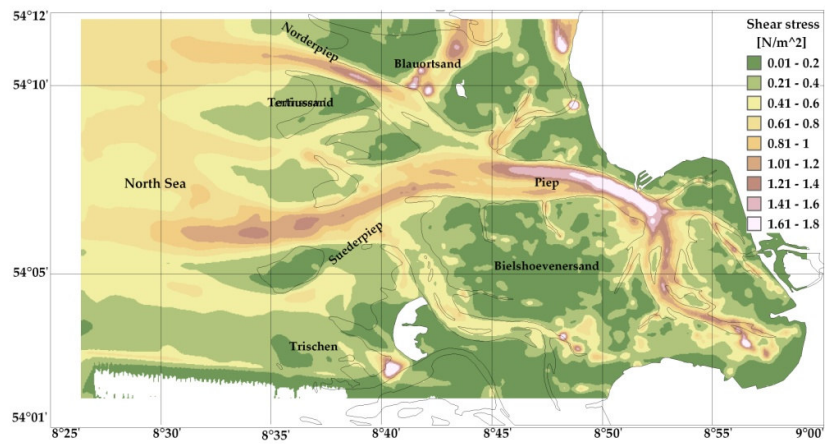


Figure 3.6 Time-averaged shear stresses during a spring tidal cycle

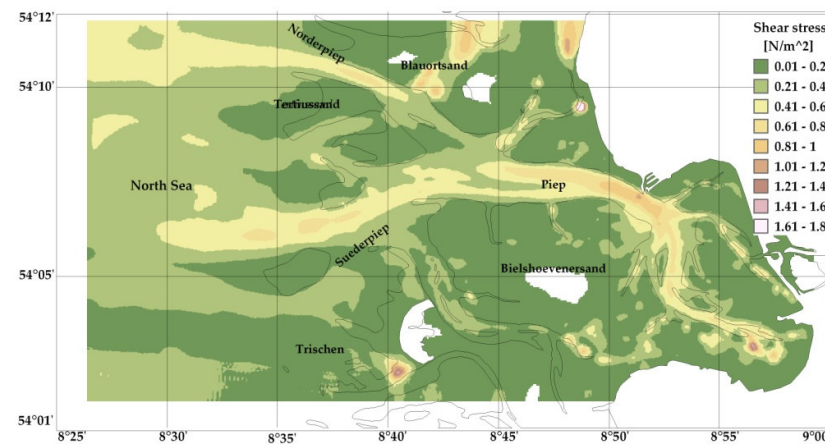


Figure 3.7 Time-averaged shear stresses during a neap tidal cycle

3.3.2 Wave patterns

Wave conditions in the study area depend basically on the swell waves approaching from the open North Sea as well as on the locally generated wind waves [Wilkens, 2004]. However, the complex bathymetry that includes tidal flats, tidal channels and sand banks combined with a tidal hydrodynamic regime greatly affect the spatial distribution of wave characteristics along the domain. At the western boundary of the domain, water depths range from 10 to 16 m. Swell waves therefore enter the area practically undisturbed by the bathymetry. Within 5 to 10 km from the western boundary, water depths reduce to values between 0 and 4m on the tidal flats, depending on the stage in the tidal cycle. Thus, most incoming swell waves will break in this part of the domain. Only in the tidal channels can waves penetrate further into the domain, although the out-flowing ebb currents may hinder them.

A coupled wave and flow model was used to simulate the wave characteristics in the Dithmarschen Bight. The SWAN wave model [Booij et al., 1999; Ris et al., 1999] and the Delft3d modelling system [Roelvink and Van Banning, 1994] were used in this study. As in the flow case, typical wave conditions are defined in the study area in order to enable subsequent correlations with the grain-size dataset. Thus, average conditions of the swell at the western boundary and mean local wind characteristics over the bight constitute the main input data required to carry out the wave simulations for the TTC.

Field measurements taken in September 1995 [Niemeyer et al., 1995] provided the mean wave forcing at the western boundary of the model due to the adjacent North Sea. The location of five wave buoys used during measurements is shown in Figure 3.8 and the time series of the significant wave heights recorded is shown in Figure 3.9. The wave buoy denoted as Pos 2 and located at the model western boundary was used to define the wave forcing inside the domain. Wave parameters at Pos 2 were 0.7 m and 3.7 s for the mean wave height and the mean wave period, respectively. Given the relatively short-term period of measurements available at Pos 2 a verification of its reliability with long-term measurements recorded at Sylt Island, 70 km away from the study area and characterized by similar conditions, was performed. Statistics of wave data at Sylt [BMFT, 1994; Froehle and Kohlhase, 1995] from 1986 to 1993 show maximum wave heights up to 5.5m and the mean wave height of about 1m, which is relatively close to the mean wave height defined by the local measurements.

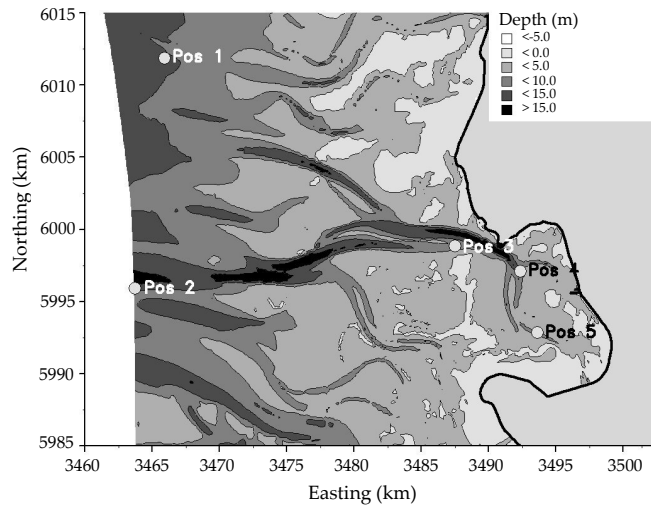


Figure 3.8 Wave buoy locations - September 1996 campaign [Niemeyer et al., 1995]

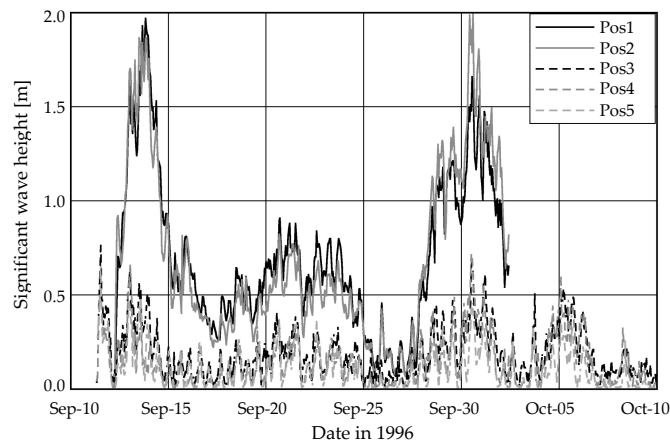


Figure 3.9 Significant wave heights at the five wave buoy locations [Wilkins, 2004]

To complement the above mentioned verification between wave patterns at Sylt and “Pos 2” locations, Figure 3.10 shows their respective wave roses. Wave roses were derived on the basis of long-term measurements and long-term modelling results for Sylt and Pos 2 respectively. They represent graphically the probability of occurrence of a specific significant wave height and its direction. Model results at Pos 2 were taken from the 40-year hindcast of wave climatology carried out by the project HIPOCAS [Guedes, et al. 2002]. This project uses the WAM model [Hasselmann et al., 1988] across a very large extent of the European waters, including the Mediterranean, North East Atlantic and North Sea.

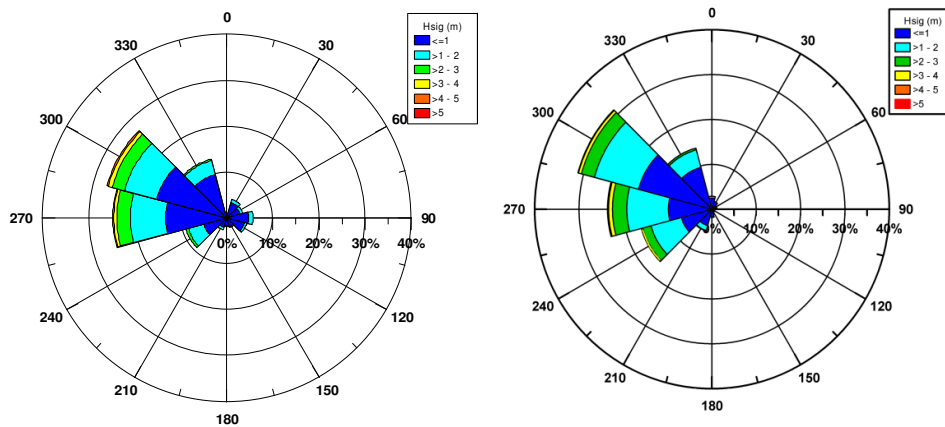


Figure 3.10 Wave rose at Pos 2 (left) and Sylt Island (right)

From measurements and model results at Sylt and Pos2, the mean wave height along the western boundary of the Dithmarschen Bight is defined within 0.7m - 1m, the typical wave direction ranges from 270° to 300° and the mean wave period is nearly 3.7s. The mean wave height, the typical wave direction and the mean period define the typical wave forcing along the west model boundary due to the North Sea swell. This forcing, however, should be complemented by waves originated in the interior of the study area by local winds. Local wave generation is driven by means of the typical wind (magnitude and direction) which is determined from measurements at the Büsum station (Research and Technology Centre Westcoast) and from the PRISMA wind model [Luthardt, 1987]. Figure 3.11 shows part of the available wind speed and direction data recorded at the Büsum station corresponding to the first semester of the year 2000. Considering wind data at the Büsum station from 2000 to 2002 (i.e. period on which grain size measurements were performed), the mean wind speed was found to be around 5m/s and the most frequent directions range from 225° to 315°.

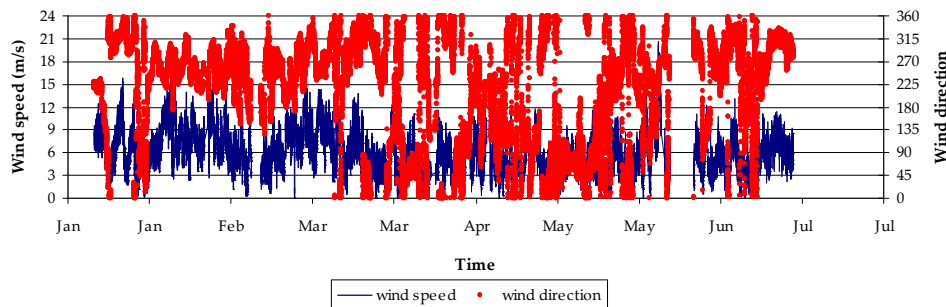


Figure 3.11 Local wind measurements at the Büsum station

In order to verify the difference of the measurements performed at the Büsum station over the 3 years from long-term data, a comparison to the PRISMA data was

performed. The wind rose velocity for the study area based on PRISMA data from 1989 to 2000 is presented in Figure 3.12.

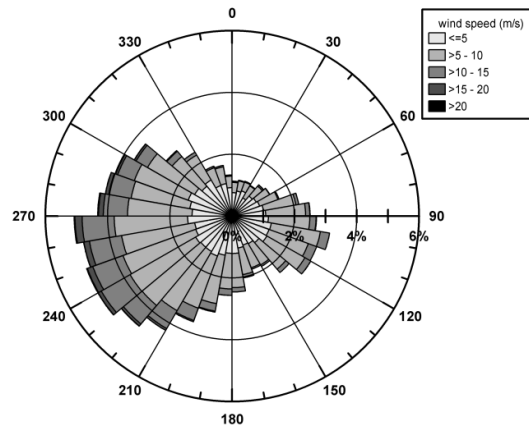


Figure 3.12 Wind rose for the Dithmarschen Bight [Luthardt, 1987]

According to this figure, the mean wind speed is around 6.1 m/s and the most frequent directions range from 210° to 300°, which are in relatively good agreement with measurements carried out at the Büsum station.

Table 3.1: Monthly averages of wind speed at Büsum station

Year	Wind Speed (m/s)											
	Jan	Feb	Mar	Apr	May	Jun	Jul	Aug	Sep	Oct	Nov	Dec
2000	6.7	6.7	5.8	4.4	4.6	5.0	4.3	3.6	5.2	6.3	6.5	5.6
2001	4.8	5.3	5.5	4.7	4.2	4.1	4.3	4.1	4.2	5.9	5.2	4.5
2002	6.0	6.9	5.0	4.2	4.0	4.5	—	3.3	3.6	5.0	4.7	5.5

Averaged wave conditions along the western boundary as well as averaged wind characteristics within the study area make up the final setup for the typical wave forcing at the Dithmarschen Bight. Table 3.2 summarizes the typical wave forcing due to the North Sea and the local wind waves. Numerical wave modelling based on this typical forcing results in the wave characteristics displayed in Figures 3.13 to 3.16. Additional input parameters were defined according to the values used in the wave model developed by Wilkens [2004] in the Dithmarschen Bight.

Table 3.2: Typical wave forcing at the Dithmarschen Bight

	North sea swell	Local wind
Significant wave height	0.8 m	-----
Peak period	3.7 s	-----
Wave direction	270°	-----
Wind speed	-----	5 m/s
Wind direction	-----	270°

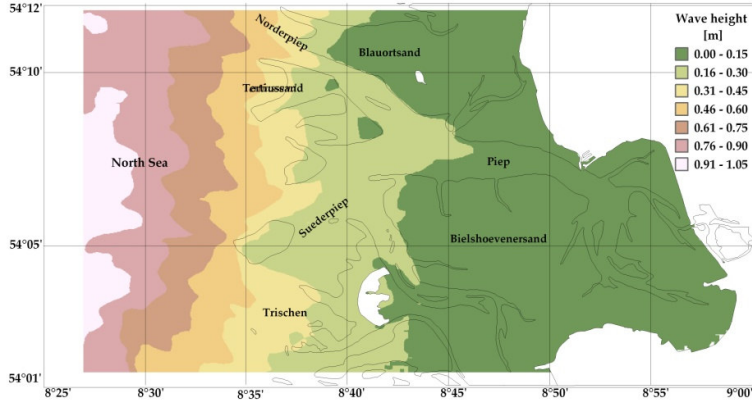


Figure 3.13 Averaged wave height at the Dithmarschen Bight during the TTC

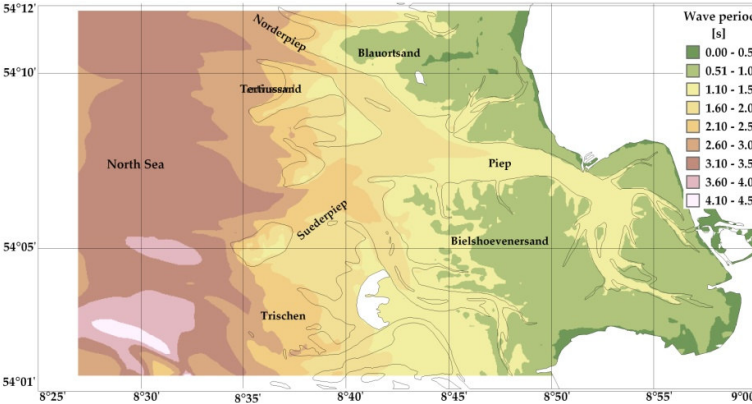


Figure 3.14 Averaged wave period at the Dithmarschen Bight during the TTC

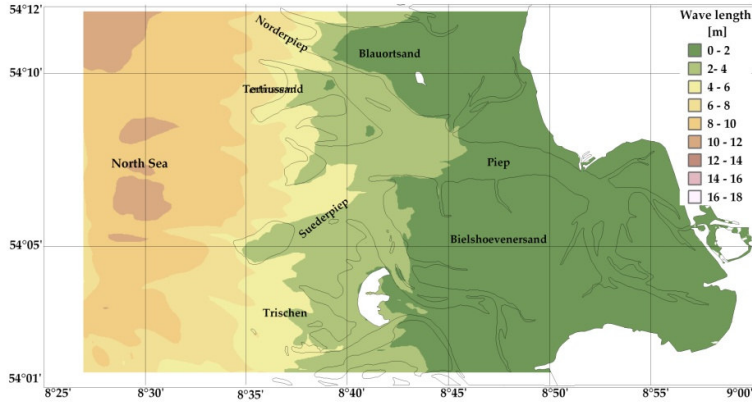


Figure 3.15 Averaged wave length at the Dithmarschen Bight during the TTC

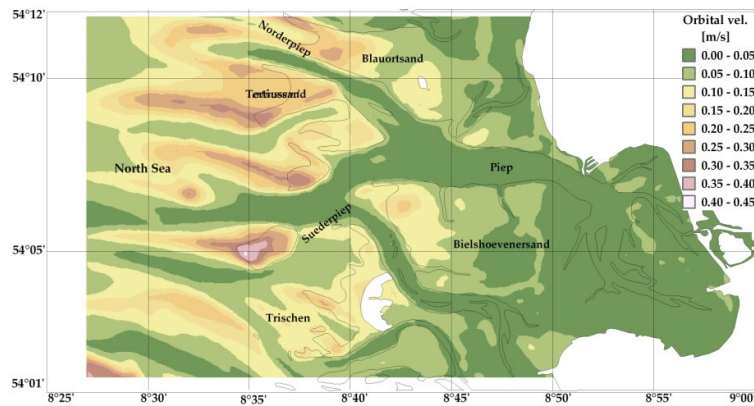


Figure 3.16 Maximum orbital velocities at the Dithmarschen Bight during the TTC

3.4 Grain size sorting and representative flow conditions

The characteristics of the surficial material in the tidal flats and channels of the Dithmarschen Bight has been investigated by Reimers [2003] and Vela-Diez [2001] respectively. Sediments in Norderpiep, Suederpiep and Piep tidal channels were studied on the basis of side scan sonar results and grab samples taken during 1999 and 2000 (see Figure 3.2). Sediment studies over the tidal flats involved the analysis of about 200 grab samples that were collected in the same period (see Figure 3.3).

This grain size dataset and the results of the flow model were used to verify a possible reciprocal relationship between hydrodynamic patterns and grain sizes. The targeted functional relationship will be used in the design of a high-resolution sediment map over the study area (i.e. flow model resolution). Hence, particle sizes over non-sampled areas might be defined on the basis of more accessible flow characteristics.

Depth-averaged velocities, bed shear stresses and water depths (time integrated over the TTC) are correlated to sediment features like d_{50} , d_{90} and fine content as shown in Figures 3.17 to 3.19. Samples from the tidal flats and channels are displayed both separately and grouped.

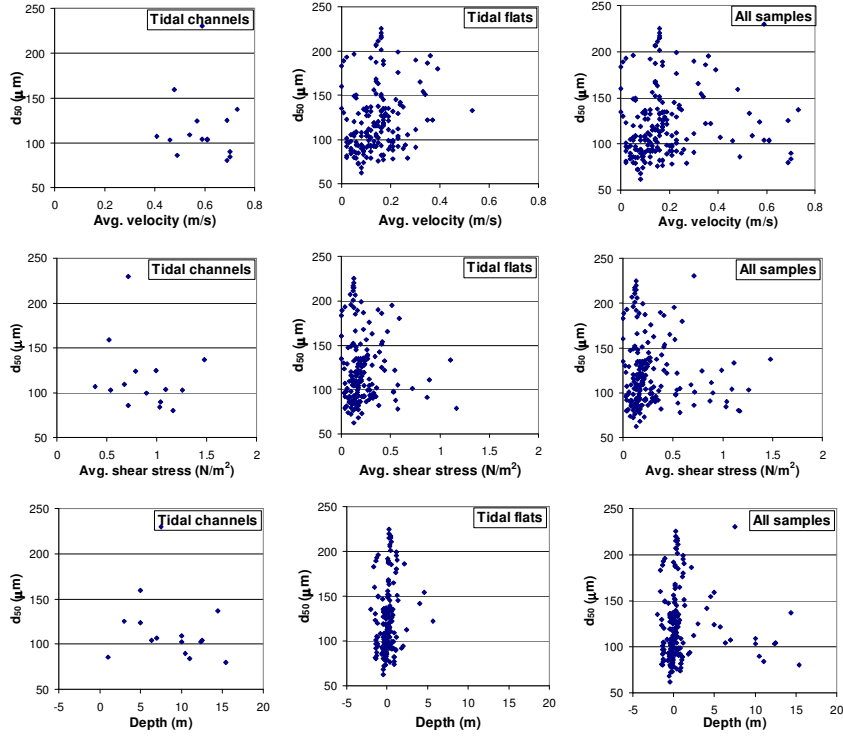


Figure 3.17 Variation of d_{50} with flow conditions in the Dithmarschen Bight

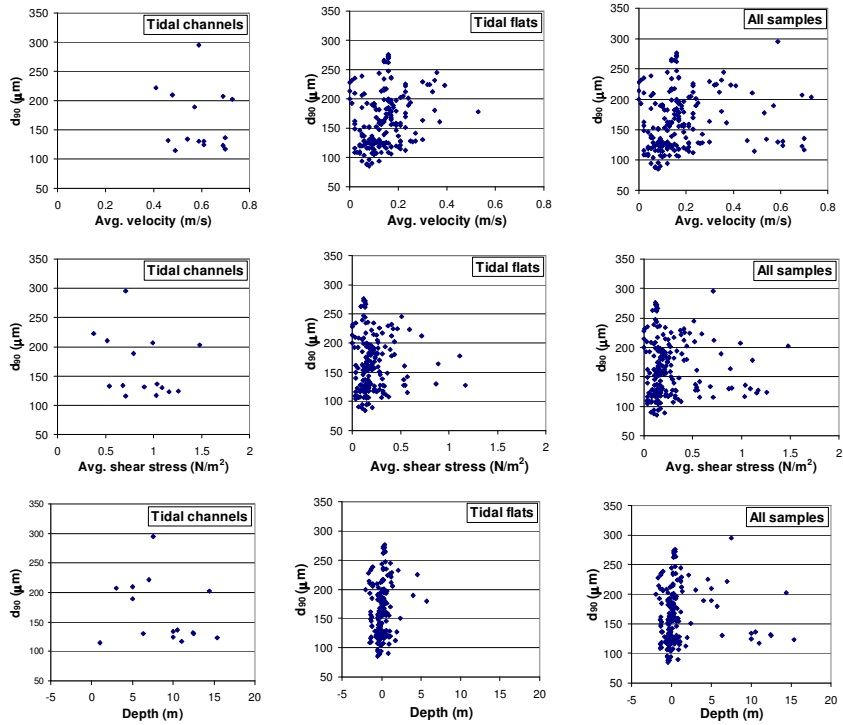


Figure 3.18 Variation of d_{90} with flow conditions in the Dithmarschen Bight

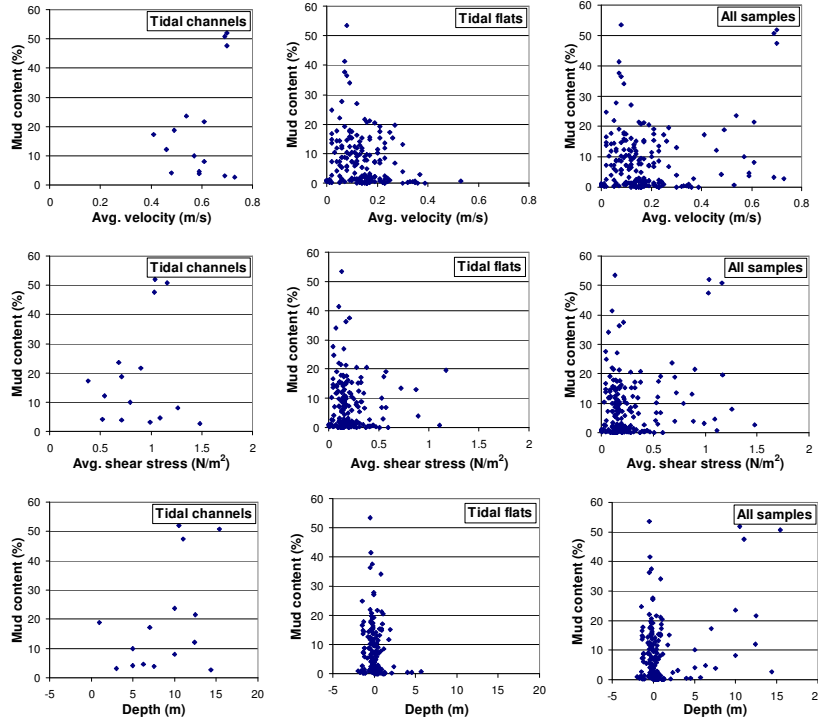


Figure 3.19 Variation of mud content with flow conditions in the Dithmarschen Bight

In spite of the fact that the flow was represented by three different variables, covering the major units from the mechanical point of view, namely dynamics (shear stress), kinematics (velocity) and longitude (depth), no effect of these variables on grain sorting was found. Moreover, all relationships between flow characteristics and grain sizes showed very poor correlation coefficients.

The analysis carried out above was repeated with maximum flow characteristics instead of the time-averaged conditions. Then, aim toward a functional relationship between maximum velocities or shear stresses with sediment features was taken. Again, no pattern nor trend was found. This fact can be seen in Figure 3.20, where for compactness sake, only the variation of d_{50} with maximum current velocities is presented.

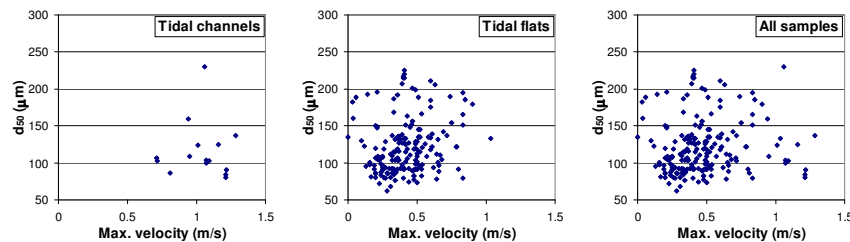


Figure 3.20 Variation of d_{50} with maximum velocities computed in a TTC

A former hypothesis explaining grain size sorting by means of current energy [Hjulström, 1939] was also verified in this study. The grain size dataset and the local depth-averaged velocities obtained from numerical simulations were superimposed on the Hjulström diagram as shown in Figure 3.21. Despite the fact that the sample data only cover a reduced range of grain sizes, the large scatter with respect to Hjulström diagram is noteworthy.

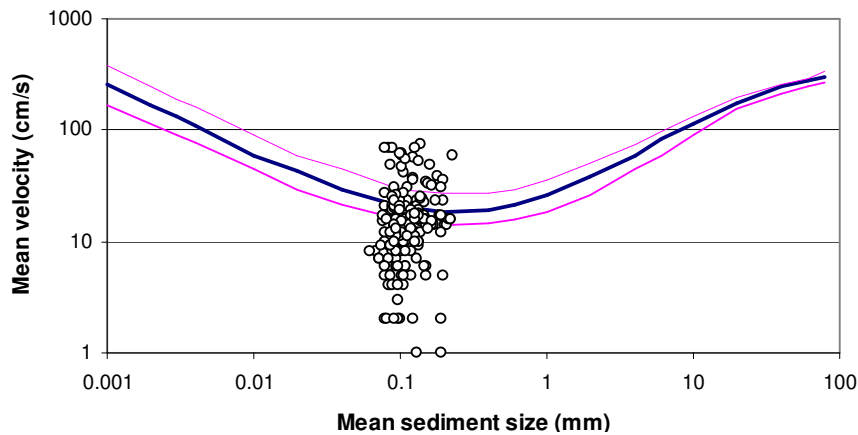


Figure 3.21 Grain size dataset from the Dithmarschen Bight superimposed on Hjulström diagram

The spatial distribution of grain sizes in a tidally dominated area such as the Dithmarschen Bight presents a low correlation with the flow characteristics: depth-averaged velocities, shear stresses and water depths. This fact has been shown through Figures 3.17 to 3.21. Neither calculated flow patterns, under maximum nor time-averaged conditions in the TTC, showed a good fit to grain sizes. Thus far, all the analysis has been performed under calm weather conditions and excluded wave characteristics. Therefore, in order to complement the investigation, waves' features are considered next.

3.5 Grain size sorting and representative wave conditions

The Dithmarschen Bight is characterised by a mean tidal range of 3.2m, which, compared to a mean wave height of around 1m at the western boundary, suggests a tidal predominance according to Figure 3.22. At first glance, wave effects are shadowed by tides. This effect is even more pronounced at the eastern areas where waves propagate with lower heights (around 0.3m) due to the wave-breaking processes over the western sand banks.

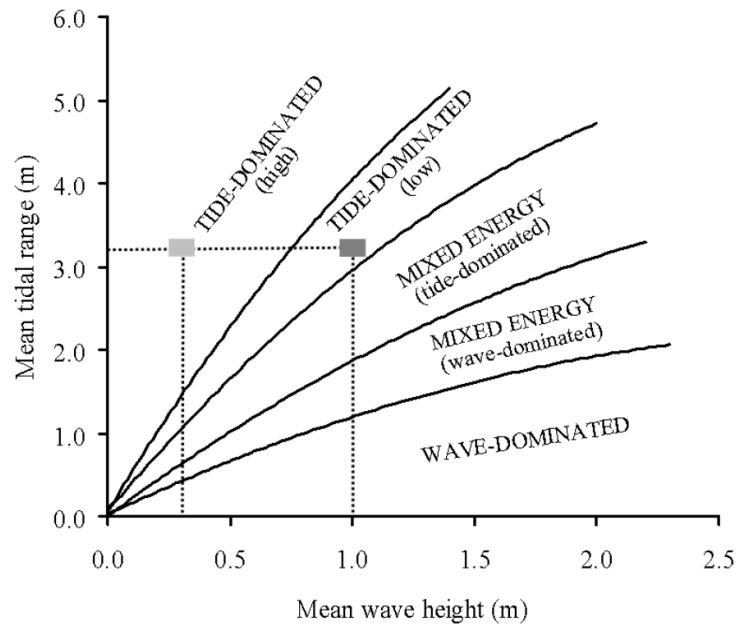


Figure 3.22 Classification of tidal areas. Hayes [1979]

The suggestion stated above should however be carefully considered on such an irregular domain as the Dithmarschen Bight. The complex bathymetry presents values ranging from -1.6m to 25m at sand banks and tidal channels respectively. This fact leads half of the study area to fall dry during low water. Therefore, a spatial variation of the tidal range takes place in the intertidal zone. Hence, shallow areas falling dry during ebb phase have a reduced tidal range in comparison with deeper regions. In order to account for this fact, a characterization of the region is presented in Figure 3.23 where the coastal zone was divided into two zones: zone 1, bounded by the segment AB where the mean tidal range H is uniform, and zone 2, which is limited by the segment BC and presents a spatial variation of the mean tidal range H' according to the local bathymetry.

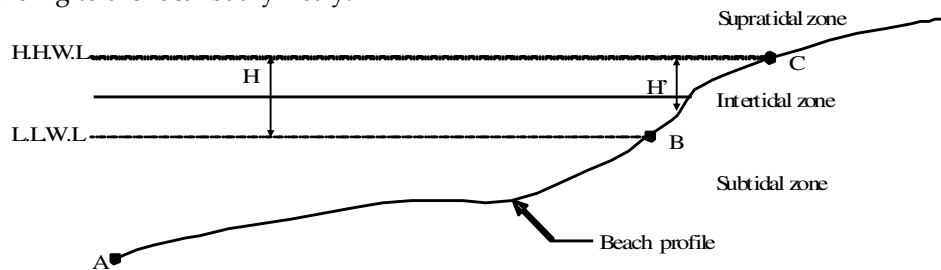


Figure 3.23 Spatial variation of the tidal range at the intertidal zone

As the mean tidal range on segment BC varies from H on position B to zero on position C, therefore, it might be possible that wave effects become dominant over the tidal ones in the intertidal zone. Given this possible domain or influence of waves along the shallow areas of the Dithmarschen Bight, a series of verifications are undertaken, especially monitoring their effect on grain size sorting.

The spectrum of grain sizes (represented by d_{50} values at several locations in the study area) was correlated with local wave parameters. The variation of grain sizes with time-averaged wave parameters obtained during the TTC (see Figure 3.24) was the first verification performed and intended to create a relationship between the wave features and equilibrium grain sizes.

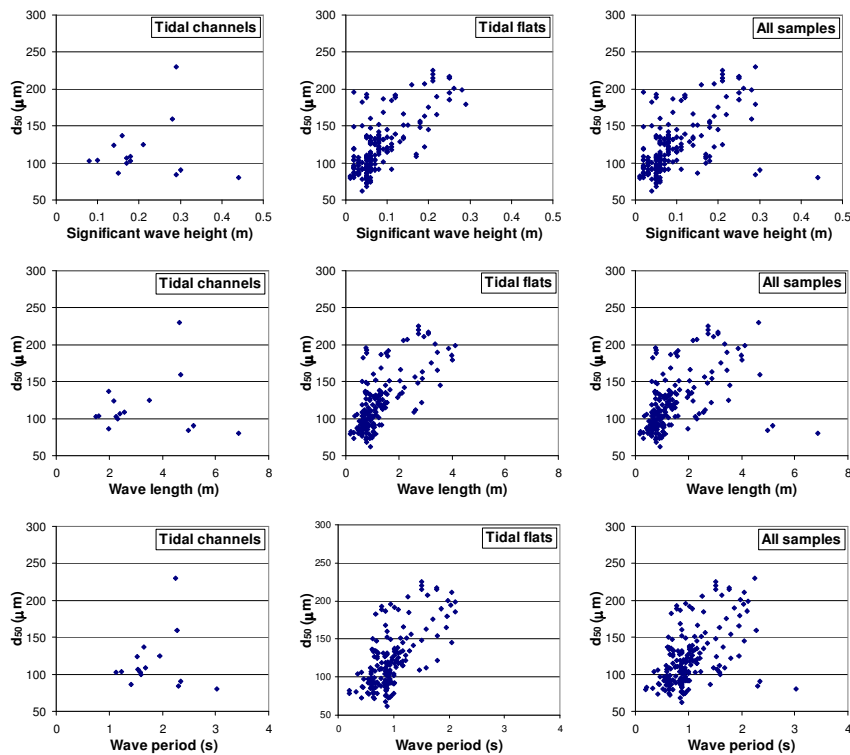


Figure 3.24 Variation of d_{50} with typical wave parameters averaged over the TTC

Results presented in Figure 3.24 show a considerable improvement in the correlation coefficients between wave parameters and grain sizes, being far higher than those obtained between flow conditions and grain sizes (see Figures 3.17 to 3.21). Fitting adjustments are better over the shallow tidal flats than along the deeper tidal channels, where low correlation coefficients still remain. The latter is explained by the lessened degree of bed exposure to wave action, which is hereafter determined by the ratio of significant wave height to mean water depth.

To complement the aforementioned analysis, additional cases were considered such as the inclusion of maximum wave characteristics, as well as other variables including orbital velocity and orbital excursion. Finally, in order to establish the relationship between grain sizes and local waves it was found that the best correlations occurred between maximum orbital velocities or excursions and grain sizes. Further details about these wave parameters can be found in van Rijn [1993]. The orbital velocity and excursion are defined respectively as:

$$\hat{U}_\delta = \sqrt{\int_0^{2\pi} \int_0^\infty \frac{\sigma^2}{\sinh^2(kh)} E(\sigma, \theta) d\sigma d\theta} \quad (3.1)$$

$$A_\delta = \frac{1}{\sigma} \hat{U}_\delta \quad (3.2)$$

Where:

- σ : wave frequency
- k : wave number
- h : water depth
- E : wave energy

During a TTC, maximum local values of orbital velocities and excursions were correlated with grain sizes as shown in Figure 3.25.

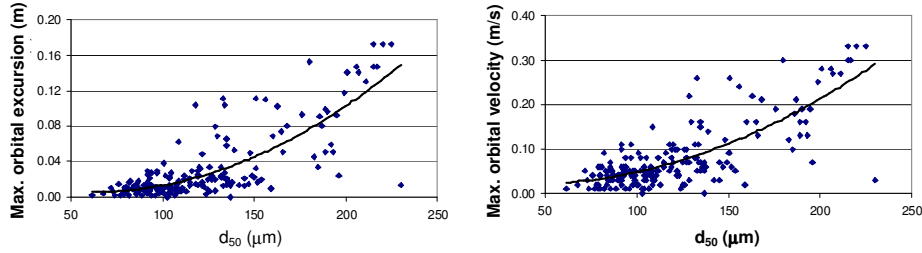


Figure 3.25 Variation of d_{50} with maximum wave parameters computed for a TTC

Given the low possibilities of determining the grain sorting in deep-water areas through wave characteristics, the dataset shown in Figure 3.25 is divided according to the degree of bed exposure to wave action, expressed in terms of the ratio between the maximum wave heights computed in a TTC (H_{sm}) and mean water depths (h). Figure 3.26 presents the relationships between the observed equilibrium grain sizes and modeled maximum orbital velocities proposed for different H_{sm}/h .

The entire dataset is divided into three subgroups according to their bed exposure. Three polynomial curves of second order were fit to each dataset by means of the minimum square error technique. From this statistical study it was found that regions in the Dithmarschen Bight with relations H_{sm}/h higher than 0.50 (shallow tidal flats) show high correlation coefficients for the proposed curve.

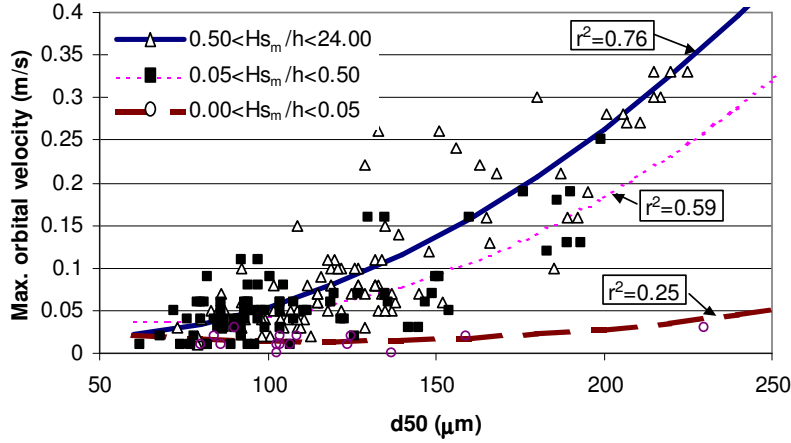


Figure 3.26 Wave effect on the equilibrium grain sizes

A threshold value of 5% for the ratio H_{sm}/h implied a negligible statistical correlation between grain sizes and wave orbital velocities. Excluding field data with a ratio H_{sm}/h lower than 5%, a new fitting is performed and presented in Figure 3.27 showing the proposed relationship for the equilibrium grain sizes.

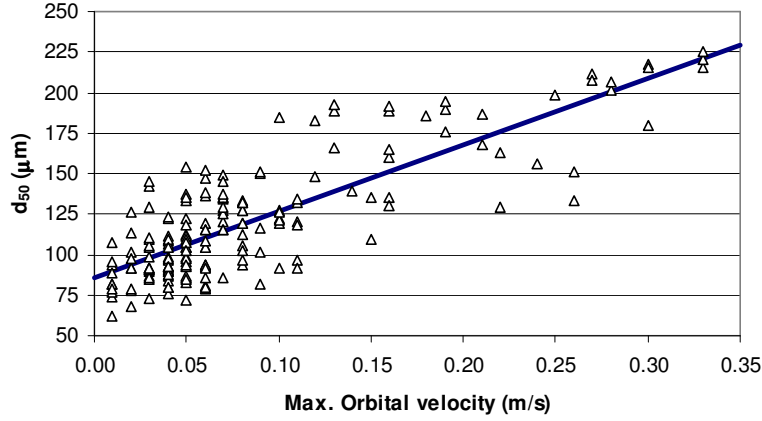


Figure 3.27 Relationship for the equilibrium grain sizes on the tidal flats

A performance assessment of this approach is carried out under the Relative Mean Absolute Error (RMAE) and Mean Absolute Error (MAE) methodologies. Grain size data is related to maximum orbital velocities by means of the following function:

$$d_{50} = 60.5 + \sqrt{-3207 + 90909 * \hat{U}_{\delta_{max}}} ; \hat{U}_{\delta_{max}} \geq 0.036 \text{ m/s} \quad (3.3)$$

$$H_{sm}/h > 0.05$$

In this equation, grain sizes are given in [μm] and orbital velocities in [m/s].

Equation 3.3 can be linearized with slight inaccuracies by:

$$d_{50} = 407.86 * \hat{U}_{\delta_{max}} + 86 \quad (3.4)$$

Figure 3.28 shows the accuracy of equation 3.3 on the prediction of grain sizes across the tidal flats of the Dithmarschen Bight.

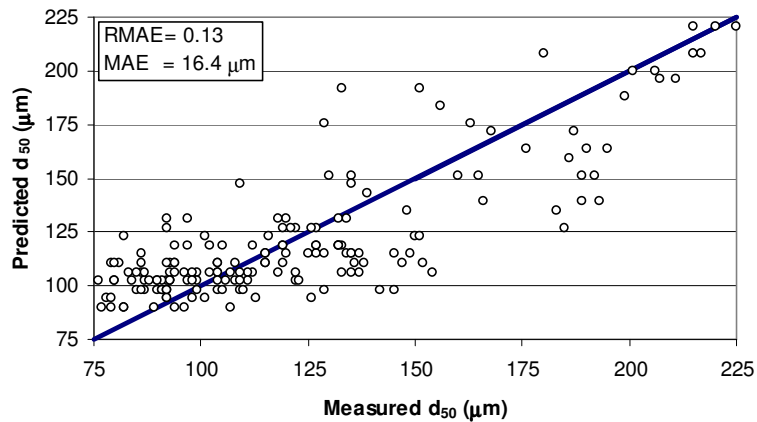


Figure 3.28 Assessment of performance for grain size predictions on the tidal flats

Absolute and relative errors of 16.4 μm and 13% represent, respectively, the MAE and RMAE criteria that assess the performance of the proposed methodology to predict equilibrium grain sizes. These errors are relatively close to the inaccuracies occurring during grain size measurements, as was observed in the analysis carried out with sieve and laser techniques during the interlaboratory intercalibration experiment hosted by the project SCCWRP [SCCWRP, 1994]. The experiment showed variations ranging from 6%-10% for sandy samples and 16%-18% for silty samples. Laser analysis for particles less than 1.0 mm in diameter registered variations from 6% to 8%.

The laboratory intercalibration results revealed a variation range between 6% to 18% for grain size measurements. Therefore, the application of the proposed methodology was found to yield accurate definitions of grain sizes in the Dithmarschen Bight. In accordance with this conclusion, the map of the equilibrium grain sizes across the domain was constructed by means of equation 3.3 and is presented in Figure 3.29. Provided appropriate validations are carried out, the procedure and functional relationships proposed here might also be applicable to similar study areas.

It is important to point out that grain size prediction in the tidal channels through eq. 3.3 might be inaccurate due to the usually low relative wave heights. Therefore, it was resorted to other sources to define the grain sizes along the tidal channels. Former sediment transport models for the Dithmarschen Bight developed by Poerbandono [2003] and Huang [2006] determined d_{50} values by means of numerical calibrations tests of about 100 μm and 63 μm respectively. As the current prediction of grain sizes in the tidal channels through equation 3.3 ranges from 90 to 110 μm (see

Figure 3.29), it can be concluded that the entire domain can be equally treated by means of the approach presented here. However, it is possible that high discrepancies occur locally.

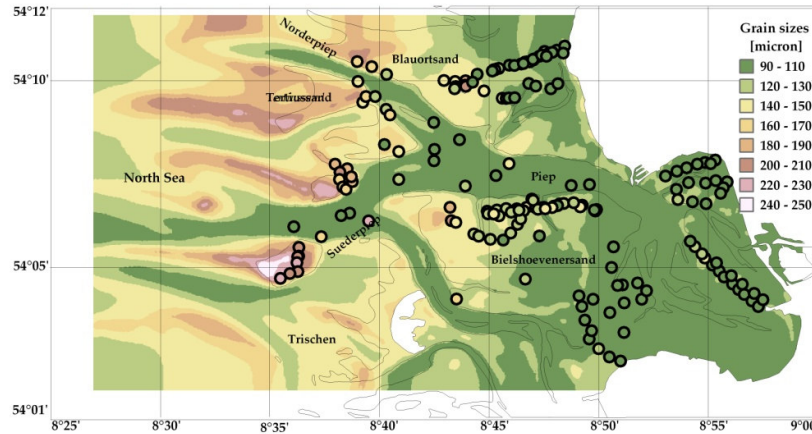


Figure 3.29 Predicted (background) and measured (circles) grain sizes in the study area

3.6 Summary

The large variation of grain sizes (60 to 230 μm) observed over the Dithmarschen Bight through the studies developed by Vela-Diez [2001] and Reimers [2003] motivated the analysis of the spatial distribution of grain sizes in order to obtain a better performance of the sediment transport model.

The methodology for predicting the grain size distribution in the Dithmarschen Bight is based on the following assumptions:

- The grain size field is stationary;
- The spatial distribution of grain sizes is a consequence of the non-uniform (flow-wave) energy conditions;
- The non-stationary flow and wave fields across the Dithmarschen Bight can be represented by stationary fields (i.e. typical flow and wave characteristics) obtained from the Typical Tidal Cycle TTC in order to enable reciprocal steady relationships with the grain size field.

A functional relationship between grain sizes and maximum orbital velocities (computed during the TTC) was found accurate on the definition of grain sizes. Better results corresponded to shallow waters with higher exposure to wave action. As the seabed in deeper areas is less exposed to waves, the grain size sorting there might require factors other than waves in its definition.

Further developments in the definition of the spatial distribution of grain sizes should focus in the tidal channels. The shortage of grain size data will be the first inconvenience to be dealt with, followed by the inclusion of geological, biological

and sedimentological characteristics such as the outcropping of the EHL, biodeposition, sediment sources and cohesive properties, which might play important rolls on the grain size sorting.

Chapter 4

Spatial and temporal variation of bedforms and roughness

4.1 Introduction

The diversity of energy, flow conditions and geological features across the study area are the main reasons for its morphological attributes. The Dithmarschen Bight morphology displays tidal flats, tidal channels and sand banks at first glance. However, a detailed observation brings up smaller morphological features such as bedforms, likewise important for this investigation. Bedforms have considerable effects on flow and sediment dynamics through the flow resistance, which in contrast to flat beds, is increased by additional drag forces.

Maps of average velocities and shear stresses computed for neap and spring tidal cycles (see Figs. 3.4 to 3.7) show a high spatial and temporal variability of flow conditions in the Dithmarschen Bight. The latter shows a non-uniformity of flow resistance over the domain, suggesting non-uniformity on bed roughness. Nevertheless, current flow and sediment transport models rarely consider a temporal variation of bed roughness (even on long scale morphological simulations), which is a very sensitive factor in predicting sediment transport rates, as stated by van Rijn et al. [2001] and Winter and Mayerle [2003].

Estimation of bedform dimensions, origin and/or classification is still under intensive investigation, which until now has shown high dependencies between bedform features, local flow conditions and characteristics of surficial sediments. A great deal of these investigations involve empirical relations developed from data obtained in laboratory channels or rivers, where quasi-steady flows are usually considered [Yalin, 1964; Allen, 1968; van Rijn, 1993]. The most recent investigations have stressed the unsteady character of bedforms [Jerolmack, 2005; van der Mark, 2006; Harbor, 1998].

Tidal environments imply an unsteady flow, where non-stationary water levels and current velocities might hinder bed features from developing and reaching

typical attributes seen in steady flows. As a consequence, the empirical equations developed for steady flow might lead to discrepancies under unsteady tidal conditions. Therefore, a methodology should be developed to derive bedform dimensions and roughness for tidal environments. The methodology formulated in this work focuses on areas with predominant current forcings (flood-ebb). The procedure can also be applied to tidal flats, although some inaccuracies can be expected across the western sand banks where a combined influence of currents and waves on the development of bedforms has been predicted (section 4.3.3).

The general approach developed in this work is based on an iterative process in which procedures extensively validated for steady flows are applied to semi-diurnal tides by means of the representative flow concept (RFC). The representative flow is assumed to be responsible for the bedform features which develop during the course of a tidal period. The procedures described in this chapter were successfully verified by direct and indirect comparisons between field measurements and model results. Implementation of the spatial and temporal variability of bed roughness in the sediment model was found to improve the performance of the model by about 35% and help to homogenize the discrepancies between the model results and observations throughout the neap-spring cycle.

This chapter is presented in six sections. In section 1, the problem definition and purpose of the study is stated. Section 2 contains the bedform datasets and materials used in this study. Section 3 presents the methodology used to define the bedform dimensions and roughness. Sections 4 and 5 present the results and accuracy of the bedform predictions. Section 6 summarizes the main aspects considered in this chapter.

4.2 Bedform measurements

Field measurements of bedform dimensions were carried out at several locations in the main tidal channels of the Dithmarschen Bight (see Fig. 4.1) within the framework of the project PROMORPH [Pramono, 2005; Razakafoniaina, 2001; Vela-Diez, 2001]. Two different devices using acoustical principles (side scan sonar, SSS, and echo sounder) were used to explore the seabed and define its surficial features. The main concern was the spatial and temporal variation of the bedform dimensions along the channels.

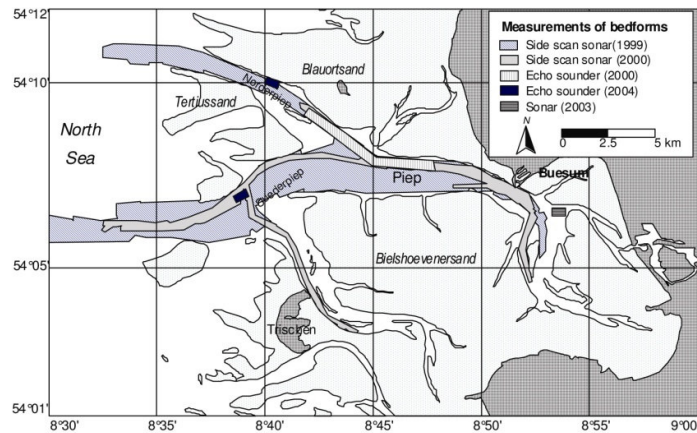


Figure 4.1 Field measurements of bedforms in the tidal channels [Mayerle et al., 2005]

4.2.1 Side scan sonar SSS

Side scan sonar maps the seafloor by emitting sound pulses from its transducer to the bed, later the reflected signals or echoes are captured by the equipment receiver and processed in terms of the strength of the incoming wave signal and the traveling time between transmission and reception.

Data from a Klein 595 side scan sonar device towed by a vessel (towfish) and emitting pulses with a frequency of 500 kHz was employed in this study (see Figure 4.2)

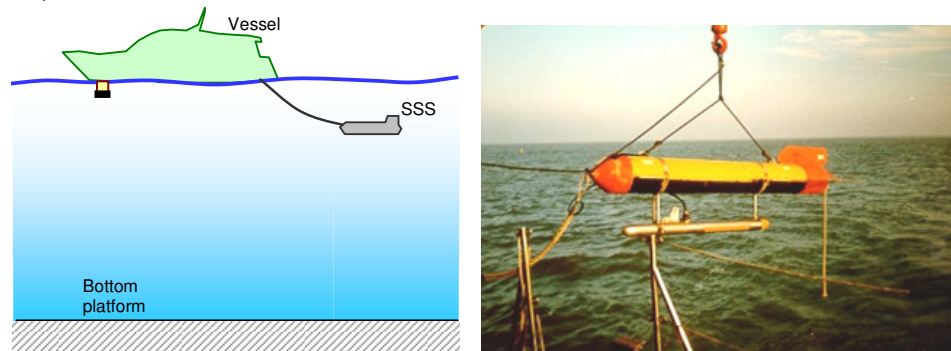


Figure 4.2 Klein 595 side scan sonar

A side scan sonar can define indirectly the characteristics of the bottom surficial sediments according to the reflectivity strength of the scanned section. The returning echoes from the emitted pulses are displayed as dark- and light- grey tones, corresponding to strong and weak echoes respectively. Hard materials such as rocks and gravel better reflect the pulses than do softer sediments such as sand and mud. Further details about sound underwater images can be found in Fish and Carr [1990]. Vela Diez [2001] determined a sediment type classification for the Dithmarschen

Bight on the basis of sediment grab samples and interpretation of greyscale tones in SSS images (see Figure 3.2).

Bedform dimensions can also be derived from SSS measurements. Ripple lengths are defined directly from images, since ripple crests can be easily recognized due to several aspects affecting the grey tones on the SSS images including: a) Differences in the angle of incidence between the sonar pulse and the seafloor across the bedform; e.g. up slopes facing the measuring device are far better reflectors than counter facing slopes, and b) Different reflectance across the bedform due to its characteristic sediment sorting. However, it is important to keep in mind that seafloor images should be first rectilinearly arranged to avoid distortions in the along-track and across-track scales.

Figure 4.3 shows a set of typical SSS images scanned at several locations in the tidal channels at different stages of the tidal cycle. The estimation of bedform heights by SSS measurements is also possible through an indirect method, based on the shadow produced by the bedform crest along the pulse direction (see Figure 4.4). This methodology results in the equation 4.1. Further details about seafloor sonar imagery can be found in Blondel and Murton [1997]:

$$\Delta = \frac{L_s H_f}{R} \quad (4.1)$$

Where: Δ : bedform height; L_s : slant range of the shadow; H_f : towfish height;
 R : slant range

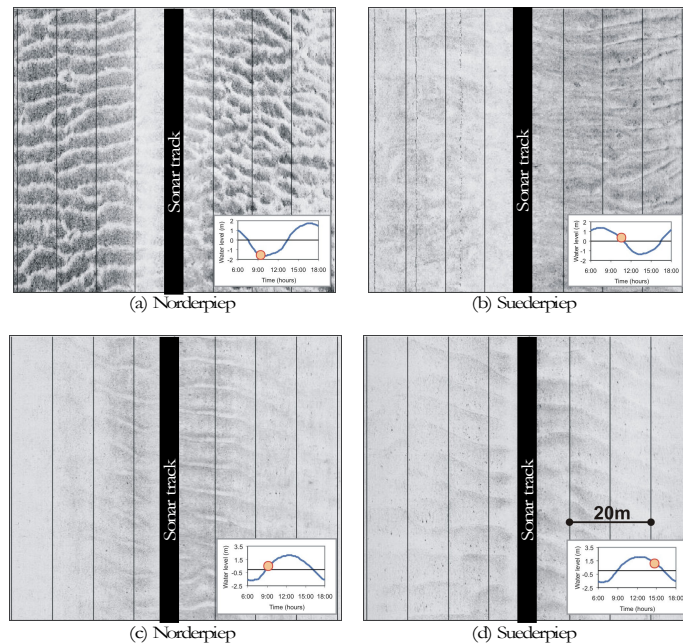


Figure 4.3 Typical SSS images [Mayerle et al. 2005]

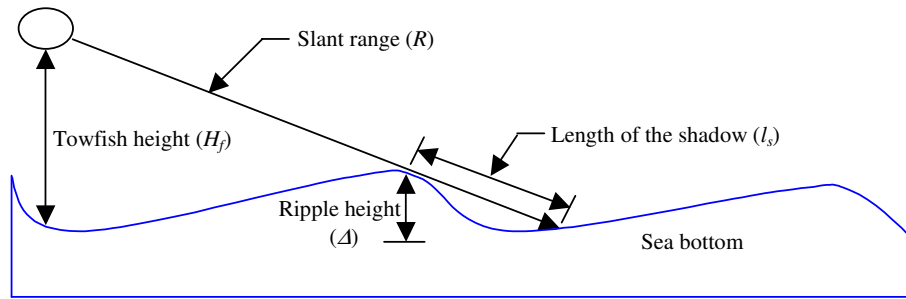


Figure 4.4 Estimation of ripple heights by side scan sonar

This indirect method assumes that the bedform crests are perpendicular to sonar pulses as shown in Figure 4.4. However, this case only occurs when the vessel moves parallel to ripple crests. Therefore, opposite cases with a vessel moving across ripples are not suitable to estimate bedform heights from SSS data (as in the measurements considered for this study). Thus, this investigation referred to data from echo sounder devices in defining the ripple heights.

Side scan sonar campaigns were performed in 1999 and 2000 as displayed in Table 4.1. Details of these measurements are given in Vela-Diez [2001]. Flow conditions corresponded mostly to mild stages with tidal ranges oscillating from 2.78 to 3.59m.

Table 4.1: Tidal ranges during SSS campaigns

Dataset	Date	Tidal Range [m]	Dataset	Date	Tidal Range [m]
1	May 10 – 1999	2.85	6	Jun 7 – 1999	3.15
2	May 11 – 1999	3.14	7	Sep 18 – 2000	3.48
3	May 12 – 1999	3.35	8	Sep 21 – 2000	3.05
4	May 21 – 1999	3.31	9	Sep 22 – 2000	2.78
5	Jun 6 – 1999	2.99	10	Nov 13 – 2000	3.59

Fig. 4.5 shows the bedform types and lengths obtained on the basis of all SSS surveys. It is noted that although the measurements achieved full spatial coverage in the tidal channels (see Fig. 4.1), the hydroacoustic detection of bedform features, particularly of smaller ripples, was not always clear. Dunes were scarcely seen on the seafloor images. Instead, megaripples were largely detected during the surveys. These surveys revealed that bedforms develop primarily in the most exposed areas of the Suederpiep, at the intersection of the Suederpiep and the Bielshoevener Loch, and along the sides of the channels [Mayerle et al., 2002].

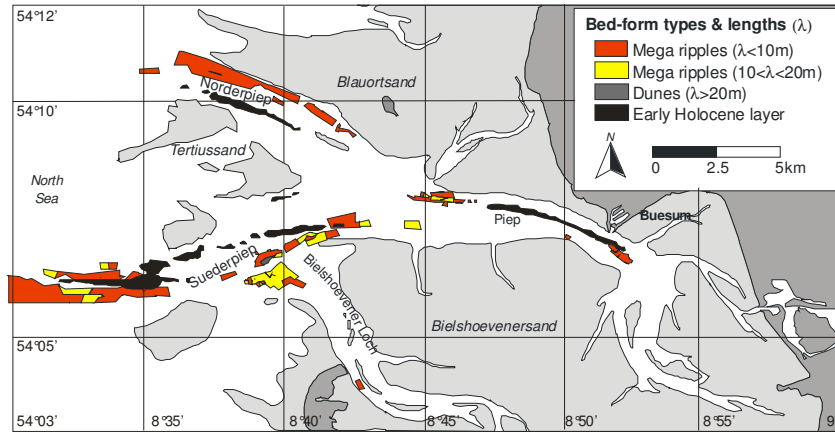


Figure 4.5 Spatial variation of bedforms [Mayerle et al., 2002]

Megaripples with lengths varying from about 3m to 22m were mainly observed. The average bedform lengths varied between 7m and 10m in the Suederpiep and Piep tidal channels and between about 3m and 6m along the Norderpiep channel. The largest bedforms were identified at the intersection of the Suederpiep tidal channel and the Bielshoever Loch, where sand dunes with lengths of up to 22m were recorded. Figure 4.6 shows the frequency distribution of the measured bed lengths. Further details about bedform measurements and their agreement with predictions are given in section 4.4.1.

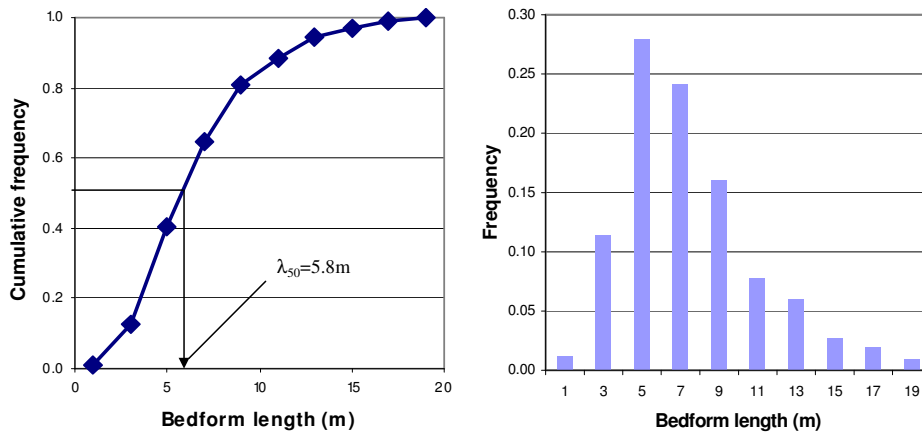


Figure 4.6 Frequency distribution of bedform lengths in the Dithmarschen channels

4.2.2 Echo sounder

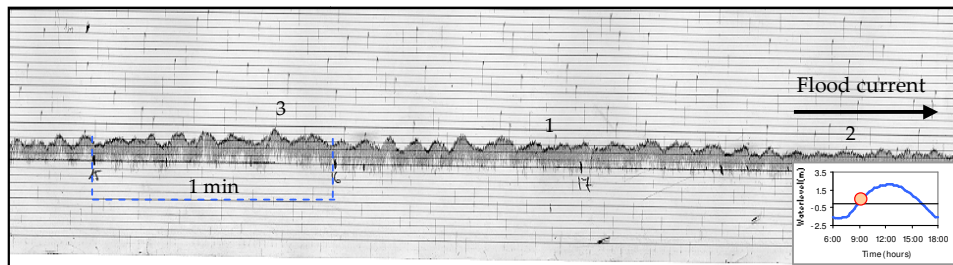
The echo sounder is an instrumentation system for indirectly determining the distance between the seafloor and the equipment location. The time interval between

sending a sonar pulse and receiving the echo from the bottom is used to determine this distance. A typical echo-sounding system consists of a transmitter, a receiver that picks up the reflected echo, electronic timing, amplification of returning echoes and a graphic recorder. The Fahrentholz and Lowrance echo sounder devices operating with a frequency of 200 kHz were used in three field campaigns (2000, 2003 and 2004) to record the bedform profiles in the Piep, Norderpiep and Suederpiep channels. Details of these measurements are given in Razakafoniaina [2001] and Pramono [2005].

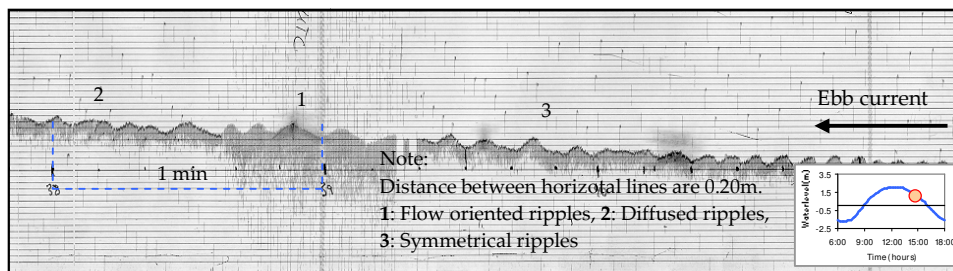
4.2.2.1 Echo sounder campaign in the year 2000

One day campaign was carried out on November 13th, 2000 and covered a narrow corridor about 6 km long at the intersection between the Piep and Norderpiep tidal channels as described by Razakafoniaina [2001]. A Fahrentholz dual frequency device was used in this campaign. Water depths were plotted on the echo sounder register, which consists of horizontal lines indicating 20 cm interval. A characteristic image of the seafloor obtained by the Fahrentholz device is shown in Figure 4.7 at flood and ebb phases.

These profiles display bedform heights ranging from 10 to 50 cm. It is pointed out that the spatial scale is not available from these measurements, though they might be inferred from the time scale and the vessel speed. However, this approach might imply large inaccuracies that deter any effort to define the bedform lengths and their localization.



a) Flood phase



b) Ebb phase

Figure 4.7 Seafloor profiles from a Fahrentholz Echo sounder, [Razakafoniaina, 2001]

Since the entire dataset lacks the horizontal positioning of individual bedform characteristics, a study of the bulk properties of the ripple heights is performed. The statistical analysis classifies the ripple heights by their size and probability of being found inside the surveyed area. Thus, the frequency distribution of the ripple heights and its cumulative curve is determined (see Figure 4.8). Further details about these measurements and their agreement with predictions are given in section 4.4.2.

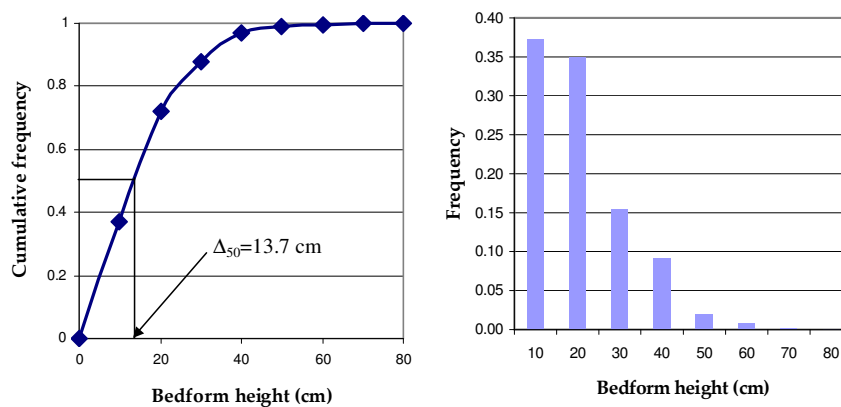


Figure 4.8 Frequency distribution of bedform heights

4.2.2.2 Echo sounder campaign in the year 2003

Different from the previous echo sounder measurements, this campaign did not cover a large region. Instead a temporal coverage within a small area for a full tidal cycle was sought. The survey was conducted in the inner part of the Piep tidal channel of the Dithmarschen Bight as described in Pramono [2005]. Two parallel transects (North and South) of about 200 m long and about 50m apart were surveyed back and forth continually for 9 hours on April 17, 2003. An echo sounder device designed by Lowrance electronics (200 kHz) was used to acquire the transect profiles. Typical images of the seafloor obtained by the Lowrance device are shown in Figure 4.9 at different tidal stages.

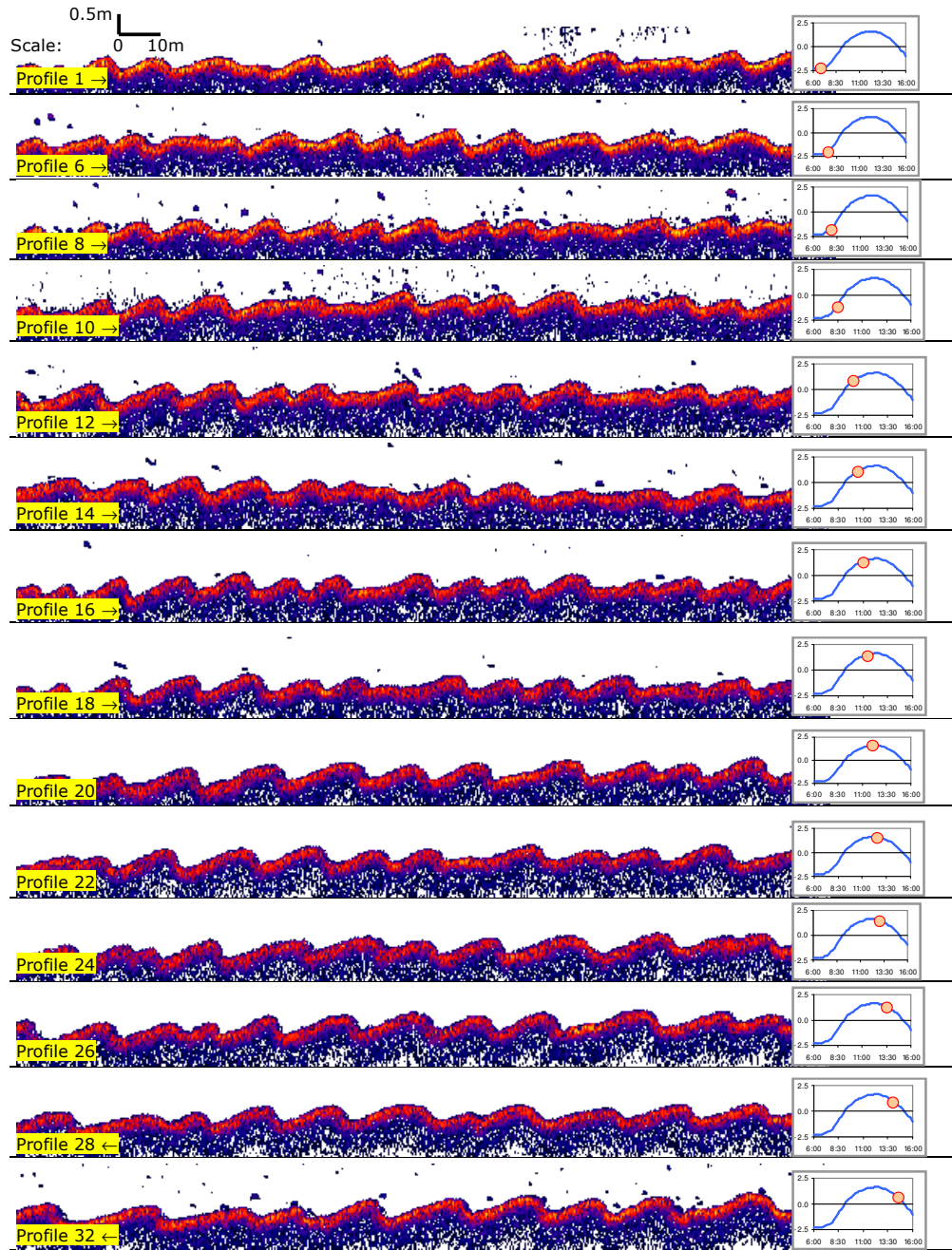


Figure 4.9 Seafloor profiles from a Lowrance echo sounder [Pramono, 2005]

A total of 40 profiles were recorded during the measuring campaign. However, only 32 profiles were selected for analysis due to accuracy reasons. The bedform heights range between 0.10 m and 0.50 m with a mean value of 0.30 m. The bedform lengths were found in the range of 3.8 m to 19.2 m with an average value of 9.9 m. A

summary of the bedform dimensions recorded is shown in Table 4.2. Further details from this campaign and data processing are given by Pramono [2005].

Table 4.2: Bedform heights and lengths at the inner Piep channel [Pramono, 2005]

Pro file	Tran sect	Time (UTC)	Tidal Phase	Depth (h)	DI vel (m/s)	Bedform height (m)			Bedform length (m)		
						Range	Mean	St dev	Range	Mean	St dev
1	North	06:48:21	Flood	2.48	NA	0.14-0.32	0.25	0.06	8.04-15.15	10.45	2.56
5	South	06:53:06	Flood	2.50	NA	0.24-0.41	0.32	0.05	5.99-12.46	9.18	2.78
6	North	07:34:38	Flood	2.81	NA	0.16-0.36	0.25	0.06	6.96-12.85	10.15	2.45
7	South	07:37:55	Flood	2.83	NA	0.16-0.42	0.33	0.11	6.05-11.53	8.39	2.29
8	North	07:56:16	Flood	3.18	NA	0.16-0.31	0.24	0.05	8.08-17.24	10.78	3.09
9	South	08:00:53	Flood	3.21	NA	0.16-0.38	0.27	0.09	6.13-12.74	7.99	2.76
10	North	08:29:24	Flood	3.60	0.61	0.17-0.35	0.26	0.06	8.66-12.96	10.34	1.92
11	South	08:34:06	Flood	3.73	0.56	0.14-0.39	0.30	0.10	4.73-11.74	7.44	3.05
12	North	09:58:26	Flood	5.53	0.66	0.10-0.39	0.27	0.08	6.53-13.70	10.48	2.52
13	South	10:03:14	Flood	5.56	0.66	0.10-0.37	0.25	0.09	5.01-12.69	8.15	3.41
14	North	10:27:20	Flood	5.81	0.60	0.19-0.36	0.28	0.05	8.36-13.40	11.24	1.88
15	South	10:31:31	Flood	5.89	0.57	0.15-0.40	0.27	0.10	3.78-9.72	6.76	2.51
16	North	11:02:03	Flood	6.07	0.51	0.10-0.36	0.27	0.09	7.77-14.73	10.75	2.30
17	South	11:05:37	Flood	6.09	0.49	0.19-0.40	0.29	0.08	5.62-12.33	7.43	3.27
18	North	11:28:48	Flood	6.23	0.46	0.19-0.40	0.28	0.08	4.77-12.73	9.75	3.21
19	South	11:31:58	Flood	6.26	0.41	0.13-0.37	0.26	0.09	5.15-12.09	7.87	3.05
20	North	12:00:43	HW	6.38	NA	0.21-0.41	0.32	0.06	4.93-17.91	10.36	3.51
21	South	12:04:08	HW	6.38	NA	0.16-0.44	0.31	0.11	6.80-17.00	11.28	3.70
22	North	12:29:44	HW	6.39	NA	0.20-0.45	0.31	0.08	7.76-16.46	10.85	2.64
23	South	12:33:22	HW	6.38	NA	0.13-0.33	0.24	0.07	6.50-16.27	9.91	3.73
24	North	12:59:30	HW	6.28	NA	0.24-0.41	0.34	0.07	5.96-16.12	12.65	3.26
25	South	13:03:00	HW	6.27	NA	0.16-0.38	0.27	0.07	8.66-14.54	11.06	2.33
26	North	13:34:34	HW	6.07	NA	0.17-0.38	0.30	0.07	6.21-19.14	12.08	3.78
27	South	13:38:34	HW	6.05	NA	0.14-0.36	0.26	0.08	6.69-12.74	10.60	2.44
28	North	14:00:01	Ebb	5.86	0.41	0.10-0.30	0.22	0.06	5.73-12.60	9.59	2.40
29	South	14:05:38	Ebb	5.82	0.39	0.25-0.50	0.36	0.09	6.18-15.64	10.38	3.02
32	North	14:31:28	Ebb	5.53	0.44	0.17-0.40	0.31	0.09	6.03-12.57	9.62	2.47
33	South	14:35:27	Ebb	5.49	0.45	0.14-0.41	0.30	0.09	6.53-11.85	8.59	2.12
34	North	15:01:36	Ebb	5.05	0.52	0.18-0.40	0.30	0.08	5.77-19.22	10.64	4.20
35	South	15:05:52	Ebb	5.00	0.48	0.16-0.44	0.31	0.09	6.80-14.82	10.19	3.00
36	North	15:31:28	Ebb	4.43	0.45	0.22-0.42	0.33	0.07	6.87-18.56	10.96	3.59
37	South	15:35:20	Ebb	3.37	0.43	0.11-0.41	0.30	0.08	8.17-12.11	10.05	1.63

Notes:

1. NA means not available. DI velocities are not available because the ADCP was not ready at the beginning of echo sounder measurements and the depth integrated values could not be calculated during high water.
2. HW means high water.

In general, bedform geometry is believed to be affected by such flow characteristics as shear stresses and water depths. Moreover, several relationships associating these flow conditions with ripple heights and lengths have been

proposed [Yalin, 1972; Raudkivi, 1988; Soulsby, 1998; van Rijn, 1993]. A positive correlation between ripple heights and lengths with shear stresses and depths, respectively, is expected during low hydraulic regimes.

A tidal cycle might imply considerable variation in both shear stresses and water levels. Therefore, the possible effects on bedform features should be verified. Fig. 4.10 shows the temporal variation of bedform heights (top) and lengths (bottom) with varying water depth and depth-integrated current velocity. Each vertical line represent the range of variation of bedform heights and lengths over the 200m transects. The differences in bedform dimensions observed during the same back-and-forth survey are due to the different paths followed by the survey vessel. Despite the expectations, the observations do not present a significant variation or trend of the mean bedform dimensions during the observed spring tidal cycle.

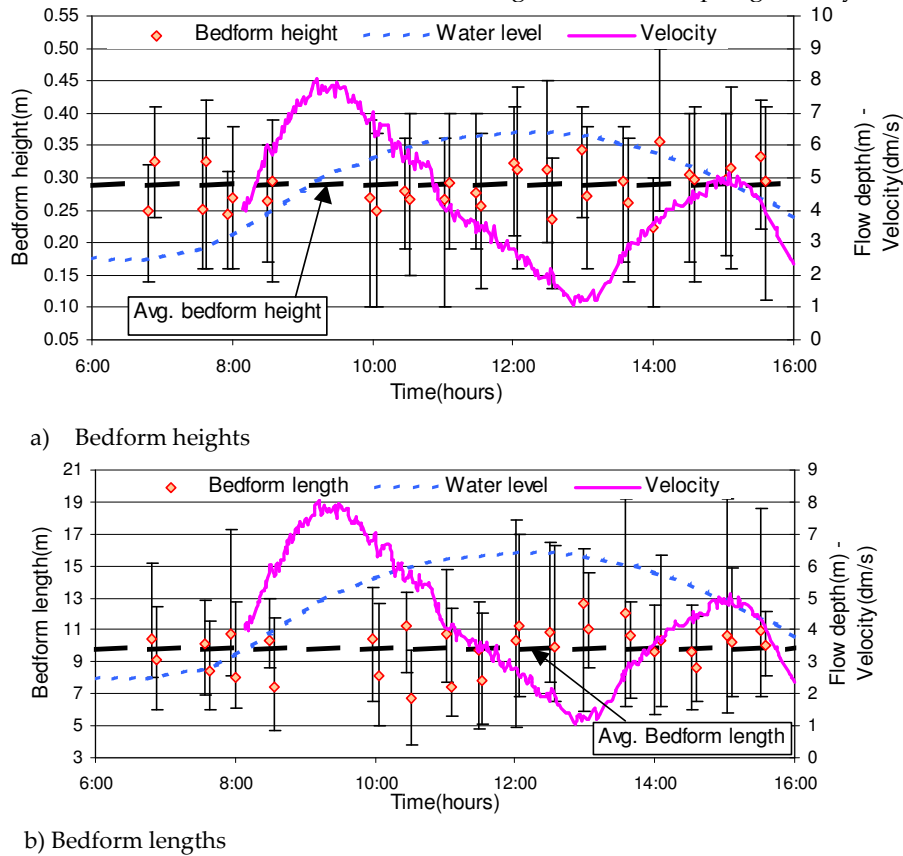


Figure 4.10 Temporal variation of bedform dimensions during a spring tidal cycle.

Modified after Pramono [2005]

Migration of bedforms was however clearly detected during the tidal cycle. Echo soundings of the bed profiles measured approximately along the same vessel path from the mean water level (MWL) during the flood phase to the MWL during the ebb

phase are plotted in Fig. 4.11. The migration of the bedforms in the shoreward direction in the order of about 1m/h is evident.

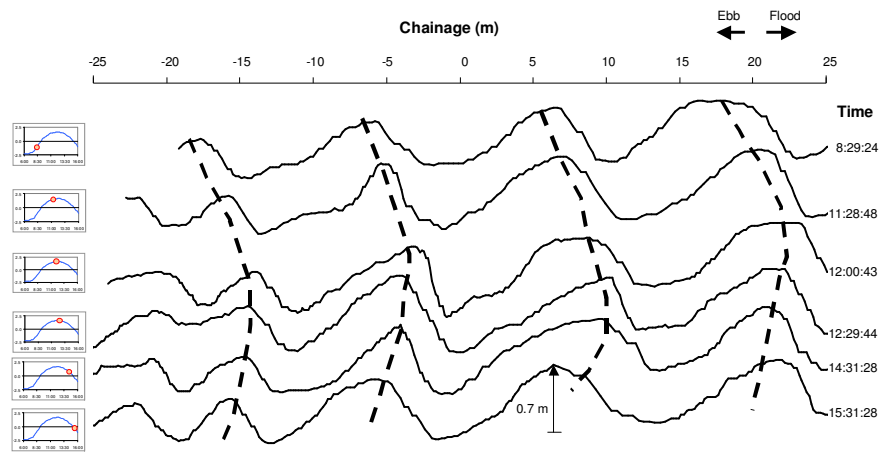


Figure 4.11 Migration of bedforms during a spring tidal cycle [Mayerle et al., 2005]

4.2.2.3 Echo sounder campaign in the year 2004

A measurement procedure similar to that followed during the campaign in 2003 in the Piep tidal channel was attempted in 2004 at two locations in Norderpiep and Suederpiep channels (see Fig. 4.1). The observation of bedform features and their temporal variability during a tidal cycle was sought. Typical seafloor profiles recorded at both measuring locations are shown in Figure 4.12.

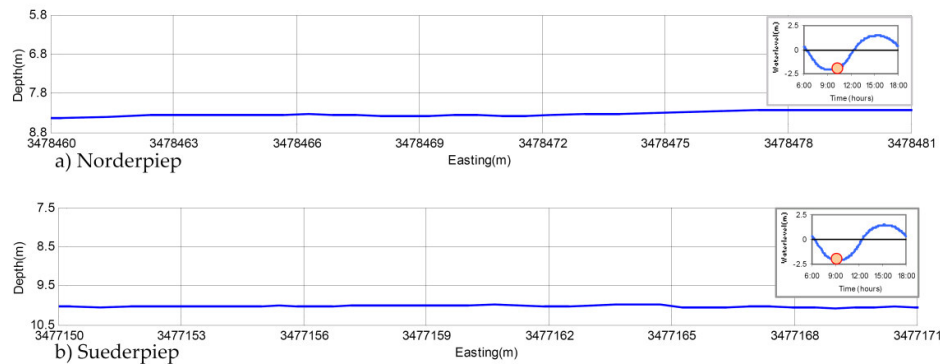


Figure 4.12 Seafloor profiles in muddy areas of the tidal channels [Pramono, 2005]

The surveyed areas are relatively flat with sparse undulating irregularities of up to 20 cm in height [Pramono, 2005]. Outcrops of the EHL were observed in the vicinity of both measuring locations. Surficial sediments at both locations presented fine sand grains with some mud content, which might have hindered the development of typical non-cohesive bedforms. This campaign confirms the effect of geological and sedimentological features on bedforms development, where beside

flow conditions, features like the EHL and the proportion of mud content might explain the absence of bedforms in large areas of the tidal channels (see Fig. 4.5).

4.3 Prediction of bedform dimensions and roughness in tidal environments

Definition of bedform dimensions and roughness in the Dithmarschen Bight under prevailing currents forcing implies the consideration of some special conditions: unsteady tidal flows, outcropping of compact cohesive materials and non-uniform distribution of grain sizes over the area. These aspects are key elements in the definition of bedform features and are all considered hereafter in defining an approach to predict ripple sizes and their associated roughness.

4.3.1 Methodology

Methodologies designed for dimensioning bedforms under steady, uniform flow are based on the statistical steady behavior displayed by bed features. Implying the mean bedform heights and lengths (and also other statistical variables) remain steady despite the dynamic migration and evolution of these features.

In order to verify the behavior of bedforms under an unsteady semi-diurnal tidal flow, local observations are performed in the main tidal channels of the Dithmarschen Bight during a tidal cycle (section 4.2.2.2) [Pramono, 2005]. The results showed low variations regarding their time-averaged dimensions (mean discrepancies were about 10%) and indistinguishable correlations with flow variables like shear stresses and water depths (see Fig. 4.10). This unexpected behavior might be attributed to the large response time (rt) required by bedforms to establish new dimensions under new flow conditions.

Therefore, the common assumption that steady flows involve bedform patterns with a constant mean value of their dimensions could be also extended to unsteady flow conditions with a cyclic character. A representative flow within a tidal period of interest is assumed to be responsible for the bedform dimensions (see Fig. 4.13). In order, however, for these assumptions to be valid, some conditions should be fulfilled by the cyclic flow: a) the tidal period (T) is short enough to guarantee small or gradual bedform readjustments (i.e. the critical shear stress is exceeded during short periods); b) The amplitude (A) of the cyclic flow should remain constant; and c) No sedimentation occurs during the tidal cycle.

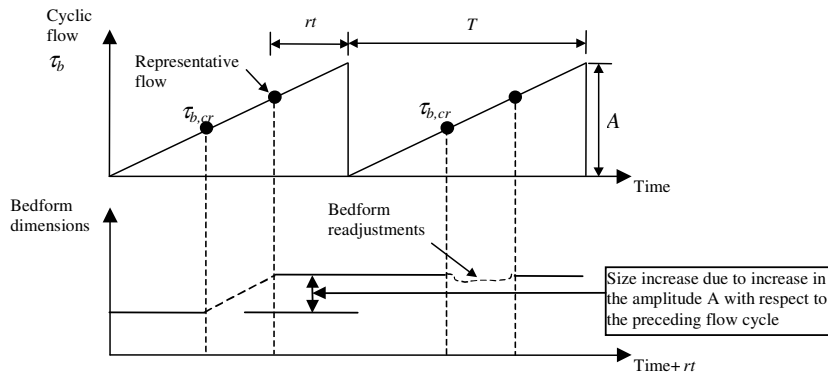


Figure 4.13 Bedform size behavior under unsteady cyclic flow (Low hydraulic regime)

To some extent a semi-diurnal tidal flow, as seen in the Dithmarschen Bight, complies with the above requirements, which leads to approximately uniform bedform dimensions during a tidal cycle. However, through the neap-spring cycle the variation in amplitudes (water levels and shear stresses) and the relative large period T involved suggest gradual changes in bedform dimensions. Hence, for any tidal cycle one map of bedform features can be defined. This map however, must be updated along the neap-spring cycle accordingly to accuracy requirements.

The definition of bedform features for a particular tidal cycle is performed on the basis of empirical relationships derived from steady flows, since one flow condition causes one pattern of bedform sizes. It is hypothesized here that one pattern of bedform sizes is the result of only one flow condition, which for unsteady cases, can be defined as the representative flow condition RFC (see Fig. 4.13). Moreover, if a steady flow coincides with the representative flow; both the steady and unsteady flows will cause similar bedform dimensions (see Fig. 4.14). Therefore, it is suggested that steady flow theories might be applicable in determining bedform sizes in unsteady cyclic flows, provided the RFC is already defined in the area of interest.

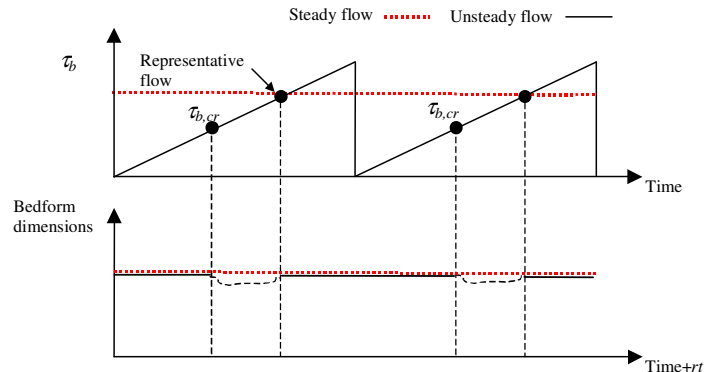


Figure 4.14 Similitude of bedform size behavior under unsteady and steady flows

In addition to unsteady flow conditions, bedform dimensions are affected by grain sizes, which in the Dithmarschen Bight exhibit a high spatial variation. Mean grain sizes measured from bed samples ranged from 60 to 230 μm . Differences in maximum orbital velocities explain mainly the sorting process of particle sizes in the area. Definition of sediment sizes at the study area was performed according to the methodology presented in chapter 3.

The definition of bedform features took also into consideration the outcrops of the cohesive layers in the deeper parts of the tidal channels (see Fig. 3.1). The lack of bedforms on the seafloor due to the open EHL was considered. Hence, along the locations with EHL exposure, a relatively flat and smooth seabed with roughness sizes about 0.06m was assumed. Roughness sizes outside the EHL will be defined according to bedform geometry and grain sizes [van Rijn, 1993].

A general overview has been given of tackling the prediction of bedform dimensions under special topics including: unsteady tidal flow, spatial variation of grain sizes and outcrops of the EHL. Particular application in the Dithmarschen Bight will be based on functional relationships established originally for steady flows. Flow parameters will be obtained from the representative flow condition RFC at the tidal cycle of interest. The classification and estimation of bedform dimensions are performed according to van Rijn's [1993] methodology (see Tables 2.2 and 2.3), which is also used to estimate the roughness sizes.

The equivalent roughness size is made up of the grain and form roughness components, as stated by van Rijn [1984c]:

$$k_s = k_s' + k_s'' \quad (4.2)$$

Where:

k_s : equivalent roughness size

k_s' : grain roughness

k_s'' : form roughness.

Table 4.3 defines the roughness sizes as a function of bedform dimensions, particle sizes and empirical coefficients.

Table 4.3: Grain and form roughness [van Rijn, 1993]

	Type of Bedforms		
	Miniripples	Megaripples	Dunes
Grain roughness	$k_s' = 3d_{90}$	$k_s' = 3d_{90}$	$k_s' = 3d_{90}$
Form roughness	$k_s'' = 20\gamma_s \Delta \frac{\Delta}{\lambda}$	$k_s'' = 20\gamma_s \Delta \frac{\Delta}{\lambda}$	$k_s'' = 1.1\gamma_s \Delta (1 - e^{-25\Delta/\lambda})$

Where:

Δ : bedform height

λ : bedform length

d_{90} : sediment grain diameter in which 90% of sample by mass is smaller

γ : ripple presence factor which is 1 for ripple bed and 0.7 for ripples superimposed on dunes or sandwaves.

μ : dune presence factor which is 0.7 for field conditions.

Among all available approaches for predicting bedform features mentioned in sections 2.2.3.1 and 2.2.3.2, van Rijn's approach was selected due to its differentiation of ripples into miniripples and megaripples, which are the bedforms usually observed in the study area. Furthermore, measurements of bedforms in the tidal channels (mostly megaripples) [Mayerle et al., 2002] show a relation λ/h of about 0.56 that agrees quite well with van Rijn's methodology (see Fig. 4.20). Table 4.4 summarizes additional methodologies to account for the grain and form roughness.

Table 4.4: Summary of grain and form roughness equations

Author	Grain Roughness	Form Roughness
Ackers and White [1973]	$k'_s = 1.25d_{35}$	-----
Kamphuis [1974]	$k'_s = 2d_{90}$	-----
Gladki [1975]	$k'_s = 2.3d_{80}$	-----
Wikramanayake [1993]	-----	$k''_s = 4\Delta$
Grant and Madsen [1982]	-----	$k''_s = 27.7\Delta \frac{\Delta}{\lambda}$
Nielsen [1983]	-----	$k''_s = 8\Delta \frac{\Delta}{\lambda}$
Raudkivi [1988]	-----	$k''_s = 16\Delta \frac{\Delta}{\lambda}$

Finally, to estimate the bedform dimensions and roughness at any place in the study area, flow characteristics such as water levels, depth-integrated velocities and bed shear stresses are required at the RFC of the particular tidal cycle. 2-DH flow simulations have been carried out in the Dithmarschen Bight for this purpose. The WL | Delft Hydraulics computer software and the flow model settings defined by Palacio [2002] are adopted in these simulations. Initially, a constant Chezy coefficient is assumed throughout the domain to determine the bed roughness, but updates are carried out continuously until the assumed k_s values approximately match the calculated ones, as outlined on the flowchart displayed next.

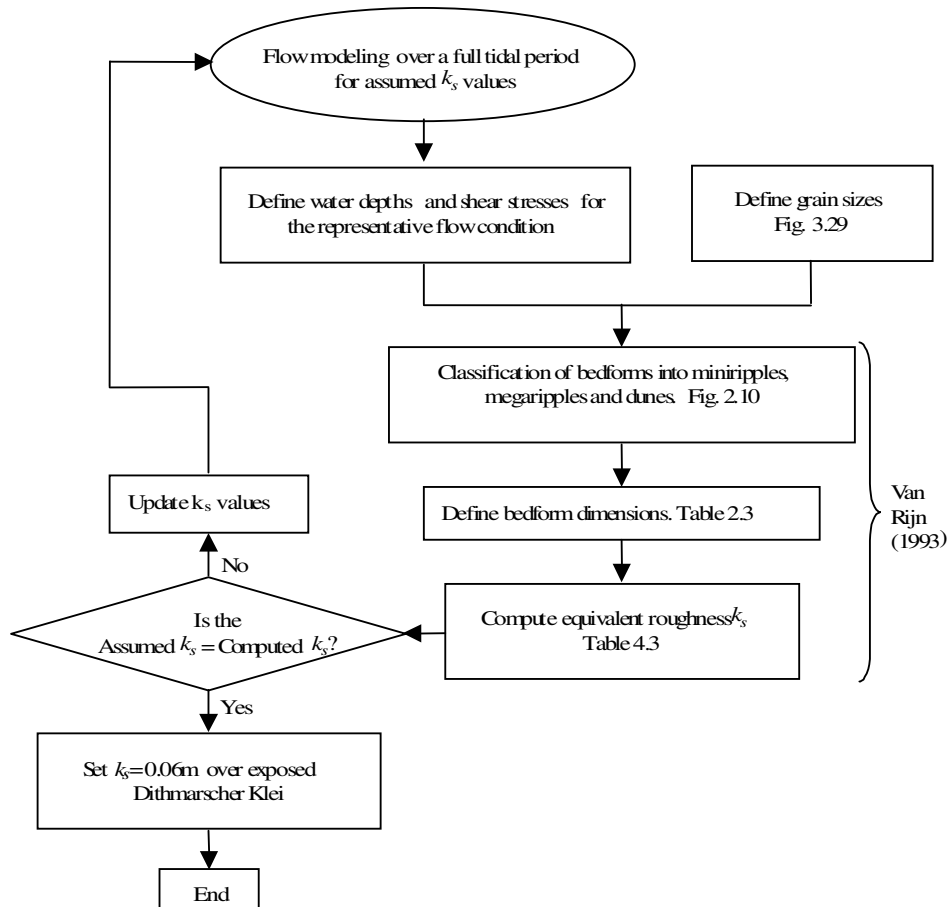


Figure 4.15 Proposed methodology for defining bedform dimensions and roughness

4.3.2 Representative flow condition

The RFC is characterized by flow variables such as water depth, shear stress, velocity, etc. occurring at a specific time during the tidal cycle of interest. Theoretically, this specific time occurs one response time (rt) earlier than the crossing of the critical shear stress (ebb phase) as indicated in Figures 4.13 and 4.14. A simplified cyclic flow is drawn in Figure 4.16 to clarify this concept. Slight adjustments in bedform sizes are expected during periods with shear stresses exceeding the critical value, although they are negligible within one tidal cycle, as was observed in the Dithmarschen Bight. Transport stages below the critical shear stress might also cause changes in bedform dimensions due to sedimentation processes, however they were disregarded. Previous restrictions about the length of the tidal period and the constant amplitude of the tidal flow should be kept in mind.

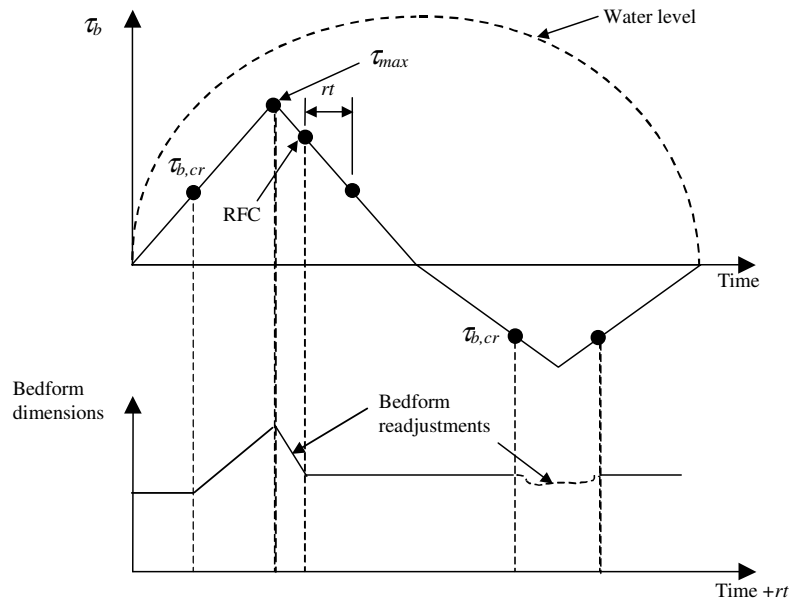


Figure 4.16 Bedform size behavior under cyclic flow conditions

Although the representative flow can be theoretically located within the cyclic flow, in the real case the solution is rather complicated as the response time rt is generally unknown due to the complex stochastic relations between flow, sediments and bedforms. Moreover, along the Dithmarschen Bight the propagation of the tide into the study area implies a lag phase of flow conditions between western and eastern locations. Hence, the representative flow does not happen at the same time in the entire area.

A particular analysis based on field measurements is required to determine the representative flow for the study area. An iterative process was adopted to determine the RFC during a full tidal period. Following the procedure outlined in Fig. 4.15, several flow conditions at different times during the tidal period were assumed as representatives for estimating bedform dimensions over each grid cell of the model. Several maps of bedform dimensions were computed and classified according to their corresponding local ratios between bed shear stress and maximum bed shear stress ($\tau_b/\tau_{b,max}$).

Measurements of bedform lengths obtained from the SSS surveys in the tidal channels of the Dithmarschen Bight (see Fig. 4.5) were used to assess the accuracy of the predicted maps of bedforms. On this basis, a flow condition marked by one specific ratio $\tau_b/\tau_{b,max}$ is chosen as the RFC, given the good agreement between bedform length observations and predictions. Fig. 4.17 shows the RMAE and MAE errors obtained from the comparison between measured and predicted bedform lengths.

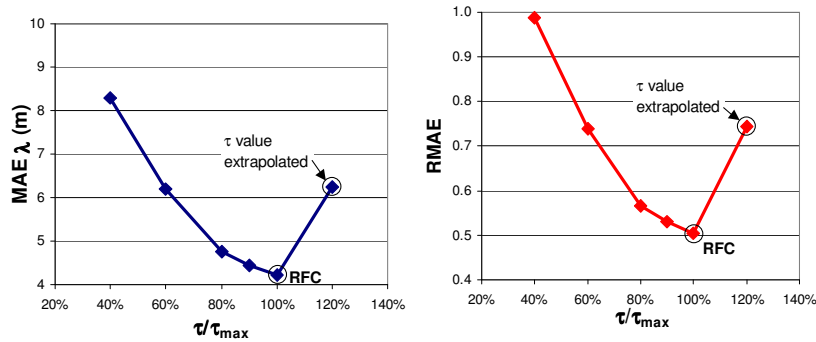


Figure 4.17 Determination of the RFC on a semi-diurnal tidal flow

The representative flow during a full tidal period coincides with the maximum local shear stress, e.g. bedforms develop as if they were subjected to a steady maximum shear stress that remains roughly constant during the tidal period. However, gradual changes are expected afterwards (next tidal cycles) due to the seasonal variation of shear stresses at the neap-spring cycle.

4.3.3 Bedforms in tidal flats and sand banks

Previous sections (4.3.1 and 4.3.2) focused only on bedforms largely influenced by current forcings. Therefore, their application on the domain area should be restricted to current predominance. Bedform features in shallow flats or sand banks in the Dithmarschen Bight might however be influenced by wave action. Wave ripples can develop once the oscillatory motion is of sufficient strength to cause general movement of the surficial particles. Figure 4.18 shows the diagram of bedforms in oscillatory flow developed by Allen [1982]. Based on Allen's diagram and the maximum orbital velocities computed during a TTC (see Fig. 3.16), the Dithmarschen Bight can be divided into two main areas: a) the tidal channels and the eastern tidal flats that are characterized by maximum orbital velocities lower than 0.1 m/s; and b) the western sand banks with higher orbital velocities.

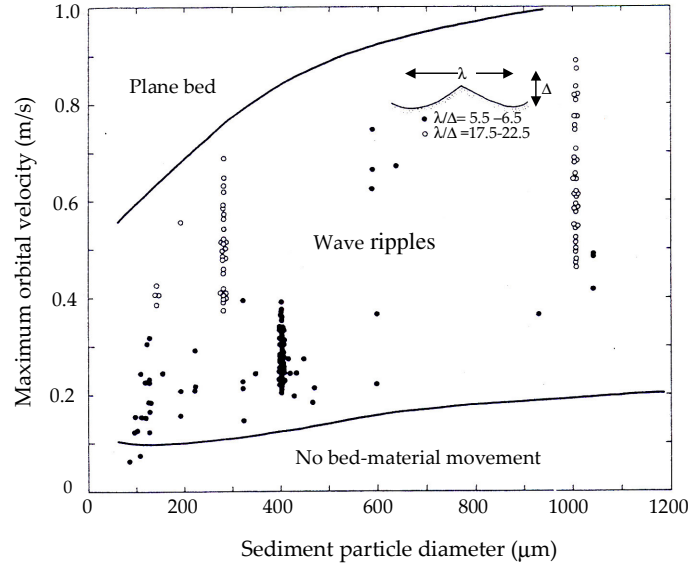


Figure 4.18 Bedform regimes in oscillatory flow [Allen, 1982]

Wave ripples might only develop over the second area, since wave action is mostly negligible over the first. The ripple data of Nieuwjaar and Van der Kaaij [1987] provide a criterion to determine if ripples are wave or current dominated.

$$\begin{aligned} u_{*,c}' / u_{*,w}' < 0.25 & ; \text{ wave - dominated ripples } (\lambda_1 / \lambda_2 < 1.3) \\ u_{*,c}' / u_{*,w}' > 2.00 & ; \text{ current - dominated ripples } (\lambda_1 / \lambda_2 > 1.5) \end{aligned} \quad (4.3)$$

Where:

$$u_{*,c}' = \left(\frac{1}{8} f_c' \right)^{0.5} u : \quad \text{Current-related effective bed-shear velocity}$$

$$u_{*,w}' = \left(\frac{1}{4} f_w' \right)^{0.5} \hat{U}_\delta : \quad \text{Wave-related effective bed-shear velocity}$$

$$f_c' = 0.24 \log^{-2} (12h / k_s) : \quad \text{Current-related friction factor } (k_s = 3d_{90})$$

$$f_w' = \exp \left[-6 + 5.2 \left(\frac{\hat{A}_\delta}{k_s} \right)^{-0.19} \right] : \quad \text{Wave-related friction factor } (k_s = 3d_{90})$$

λ_1 : Horizontal projection of stoss side

λ_2 : Horizontal projection of lee side

Figure 4.19 shows ratios $u_{*,c}' / u_{*,w}'$ ranging between 0.25 and 2 over the western sand banks. Therefore, ripples on that area might form under a combined action of currents and waves with the asymmetry parameter λ_1 / λ_2 between 1.3 and 1.5. However, no in situ confirmation of this result is yet available. Future measurements across the sand banks can provide further elements to clarify this issue. A

confirmation should lead to local adjustments of the approach in sections 4.3.1 and 4.3.2 that assume current-dominated ripples along the entire domain.

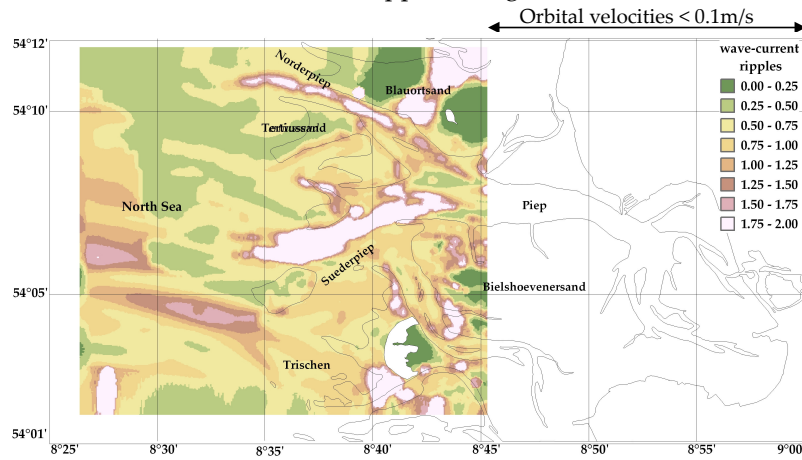


Figure 4.19 Ratio $u_{s,c}'/u_{s,w}'$ in the Dithmarschen Bight

4.4 Performance assessment of bedform predictions

4.4.1 Bedform Lengths

RMAE and MAE error criteria were used to define the accuracy of the bedform size predictions. The accuracy of the estimation of ripple lengths was already assessed during the determination of the representative flow (see Fig. 4.17), where the RMAE and MAE errors were about 50% and 4.2m respectively. Measurements showed a mean value of the ratio of the bedform length to the water depth λ/h of about 0.56, which is in relative good agreement with Van Rijn's empirical equation for megaripples ($\lambda/h=0.50$). Figure 4.20 shows the frequency distribution of λ/h at the Dithmarschen channels.

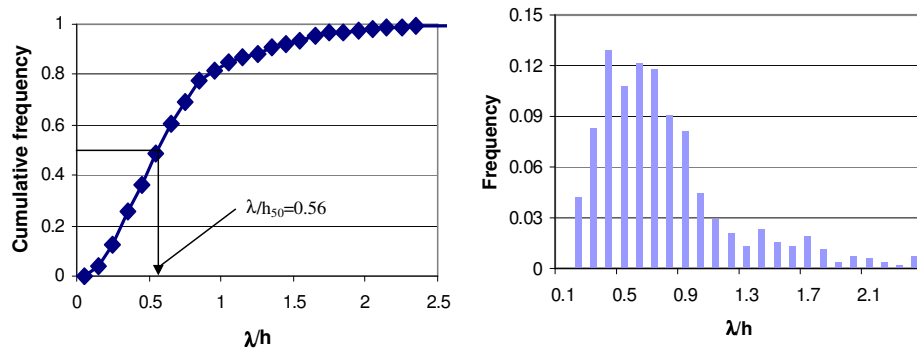


Figure 4.20 Frequency distribution of λ/h in the tidal channels

A comparison of the distribution frequency curves of predicted and computed bedform lengths can be seen in Figure 4.21. The cumulative curves show mean values of about 5.8 m for measurements and 5.0 m for predictions. This implies a relative difference of about 14%. The frequency function shows a bias toward the left side and unimodal character, which might be explained by the predominance of megaripples all along the tidal channels.

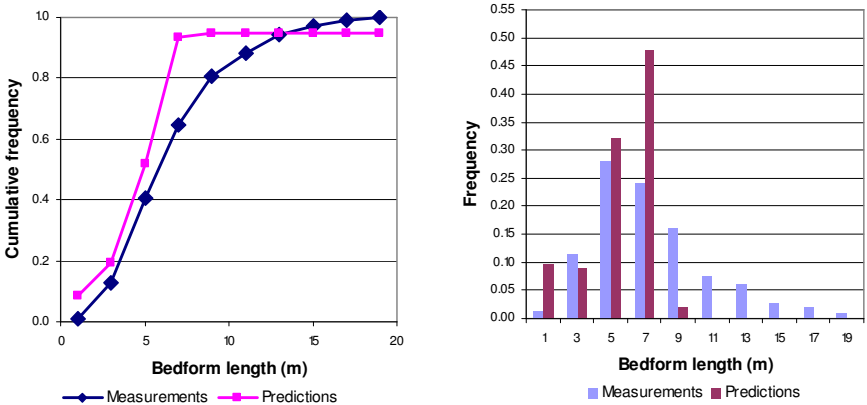


Figure 4.21 Comparison of the bulk of bedform lengths

4.4.2 Bedform heights

The accuracy assessment of ripple height predictions is based on the results of echo sounder measurements carried out at the intersection between the Norderpiep and Suederpiep tidal channels (see section 4.2.2.1). As individual localizations of ripple features were not possible, a statistical analysis of the bulk of the ripple heights was performed in the surveyed area. Figure 4.22 displays the predicted bedform heights for the Dithmarschen Bight on November 13th, 2000 that coincides with the measurement date.

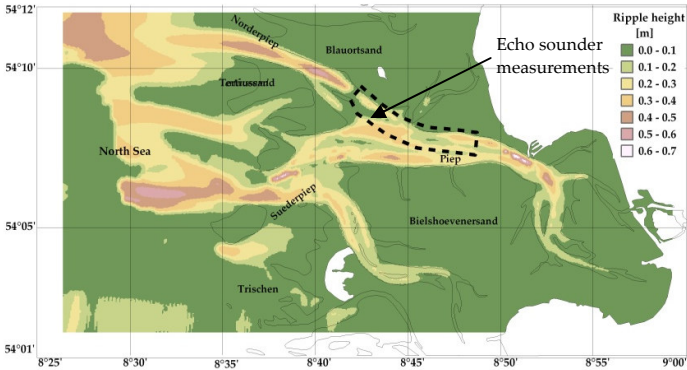


Figure 4.22 Prediction of bedform heights in the Dithmarschen Bight

Measurements and predictions were compared on the basis of their frequency distribution curves, as shown in Figure 4.23. The cumulative curve shows mean values of about 13.7 cm and 14.3 cm for measured and predicted heights respectively, values that imply a relative difference of about 4%. The predicted distribution curve agrees quite well with measurements, although some discrepancies were found in the prediction of miniripples. The under-prediction of miniripples might be due to factors not yet included in this approach such as the existent fraction of mud content. Cohesive materials hinder the development of large bedforms, which instead are replaced by small bed irregularities.

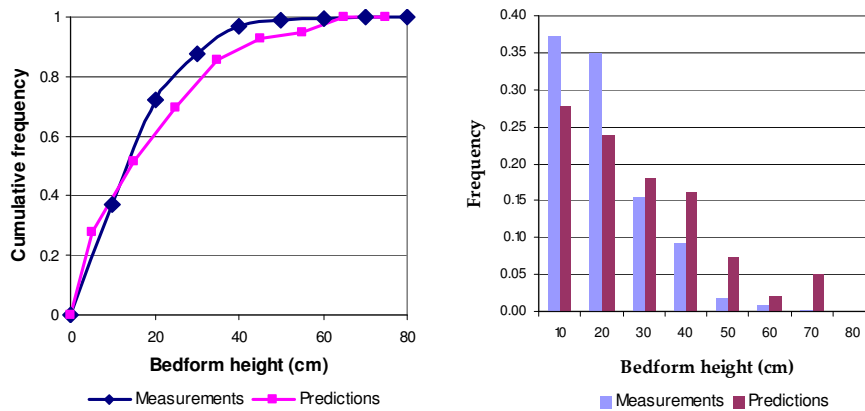


Figure 4.23 Comparison of the bulk of bedform heights

Local echo sounder measurements in the inner part of the Piep channel (see section 4.2.2.2) were also considered in the accuracy study. Measurements covered an area about 200 m x 50 m. Figure 4.24 shows the bottom profile where echo sounder measurements were performed. Despite the small area surveyed and its uniform bathymetry, a large spatial variation in bedform dimensions was found. Measurements displayed bedform heights ranging from 0.10 m to 0.50 m and bedform lengths from 3.8 m to 19.2 m [Pramono, 2005].

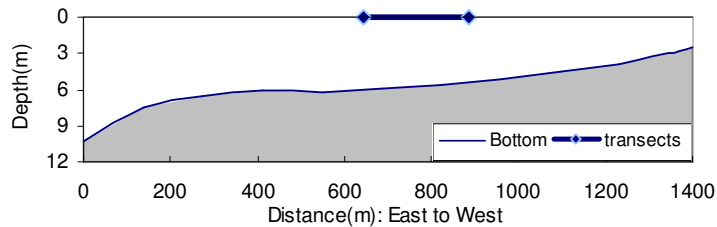


Figure 4.24 Seafloor topography at the surveyed area [Pramono, 2005]

Therefore, from current knowledge, dimensions of individual bedforms are unpredictable given their discontinuous behavior under small spatial scales. They can however be acceptably well determined on larger scales (i.e. as aggregated values) provided flow conditions and grain sizes are available. Figure 4.25 shows the bedform height and length predictions at the local surveyed spot. The predicted ripple height and length were about 0.23 m and 4 m respectively, lying within the range of observed bedform dimensions (heights: 0.10-0.50m and Lengths: 3.8-19.2m).

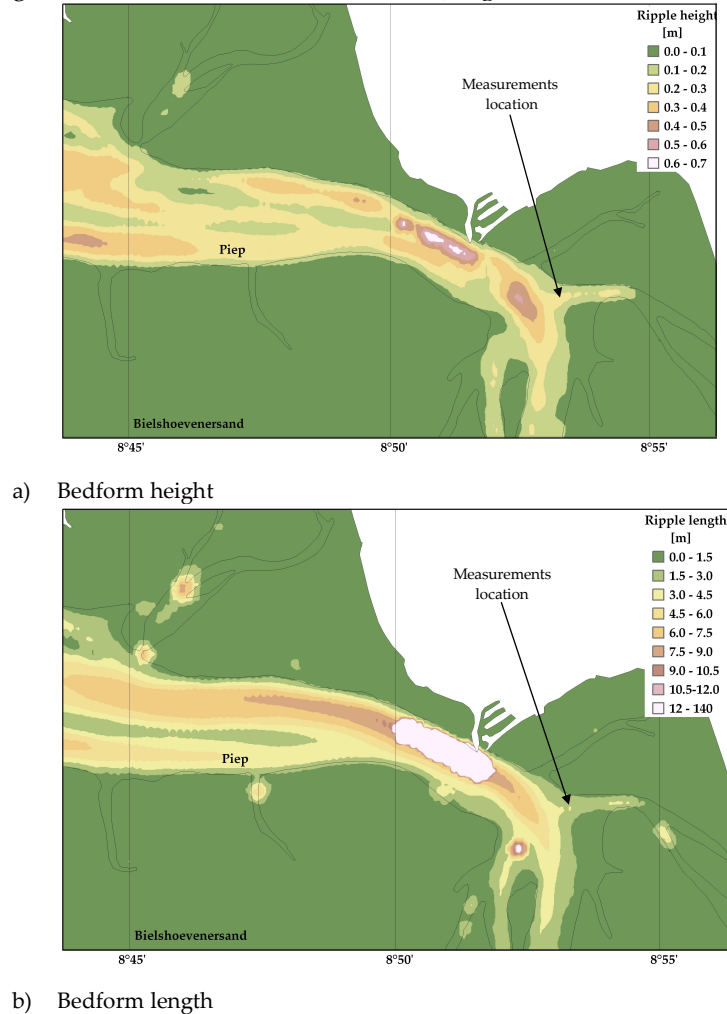


Figure 4.25 Bedform predictions on April 17, 2003

4.5 Seasonal variation of bedform dimensions

Tidal hydrodynamics is dominated by non-stationary gravitational forces leading to distinctive spring-neap cycles. From neap to spring, field observations show

increasing tidal ranges, mean velocities, suspended sediment rates, etc. Process-based models partially consider this phenomenon by means of a proper set of boundary conditions (i.e. astronomical constituents), which are adequate in describing flow characteristics under rigid or armoured beds. However, flow over movable beds during the spring-neap cycle present an important variation on bedform dimensions and spatial coverage that is usually overlooked by current models. To neglect this phenomenon implies inaccuracies in the estimation of the flow resistance, which is a very sensitive factor in the prediction of sediment transport rates.

A comparison between two extreme conditions during the neap and spring phases will be considered next. The methodology proposed in this chapter to predict bedform dimensions is applied for both cases. Tidal ranges of 4.2 m and 2.4 m characterize the flow conditions at the spring and neap cycles respectively. Maps of the flow characteristics, type of bedforms, bedform dimensions and roughness are shown throughout Figures 4.26 to 4.30 for both neap and spring conditions. Chapter VI, highlights the importance of including the seasonal variation of bedform dimensions in sediment transport models. The roughness maps obtained by the proposed method led to a considerable improvement in the predictive capability of the numerical model with regard to suspended sediment concentrations. Indirect verifications of the accuracy of the roughness maps were carried out over five tidal cycles including neap and spring conditions. A sediment model implemented with the proposed roughness maps showed accuracy improvements of about 35% with respect to the model implemented with roughness maps derived from constant Chezy coefficients.

4.5.1 Excess bed-shear stress parameter

The transport stage or excess bed shear stress parameter, T , is defined by equation 2.13. Positive values of T indicate sediment motion. Maps in Figure 4.26 show the T parameter at the RFC (maximum local shear stress) for neap and spring tidal cycles. It can be noticed that the tidal channels are the main conveyance systems for sediments under both cases.

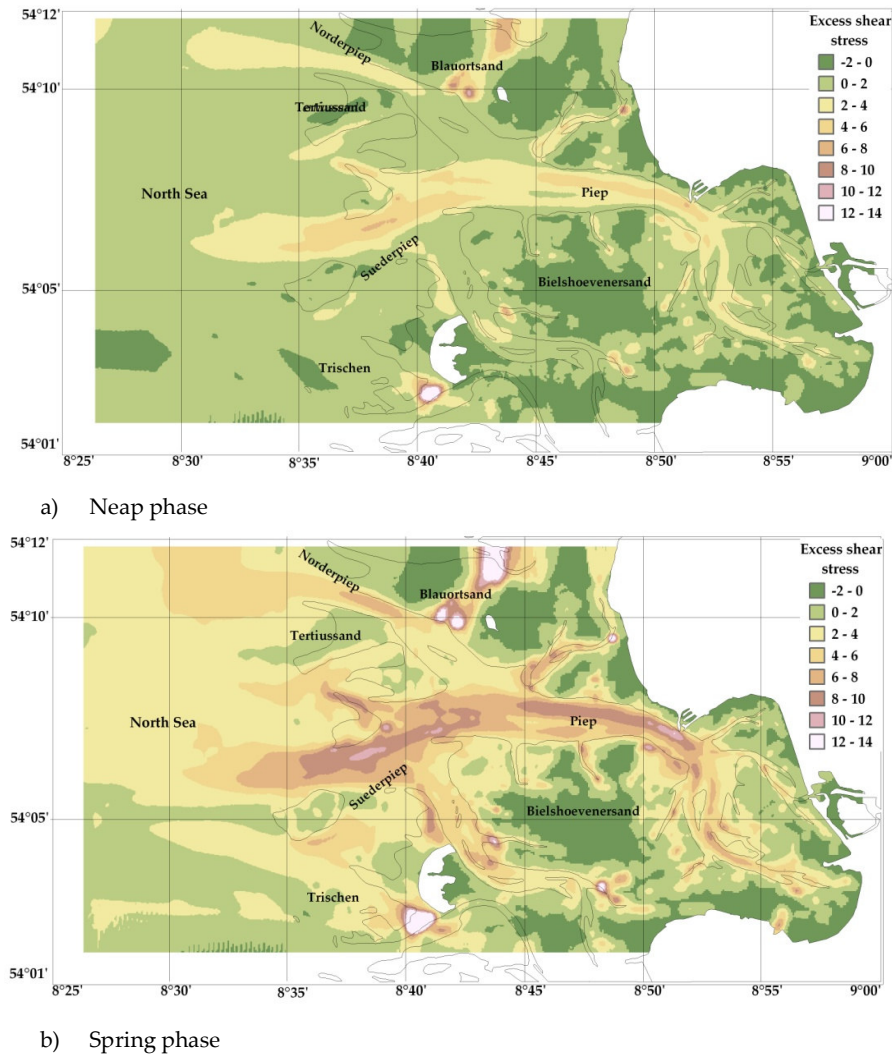


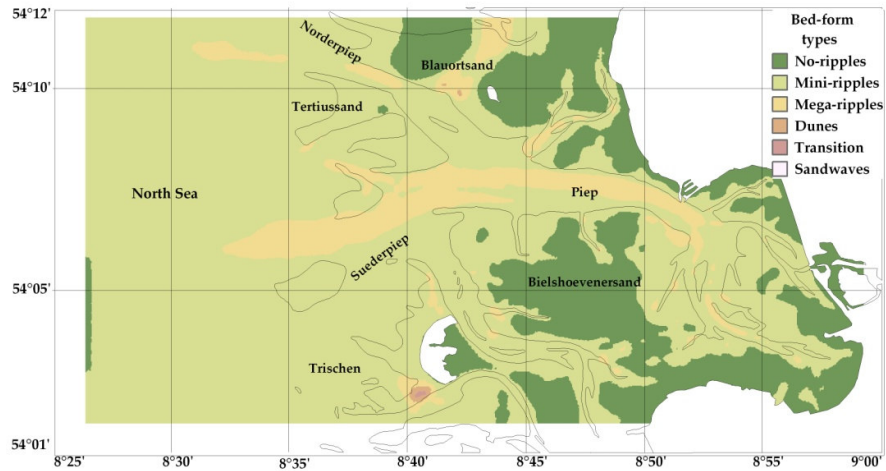
Figure 4.26 Excess bed-shear stress predictions at the RFC in the Dithmarschen Bight

4.5.2 Bedform types

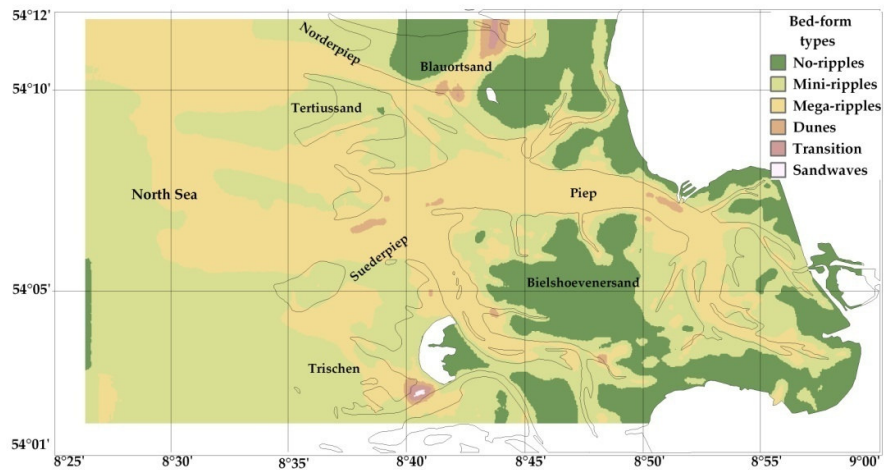
A subdivision of the study area for miniripples, megaripples and dunes is carried out on the basis of the T parameter, the dimensionless particle D^* and van Rijn's classification of bedforms (see Fig. 2.10). Maps in Figure 4.27 show the spatial distribution of bedform types predicted at neap and spring tidal cycles.

Megaripples are mainly located in the tidal channels and miniripples in tidal flats and sand banks. At neap phase it is noteworthy that megaripples stay confined to a narrow strip along the central part of the tidal channels and even disappear in Norderpiep. During spring phase, megaripples occupy a wider strip along the channels. Dunes are scarcely seen in the predictions, except for some small areas at

the intersection between the Suederpiep tidal channel and the Bielshoever Loch (spring phase), which match quite well with observations.



a) Neap phase



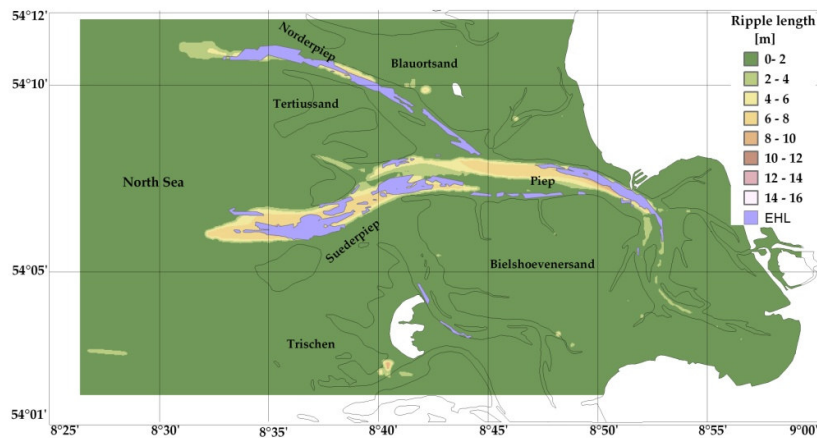
b) Spring phase

Figure 4.27 Bedform type predictions at the RFC in the Dithmarschen Bight

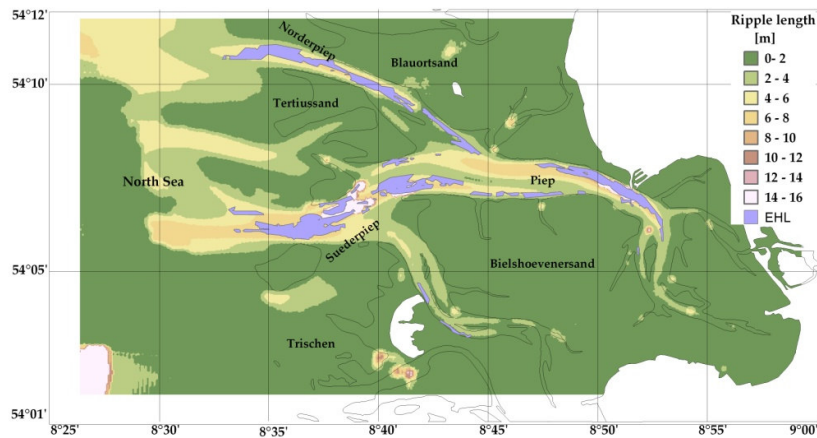
4.5.3 Bedform lengths

Water depths at the RFC and their functional relationship with bedform lengths (see Table 2.3) led to the definition of megaripples and dune lengths throughout the study area. Miniripple lengths were determined according to the local grain sizes predicted in previous chapters, where lengths were about 500 to 1000 times the mean particle size. Maps in Figure 4.28 show the spatial distribution of bedform lengths predicted at neap and spring tidal cycles in the Dithmarschen Bight.

Predictions of megaripple lengths vary between 3m to 7m in the Norderpiep channel and between 5m to 9m in the Suederpiep and Piep tidal channels. From SSS measurements, average bedform lengths ranging from 3 m to 6 m in Norderpiep and from 7 m to 10 m in Suederpiep and Piep channels were observed, which is in close agreement with predictions. Variations in shear stresses at neap-spring phases result in an increase or decrease of miniripples and megaripples coverage.



a) Neap phase



b) Spring phase

Figure 4.28 Bedform length predictions in the Dithmarschen Bight

4.5.4 Bedform heights

The spatial distribution of the predicted bedform heights at neap and spring phases in the study area is shown in Figure 4.29. Flow results from numerical modelling at the RFC, sedimentological data and van Rijn's empirical equation (see Table 2.3) are the basis of the methodology of determining ripple heights.

Bedform height predictions varied between 0.10m to 0.60m in the Norderpiep channel and between 0.15 m to 0.90 m in the Suederpiep and Piep tidal channels. Along the Norderpiep and the Piep tidal channels, echo sounder measurements report bedform heights ranging from 0.10 m to 0.50 m, which is again pretty close to predictions, therefore proving the reliability of the proposed methodology in the definition of bedform dimensions.

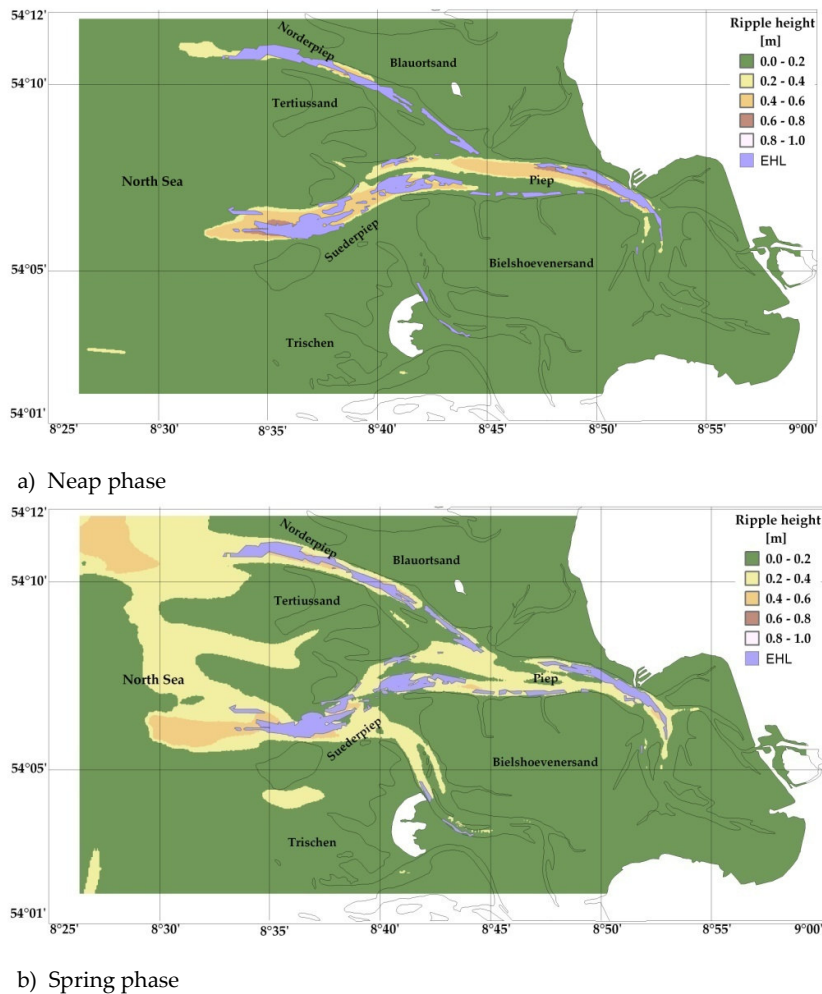


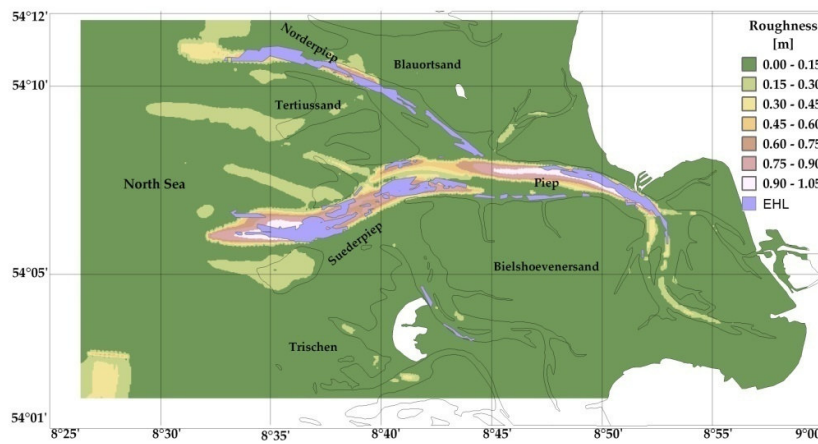
Figure 4.29 Bedform height predictions in the Dithmarschen Bight

4.5.5 Bedform roughness

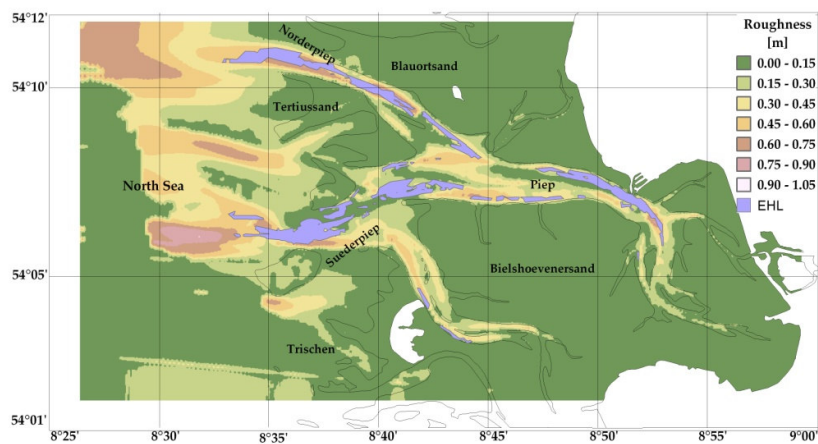
Finally, and directly related to bedform dimensions and grain sizes, is the prediction of the equivalent roughness size (k_s). Bed resistance is computed through the k_s parameter, which affects both flow and sediment dynamics. Skin friction caused by viscosity forces plus form roughness due to pressure differences make up

the equivalent roughness parameter. Hence, empirical relationships (Table 4.3), flow conditions, grain sizes and outcropping of the EHL were considered on the prediction of bedform roughness in the Dithmarschen Bight.

Figure 4.30 shows equivalent roughness sizes varying from 0.06 m to 1.20 m. The largest values are observed in the tidal channels. Higher roughness extends wider during the spring tidal cycle along the channels than at neap phase. The maximum roughness of about 1.2m was computed during the neap tide over an area of megaripples. The same area transforms into a dune area during spring phase with a lower roughness due to the reduction on the ratio Δ/λ (bedform steepness).



a) Neap phase



b) Spring phase

Figure 4.30 Bedform roughness predictions in the Dithmarschen Bight

4.6 Summary

The relevant effect of bed roughness on the sediment transport load has been reported by several authors [van Rijn, 2001; Winter and Mayerle, 2003]. This fact motivated the study carried out through this chapter. Bed roughness is made up of grain roughness (skin friction) and form roughness (drag forces).

The skin friction can be defined through the size of bed surficial sediments. The grain size map determined through eq. 3.3 is used for this purpose. However, this map might be inaccurate in deeper locations where the wave influence is negligible (relative wave heights lower than 5%). High discrepancies between predictions and observations in the deep channels can be noted locally (see Fig. 3.29).

These local discrepancies, however, should not affect much the prediction of bed roughness, since in general the grain size predictions were not far from the observations and also because the bed roughness in the channels is more affected by the presence of larger bedforms such as megaripples or dunes (form roughness) than by grain sizes (skin friction).

This chapter focused mostly on bedform characteristics. The proposed methodology in predicting bedform dimensions and their corresponding roughness implied several assumptions:

- a) Mean bedform dimensions (λ and Δ) present negligible variations during one tidal cycle;
- b) Bedform dimensions within one tidal cycle are the result of only one flow condition, which correspond to the representative flow condition (RFC);
- c) Methodologies to predict bedform dimensions under steady flow conditions such as van Rijn's [1993] can be applied on tidal flows by means of the RFC. The RFC must be determined for each particular study area. Across the Dithmarschen Bight the flow condition coinciding with the maximum bed shear stress was defined as the RFC.

The approach presented in this chapter to determine bedform features and roughness is valid over areas where currents are predominant. Hence, predictions using this approach along shallow areas with a combined action of currents and waves would require some modifications. It is pointed out that bedforms on the western sand banks of the study area are likely to develop under both wave and current actions (section 4.3.3). In the case that future investigations verify this evidence, local adjustments of the bedform dimensions should be considered.

Chapter 5

Sediment transport model

5.1 Introduction

In this chapter, we focus our attention in the determination and application of a numerical model to predict the sediment transport in a tidal area. Numerical modelling allows the study of sediment dynamics across extensive regions, that besides accuracy, flexibility and economical reasons make this method highly advantageous over others. Nowadays, with the modern computing systems, the evolution of numerical algorithms in terms of efficiency and stability, the advances in analytical and empirical theories for sediment dynamics, the higher resolution and accuracy on measuring technologies, etc. derive in relatively fast and precise estimation of sediment transport rates over short temporal scales.

The great and undeniable benefits of covering extensive areas in sediment transport studies (or other processes) by numerical modelling require a proper knowledge of the studied domain, within which involved input factors should be accurately accounted for in accordance with the model spatial discretization. Thus, the initial part of this chapter is devoted to outlining the model input data concerning morphology, hydrodynamics and sedimentological characteristics, as well as their spatial and temporal variability.

Subsequently, a summary of the adopted methodologies used in describing the sediment dynamics is presented. The analysis of the sediment dynamics is divided into 3 components: a) particle entrainment and the transfer function at the flow-bed interface; b) Mechanics of different transport modes i.e. bed or suspended motion; and c) Particle settling.

Finally, the input data and methodologies defining the flow and sediment dynamics are compiled into the numerical model platform. The TRISULA and SED models developed by WL | Delft Hydraulics are used to simulate 2-DH non-steady flows and transport phenomena in the Dithmarschen Bight. Due to the effect of some parameters like critical shear erosion, sediment erosion rate, specific density, time

step, etc. on sediment concentrations, a series of sensitivity tests were carried out for some of the model's physical and numerical parameters.

5.2 Model input

Hydrodynamic, morphological and sedimentological factors are essential in the study of sediment transport in coastal environments. Among all possible input variables included in these three fields, a brief selection is presented: a) Shear stresses, water depths and velocities are relevant hydrodynamic characteristics affecting the sediment motion cycle; b) Morphological factors such as bathymetry and bedforms define the main transport channels and the crucial flow resistance parameter; and c) Cohesive forces and particle weight are essential sedimentological characteristics affecting both erosion and deposition fluxes.

In most cases, a shortage of basic information or input data is one of the main inconveniences in sediment transport modelling. Obvious difficulties of in situ observation and measurement explain the deficit of reliable field data. Modern technologies based on acoustic, optic or mechanical principles have mostly overcome the inconvenience of measuring through the water barrier, although they generally imply high costs. Some alternative procedures and functional relationships have been proposed in this thesis that, combined with reduced field campaigns, can increase the resolution and coverage of several input parameters, thus reducing the project expenses.

5.2.1 Morphology input

5.2.1.1 Bathymetry

Bathymetry is usually the more accessible information. This investigation obtained data from the Federal Maritime and Hydrographic Agency (BSH), which is located in Hamburg (Germany) and performs bathymetric measurements through the use of Echo Sounder equipment in the Dithmarschen Bight. The model bathymetry is constructed from measurements performed in 1999 and 2000 along the tidal channels (approx. 600 km²). Usually, each annual dataset comprises a mean density of information of one value every 100m. The restricted access of vessels over the tidal flats prevents the total coverage of the study area with Echo Soundings. Therefore, bathymetric data edited in 1990 and provided by the Office of Rural Areas (ALR) in Husum was considered for the shallow regions.

Figure 5.1 describes the main features of the Dithmarschen Bight bathymetry. Tidal channels, sand banks and tidal flats can be distinguished on the complex and

irregular field of water depths. Three main channels are marked: Norderpiep located in the northwest part of the domain, Suederpiep in the southwest, and the Piep tidal channel that extends to the coast line. Maximum water depths range up to 23m. Along the western boundary, water depths range from 10 m to 15 m. Between the Norderpiep and Suederpiep, the tidal flat Tertiusand can be found. The flat Blauortsand is located further north up to the Norderpiep and Piep. In the middle of the domain is the flat Bielshoeversand that together with the D-Steer shoal define the southern limit of the domain.

Model simulations performed in this investigation covered only short periods ranging from 3 to 5 days, and due to the relative stability of the main tidal channels, bathymetry changes were neglected. It is pointed out though that submarine slides due to erosional and depositional process along the channel slopes can occur even during temporal scales of weeks to months [Ricklefs and Asp, 2005].

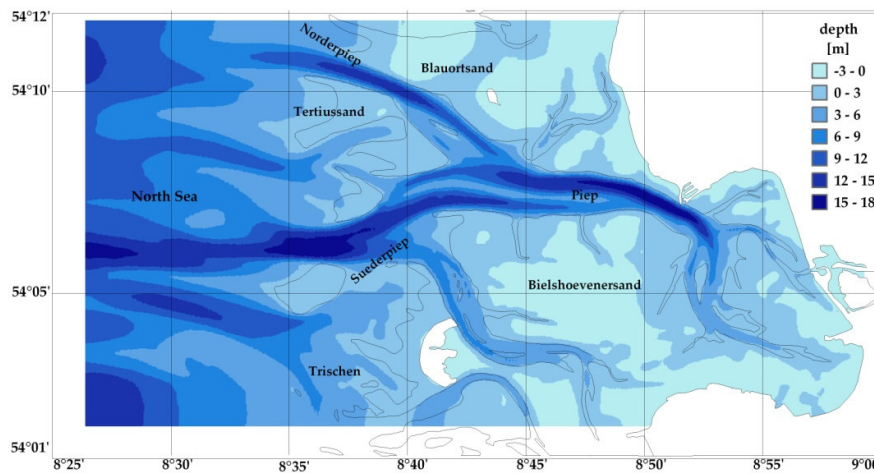


Figure 5.1 Model bathymetry

5.2.1.2 Bedforms

Bedforms are a determinant factor in the study of flow resistance, affecting greatly the sediment transport processes. However, bedform maps are practically unavailable anywhere. To overcome this inconvenience an extensive number of investigations have reported several procedures to estimate bedform dimensions for steady or quasi-steady flows. Their application across the Dithmarschen Bight is not straightforward given the unsteady tidal conditions prevailing.

Through the project PROMORPH, however, an study of bedforms in unsteady environments has been carried out by measuring campaigns performed during 1999 and 2000. Subsequent analysis of the field data by Razakafoniana [2001], Vela-Diez [2001], and Pramono [2005] made possible the visualization of the seabed along the tidal channels of the Dithmarschen Bight. Images and profiles of the seafloor were

obtained from Side Scan Sonar (SSS) and Echo Sounder devices. Field information made available from the above authors is used in this investigation to validate the proposed methodology in predicting bedforms under non-stationary conditions (see section 4.3).

This methodology is based on numerical modelling, empirical relationships and the RFC concept, which was successfully verified in the domain through direct comparisons with field data obtained from the tidal channels. However, it is pointed out that these predictions are not applicable for the definition of individual bedform features (i.e. small spatial scales), which present random, discontinuous behavior. Nevertheless, an aggregated value of bedform dimensions in an area or transect (at least ten times larger than the maximum ripple length observed) can be fairly well estimated.

Based on the results obtained in this work, the methodology outlined throughout section 4.3 is recommended in establishing a spatial variation of bedform dimensions and roughness in the Dithmarschen Bight, as well as in similar study areas, provided appropriate validations are carried out. This approach also considers the temporal variation of bedform features. Maps of bedform roughness are updated along the neap-spring cycle accordingly with accuracy requirements (ideally after each tidal cycle).

5.2.2 Hydrodynamic input

The TRISULA model from WL | Delft Hydraulics was used to determine the non-steady flow in the Dithmarschen Bight. The flow is mainly forced by tides although waves and wind might prevail during extreme weather conditions. The 2DH flow model extensively calibrated in the study area by Palacio [2002] provides the sediment model with valuable information (e.g. shear stresses, velocities, water depths, etc) in accordance to its spatial and temporal discretization.

In spite of the fact that all real flows are 3-D, a 2DH-model is implemented in the study area, since depth-averaged flow equations are usually suitable to model tidal wave flows [WL | Delft Hydraulics, 2006] such as those prevailing in the Dithmarschen Bight. However, a uniform distribution of temperature and salinity has to be assumed (i.e. vertically homogeneous fluid) in order to reduce density currents. This assumption fits well in the study area given the combined occurrence of limited water depths and strong tidal and wave action that should lead to a well-mixed region.

The effect of river discharges such as the Elbe and Eider rivers might cause 3-D flow patterns as well. However, the large distance separating the river mouths and the study area limit the possibility of any alteration on the established 2DH flow. To verify the reliability of the 2DH-model, in Palacio et al. [2001] a comparison between

the results of a 2DH-model and a 3D model with 10 layers was made, leading to the conclusion that only minor differences in terms of water levels at several locations and flow discharges at several channel cross-sections were found.

5.2.2.1 Model grid

The spatial discretization of the study area is carried out through a curvilinear grid with approximately 35,000 cells that are superimposed on the domain (as shown in Fig. 5.2). The grid resolution ranges from 90m in the tidal channels to 230m in the remote areas. Space derivatives involved in the hydrodynamic equations are solved in agreement with this grid. Grid orthogonality and smoothness criteria can be found in the Delft3D user manuals [WL | Delft Hydraulics, 2003]. Grid lines preferably follow the tidal channel axes, which reduce the magnitude of the convective accelerations and therefore the associated non-linearity.

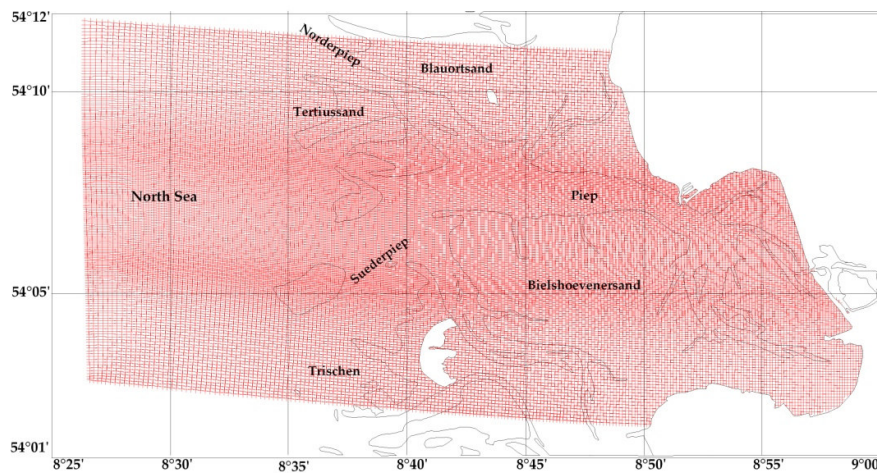


Figure 5.2 The curvilinear model grid

5.2.2.2 Hydrodynamic governing equations

The flow field solution (e.g. water depths and velocities) is obtained through the numerical integration of the conservation of mass and momentum equations. The implicit finite difference scheme adopted for the time integration enables simulations to be performed for Courant numbers as high as 10, where an algebraic approach for turbulence closure using a constant value of eddy viscosity is considered [Roelvink and Van Banning, 1994].

The conservation of mass equation expresses a conservation law by equating a net mass flux over a surface with a loss or gain of material within the surface. The differential form of the continuity equation is given by:

$$\frac{\partial \zeta}{\partial t} + \frac{1}{\sqrt{G_{\xi\xi}}\sqrt{G_{\eta\eta}}} \frac{\partial [(h+\zeta)u\sqrt{G_{\eta\eta}}]}{\partial \xi} + \frac{1}{\sqrt{G_{\xi\xi}}\sqrt{G_{\eta\eta}}} \frac{\partial [(h+\zeta)v\sqrt{G_{\xi\xi}}]}{\partial \eta} = Q \quad (5.1)$$

Where:

ζ : free surface elevation above the reference

ξ, η : horizontal curvilinear coordinates

G : coefficient used to transform curvilinear to rectangular coordinates

u : flow velocity in ξ direction

v : flow velocity in η direction

Q : discharge source or sink per unit area

The momentum conservation equation is a statement of Newton's Second Law and relates the resultant of the forces acting on an element of fluid to its acceleration or rate of change of momentum. Given its vectoral character, the momentum conservation equation is represented as a set of scalar equations, as it is shown in equations 5.2 and 5.3 for the horizontal curvilinear coordinate system (ξ, η):

$$\begin{aligned} \frac{\partial u}{\partial t} + \frac{u}{\sqrt{G_{\xi\xi}}} \frac{\partial u}{\partial \xi} + \frac{v}{\sqrt{G_{\eta\eta}}} \frac{\partial u}{\partial \eta} + \frac{uv}{\sqrt{G_{\xi\xi}}\sqrt{G_{\eta\eta}}} \frac{\partial \sqrt{G_{\xi\xi}}}{\partial \eta} \\ - \frac{v^2}{\sqrt{G_{\xi\xi}}\sqrt{G_{\eta\eta}}} \frac{\partial \sqrt{G_{\eta\eta}}}{\partial \xi} - f_v = -\frac{1}{\rho_o \sqrt{G_{\xi\xi}}} P_\xi + F_\xi + M_\xi \end{aligned} \quad (5.2)$$

and,

$$\begin{aligned} \frac{\partial v}{\partial t} + \frac{u}{\sqrt{G_{\xi\xi}}} \frac{\partial v}{\partial \xi} + \frac{v}{\sqrt{G_{\eta\eta}}} \frac{\partial v}{\partial \eta} + \frac{uv}{\sqrt{G_{\xi\xi}}\sqrt{G_{\eta\eta}}} \frac{\partial \sqrt{G_{\eta\eta}}}{\partial \xi} \\ - \frac{u^2}{\sqrt{G_{\xi\xi}}\sqrt{G_{\eta\eta}}} \frac{\partial \sqrt{G_{\xi\xi}}}{\partial \eta} + f_u = -\frac{1}{\rho_o \sqrt{G_{\eta\eta}}} P_\eta + F_\eta + M_\eta \end{aligned} \quad (5.3)$$

Where:

f_u, f_v : Coriolis force per mass unit

ρ_o : reference density of water

P_ξ, P_η : pressure gradients

F_ξ, F_η : turbulent momentum flux

M_ξ, M_η : external sources or sinks of momentum.

5.2.2.3 Boundary conditions

Mass and momentum conservation differential equations require imposing a set of boundary conditions to fit the actual problem, since only one of the infinitely many solutions from the differential equation satisfies the boundary conditions.

Thus, a unique and well-defined flow condition can be determined, matching what is expected.

The model has three open sea boundaries describing the behavior of the water levels at the edges of the study area, i.e. western, northern and southern (see Fig. 5.3). As the tidal waves propagate mainly through the western boundary, their conditions are crucial on the determination of the flow field in the model. The contrary, low influence is expected from the northern and southern boundaries, which are located on the tidal flats and fall dry during low tide [Palacio, 2002].

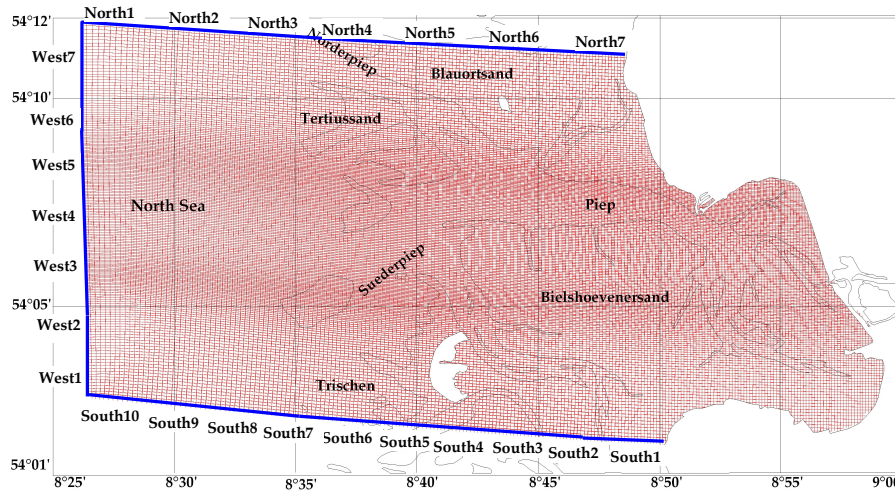


Figure 5.3 Open sea boundaries for the study area

As the northern, western and southern boundaries have lengths of around 24 km, 16 km, and 26 km respectively, they were split into a number of segments to ensure a proper representation of the varying conditions along them. Water levels on each segment are determined by nesting the Dithmarschen Bight model into larger models, since measurement data with sufficient resolution in time and space are not available for the open boundaries. The nesting procedure has been validated by Winter [2003] for the German North Sea coast.

In this study the nesting sequence starts with the north-west European Continental Shelf Model (CSM) that defines its own boundary conditions by means of 10 main harmonic tidal constituents (M2, S2, N2, K2, O1, K1, Q1, P1, NU2, and L2) as defined by Verboom et al. [1992]. Then, the CSM was nested with the German Bight Model (GBM) set by Hartsuiker [1997] which in turn is nested with the Dithmarschen model to yield the required boundary information, as is shown in Figure 5.4.

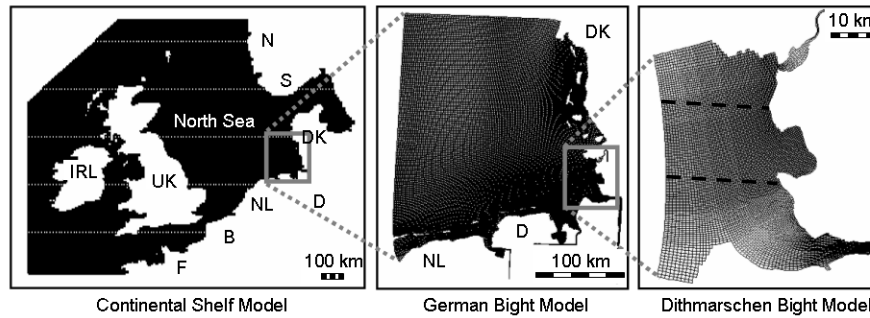


Figure 5.4 Nesting sequence for the generation of open sea boundary conditions for the Dithmarschen Bight [Winter, 2003]

5.2.3 Sedimentological input

The Dithmarschen Bight is a complex environment subject to multiple forcing factors. Tides, waves and wind affect, with variable intensities, distinguishable sub-regions in the study area (e.g. tidal channels, tidal flats and sand banks). Tidal currents govern the main processes in the deeper parts of the tidal channels, and combined actions of currents and waves prevail in the shallower tidal flats and sand banks. Hence, a high variable map of energy levels can be found in the area, which is largely responsible for the grain size sorting of bed surficial materials.

The analysis of bed sediment samples taken over the area showed particle sizes ranging from 60 μm to 230 μm . The coarser sediments can be found mostly over areas exposed to wave action while the smaller particles tend to reside in sheltered regions. The spatial variation of grain sizes has considerable effects on the numerical transport model given the high importance on the definition of both suspended and bed sediment rates. Considering uniform grain sizes over the entire domain implies large discrepancies with the real case and therefore inaccurate predictions.

Hence, special emphasis was given in chapter 3 to determine the spatial distribution of grain sizes in the study area during which, an extensive scrutiny on the functional relationships between hydrodynamic parameters and grain sizes was carried out. Particle sizes determined from about 200 sediment samples were correlated with local hydrodynamic characteristics, from which a relationship between equilibrium grain sizes, maximum orbital velocities and seafloor exposition to wave action was proposed (see Figure 3.26). Furthermore, a simplified empirical relationship, applicable throughout the domain, is also recommended to predict grain sizes, provided maximum orbital velocities during a Typical Tidal Cycle TTC are available (see eqs. 3.3 and 3.4).

5.3 Sediment dynamics

This section makes specific reference to methodologies or formulae applied in the sediment transport model. Sediment motion is analyzed according to the entrainment, transport and settling stages. Both, cohesive and non-cohesive materials were included in the model. However, their entrainment and settling processes were modeled separately given their notoriously dissimilar behavior.

5.3.1 Boundary conditions for sediment transport

The methodology referred above, in obtaining the hydrodynamic boundary conditions through a nesting sequence (see section 5.2.2.3) might be inaccurate for the sediment transport case, as the larger models are not yet validated for sediment dynamics (e.g. the Continental Shelf Model CSM and the German Bight Model GBM).

Thus, it was necessary to use equilibrium equations to define the sediment concentrations on each segment of the model boundaries. This procedure implies that the sediment load entering-leaving through the model boundaries is almost perfectly adapted to the local flow conditions. Therefore very little accretion or erosion should be experienced near the boundaries. This condition will be the desired situation if the model boundaries are properly selected.

The calculation of equilibrium sediment concentration profiles along the boundaries can be done by means of two approaches, each turning out similar results for the study area. The first approach assumed the standard Rouse profile [Rouse, 1937]:

$$\frac{c(z)}{c_a} = \left[\frac{a(h-z)}{z(h-a)} \right]^\beta \quad (5.4)$$

Where,

z : elevation above the bed

β : Rouse number or suspension number

c_a and a are Van Rijn's reference concentration and reference height respectively,

which are defined as follows:

$$c_a = 0.015 SUS \rho_s \frac{d_{50} T^{1.5}}{a D_s^{0.3}} \quad (5.5)$$

$$a = \min[\max\{AKSFAC \cdot k_s, 0.01h\}, 0.20h] \quad (5.6)$$

Where, SUS and $AKSFAC$ are user-specified proportionality factors. The current model sets unit values for both of them.

The second approach solves a simplified stationary advection-diffusion equation, where the erosion flux is equated to the depositional rate. It implies, therefore, a negligible variation of the bottom level:

$$-w_s c - \varepsilon_{s,z} \frac{\partial c}{\partial z} = 0 \quad (5.7)$$

The turbulent mixing coefficients required in equation 5.7 are obtained from the hydrodynamic input data.

5.3.2 Sediment transfer functions at the flow-bed interface

The exchange of sediment material between the bed and the main flow is determined through the erosion and sedimentation fluxes. Through these fluxes the bed boundary conditions are defined, and together with the lateral boundary conditions (described in the preceding section) a well-posed mathematical initial boundary-value problem is ensured. Thus, the boundary conditions on the bed are given by:

$$-w_s c - \varepsilon_{s,z} \frac{\partial c}{\partial z} = D - E; \text{ at } z = a \quad (5.8)$$

Where:

D : sediment deposition rate

E : sediment erosion rate

In order to obtain an explicit solution from equation 5.8, the concentration and concentration gradient at the reference height are approximated by means of the Rouse profile (see eq. 5.4).

Entrainment and settling processes strongly differ for cohesive and non-cohesive sediments due to their differences in physical and chemical properties. Electrostatic bonds and flocculation processes steer erosion and deposition for cohesive sediments, while gravity is relevant in sandy materials.

5.3.2.1 Erosion fluxes and sediment entrainment

Erosion and entrainment fluxes are computed by two different approaches, depending on the cohesivity of the material.

a) For non-cohesive materials the erosion flux is defined by the upward diffusion of sediments:

$$E = \varepsilon_{s,z} \frac{\partial c}{\partial z} \quad (5.9)$$

Where the vertical gradient of sediment concentrations is evaluated at the reference height through the differentiation of equation 5.4:

$$E = 0.015 \varepsilon_{s,z} S U S \rho_s \frac{d_{50} T^{1.5}}{a D_*^{0.3}} \frac{\partial}{\partial z} \left[\frac{a(h-z)}{z(h-a)} \right]^\beta \quad (5.10)$$

Erosional fluxes are possible when the threshold of incipient motion is reached or exceeded due to increasing shear stresses. Incipient motion was determined by means of the critical bed-shear stress from Shields formulation. It was included in eq. 5.10 through the excess bed-shear stress parameter T .

b) For cohesive sediments the erosion flux is computed according to the Partheniades and Krone formulations [Partheniades, 1965]:

$$E = M \left(\frac{\tau_b}{\tau_{cr,e}} - 1 \right), \text{ when } \tau_b > \tau_{cr,e} \quad (5.11)$$

$$= 0, \text{ when } \tau_b \leq \tau_{cr,e}$$

Where, M : Erosion rate coefficient. $\tau_{cr,e}$: Critical erosion shear stress

The determination of the entrainment of cohesive sediments is far more complex than the previous non-cohesive case. Many attempts have been made to relate the critical shear stress to basic parameters such as plasticity, voids ratio, water content, yield stress and others. However generally accepted relationships are not available [van Rijn, 1989]. The $\tau_{cr,e}$ and M values for the study area were therefore defined through the calibration of the sediment transport model (see section 6.3).

5.3.2.2 Deposition fluxes and sediment fall velocity

As in the previous case, the sediment fall velocity and the deposition fluxes depend on the type of sediments.

a) For non-cohesive sediments the deposition flux is highly dependent on the settling velocity:

$$D = cw_s \quad (5.12)$$

The settling velocity is initially defined by van Rijn's methodology (see eqs. 2.33 to 2.35) and then adjusted in accordance to the hindered settling effect [Richardson and Zaki, 1954].

$$w_s = \left(1 - \frac{c}{CSOIL} \right)^5 w_{s,o} \quad (5.13)$$

Where,

$w_{s,o}$: basic settling velocity without consideration of hindered effect

$CSOIL$: reference density

b) For cohesive sediments the deposition flux is computed according to the Partheniades and Krone formulation:

$$D = w_s c \left(1 - \frac{\tau_b}{\tau_{cr,d}} \right), \text{ when } \tau_b < \tau_{cr,d} \quad (5.14)$$

$$= 0, \text{ when } \tau_b \geq \tau_{cr,d}$$

Where, $\tau_{cr,d}$: critical deposition shear stress

The settling velocity w_s is affected by flocculation processes, which in salty waters is enhanced due to the reduction of the electrokinetic potential that repels particles

from one another and the increment of molecular attractive forces. Flocs, therefore, become much larger than the individual sediment particles and settle at a faster rate. Thus far, neither the flocculation effect nor an algorithm defining the critical deposition shear stress have been included into the sediment model. The w_s and $\tau_{cr,d}$ values were therefore defined through the calibration of the sediment model (see section 6.3).

5.3.3 Sediment transport

The transport of bed sediments starts when the bed shear-stress just exceeds the critical value for initiation of motion. Shear stress also determines the particles mode of transport. At low shear stress values, the particles will roll and slide in continuous contact with the bed (bed load). For higher shear values, the particles can be lifted and move into suspension, supported by upward turbulent forces (suspended load).

5.3.3.1 Bed load transport

The bed load transport is characterized by particles rolling, sliding or saltating with continuous bed contact. Gravity is the main driving force and turbulent effects are negligible. Van Rijn's [2000] methodology is adopted in the current sediment transport model. This approach assumes that bed particle movement is dominated by particle saltations under the influence of hydrodynamic and gravity forces. According to these assumptions, the bed load transport rate is defined as:

$$q_B = 0.5\eta\rho_s d_{50} \dot{u}_* D_*^{-0.3} T \quad (5.15)$$

Where η is the relative availability of the sediment fraction in a mixed layer; \dot{u}_* , D_* , and T are the effective bed shear velocity, the dimensionless particle diameter, and the dimensionless bed-shear stress respectively.

In spite of the fact that this functional relationship was defined for steady flow, its application to non-steady and non-uniform cases is also possible due to the swift response of near bed particles to new hydraulic conditions. This can be seen in Figure 5.5, showing a negligible lag phase between current velocities and near bed concentrations during a flood phase. Different behavior is observed for suspended load concentrations where lag phases can be about 45 minutes.

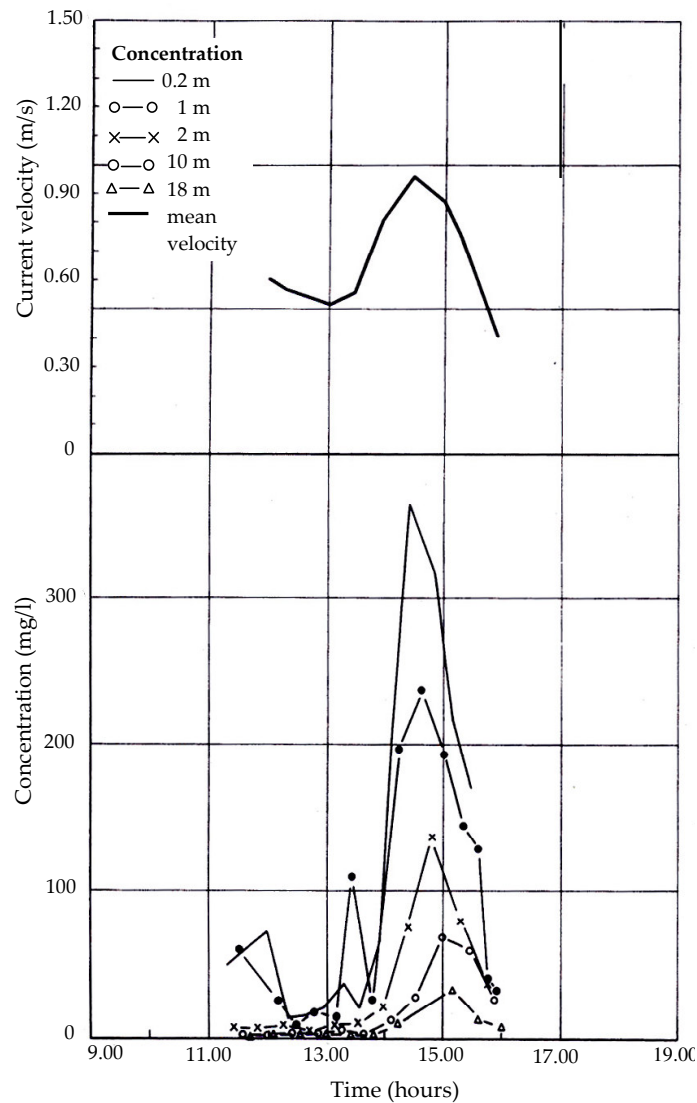


Figure 5.5 Lag phase between current velocities and sediment load [Van Rijn, 1989]

5.3.3.2 Suspended load transport

Continued increases in flow shear stresses result in more intense turbulence, that can reduce the viscous layer and even reach the bed surface. Grains jumping near the bottom can then be caught by eddies and lifted into suspension. To remain in suspension, the upward turbulent velocity must exceed the fall velocity of the particles. As the turbulent flow velocities $\overline{u'v'}$ can be represented by the bed-shear stress u_* , an approximated criterion to determine the threshold for suspended load (see other criteria in Fig. 2.19) is given as follows:

$$u_* = w_s \quad (5.16)$$

Several methodologies have been proposed to define the suspended sediment load for steady uniform flow. Einstein [1950], Bijker [1971], van Rijn [1984], Bagnold [1966], etc. are part of these formulations, which are mostly based on the advection-diffusion concept or the energy balance. Despite the relative success of these methodologies, their application to the Dithmarschen Bight is restricted due to its non-steady flow condition. Hence, the transport of suspended sediment is calculated by solving the advection-diffusion equation, from which the most general form is given by:

$$\begin{aligned} \frac{\partial c}{\partial t} + \frac{\partial uc}{\partial x} + \frac{\partial vc}{\partial y} + \frac{\partial(w-w_s)c}{\partial z} - \frac{\partial}{\partial x} \left(\epsilon_{s,x} \frac{\partial c}{\partial x} \right) - \frac{\partial}{\partial y} \left(\epsilon_{s,y} \frac{\partial c}{\partial y} \right) + \\ - \frac{\partial}{\partial z} \left(\epsilon_{s,z} \frac{\partial c}{\partial z} \right) = 0 \end{aligned} \quad (5.17)$$

The depth-integrated form of this equation is defined by Galappatti [1985]:

$$\frac{\partial hc}{\partial t} + \frac{\partial huc}{\partial x} + \frac{\partial hvc}{\partial y} - \frac{\partial}{\partial x} \left(\epsilon_{s,x} h \frac{\partial c}{\partial x} \right) - \frac{\partial}{\partial y} \left(\epsilon_{s,y} h \frac{\partial c}{\partial y} \right) = \frac{h(c_{se} - c)}{T_s} \quad (5.18)$$

Where:

- c : suspended sediment concentration
- t : time coordinate
- x, y, z : space coordinate axis
- u, v, w : velocity components in x, y and z directions
- h : water depth
- w_s : settling velocity in a suspension
- $\epsilon_{s,x}, \epsilon_{s,y}, \epsilon_{s,z}$: eddy diffusivities or mixing coefficients
- c_{se} : local equilibrium concentration
- T_s : dimensionless adaptation time

The local flow velocities, water depths and eddy diffusivities are obtained from the hydrodynamic model TRISULA.

5.3.4 Interaction of several sediment fractions

The formulations presented above for sediment transport have been developed for uniform sediment beds comprised by only one grain size. The Dithmarschen Bight is made up of a range of sediment types and sizes. In this case, the reference concentrations, erosion rates and sediment transport rates will be reduced proportionally to the availability of the sediment fraction in the bed.

If the composition of the top-most layer of the bed stratigraphy is almost uniform, the latter approach is reasonable and therefore always applied for non-cohesive sediments. However, as cohesive sediments might preferably form a layer that covers the other sediment fractions, the bed surface would have a higher content of

fine materials. Hence, for cohesive material a proportional reduction factor determined through the model calibration process is used.

In order to reduce computational efforts and fulfill restrictions from the modeling system, the non-cohesive sediments in the Dithmarschen Bight have been grouped into 4 categories according to their size (four sediment constituents). Ranges of grain sizes for each category are shown in Table 5.1. Based on the spatial distribution of grain sizes in the Dithmarschen Bight (see Fig. 3.29) are defined four regions on which the four sediment categories are located [Escobar, 2006]. Each sediment constituent or category is characterized by their own physical properties such as grain size (d_{50}), specific density and dry bed density.

Additionally, to consider the dynamics of cohesive materials in the sediment transport model, a 5th cohesive sediment constituent is included. The cohesive properties of this constituent have been determined through the model calibration process (see section 6.3).

Table 5.1: Non-cohesive sediment constituents used in the sediment transport model

Category	Range of grain sizes [μm]	Adopted d_{50} [μm]
1	$d_{50} < 110$	100
2	$110 < d_{50} < 120$	115
3	$120 < d_{50} < 150$	135
4	$d_{50} > 150$	180

5.4 Sensitivity analysis of the sediment transport model

After defining the basic set up of the numerical model, this study assesses the effect of numerical and physical parameters on the sediment transport phenomena by means of a sensitivity analysis. It considers the response of the numerical approach with respect to changes of the parameters included in the model. On the basis of the sensitivity analysis it is possible to identify some particular parameters that have a predominant effect on the computation of suspended concentrations. Thus, the degree of effort can be assigned in defining the input parameters in the field campaigns. Furthermore, from this study the range of accuracy of the suspended load predictions can also be estimated, provided the actual range of variation for the most sensitive parameters is available.

The sensitivity analysis was performed at several locations spread throughout the study area and over representative time periods. A plan view of the Dithmarschen domain indicating the selected monitoring stations for the sensitivity analysis is shown in Fig. 5.6. Please note that while the stations inside the tidal channels

coincide to the positions of the field measurement stations (section 6.2), the stations over the tidal flats were randomly spread.

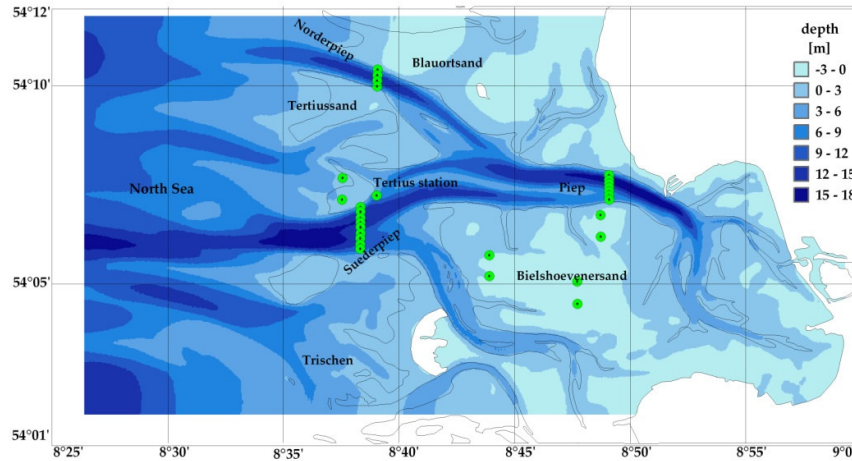


Figure 5.6 Monitoring stations in the Dithmarschen Bight

5.4.1 Numerical parameters

The variability of suspended load concentrations over the selected monitoring stations was investigated in relation to the computational time step, initial conditions, and other sets of parameters indicated in Table 5.2.

5.4.1.1 Time step

A benefit-cost analysis is performed in order to define the computational time step. The right time step is chosen according to the relation between accuracy arguments and the computational time cost. As the numerical model is unconditionally stable, the stability issue did not affect the time step choice. The accuracy of the model depends on the Courant number, which should not exceed a value of 10 for the Alternating Direction Implicit (ADI) method used in the time integration.

Model simulations were performed for time steps equal to 0.1, 0.5, 1, and 2.5 minutes. The results from these simulations were very similar for time steps up to 1 minute but for higher time step values and therefore higher Courant numbers the computed concentrations deviate from the other cases. Typical results from these simulations are shown in Figure 5.7 for the monitoring station Tertius (see Fig. 5.6). Maximum Courant numbers recorded on the simulations were about 2, 16, 32 and 82 for time steps of 0.1, 0.5, 1 and 2.5 min. respectively. A time step of about 1 minute seems to be appropriate for the current simulations, since it offers the less computational cost and an acceptable accuracy. However, the final decision was

inclined toward a time step of 0.5 minutes because only small areas presented Courant numbers higher than 10.

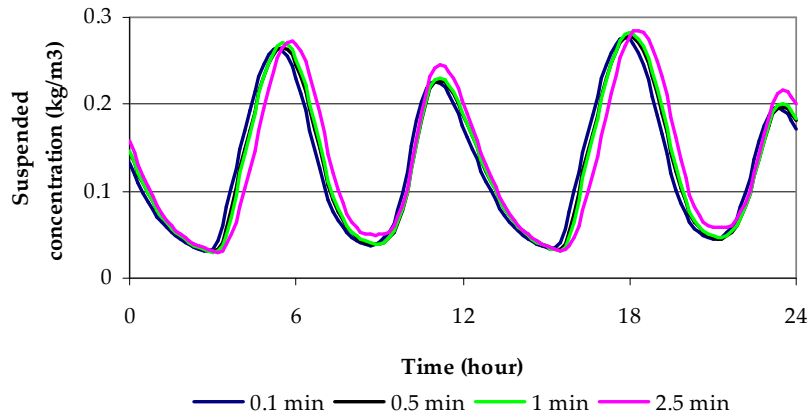


Figure 5.7 Time step sensitivity

5.4.1.2 Initial conditions

Generally, the initial conditions required for all dependent variables (i.g. water depths, velocities and suspended concentrations) in a coupled flow-sediment model are unknown and therefore they must be assumed. A large discrepancy between the initial conditions and the boundary conditions at the starting time can result in short wave disturbances that can propagate into the domain. These inaccuracies however are continually reduced by internal dissipation (bottom friction).

The time required for the model to reduce the short wave disturbances (warming-up time) was determined by means of the next procedure. Two simulations were run with the same model settings but starting with 24 hours difference. The later simulation started at the flood phase, that is the most critical, since all disturbances propagate into the model domain. Figure 5.8 shows the suspended concentration time series for the selected monitoring station Tertius. The perfect match between the two curves indicates the end of the initialization time, which can be estimated around 9 hours for this case. In order to prevent inaccuracies due to the initial conditions, all simulations should be run with warming-up times higher than 9 hours. As a conservative criterion, this investigation always allowed 24 hours for warming-up periods.

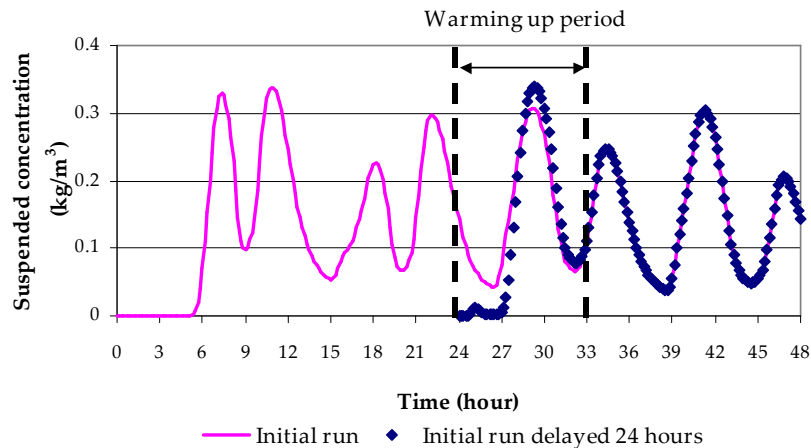


Figure 5.8 Definition of the warming-up period – Tertius station

5.4.1.3 Additional set of numerical parameters

Several methodologies or numerical schemes with variable discretizations, accuracy restrictions, parameters, etc. are available to define a sediment transport model. For consistency reasons, the modeler's choice should be invariably applied in each stage of the model development e.g. sensitivity analysis, calibration and validation. A brief descriptive summary of the numerical aspects adopted in this investigation is given in Table 5.2. Full details about these parameters can be found in the Delft3D user manuals [WL | Delft Hydraulics, 2003].

Table 5.2: Set of additional numerical parameters

Parameter	Choice	Description
Drying and flooding check	At water level and vel. points	Verification of water depths is accomplished at the four corners and middle of the grid cell
Depth at water level points	Max	The max. depth from the four values surrounding the depth point is chosen
Depth at velocity points	Mean	The depth at the velocity point is the mean of the depths at the adjoining depth points
Threshold depth	0.10 m	Value above which a cell is considered wet
Smoothing time	60 min	The time interval used at the start of a simulation for a smooth transition between initial and boundary conditions
Advection scheme for transport	Cyclic	Advection terms are approximated by the sum of a third-order upwind scheme and a second order scheme applied interchangeably on ξ, η directions

5.4.2 Physical parameters

A sensitivity analysis is carried out for representative parameters related to the physical condition of the modeled area. Each of these parameters is systematically changed and its effect on the model output measured. Tables 5.3 and 5.4 present in a compact form all physical parameters considered for the sensitivity tests for non-cohesive and cohesive sediments respectively. Ranges of variation of each physical parameter are contrasted with their effect on suspended concentration peaks at selected monitoring stations (see Fig. 5.6). A typical representation of the sensitivity tests is shown in Figure 5.9 for the critical shear erosion and erosion rate coefficient at the Tertius station.

Table 5.3: Sensitivity analysis of physical parameters (non-cohesive materials)

Physical Parameter	Parameter Range	Parameter Variation	Effect on suspended concentration peaks (relative variation)
Ref. density for hindered effect	800-3200 kg/m ³	+300%	0.21% (0.21/300=7e-4)
Specific density	1325-4000 kg/m ³	+202%	53.35% (0.26)
Dry bed density	800-3000 kg/m ³	+275%	0.0%(0)
Grain size	70-100 μm	+30%	0.64%(0.02)

Table 5.4: Sensitivity analysis of physical parameters (cohesive materials)

Physical Parameter	Parameter Range	Parameter Variation	Effect on suspended concentration peaks (relative variation)
Ref. density for hindered effect	800 -3200 kg/m ³	+300%	0.21%(7e-4)
Specific density	900 -3600 kg/m ³	+300%	0.0%(0.0)
Dry bed density	800 -1600 kg/m ³	+100%	0.0%(0.0)
Settling velocity	1.0 -2.0 mm/s	+100%	44.74%(0.45)
Critical deposition shear stress	1.62 -3.24 N/m ²	+100%	30.99%(0.31)
Critical erosion shear stress	0.5 - 1.0 N/m ²	+100%	56.48%(0.56)
Sediment erosion rate coefficient	0.00047-0.00094 kg/m ² /s	+100%	78.53%(0.78)

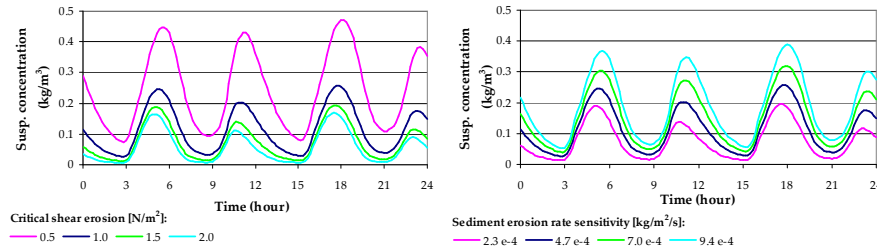


Figure 5.9 Sensitivity of suspended sediment concentrations due to critical shear erosion (left) and erosion rate (right) variations at the Tertius station

Finally, a summary of physical parameters on which sensitivity analysis was not performed is shown on Table 5.5. These parameters are generally well known over the study area or they were previously defined in the flow model by Palacio [2002].

Table 5.5: Set of physical parameters without sensitivity analysis

Parameter	Choice
Gravity	9.81 m/s ²
Water density	1024 kg/m ³
Air density	1 kg/m ³
Horizontal eddy viscosity	1 m ² /s
Horizontal eddy diffusivity	10 m ² /s

Thus far, all physical parameters considered in the sensitivity analyses were set uniform throughout the study area. Hence, the influence of the spatially variable bed resistance and grain size fields on suspended sediment transport is not yet studied. In the next chapter these parameters with spatial variability will be considered.

5.5 Summary

All input data required by the sediment transport numerical model has been gathered in this chapter. Morphology, hydrodynamic and sedimentological data feed the 2DH sediment model. The sediment model SED developed by WL|Delft Hydraulics supporting both bed load (non-cohesive sediments) and suspended load (cohesive and non-cohesive sediments) is applied in the study area.

The bed and suspended loads were treated separately in the sediment transport model. Whereas bed load was determined through an algebraic-explicit equation [van Rijn, 2000], suspended load is obtained from the differential advection-diffusion equation. This differential equation requires for its solution the definition of

boundary conditions along the model lateral boundaries and also at the bed-flow interface. Lateral boundary conditions were determined from equilibrium sediment concentration profiles [Rouse, 1937]. While, expressions determining erosion and deposition fluxes for cohesive [Partheniades, 1965] and non-cohesive [Van Rijn, 1984b] materials defined the boundary conditions at the bed-flow interface.

The initial setup of the sediment model is followed by a series of sensitivity tests, on which numerical and physical parameters were considered. An extensive number of input parameters were subjected to deliberate variations in order to assess their effect on suspended sediment concentrations. The model sensitivity was far higher to physical variables concerning cohesive materials than on sandy parameters. The latter might be explained through the predominance of fine materials moving in suspension.

Chapter 6

Prediction of sediment transport

6.1 Introduction

The numerical integration of any differential equation implies certain assumptions in their spatial and temporal discretizations that always raise some concerns about the accuracy of the solution. As a consequence, before any application of this kind, calibration and validation processes of the model are firstly required at the interest area. In this way the discrepancies between the predictions and observations might be reduced through the tuning of some physical parameters, from which the local values are unknown. Different statistical parameters can be used to estimate the model accuracy such as the RMAE and MAE.

Calibration and validation processes should be independent from each other and cover as much as possible the entire range of circumstances of the modeled phenomena. To accomplish this requirement several field campaigns designed by Poerbandono [2003] to observe the sediment dynamics at different tidal phases and tidal cycles as well as in different meteorological conditions were used. However, extreme events such as storms were out of the scope of this research. Measurements of suspended concentrations were compared to the model outputs in calibration and validation tasks. The accuracy of the final model results was highly improved through the spatial and temporal discretization of relevant physical parameters such as grain sizes, bed roughness, critical shear stress, settling velocity, and erosion rates. Furthermore, relative errors between model results and measurements were pretty close to the range of accuracy of the measuring devices and remained largely uniform throughout the testing of all cases.

An evolutionary construction of the sediment model is highlighted in this chapter. Starting with a plain model for non-cohesive sediments, uniform grain sizes and constant friction coefficients, a progressive methodology is adopted in which new elements are coupled into the basic model. Improvement on predictions of suspended concentrations is verified after the inclusion of each new factor. The initial model is enriched with: spatial variability of grain sizes, dynamics of cohesive

materials, spatial and temporal variations of bed roughness, seasonal variation of cohesive parameters and restriction of sediment supply over areas where the EHL has outcropped. Finally, the results of the sediment model are visualized across the entire domain at characteristic phases of the tidal cycle as well as at different stages along the neap-spring cycle where the different seasonal behavior is observed.

This chapter is presented in seven sections. In section 1, the importance of calibration and validation of the sediment transport model before any practical application is stated. Section 2 comprises the materials and datasets used in the study. Section 3 presents the methodology used to calibrate and validate the sediment transport model. Sections 4, 5 and 6 present the results and accuracy of the proposed sediment transport model. Section 7 summarizes the main aspects considered in this chapter.

6.2 Measurement of suspended sediment concentrations

Different measuring techniques were used to obtain the suspended sediment concentrations in several campaigns developed in the Suederpiep, Norderpiep and Piep tidal channels. Field measurements were performed in the year 2000 at different stages of the neap-spring cycle (PROMORPH project). The tidal ranges varied between 2.3m and 4.2m. Each campaign lasted a full tidal cycle, on which continuous measurements were performed. Both, direct and indirect techniques (e.g. mechanical sampling and optical devices) were used in the field to assess the suspended concentrations. The accuracy of the optical device was verified against direct mechanical sampling and an estimated relative error of about 30% was found [Poerbandono, 2003].

6.2.1 Measuring techniques

Techniques for measuring sediment concentration in suspension can be based on mechanical, optical or acoustical principles. In this study, data from the two first techniques are regarded. A comprehensive discussion on these topics can be found in Wren et al. [2000].

6.2.1.1 Mechanical sampling

Mechanical sampling is the direct way to obtain suspended sediment concentrations and therefore the most reliable method available. Mechanical samplers can be classified into two main categories: discrete and continuous samplers, according to their ability to measure the suspended concentrations along

time. Bottle samplers and pump samplers are representative examples of discrete and continuous samplers respectively. Both have the same working principle in the collection of water samples, which are filtered for suspended particles. These are then weighed to define the relative proportion to the water volume.

Figure 6.1 shows the sampler device (Niskin bottle modified) used in the measurement campaign by Poerbandono [2003]. It only allows an instantaneous or discrete measurement and therefore, several samples need to be taken along the tidal cycle to describe the temporal behavior of the sediment concentration. The Niskin bottle sampler is a cylinder-shaped device with a two liter volume.

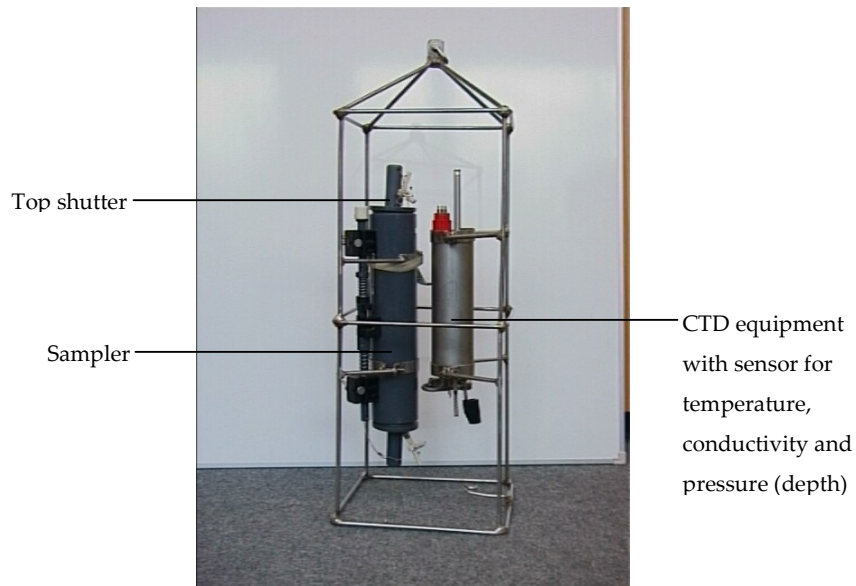


Figure 6.1 Sampler mounted with CTD equipment

6.2.1.2 Optical sampling

Optical sampling is an indirect technique to determine suspended sediment concentrations by means of an optical beam transmission. This device is comprised of a transmitter and light detector, from which light signals are sent and received through the water media (see Figure 6.2). The difference between the transmitted and received optical signal corresponds to the scattering and absorption of the light beam due to the existence of suspended materials. Therefore, higher differences will be associated with large suspended concentrations and vice versa.

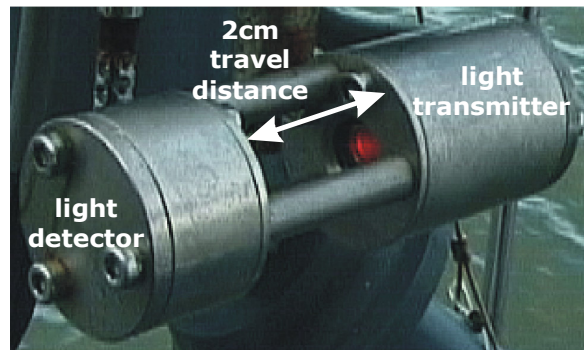


Figure 6.2 Optical beam transmissometer

The optical beam transmissometer measures the voltages from the light intensity that reach the light detector. To convert this optical transmission to suspended sediment concentrations a calibration curve is required. This curve can be determined through the adjustment of simultaneous measurements from optical and mechanical devices. The general calibration curve is given by Holdaway et al. [1999]:

$$c = \frac{1}{k_2} \ln \left(\frac{k_1}{I} \right) \quad (6.1)$$

Where:

c : suspended sediment concentration

I : optical transmission

K_1, k_2 : calibration constants

6.2.2 Field campaign

The field data used in the calibration and validation of the sediment transport model was obtained in March, June, September and December 2000 within the framework of the research project PROMORPH. Measurements were carried out along three transects located in Norderpiep (T1), Suederpiep (T2) and Piep (T3) tidal channels as shown in Figure 6.3. These three transects were 770 m, 2040m, and 1200m long respectively [Winter et al., 2005].

Several stations separated from one another about 180m were defined on each transect. Hence the number of measuring stations in cross-sections T1, T2 and T3 were 4, 10 to 12, and 6 to 7 respectively as indicated with the vertical red lines on Figure 6.4. Deployments of mechanical and optical devices were performed at each station from a vessel that was moving back and forth over the cross-section throughout entire tidal cycles. Further details about the field data considered in this study are given in Table 6.1.

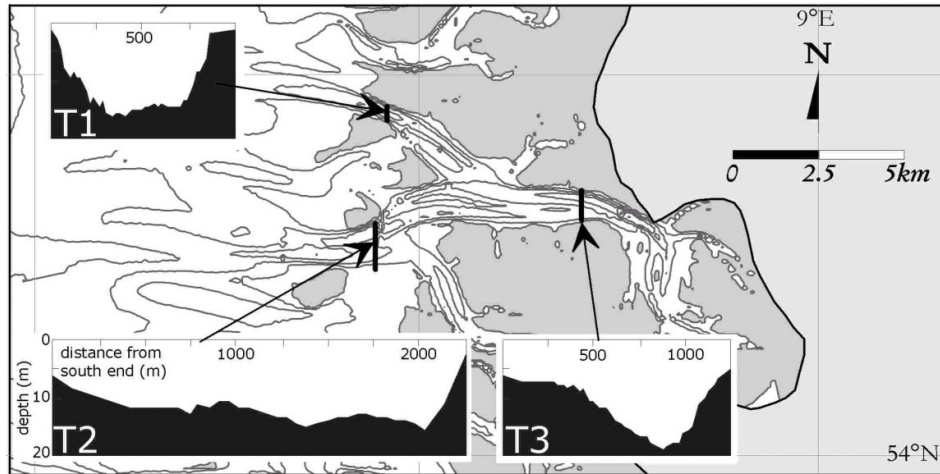


Figure 6.3 Measuring transects in the tidal channels of the Dithmarschen Bight
[Poerbandono, 2003]

Table 6.1: Datasets of suspended sediment concentration [Poerbandono, 2003]

Measuring campaign	Date	Tidal range (m)	Cross section	Stations	Dur. (hours)	Max. conc. Depth-avg Kg/m ³	Min. conc. Depth-avg Kg/m ³
March, 2000	22	3.8	T1	4	12 :00	0.20	0.09
	21	3.8	T2	10	11 :55	0.55	0.11
	23	3.7	T3	6	13 :04	0.40	0.11
Jun, 2000	5	4.0	T1	4	6 :36	0.19	0.05
	5	4.1	T2	12	8 :26	0.26	0.06
	6	4.2	T3	7	8 :12	0.34	0.06
Sept., 2000	5	3.1	T1	4	10 :28	0.10	0.04
	5	3.1	T2	12	9 :54	0.26	0.06
	6	2.5	T3	7	10 :47	0.33	0.07
Sept., 2000	12	3.2	T1	4	11:38	0.19	0.05
	12	3.2	T2	10	10:59	0.42	0.06
	13	3.4	T3	7	4:34	0.30	0.07
Dec., 2000	5	2.3	T1	4	5:33	0.12	0.07
	5	2.3	T2	10	10:50	0.28	0.06
	6	2.4	T3	6	12:06	0.20	0.07

6.2.3 Sediment concentration profiles

In order to compare measured and modeled suspended sediment concentrations, the observations are integrated along the depth to fit the 2DH model output. Hence, measured concentration profiles were integrated according to the following equation:

$$c = \frac{1}{h-a} \int_a^h c(z) dz \quad (6.2)$$

$c(z)$ was not directly determined in the field. Instead, point concentrations at 1m above the bottom and vertical profiles of light transmission $I(z)$ were measured through mechanical samplers and optical devices respectively.

Then, a calibration curve was used for converting the optical transmission $I(z)$ into concentrations $c(z)$. The calibration constants k_1 and k_2 from equation 6.1 were determined by Poerbandono [2003] on the basis of 225 simultaneous measurements of optical transmissions and direct sampling. Measurements were carried out in T1, T2, and T3 in the year 2000. The resulting calibration curve is given by:

$$c = \frac{1}{2.86} \ln\left(\frac{110}{I}\right) \quad (6.3)$$

Equation 6.3 is used to convert optical transmission $I(z)$ into suspended concentrations profiles $c(z)$, which extend down from the free surface to about 0.25m above the bottom. Technical reasons restricted the optical device to access the lowest near-bed layer. This restriction is due to the separation distance between the optical transmissometer and the protective frame mounted below the device (see Fig. 6.1). Hence, to estimate the complete concentration profile $c(z)$ an extrapolation approach based on the last three lowest measurements [van Rijn, 1993] was used:

$$c_e = e^{az_e+b} \quad (6.4)$$

Where: c_e is the extrapolated concentration, z_e is the height above the sea bed and a, b are the slope and intercept of the regression line: $\ln(c) = az + b$, which is obtained from the three lowest measurements.

The aforementioned approach was used to process all data obtained from the optical device into depth averaged concentrations. Cross-sectional distributions of suspended materials at T1, T2 and T3 in March 21 to 23, 2000, is shown in Figure 6.4. Intermediate values of suspended concentrations were determined by interpolation between the observed values at the measuring stations, which are indicated by red lines on the figures.

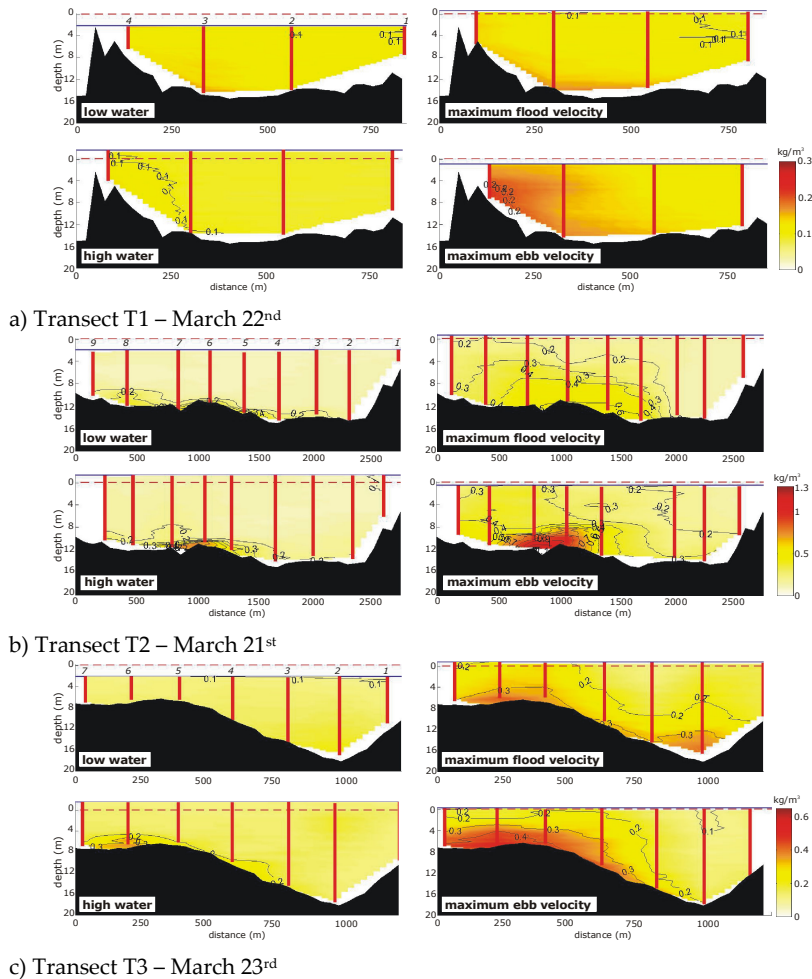


Figure 6.4 Cross-sectional variations of measured concentration [Poerbandono, 2005]

The results reveal that the distributions of suspended material concentration are fairly uniform, particularly over the cross-section T1 and at slack waters. Resuspension of the seabed material is clearly evident during maximum flood and ebb currents, leading to non-uniform variations of these quantities over some parts of cross-sections T2 and T3.

6.3 Calibration of the sediment transport model

The sediment transport numerical model was calibrated on the basis of field measurements performed in March and December 2000 (see Table 6.1). Measurements corresponded to spring and neap cycles with tidal ranges of about

3.7m and 2.3m respectively. As the Dithmarschen Bight has a mean tidal range of about 3.2m, it can be said that the calibration study covered two extreme cases under calm weather conditions.

Field observations have shown an increasing variation in tidal ranges, mean velocities, suspended sediment rates, etc. from neap to spring stages. This trend might be explained largely by the variation of the tidal gravitational force, which is the main driving force affecting hydrodynamics in the study area. Other parameters such as bedform dimensions, roughness and properties of cohesive materials (settling velocity, erosion rate, and critical shear stresses) seem to present a non-stationary behavior as well. This fact is not fully proven yet due to field data scarcity, although theoretical reasoning and its positive effect on the accuracy of the sediment model supports its certainty. However, it is pointed out that this favorable effect is negligible with respect to the flow model since water levels and depth-averaged velocities are only slightly affected.

Given the large number of input parameters showing non-stationary behavior, a so-called non-stationary calibration process is carried out. The calibration process is divided in two parts, e.g. spring and neap stages, where the input parameters are independently determined for each case. The parameters for spring and neap stage would be tied to a tidal range of 3.7m and 2.3m respectively. These two settings of parameters are then used to determine the input settings for any other tidal condition by means of interpolation or extrapolation methods. Since, it is assumed a linear variation of the input parameters with the tidal range.

As the calibration approach intends to define the input parameters as a function of the tidal range which is time dependant, hence, it is here called this approach a non-stationary calibration.

6.3.1 Calibration at spring tide

The spring tide occurs around New and Full Moon when the Sun, Moon and Earth form a line, the tidal forces due to the Sun reinforce those due to the Moon. As a consequence the tidal range is then at its maximum. Therefore, spring tides result in high and low waters that are higher and lower than average. Also, slack water periods are shorter and currents are stronger than average.

Field measurements on spring tidal cycles from March 21 to 23, 2000 provided a large set of suspended sediment concentration data at 20 measuring stations over the cross-sections T1, T2, and T3 (see Figs. 6.3 and 6.4), used for the calibration process. Measured and modeled results were spatially and temporally compared to determine the best setting of physical parameters that might appropriately predict the suspended sediment concentrations in the Dithmarschen Bight during spring conditions.

All parameters showing high influence on sediment concentrations are included in the calibration study (see sensitivity analysis in section 5.4). Exception is made for the specific density that was set according to field observations (2650 kg/m^3). The 1st round of parameter values for which simulations were run are shown in Table 6.2, where bold values correspond to the basic setting established. As only one parameter was changed per simulation, the other parameters were fixed in agreement with the basic setting.

Considering a typical calibration, in which input parameters are specified uniformly over the whole area (actual values in nature are unknown) and tuned until the simulation results match an observed data set within a prescribed accuracy interval, it can be said that an atypical calibration was carried out for the mean grain sizes and flow resistance parameters given their spatial variability.

Excluding these two variables, all others are handled as uniform values throughout the study area. To perform the calibration for bed resistance coefficients four alternatives were verified: a) the k_s map computed for the actual spring cycle, when shear stresses were 80% of the maximum value; b) the k_s map computed for the actual spring cycle, when shear stresses were at the maximum value, which fits the recommended RFC; c) the k_s map computed deliberately for a neap tidal cycle. This case is intended as an indirect verification of the seasonal variation of the bed roughness and its effect on suspended concentrations; and d) the k_s map computed assuming a constant Chezy coefficient of $60 \text{ m}^{1/2}/\text{s}$. The k_s maps for cases a, b, and c are defined according to the methodology indicated in section 4.3.

Regarding the mean grain sizes only two alternatives were assessed: a) Spatial variation of grain sizes d_{50} according to equation 3.3, and b) uniform d_{50} value equal to $100 \mu\text{m}$ over the entire study area.

Table 6.2: Calibration of physical parameters at spring tide

Parameter	Symbol (units)	Choice
Effective bed roughness	k_s or C	k_s map for spring case ($\alpha/\alpha_{max}=80\%$) k_s map for spring case ($\alpha/\alpha_{max}=100\%$) k_s map for neap case Chezy coefficient of 60 m ^{1/2} /s
Grain size	d_{50}	d_{50} map from eq. 3.3 100 μ m(cte.)
Settling velocity (cohesive sediments)	w_s (mm/s)	1.3 2.0 2.6 4
Critical erosion shear stress (cohesive sediments)	$\tau_{cr,e}$ (N/m ²)	0.65 0.89 1.10
Critical sedimentation shear stress (cohesive sediments)	$\tau_{cr,d}$ (N/m ²)	1.40 2.15 2.88 3.60
Sediment erosion rate coef. (cohesive sediments)	M (kg/m ² /s)	0.00047 0.00063 0.00079
Cohesive fraction	MC (%)	20 25 30 35

After the first calibration round is completed, the best setting of parameter values that lead to the best agreement between modeled and measured suspended concentrations is achieved. The model performance is assessed in terms of the Relative Mean Absolute Error (RMAE) criterion for each combination of setting parameters. When the best setting does not coincide entirely with the basic setting originally established (as in the example shown on Table 6.3), a new calibration round is performed after first adjusting the basic setting to the best setting found in the preceding round.

Hence, the basic setting for the second calibration round is: $w_s = 1.3$ mm/s (instead of 2 mm/s used in the first calibration); $\tau_{cr,e} = 0.89$ N/m²; $\tau_{cr,s} = 2.88$ N/m²; $M = 0.00063$ kg/m²/s; Fine content = 25%; K_s : computed for the actual spring cycle and using the maximum shear stresses; d_{50} : variable in space as defined from eq. 3.3.

Table 6.3: Performance assessment of numerical model after first calibration round

Parameter	Choice	RMAE
Effective bed roughness	k_s map for spring case ($\tau/\tau_{max}=80\%$)	0.48
	k_s map for spring case ($\tau/\tau_{max}=100\%$)	0.42*
	k_s map for neap case	0.50
	Chezy coefficient of 60 m ^{1/2} /s	0.77
Grain size	d_{50} map from eq. 3.3	0.48*
	100 μm (cte.)	0.50
Settling velocity (cohesive sediments) [mm/s]	1.3	0.47*
	2.0	0.48
	2.6	0.51
	4	0.59
Critical erosion shear stress (cohesive sediments) [N/m ²]	0.65	0.60
	0.89	0.48*
	1.10	0.52
Critical sedimentation shear stress (cohesive sediments) [N/m ²]	1.40	0.60
	2.15	0.50
	2.88	0.48*
	3.60	0.48
Sediment erosion rate coef. (cohesive sediments) [kg/m ² /s]	0.00047	0.50
	0.00063	0.48*
	0.00079	0.52
Cohesive fraction [%]	20	0.50
	25	0.48*
	30	0.49
	35	0.53

Notes: Bold values represent the basic setting and the sign (*) identifies the best setting at the initial calibration round

Then, an iterative procedure is performed until a round where a total agreement between the basic and the best setting is reached. After each calibration round is completed, the range of variation of each parameter is refined in order to tune the best possible setting. Table 6.4 presents the final, or best, parameter setting found in the spring cycle, from which the overall RMAE estimated in terms of the depth-averaged suspended sediment concentrations was about 42%. For cross sections T1, T2 and T3 the RMAE were 38%, 46%, 39% respectively.

Table 6.4: Best parameter settings at spring tidal cycle

Parameter	Best adjusted values
Effective bed roughness	k_s map for spring case ($\tau/\tau_{max}=100\%$)
Grain size	d_{50} map from eq. 3.3
Settling velocity (mud)	1.8 mm/s
Critical erosion shear stress (mud)	0.9 N/m ²
Critical sedimentation shear stress (mud)	3.15 N/m ²
Sediment erosion rate coef. (mud)	5.1E-4 kg/m ² /s
Mud content	22 %

Note: mud is the term used for fine cohesive materials.

6.3.2 Calibration at neap tide

Opposite to the spring tide referred above, the neap tide occurs when the Moon is at first quarter or third quarter. Hence, the Sun and Moon are at 90° to one another and the forces due to the Sun partially cancel out those due to the Moon. At these points in the lunar cycle, the tide range is at its minimum, so that neap tides result in less extreme tidal conditions.

The calibration process at the neap stage was performed according to the methodology previously described for the spring tide. The assisting field campaign was carried out at the neap tidal cycle occurring on December 5th and 6th, 2000, and the suspended sediment concentrations were measured at almost the same monitoring stations chosen for the spring case. Final results for this calibration process are summarized in Table 6.5, where a comparison between the best settings found at neap and spring tidal conditions is displayed. The model accuracy under neap conditions turned out an overall RMAE of about 49% in terms of the depth-averaged suspended sediment concentrations. For cross sections T1, T2 and T3 the RMAE were 62%, 41%, 51% respectively.

Noteworthy is the ability of the sediment model to reproduce the suspended sediment concentrations (RMAE values between 0.5 and 1 or less are usually considered as excellent) as well as the homogeneity of the discrepancies (all stations) which remain close to 0.5 despite the diverse forcing conditions.

Table 6.5: Best calibration settings at neap and spring tidal cycles

Parameter	Setting for neap tide	Setting for spring tide
Effective bed roughness	k_s map for neap case ($\tau/\tau_{max}=100\%$)	k_s map for spring case ($\tau/\tau_{max}=100\%$)
Grain size	d_{50} map from eq. 3.3	d_{50} map from eq. 3.3
Sediment density (sand)	2650 kg/m ³	2650 kg/m ³
Sediment density (fines)	1800 kg/m ³	1800 kg/m ³
Settling velocity (fines)	1.3 mm/s	1.8 mm/s
Critical erosion shear stress (fines)	0.65 N/m ²	0.9 N/m ²
Critical sedimentation shear stress (fines)	2.88 N/m ²	3.15 N/m ²
Sediment erosion rate (fines)	6.3E-4 kg/m ² /s	5.1E-4 kg/m ² /s
Cohesive fraction	25 %	22 %

Future investigations including wave effects on the current sediment model might not improve the above accuracy results by much, as the ratio H_s/h is generally low for the measuring stations considered, all located in the deep tidal channels. Nevertheless, it is pointed out that western sand banks might be greatly affected by waves, as is denoted by the maximum orbital velocities in Fig. 3.16. Further improvements should involve measurements of sediment transport rates across the sand banks to determine the relevance of wave processes in their dynamics.

The calibrated values shown in Table 6.5 have been defined through a numerical process where model accuracy reasons prevail. To verify whether those values correspond or not to the real case, comparisons between the calibrated and reported values (laboratory, field measurements, models, etc.) by different authors are shown in Table 6.6 for relevant cohesive parameters. Generally, the calibrated values for relevant cohesive properties lie inside the range of reported values in different investigations. Hence, certain confidence in the numerical approach has been gained. However, the critical deposition shear stress obtained through the model calibration process exceeds the critical erosion shear stress. This result contradicts the classical cohesive sediment paradigm i.e. deposition and erosion are mutually exclusive. In spite of the latter, the sediment transport model reproduces the observed concentrations better when uses relative high values of the critical deposition shear stress. Several studies have shown similar conclusions that also contradict this paradigm such as Sanford and Halka [1993], Winterwerp [2003] and Chan et al. [2006].

Table 6.6: Variation range of cohesive input parameters

Parameter	Calibrated values	Range of variation from relevant cohesive parameters
Settling Velocity	1.3 -1.8 mm/s	$w_s < 3$ mm/s [Interagency report No. 12, 1957] $w_s < 2.5$ mm/s for the Severn [Thorn, 1982] $w_s = 0.5$ mm/s in the Friesche Zeegat [van Ledden, 2006] $w_s < 0.7$ mm/s in the Western Scheldt [Winterwerp, 1991]
Critical erosion shear stress	0.65 -0.9 N/m ²	$\tau_{cr,e} = 0.5$ N/m ² in the Friesche Zeegat [van Ledden, 2006] $0.1 < \tau_{cr,e} < 5$ N/m ² [Briaud, 2004] $0.36 < \tau_{cr,e} < 2.4$ N/m ² in the Wadden Sea [Mahatma, 2004] $1.5 < \tau_{cr,e} < 2$ N/m ² [Jacoub, 2002]
Critical deposition shear stress	2.88 -3.15 N/m ²	$\tau_{cr,s} = 0.15$ N/m ² in the Friesche Zeegat [van Ledden, 2006] $0.25 < \tau_{cr,s} < 0.5$ N/m ² [Jacoub, 2002] $0.12 < \tau_{cr,s} < 0.52$ N/m ² in Lake Okeechobee [Hwang, 1989] $\tau_{cr,s} = 0.2$ N/m ² in the Western Scheldt [Winterwerp, 1991] $0.3 < \tau_{cr,s} < 0.5$ N/m ² in the Gironde [Li et al., 1994]
Erosion rate coefficient	5.1E-4 – 6.3E-4 Kg/m ² s	$M = 1E-4$ Kg/m ² s in the Friesche Zeegat [van Ledden, 2006] $5.1E-4 < M < 10.9E-4$ Kg/m ² s derived from Mahatma[2004] $0.1E-4 < M < 4 E-4$ Kg/m ² s [van Rijn, 1989]
Mud content	22-25%	$25 < \text{Mud} < 50\%$ in the Friesche Zeegat [van Ledden, 2006] $15 < \text{Mud} < 60\%$ in the Wadden Sea [Mahatma, 2004] $5 < \text{Mud} < 80\%$ in the Dithmarschen [Poerbandono, 2005]

Figures 6.5 to 6.7 present the comparison between measured and modeled suspended concentrations at each of the 20 stations surveyed during a spring tide. The monitoring stations are numbered as an increasing sequence from south to north at the corresponding cross sections T1, T2, and T3. The location of transects T1, T2, and T3 is shown in Figure 6.3 while the position of the monitoring stations inside the transects is indicated in Figure 6.4. The corresponding water levels for the simulation period are shown in Figure 6.11.

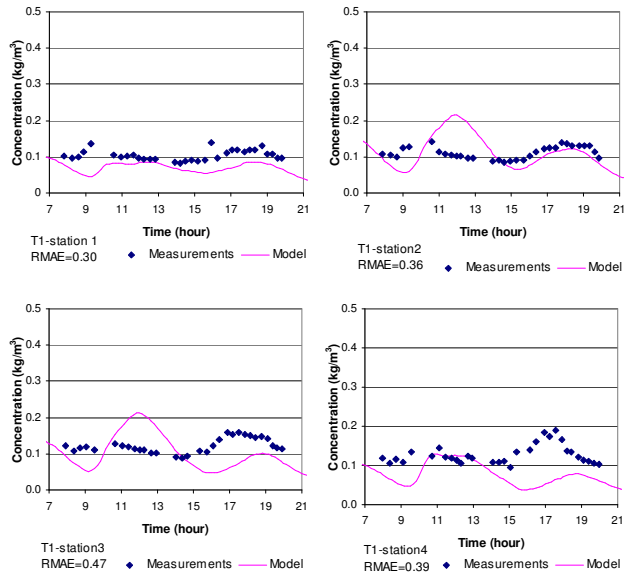


Figure 6.5 Suspended concentrations at spring tidal cycle (Transect T1, March 22)

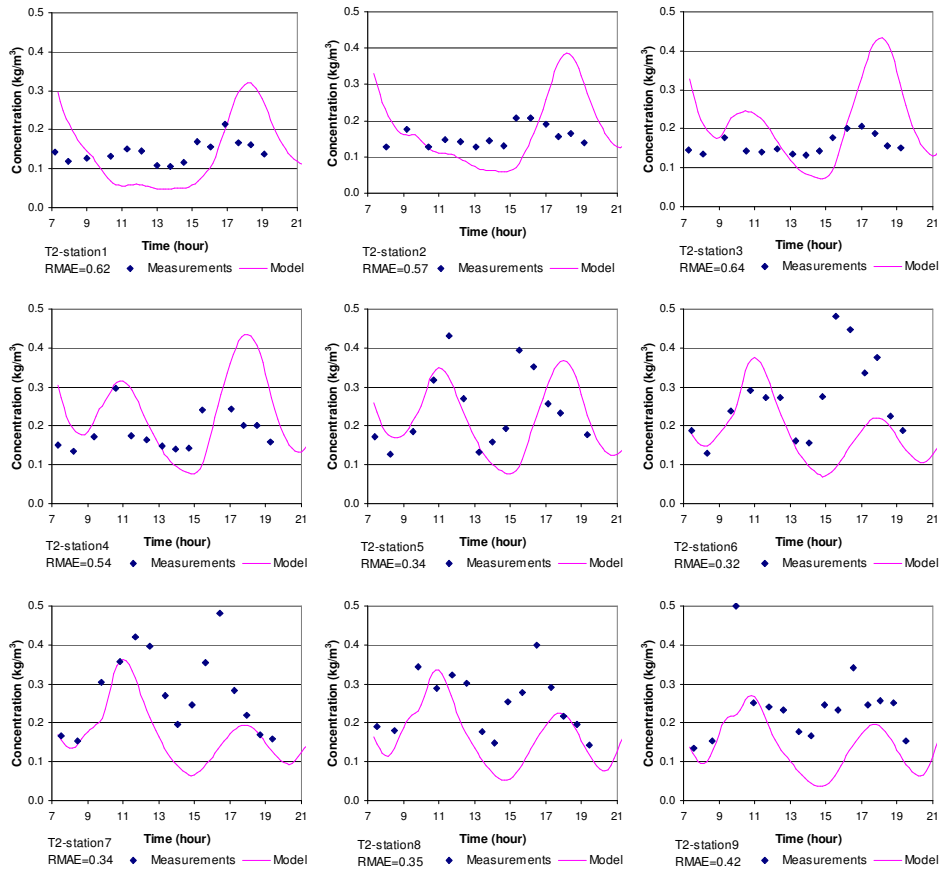


Figure 6.6 Suspended concentrations at spring tidal cycle (Transect T2, March 21)

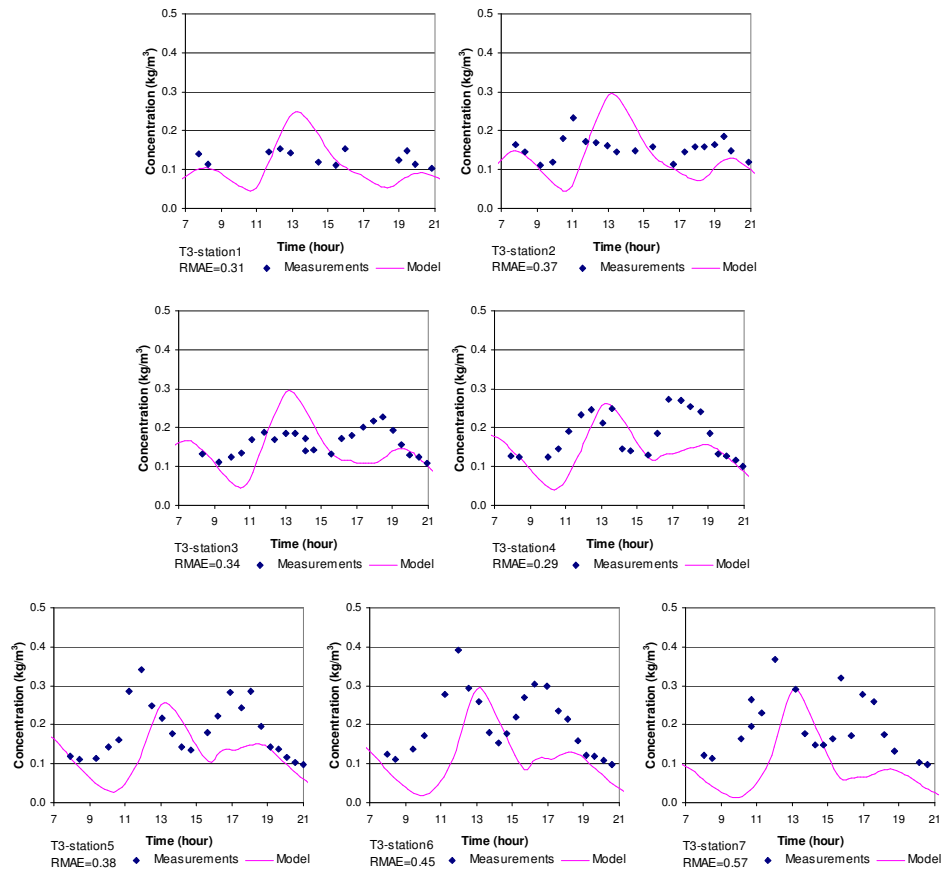


Figure 6.7 Suspended concentrations at spring tidal cycle (Transect T3, March 23)

Figures 6.8 to 6.10 present the comparison between measured and modeled suspended concentrations at each of the 20 stations surveyed in December 2000 for a neap tide. The locations of the monitoring stations correspond largely to those considered above in the spring tidal cycle. Therefore, the monitoring stations are increasingly numbered from south to north at the corresponding transects T1, T2, and T3 as displayed in Figures 6.3 and 6.4. The corresponding water levels for the simulation period are shown in Figure 6.12.

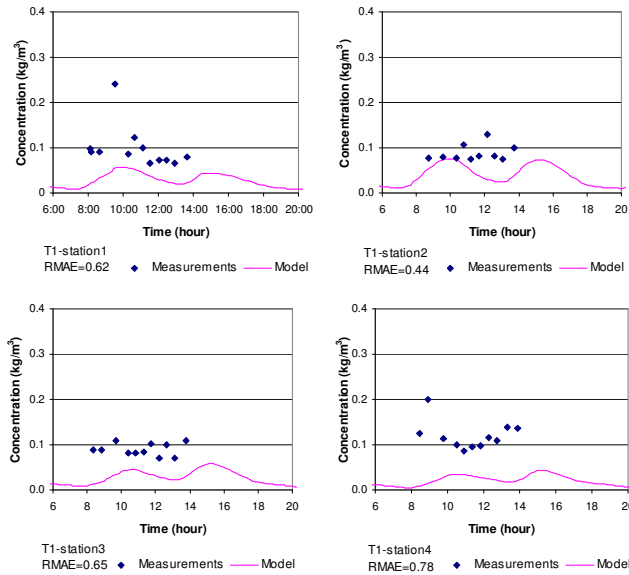


Figure 6.8 Suspended concentrations at neap tidal cycle (Transect T1, December 5)

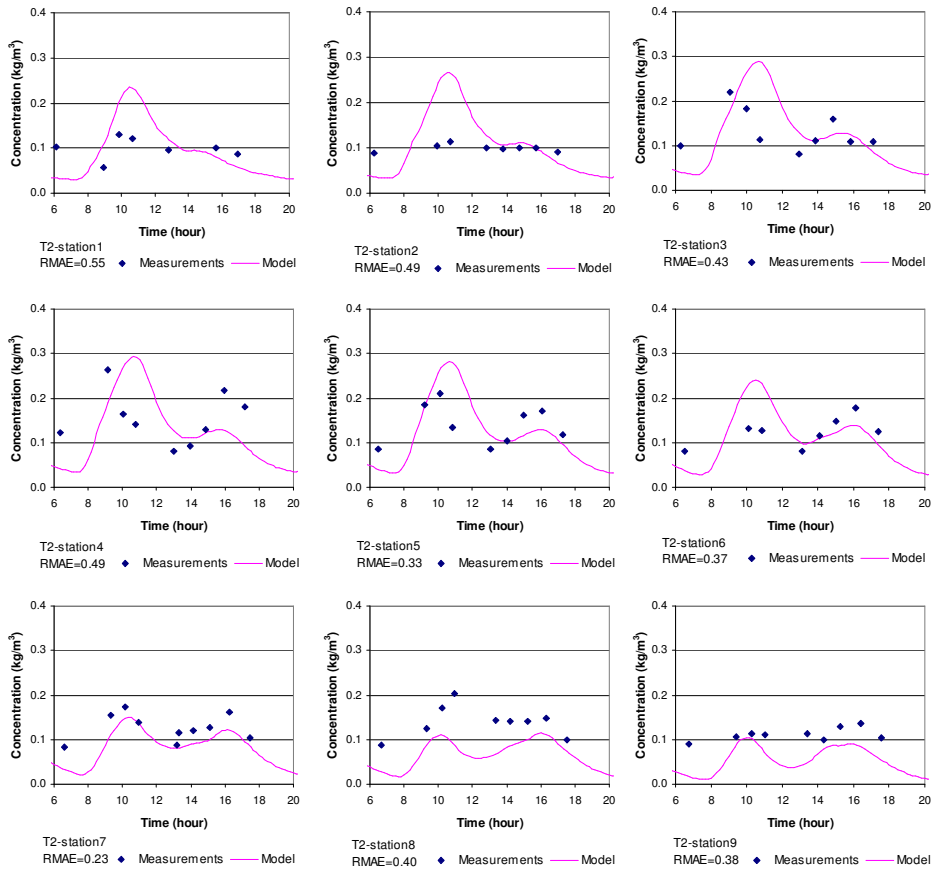


Figure 6.9 Suspended concentrations at neap tidal cycle (Transect T2, December 5)

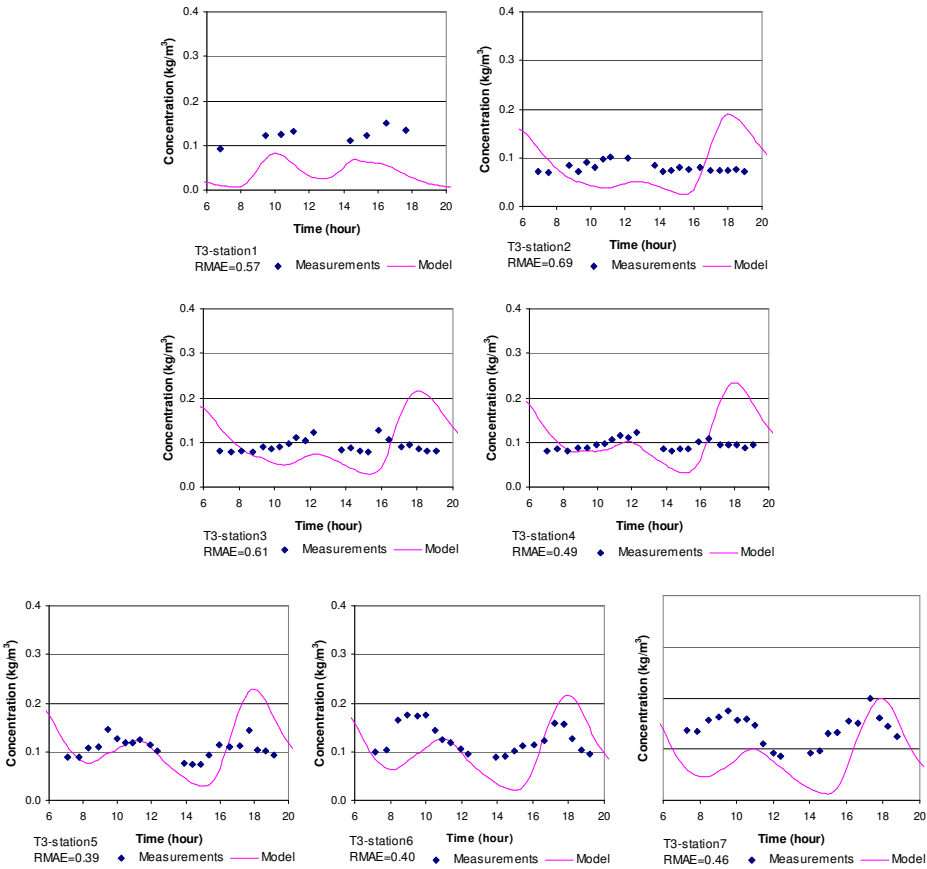


Figure 6.10 Suspended concentrations at neap tidal cycle (Transect T3, December 6)

Despite the excellent agreement between observations and measurements of suspended sediment concentrations which is remarked by the low RMAE obtained on each measuring station (see Figs. 6.5 to 6.10), it is pointed out about some modeling drawbacks: (a) there is a lag-phase between observations and predictions of suspended concentrations. This disagreement is mainly due to the inaccuracies from the hydrodynamics input which present lag-phases of the same magnitude order than those observed in the sediment transport model. Water level forcing in the Dithmarschen Bight has been obtained through a nesting process (see section 5.2.2.3) and the lag-phases between water level observations and predictions range from 30 to 60 minutes. Figure 6.11 and 6.12 shows the observed and computed water level at Büsum station (located near the transect T3) during the spring (March, 2000) and neap (December, 2000) calibration periods respectively. Additionally, it is noticed that equilibrium transport formulations have been adopted to estimate the amount of sediment entering and leaving the coastal area. The latter implies an instantaneous response of suspended sediment to local hydrodynamics along the open sea boundaries which is inaccurate (see Fig. 5.5) and might have also some

influence on the lag-phase discrepancies; (b) in transect T3 (Located in the Piep channel) the sediment transport model under predicts suspended peak concentrations at ebb phase for the spring tidal cycle considered (see Fig. 6.7). These inaccuracies might be due to the lack of information about the cohesive properties at the study area which at the present have been set uniform over the entire region disregarding their spatial variation; (c) There is a trend to underpredict background concentrations. Though, it is notorious the improvement achieved in the prediction of these concentrations after including the cohesive transport module into the modelling system (see section 6.5).

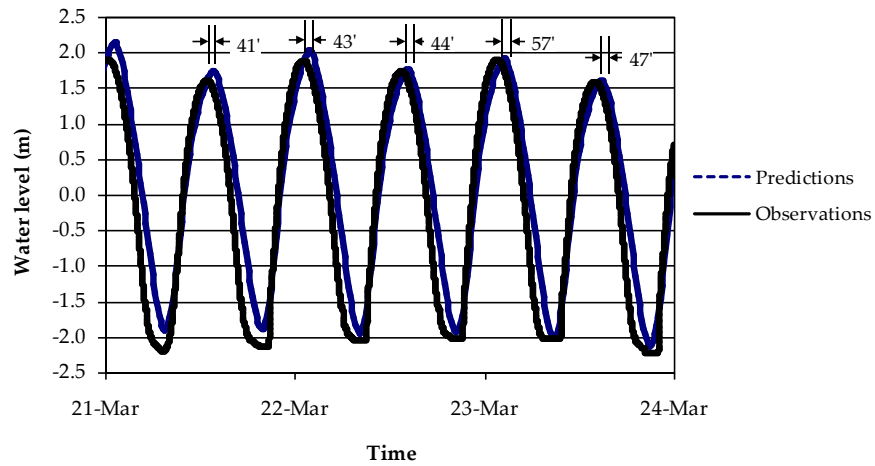


Figure 6.11 Water level lag-phases at spring tidal cycle (Büsum station)

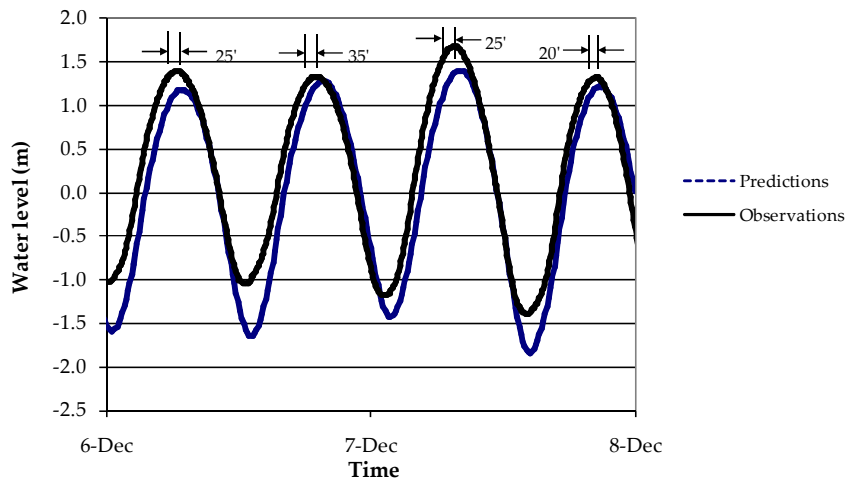


Figure 6.12 Water level lag-phases at neap tidal cycle (Büsum station)

6.4 Validation of the sediment transport model

The validation of the sediment model was performed for tidal cycles occurring during June 5-6, September 5-6, and September 12-13, 2000. The tidal ranges were around 4.2m, 2.9m and 3.3m respectively. The tidal cycles in September were very close to the mean tidal range of about 3.2m and the tidal cycle in June corresponded to one spring cycle. The tidal cycles selected for the validation corresponded to tidal range values differing from those considered in the calibration study. The two model settings found in the calibration study for spring and neap tides should be adjusted for the particular tidal cycles considered in the validation process. Since, it is assumed that some input parameters present a seasonal variation along the neap-spring cycle. Thus, a methodology to design the validation study in terms of the calibrated settings is hereafter presented. Some remarks about the seasonal behavior of several parameters and their physical sense are also noted.

From the numerical point of view it is clear that at least two different settings of physical parameters fit well the sediment dynamic model in the Dithmarschen Bight (see Table 6.5). As both settings were defined at different tidal conditions (neap – spring), it is herein suggested that these parameters vary through the neap-spring cycle due to natural reasons that are proven by the numerical procedure. The seasonal variation in each of the concerned physical parameters is supported mostly by the hypothesis that the neap-spring cycle runs parallel to a deposition-erosion cycle, as is explained next.

The time period from spring to neap stages implies a reduction in tidal ranges, current velocities and turbulence intensities, which, together with longer slack water intervals, favor the deposition of suspended materials. Hence, settling of fine particles creates fresh mud deposits remaining on the bottom due to low current velocities. As a logical consequence, the mud content increases over the bed surface layer while critical shear stresses and sediment erosion rates decrease and increase, respectively, due to the low cohesive forces within the not yet consolidated deposits.

Previous depositional behavior remains until the counter period from neap to spring starts bringing with it higher current velocities and shorter slack intervals. An erosive phase then begins where fresh mud deposits are removed due to their low critical shear stresses. The erosion process gradually uncovers a more consolidated layer of mud with higher critical shear stresses and lower sediment erosion rates. Based on this hypothesis, a temporal variability of mud content, critical shear stress and erosion rate parameters is suggested along the neap-spring cycle. The highest and lowest parameter values might occur at spring or neap tidal cycles when deposition and erosion phases begin. The numerical model captured this seasonal behavior by means of the two different settings found during the calibration process.

Moreover, given the seasonal variation of suspended sediment concentrations the settling velocity of cohesive materials is another physical parameter in which a temporal fluctuation along the neap-spring cycle is anticipated. Measurements in the Dithmarschen Bight show concentrations far higher at spring tide than those observed at neap tide (see Figs. 6.5 to 6.10). Mean concentrations show an increase of about 50% from neap to spring conditions affecting the settling velocity of cohesive sediments which can be assessed through the generally accepted formula:

$$w_s = kc^m \quad (6.5)$$

Where k and m are empirical variables.

As the exponent m varies over a wide range from 0.6 to 3.0, the settling velocities might be increased from neap to spring cycles within a range of 30% to 250% for a concentration change of about 50%. Results from the calibration study in Table 6.5 indicate an increase of settling velocities of about 38% from neap to spring tides. This result lies inside the possible range of variation determined by equation 6.5.

Keeping in mind the non-stationary behavior of some physical parameters, it was assumed that their variation through the neap-spring cycle could be related to the tidal range. The tidal range is one of the most characteristic variables over the neap-spring cycle keeping also a close connection with current velocities and shear stresses. Therefore, the input, or model settings, required to run the sediment model for a particular tidal cycle are defined according to its tidal range and the calibrated settings found for neap and spring tides (see Table 6.5). This process is carried out by means of an interpolation or extrapolation method as shown in Figure 6.13.

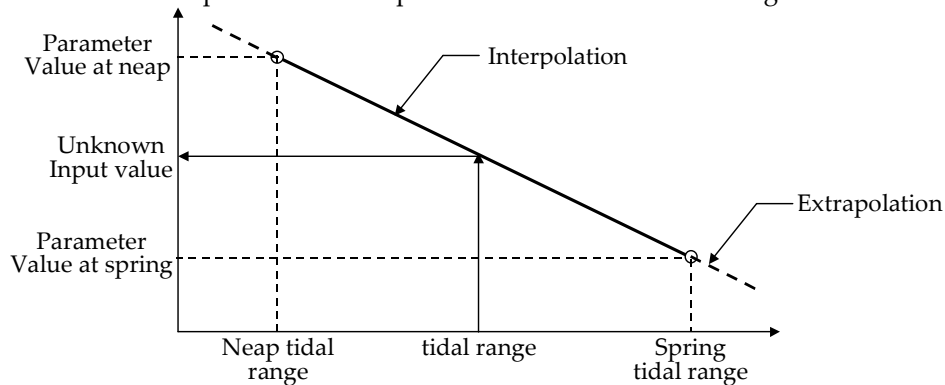


Figure 6.13 Definition of non-stationary physical parameters

Results from this approach, used to define the input settings for all validation cases in June and September 2000, is summarized in Table 6.7. This table displays the input parameter settings for the validation cases, where tidal ranges from Table 6.1 and parameter values from neap and spring conditions in Table 6.5 were used.

Table 6.7: Parameter settings for the validation study

Parameter	Tidal cycles on June 5-6, 2000	Tidal cycles on Sept. 5-6, 2000	Tidal cycles on Sept. 12-13, 2000
Settling velocity (fines)	2.0 mm/s	1.6 mm/s	1.76 mm/s
Critical erosion shear stress (fines)	1.0 N/m ²	0.79 N/m ²	0.88 N/m ²
Critical sedimentation shear stress (fines)	3.24 N/m ²	3.02 N/m ²	3.12 N/m ²
Sediment erosion rate (fines)	4.7 E-4 kg/m ² /s	5.7 E-4 kg/m ² /s	5.2 E-4 kg/m ² /s
Cohesive fraction	20%	23%	21.7%

Results of the sediment transport simulations with the above input settings were compared to measurements of suspended sediment concentrations at 20 stations located across the T1, T2, and T3 transects (see Figs. 6.3 and 6.4). The Relative Mean Absolute Errors (RMAE) of the discrepancies between observed and predicted concentrations are shown in Table 6.8.

A number of publications e.g. [Damgaard et al., 2001] consider that model performances may be assessed on the basis of the percentage of computed versus observed concentrations that range within a certain distance from the parity line. Usually, it is assumed that suspended concentrations with accuracy smaller than a factor 2 are very difficult to predict because of measurement errors. As a factor of 2 corresponds to RMAE values ranging from 0.5 to 1, it is concluded, therefore, that an excellent accomplishment for the sediment transport model was reached as RMAE values of about 0.48 and 0.53 were determined.

Table 6.8: Performance assessment of sediment model

Tidal cycle	RMAE			
	T1	T2	T3	All stations
June 5-6, 2000	0.57	0.55	0.48	0.53
Sept. 5-6, 2000	0.47	0.46	0.51	0.48
Sept. 12-13, 2000	0.61	0.38	0.63	0.51

6.5 Evolution of the sediment transport model

An evolutionary construction of the sediment model is highlighted in this section. The initial case was a plain model for non-cohesive sediments, uniform grain sizes and resistance coefficients. The sediment model was then improved through the spatial and temporal refinement of several input parameters as well as the inclusion

of geological features, like the EHL, restricting the sediment supply, and the dynamics of cohesive sediments.

Five cases are displayed through a chronological sequence that indicates the development of the sediment model. The establishment of each new case implies the refinement of the model in a particular aspect, from which benefits in terms of the model accuracy are verified by the RMAE criterion. A brief description for each of the five cases is presented next.

Case 1: The initial model, grain sizes are uniform and equal to 100 μm , Chezy resistance coefficients are set constant and equal to 60 $\text{m}^{1/2}/\text{s}$. Only dynamics of non-cohesive materials are considered.

Case 2: model for case 1 is modified by including a spatial distribution of grain sizes, which was determined from equation 3.3.

Case 3: model for case 2 is modified by including cohesive materials.

Case 4: model for case 3 is modified by including a spatial distribution of resistance coefficients, as was determined in chapter 4.

Case 5: model for case 4 is modified by including areas where the Dithmarscher Klei or EHL has outcropped (see Fig. 3.1) and the corresponding restrictions for sediment erosion are in effect.

Based on the discrepancies between observed and modelled suspended sediment concentrations, it can be deduced that the model accuracy was improved by about 50%. The inclusion of cohesive materials into the model might claim the largest contribution from the total improvement of about 25%. The second largest accuracy contribution of about 15% is due to the implementation of the methodology to determine the bed roughness (indicated in chapter IV). The restriction of sediment supply over areas where the EHL is exposed contributed to the remaining 10% of the model accuracy improvement. The accuracy improvement in the sediment model due to the grain size variation across the study area was negligible. This poor contribution can be basically attributed to the low fraction of sand material in suspension as well as the fact that all stations considered were located in the tidal channels where grain sorting due to waves exhibits less of an effect. The distributions of suspended sediment material at each cross section T1, T2 and T3 for the spring cycles on March 21 to 23, 2000 are shown in Figures 6.14 to 6.16.

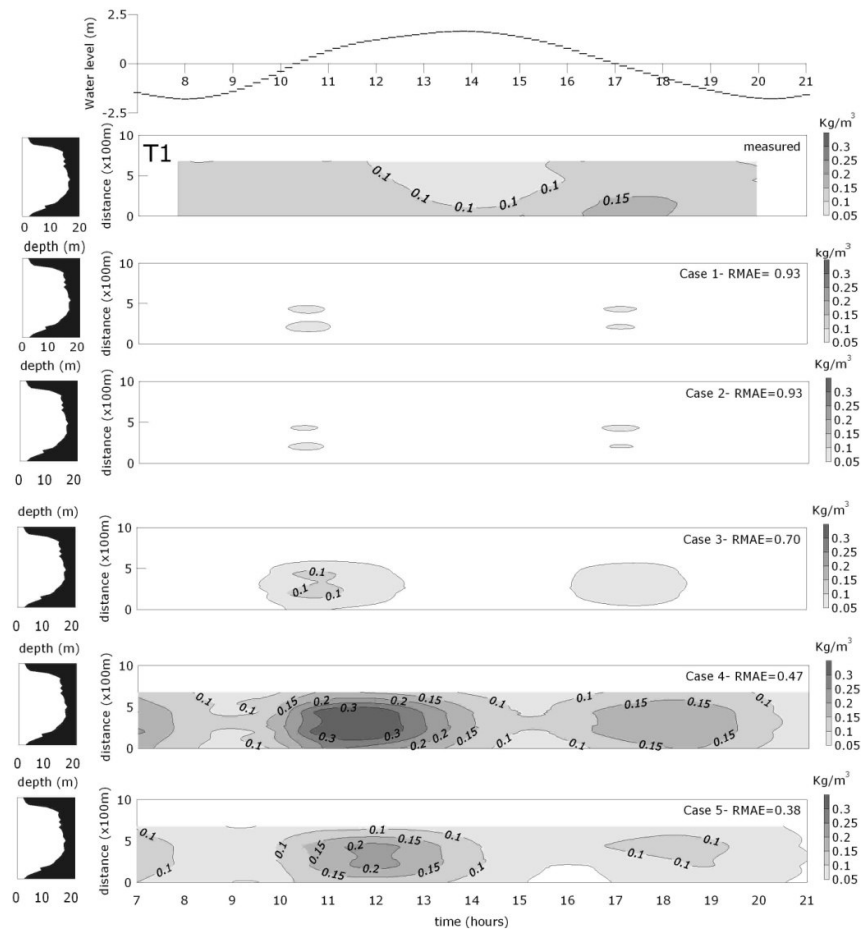


Figure 6.14 Depth-integrated suspended sediment concentrations at cross section T1 for the five cases considered on the evolution of the sediment transport model

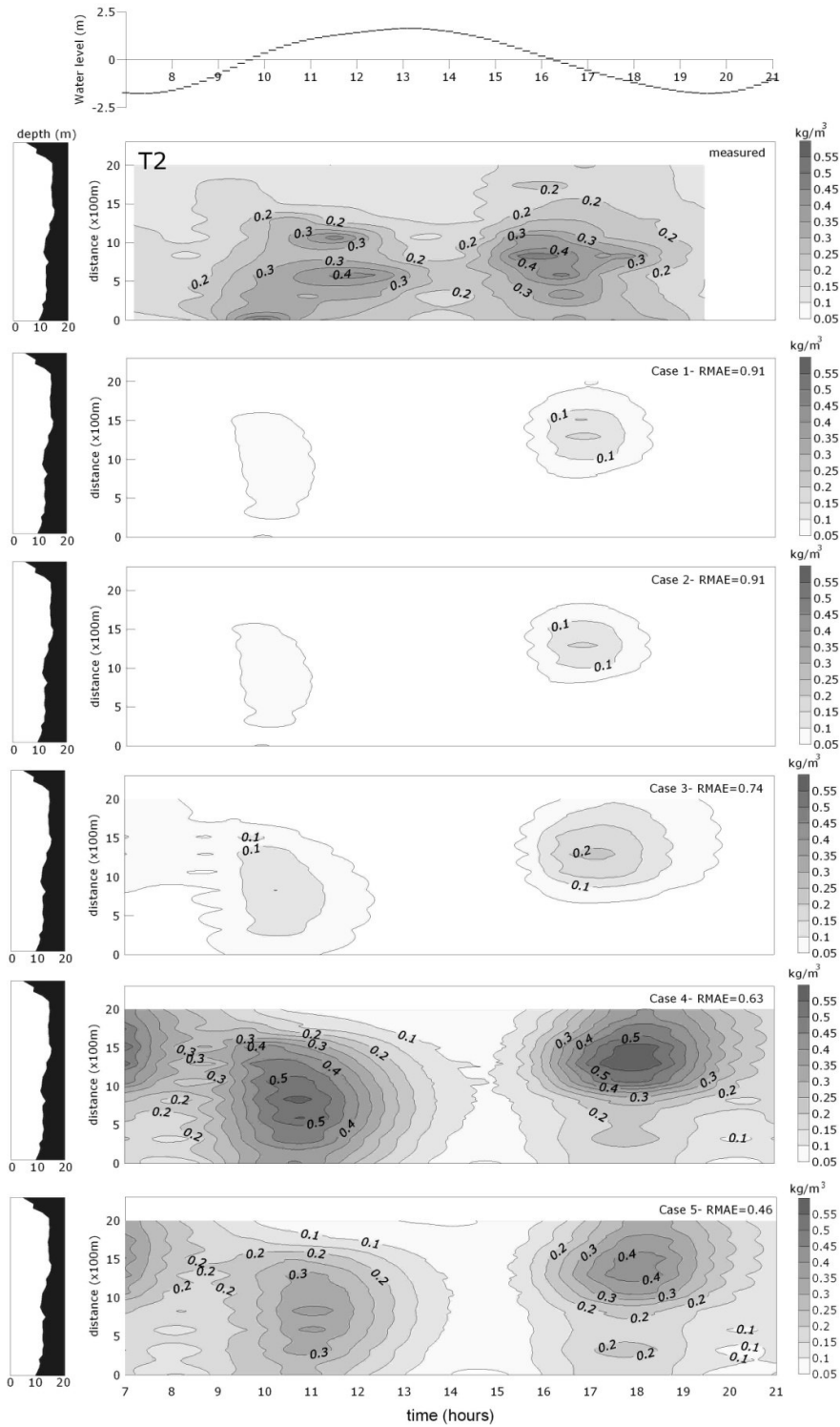


Figure 6.15 Depth-integrated suspended sediment concentrations at cross section T2 for the five cases considered on the evolution of the sediment transport model

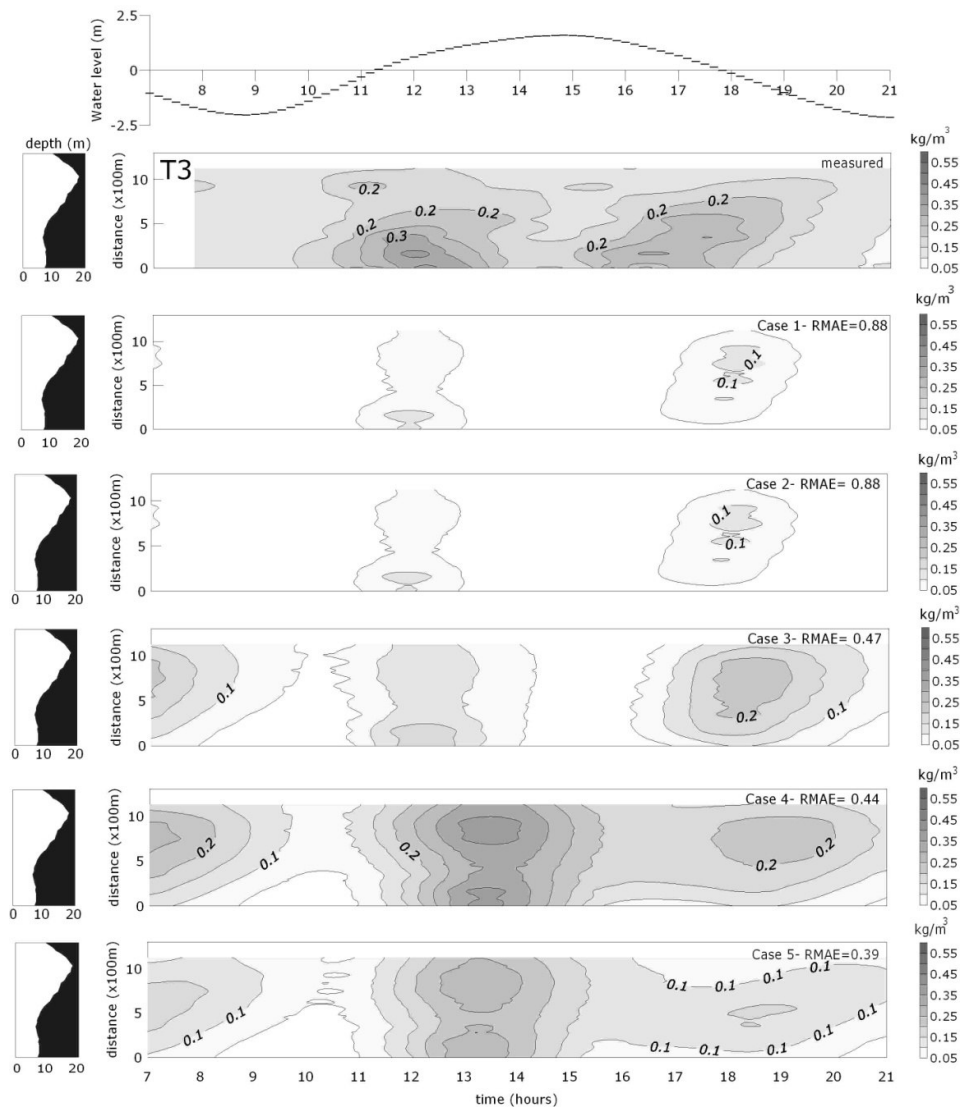


Figure 6.16 Depth-integrated suspended sediment concentrations at cross section T3 for the five cases considered on the evolution of the sediment transport model

Figures 6.17 to 6.19 show the distribution of bed load material at each cross section T1, T2 and T3 for the spring cycle on March 2000. Three cases are displayed through a chronological sequence as the analysis previously illustrated for suspended concentrations. The effect of the grain size spatial variability is neglected since all monitoring stations are located in the tidal channels and no variation of this parameter among the stations was observed (due to the low relative wave height). The bed load is not affected by the inclusion of cohesive materials, either, since these materials are mostly transported in suspension and because aspects regarding the interactions between both cohesive and non-cohesive materials are beyond the scope

of this investigation, i.e. cohesive and non-cohesive materials were treated separately.

A brief description for each of the three cases is presented next: Case 1: the sediment model roughness is defined through a constant Chezy coefficient of $60 \text{ m}^{1/2}/\text{s}$ (this case is equivalent to case 3 in Figures 6.14 to 6.16).

Case 2: model for case 1 is modified with a spatial distribution of resistance coefficients, as they were determined in chapter 4 (this case is equivalent to case 4 in Figures 6.14 to 6.16).

Case 3: model for case 2 is modified with the inclusion of areas where the Dithmarscher Klei or EHL has outcropped and the corresponding restrictions for sediment erosion are in effect (this case is equivalent to case 5 in Figures 6.14 to 6.16).

It is pointed out that bed load measurements were not available. Therefore, comparisons between observations and predictions were not possible. Figures 6.17 to 6.19 show the modeled bed load rates affected by a new roughness map and the total restriction of surficial sediment entrainment in areas where the EHL has outcropped. Noteworthy is the reduction of bed load transport rates up to a factor of 2, especially after the inclusion of the high compact EHL in the model.

A comparison between the bed load transport (Figs. 6.17 to 6.19) and the suspended sediment transport (Fig. 6.24) for the spring tidal cycle on March 2000 clearly shows the low contribution of bed load to the total sediment transport. The bed load transport in the cross sections range from 0 to 0.02 Kg/ms while the suspended sediment transport can reach up to 9 kg/ms during the ebb phase.

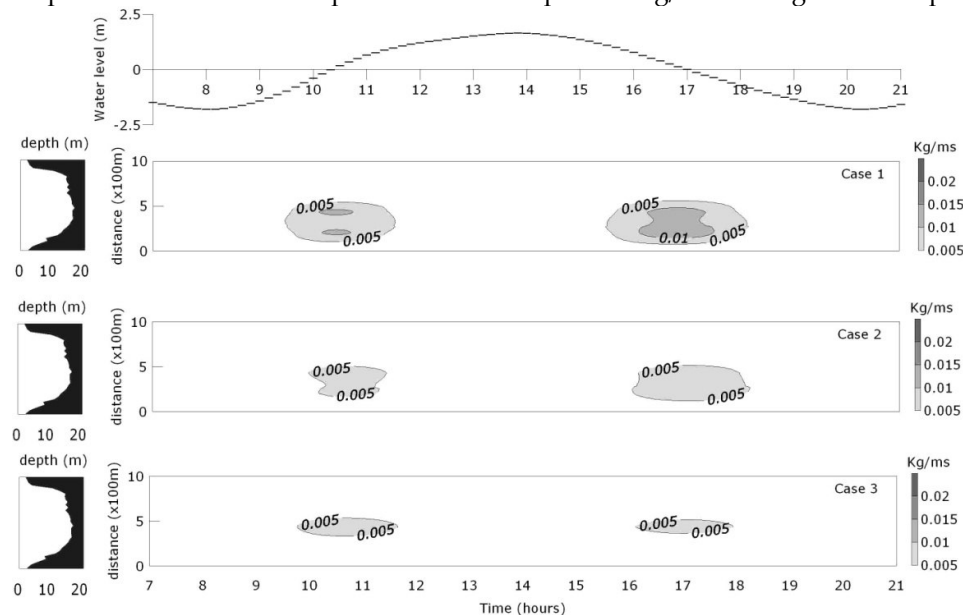


Figure 6.17 Bed load transport at cross section T1

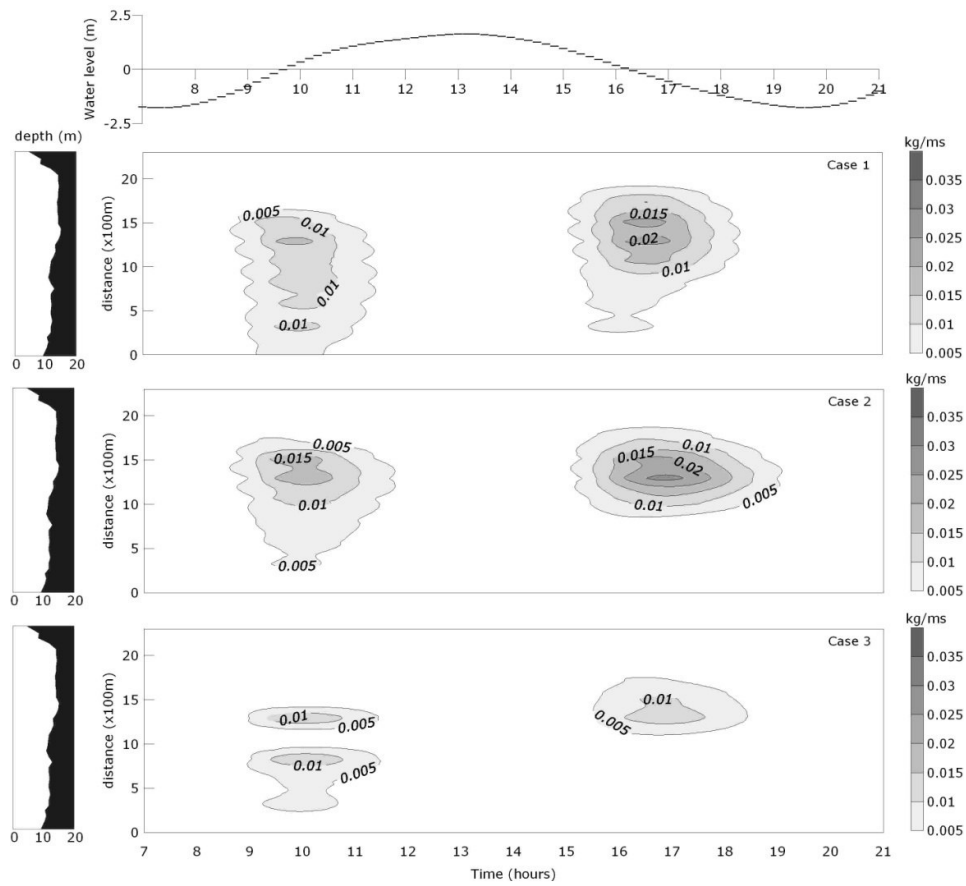


Figure 6.18 Bed load transport at cross section T2

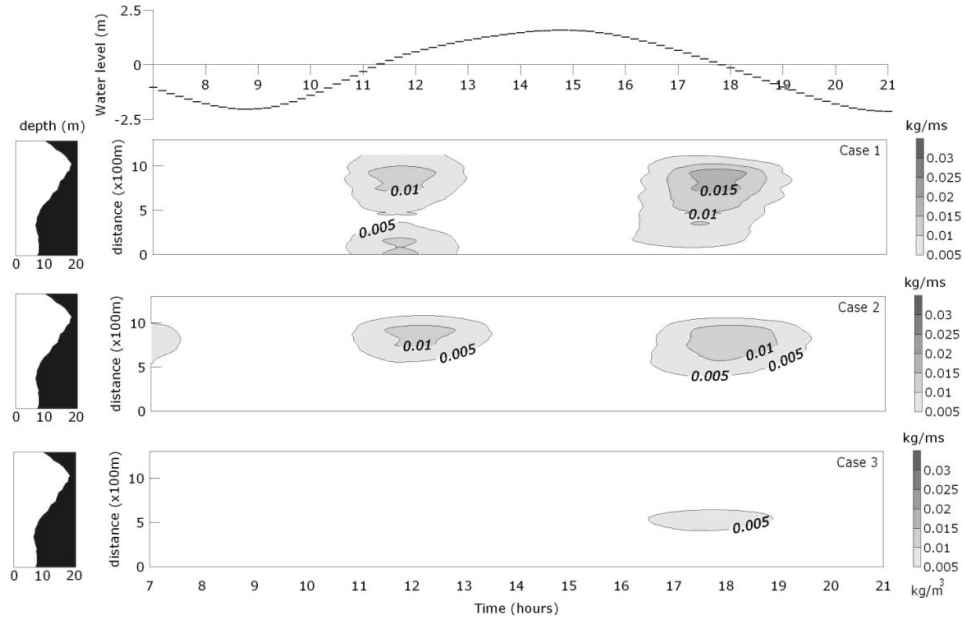


Figure 6.19 Bed load transport at cross section T3

6.6 Modelling applications

Results from the validated sediment model are visualized across the entire domain at characteristic tidal cycle phases as well as at different stages of the neap-spring cycle. Characteristic suspended sediment concentrations at the different phases within a tidal cycle are depicted in Figures 6.20 to 6.23, as is the case for ebb phase, slack water and flood phase.

Each figure shows the spatial distribution of predicted suspended concentrations along with the velocity field over the study area. Sediments are moving in and out of the Dithmarschen Bight mainly through the tidal channels. Higher concentrations are largely enclosed in the tidal channels Norderpiep, Suederpiep and Piep that correspond to areas where maximum shear stresses and velocities were estimated (see Figs. 3.4 to 3.7). Sand banks and tidal flats show the lower concentrations of material in suspension, which is expected due to the larger grain sizes and the weaker currents flowing over them. However, it is important to keep in mind that a future inclusion of the wave process into the numerical model might increase the entrainment of sediment across these shallow regions.

During slack waters, background concentrations ranged from 0.05 to 0.15 kg/m³; from which the minimum values corresponded to neap conditions where the longer slack periods led to higher deposition rates. Usually, lower concentration values corresponded to neap conditions and higher values to the spring tidal cycles. In the same way, the ebb phases showed higher concentrations than the flood phases. Maximum suspended concentrations of up to 0.5 kg/m³ were predicted at ebb phases in the Piep and Suederpiep channels.

Figures 6.24 and 6.25 illustrate the magnitude of the suspended load transport q_s per unit width throughout the Dithmarschen Bight during spring and neap stages respectively. For brevity's sake only the transport rates during ebb and flood phases are displayed. The suspended load transport is computed as:

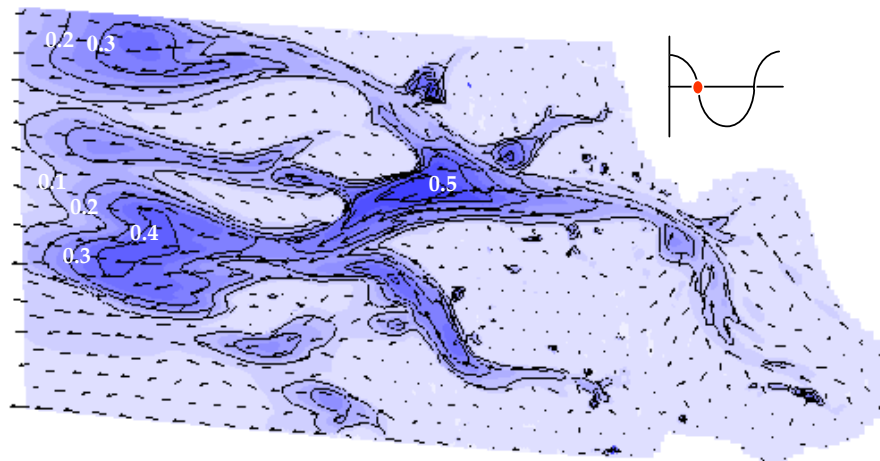
$$q_s = \sqrt{q_{s,x}^2 + q_{s,y}^2} \quad (6.6)$$

Where:

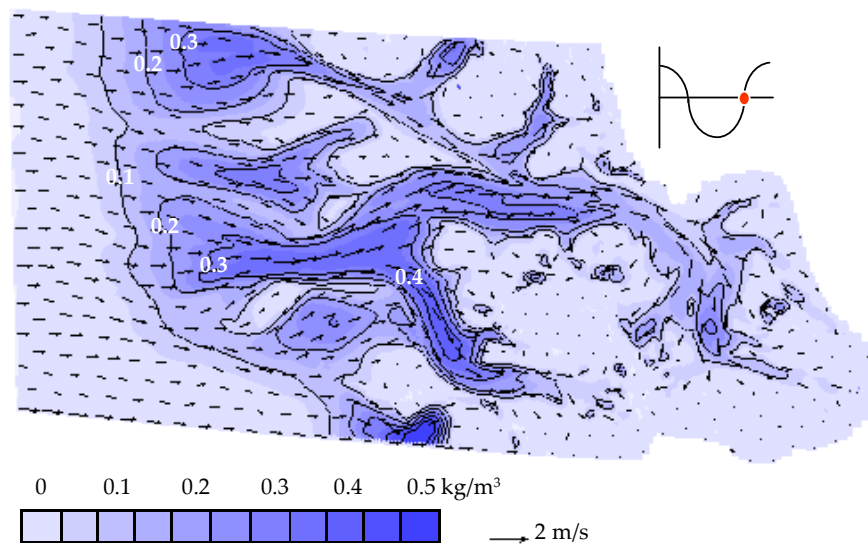
$$q_{s,x} = \frac{1}{h} \int_a^h u(z)c(z) dz = \frac{1}{h} \int_a^h q_{s,x}(z) dz \quad (6.7)$$

$$q_{s,y} = \frac{1}{h} \int_a^h v(z)c(z) dz = \frac{1}{h} \int_a^h q_{s,y}(z) dz \quad (6.8)$$

Negligible transport rates during slack water contrast the high values at flood and ebb phases, reaching up to 9 kg/ms in the Suederpiep channel. In general, sediments enter and leave the study area through the Norderpiep and Suederpiep channels directing toward the Piep channel or the open sea.



a) Ebb phase



b) Flood phase

Figure 6.20 Depth-averaged suspended sediment concentration for high currents during a spring tide

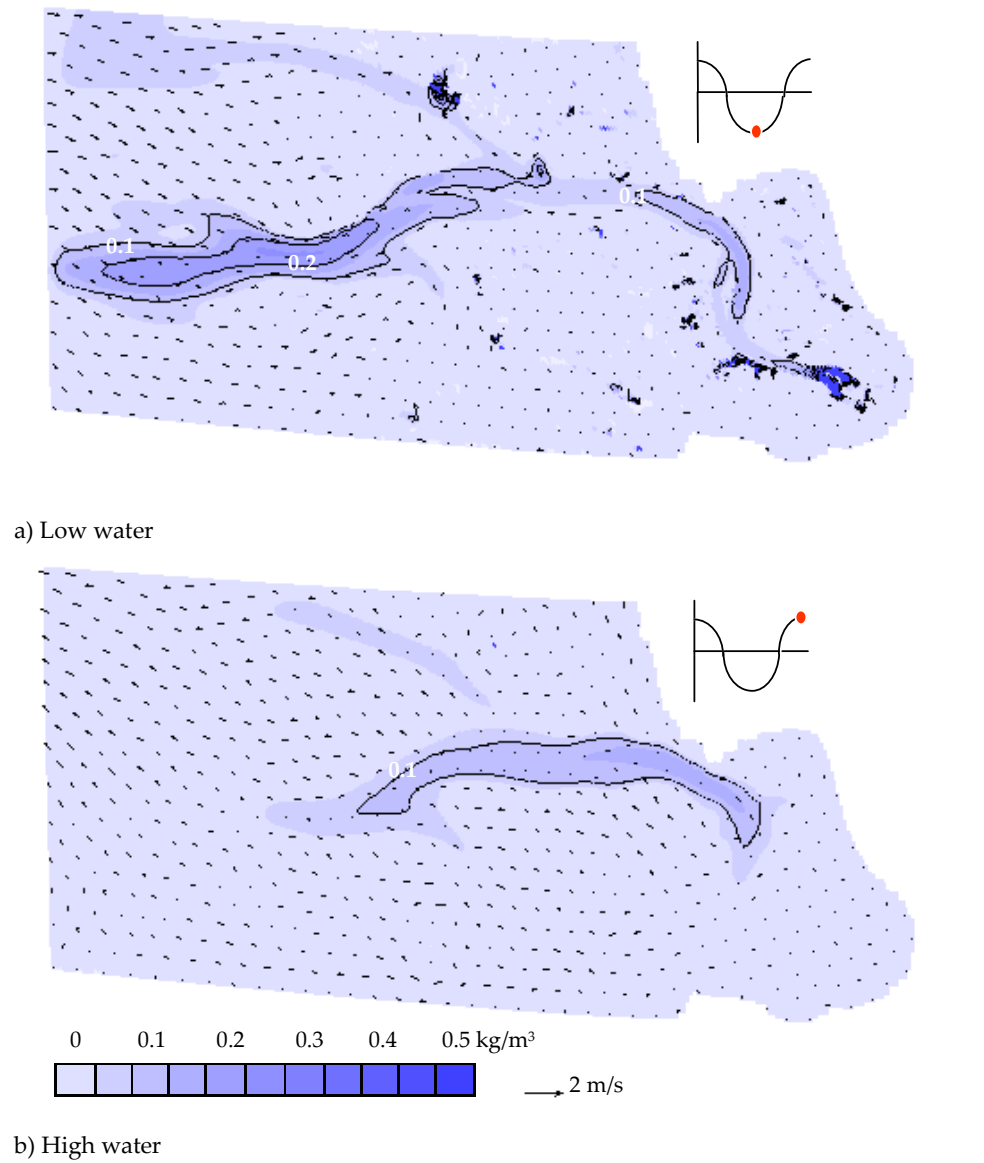


Figure 6.21 Depth-averaged suspended sediment concentration for slack water during a spring tide

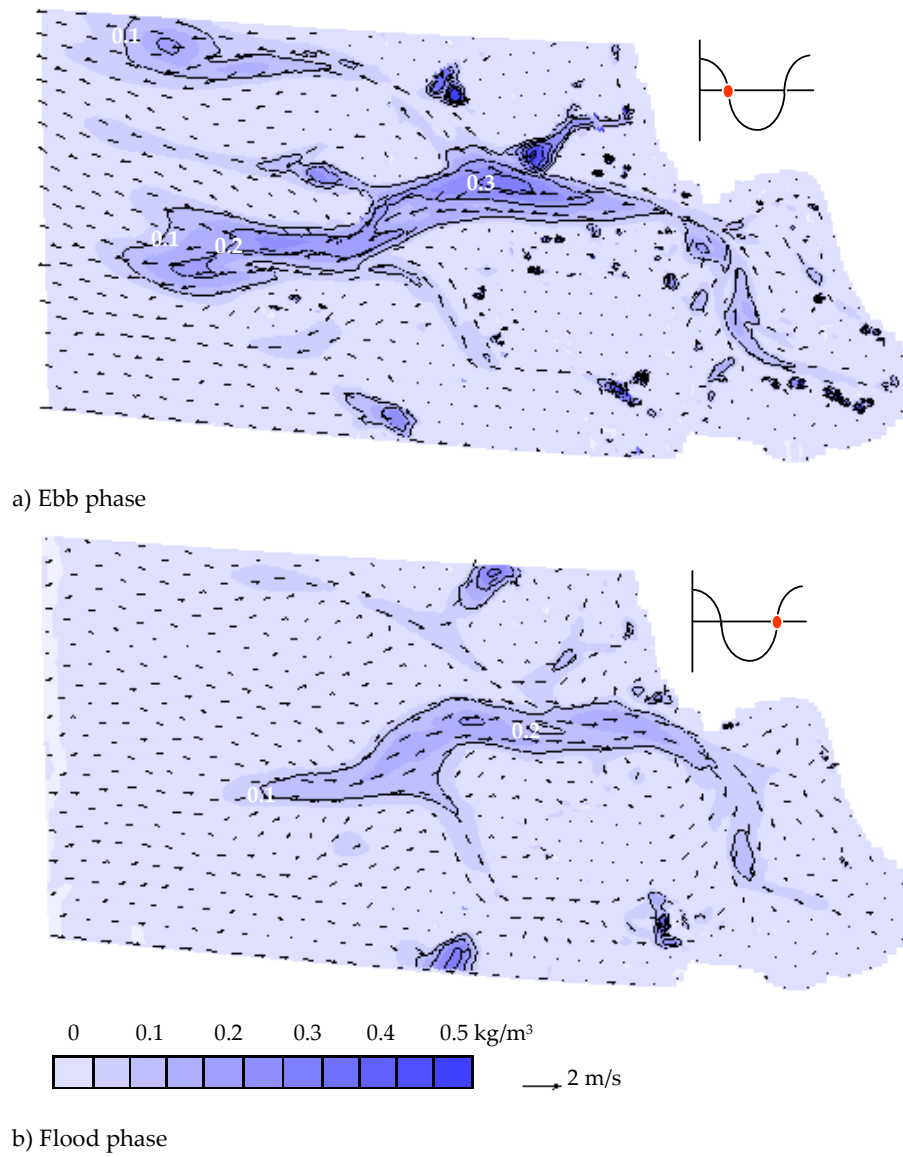
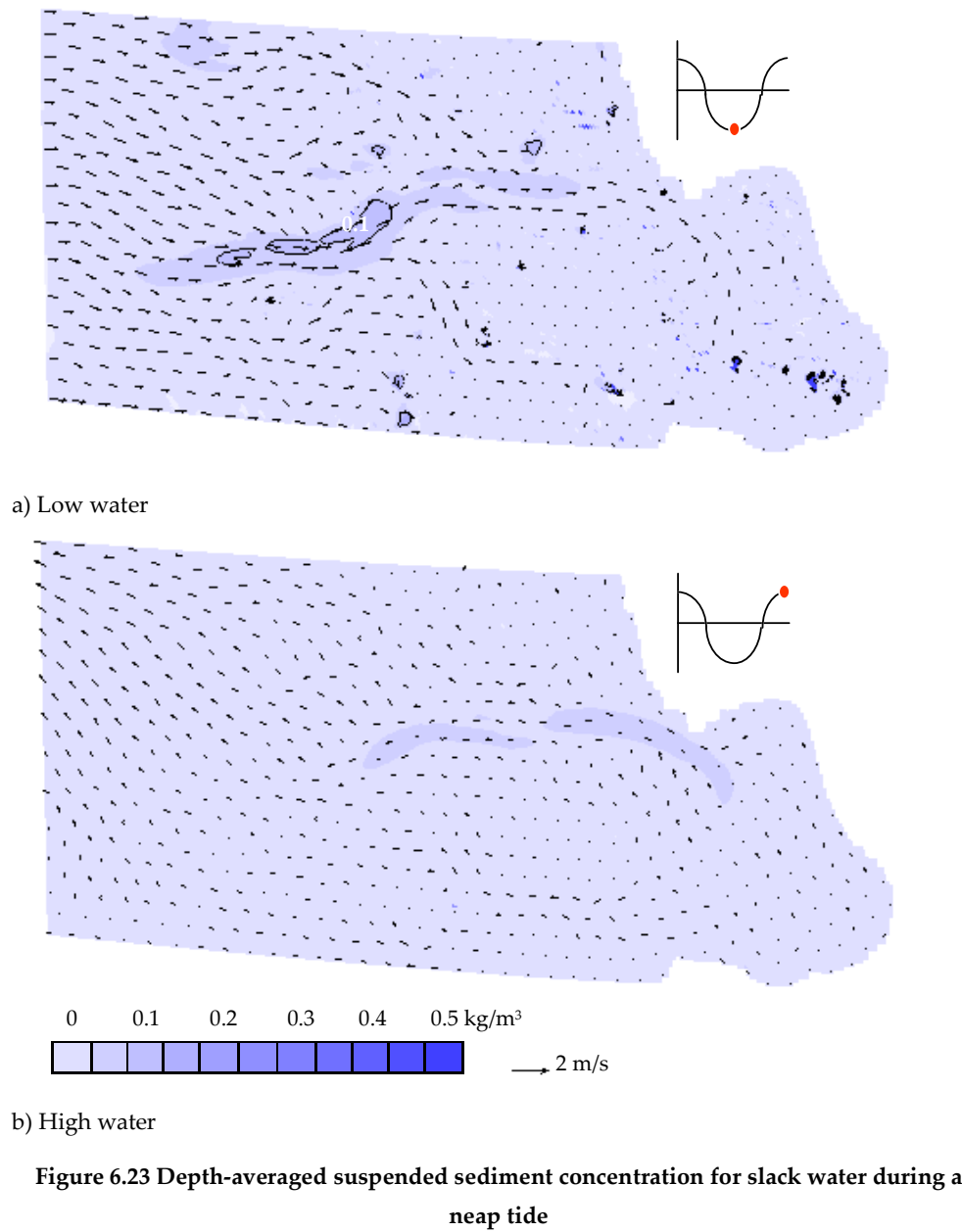


Figure 6.22 Depth-averaged suspended sediment concentration for high currents during a neap tide



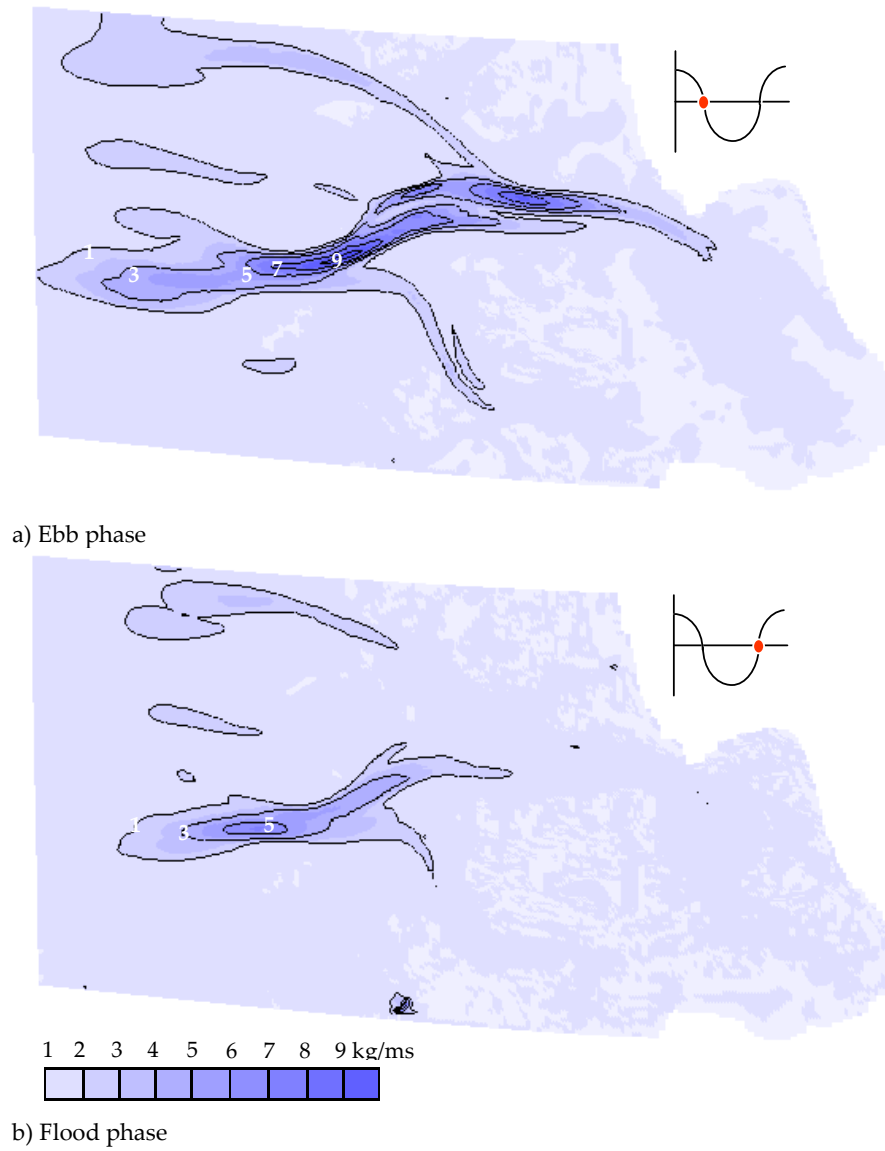


Figure 6.24 Suspended load transport during a spring tide

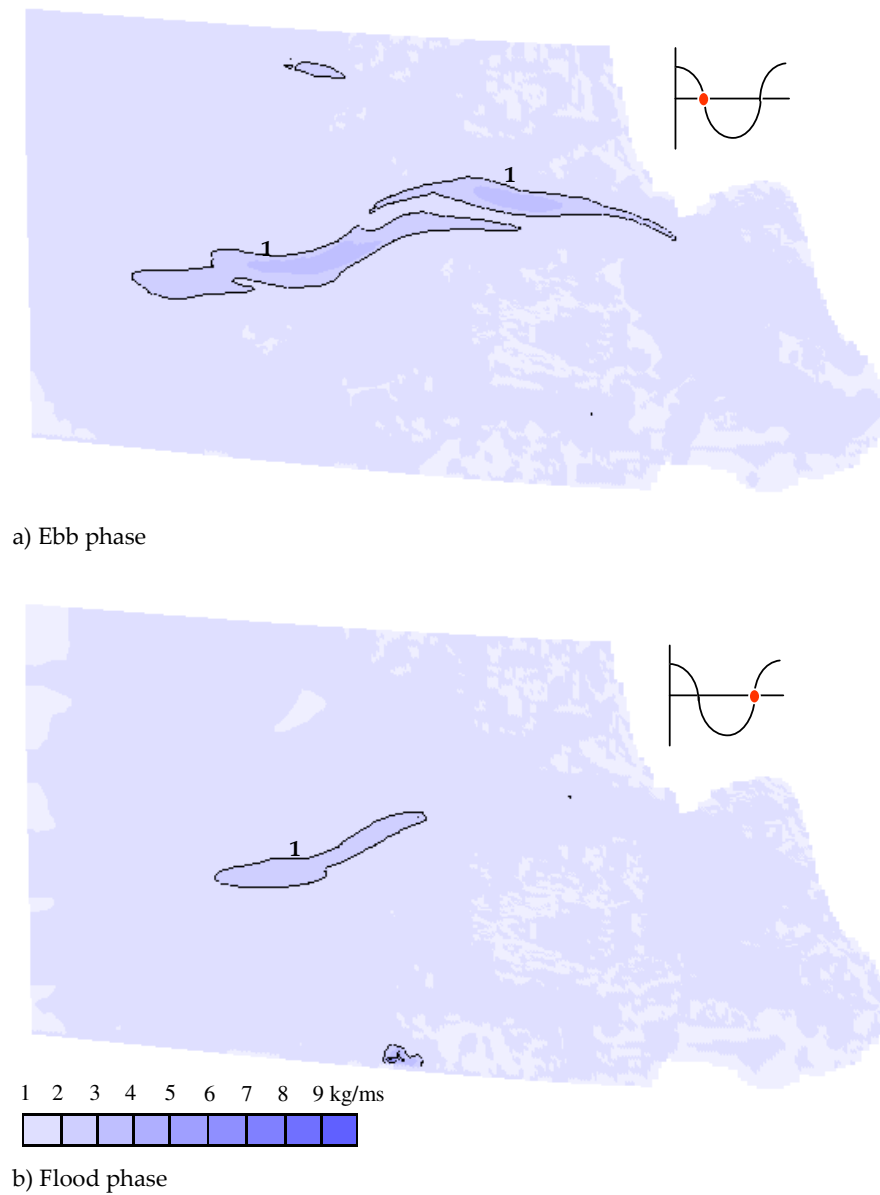
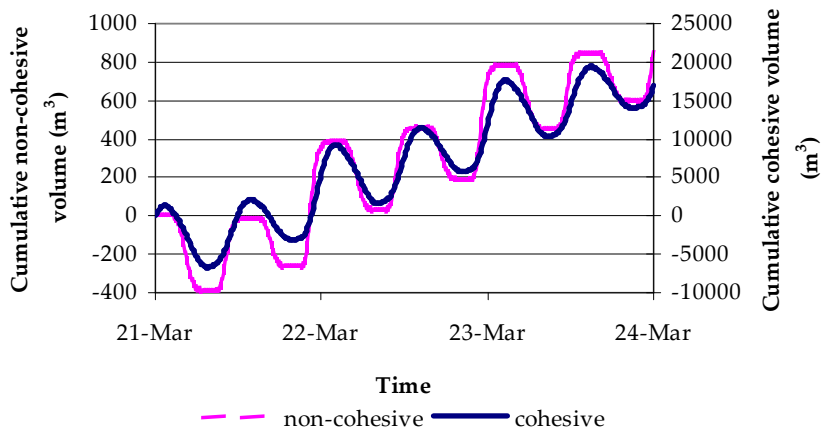
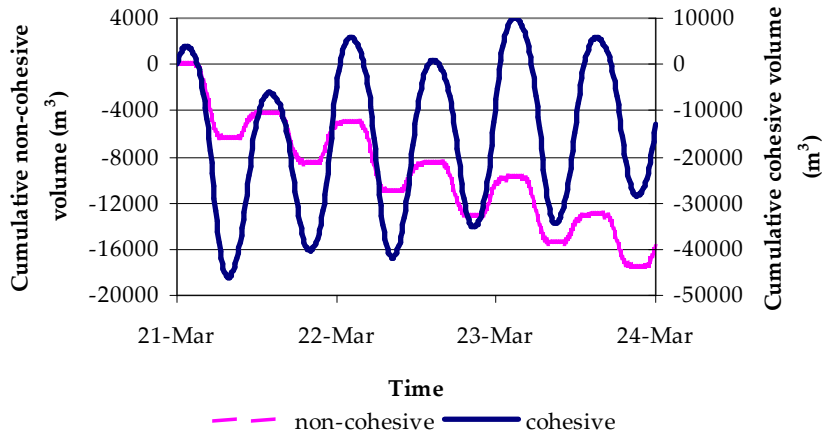


Figure 6.25 Suspended load transport during a neap tide

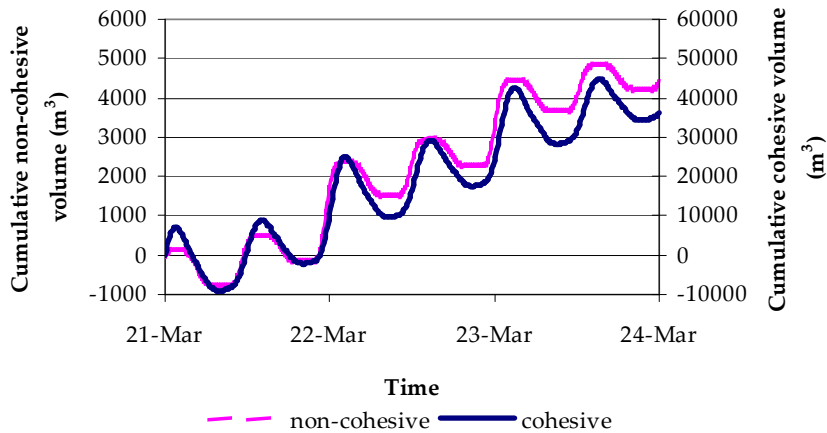
Figures 6.26 and 6.27 display the cumulative volume of sediment moving through T1, T2, and T3 (see Fig. 6.3) at spring and neap phases respectively. The cumulative volume of sediment during a flood phase is accounted by positive values; while the volume during ebb phase corresponds to negative values. Hence a positive slope in the sediment volume curve denotes a flood stage condition (sediment moves inside the domain) and vice versa.



a) Cross section T1 - Norderpiep

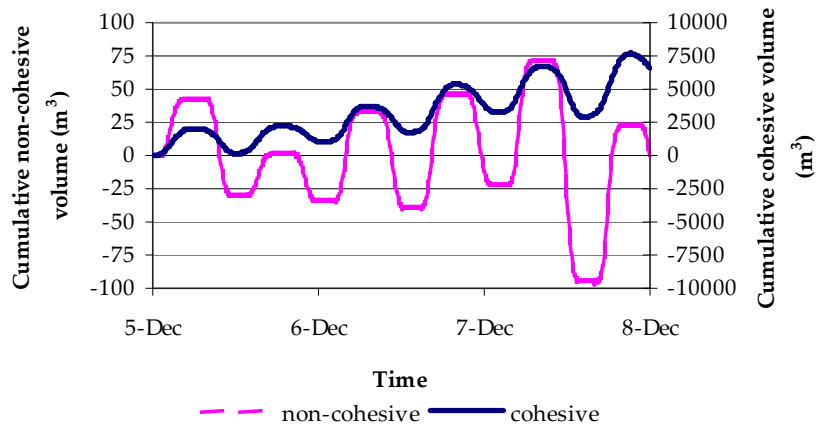


b) Cross section T2 - Suederpiep

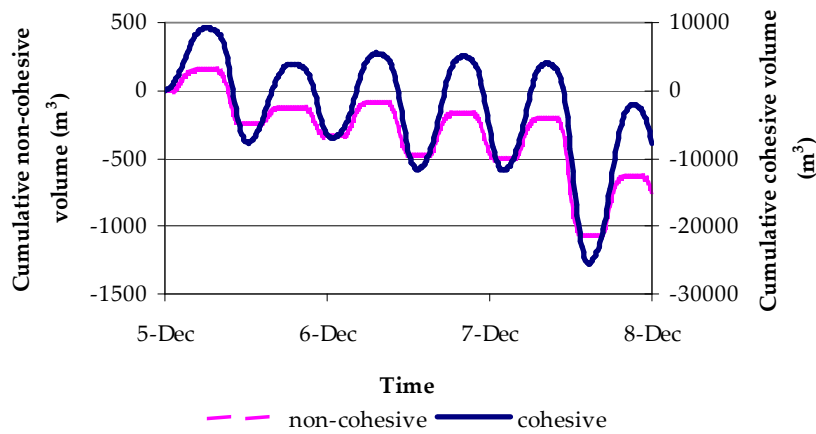


c) Cross section T3 – Piep

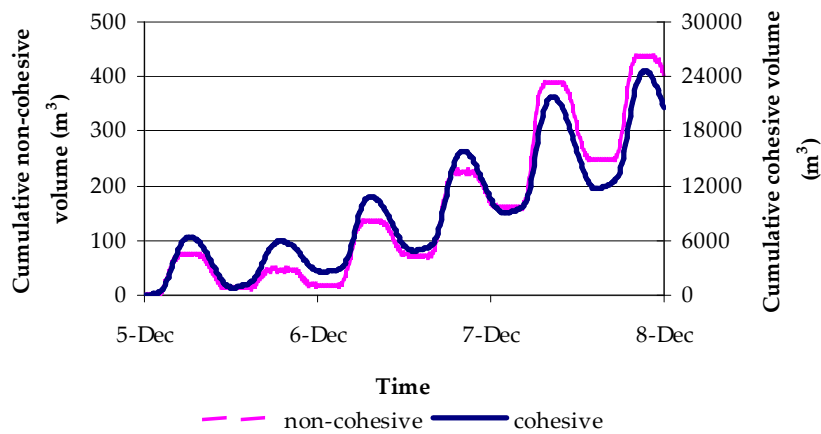
Figure 6.26 Cumulative volume of sediment through cross sections T1, T2 and T3 during spring phase



a) Cross section T1 - Norderpiep



b) Cross section T2 - Suederpiep



d) Cross section T3 - Piep

Figure 6.27 Cumulative volume of suspended sediment through cross sections T1, T2 and T3 during neap phase

From Figures 6.26 and 6.27 it is obvious the large difference between cohesive and non-cohesive suspended load. Cohesive load is from 8 to 50 times larger than the non-cohesive load. It can be noticed also, that in slack waters non-cohesive material will settle down entirely (cumulative curves flat out at peaks and troughs) while cohesive sediments remain in suspension.

The Piep cross section shows a clear trend of a positive supply of sediment landwards. This might be explained through the fact that water and sediment volumes spread out of the main channel and are stored over the nearshore flats during flood phase. Low velocities across the tidal flats drain all water back during ebb phase, but are not strong enough to entrain and transport all sediment material deposited during high waters.

Norderpiep and Suederpiep cross-sections present an opposite behavior from one another. Through the Norderpiep section a positive landward supply of sediments is predicted while Suederpiep shows a higher sediment load seawards.

The cumulative volume of sediment was computed during two different conditions: spring and neap at cross sections T1, T2 and T3 over the main tidal channels. To include the sediment load moving across the tidal flats, an additional test was performed for an extra cross section, T2', extending through the entire width of the domain, as it is an extension of T2, which was stretched North and South to the model's boundaries. The cumulative volume of suspended sediment through cross section T2' is shown in Fig. 6.28.

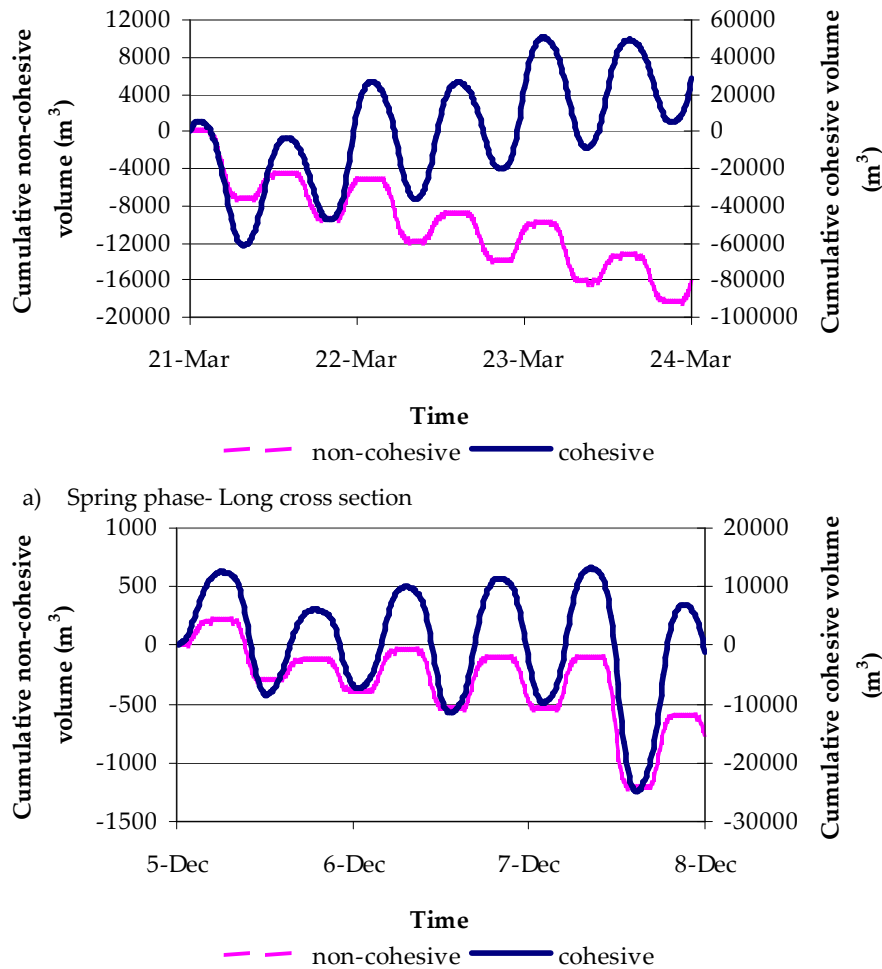
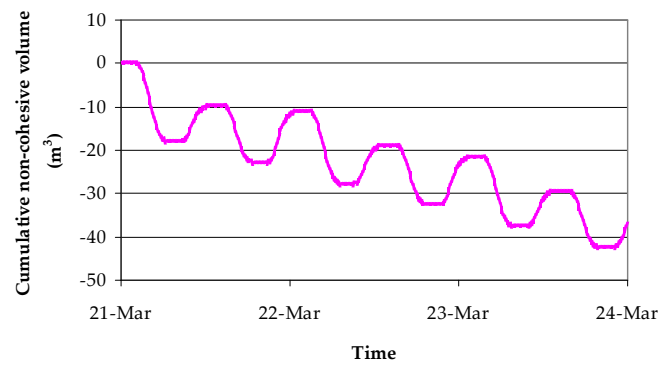


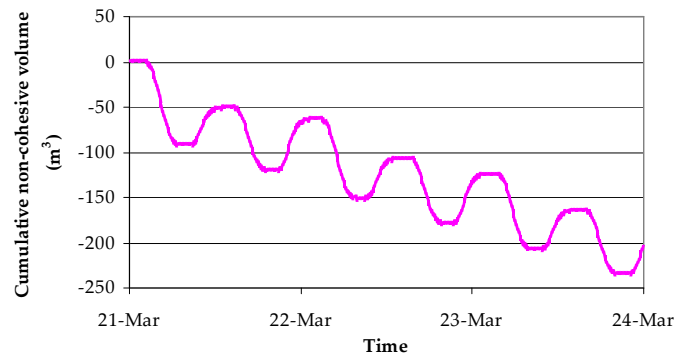
Figure 6.28 Cumulative volume of sediment through cross section T2' extending through the entire width of the domain

Comparison of suspended load through cross sections T2 and T2' clearly shows a negligible transport of sand (non-cohesive) material across the tidal flats. Transport of fine cohesive material occurs along both the tidal flats and channels while non-cohesive material is only restricted to tidal channels.

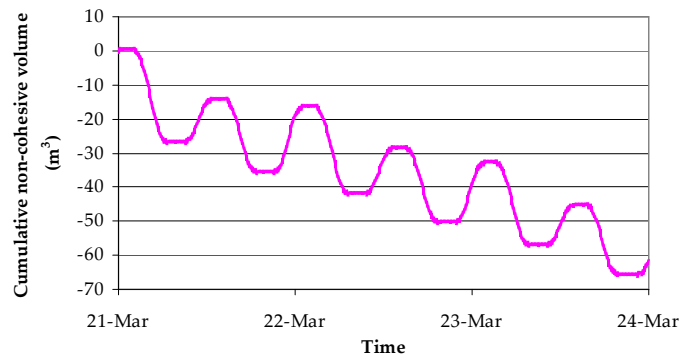
Finally, Figures 6.29 and 6.30 illustrate the contribution of bed load to the total load transport during a spring tidal cycle. The average contribution of bed load transport in the entire area was estimated to be around 2% of the total non-cohesive load. These results confirm Poerbandono's [2003] findings that declare the importance of suspended sediment as the primary mode of transport in the Dithmarschen Bight due to the low contribution of bed load to the total transport.



a) Cross section T1- Norderpiep



b) Cross section T2- Suederpiep



c) Cross section T3 - Piep

Figure 6.29 Cumulative volume of bed load through cross sections T1, T2 and T3

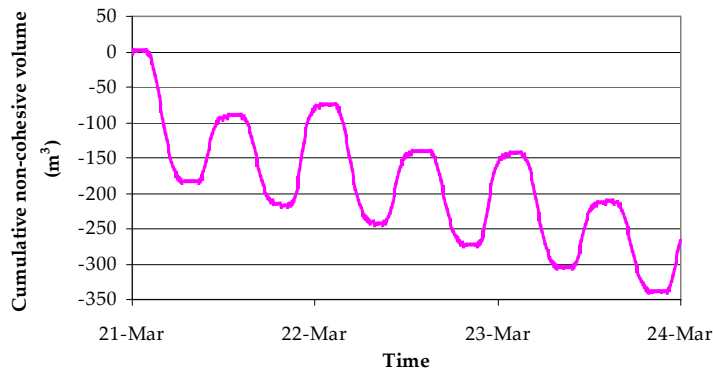


Figure 6.30 Cumulative volume of bed load through cross section T2'

6.7 Summary

Measurements of suspended sediment concentrations along the transects T1 (Norderpiep), T2 (Suederpiep), T3 (Piep) were used in both calibration and validation of the sediment transport model. Five measuring campaigns performed in the year 2000 and covering different stages within the neap-spring cycle have been divided as follows: calibration (March 22-23 and December 5-6) and validation (June 5-6, September 5-6 and September 12-13).

The calibration study developed through this investigation implied distinguishable aspects such as the non-stationary character of some variables as well as the inclusion of spatially variable parameters. Therefore, a dynamic calibration was intended to provide accurate input parameters according to the tidal cycle of interest, since, through the neap-spring cycle some physical parameters experience a non-stationary behavior that should be accounted for. Hence, the dynamic calibration assesses the value of input parameters at extreme conditions (spring-neap), from which through inter/extrapolation methods the input settings for any other tidal condition can be derived.

Another remarkable aspect from the calibration process refers to the analysis of input parameters with spatial variability. Usually, a calibration analysis determines for a particular variable a unique value that is applied uniformly over the area of interest. This investigation considered for two variables, grain size and bed roughness, a non-uniform distribution over the area, implying a sort of atypical calibration based on different scenarios. Hence, various maps of grain sizes and bed roughness were tested in terms of their effect on the sediment model accuracy.

The validation of the sediment model was performed for three cases with tidal ranges varying from 3.1 to 4.1m. Input settings were determined for each case

according to their tidal range (i.e. location in the neap-spring cycle). Discrepancies between model results and observations were quite homogeneous for the three cases tested with RMAE of the suspended sediment concentrations ranging from 0.48 to 0.53. This indicates the positive effect of using non-stationary input settings in the sediment model. Moreover, considering that RMAE values in the range of 0.5 to 1 are excellent for suspended concentrations, the model's robustness is proven.

Chapter 7

Conclusions

An accurate definition of equilibrium grain sizes across the tidal flats of the Dithmarschen Bight was possible (RMAE=0.13 and MAE=16.4 μm) on the basis of a functional relationship between maximum orbital velocities, relative wave heights and grain sizes. Hence, the relevant effect of waves on grain sorting was confirmed, although it is restricted to shallow areas. Grain sorting due to waves in tidal channels and deep regions, where relative wave heights are lower than 5%, is negligible. The best correlations between maximum orbital velocities and grain sizes were found for relative wave heights higher than 50%.

The well accomplishment of the proposed methodology in estimating equilibrium grain sizes indicates (indirectly) the validity of the made assumptions. Hence, temporal variability of grain sizes are negligible or not prevailing in the long run. This conclusion also applies to extreme hydrodynamic conditions (i.e. high differences with respect to the typical tidal cycle TTC), which might affect grain sorting only temporally, since reworking processes will reinstate the original condition.

Water depths, current velocities and shear stresses (due to currents) present little or negligible effect on grain sorting. Further verifications are however recommended especially along the tidal channels where only a few sediment samples were available.

A predicted map of grain sizes for the Dithmarschen Bight shows relatively large grain sizes on the western sand banks (see Fig. 3.29) which reproduces the natural mechanisms over these areas affected by wave-breaking processes. Therefore, this map of sediments will highly improve the performance of the sediment transport model and increase the accuracy of estimates regarding morphological developments.

Local observations of mean bedform dimensions during a tidal period (averaged values along transects 200m long) exhibit low variations with respect to their time-averaged values (mean discrepancies were about 10%), although it is important to notice the high spatial variability of the bedform dimensions within each transect

surveyed. This finding shows a non-continuous behavior that cannot be explained by bathymetry, hydrodynamics nor sedimentological variations, as they remain fairly uniform throughout the transect. However, it is pointed out that aggregate values of bedform dimensions (over transects with lengths 10 to 15 times the maximum bedform length) show a rather continuous behavior.

The proposed approach to predicting bedform dimensions and their associated roughness in the tidal channels of the Dithmarschen Bight proved to be accurate after successful verifications through direct and indirect comparisons between observations and model results. This approach tackles the prediction of bedform dimensions under non-steady tidal flows through an iterative process in which procedures extensively validated for steady flows are applied by means of the representative flow condition RFC. The RFC is assumed to be responsible for bed features developing during the course of a tidal period.

The RFC assumption enables prediction of bedform dimensions in the tidal channels of the Dithmarschen Bight. Comparison of cumulative frequency curves between observations and predictions of bedform lengths and heights show a very close agreement. The RFC in a tidal cycle coincides with the maximum shear stress. This finding can vary from place to place due to particular characteristics regarding hydrodynamics, sediments and geological features.

The seasonal variation of bedform features through the neap-spring cycle is highlighted in this research. The implementation of this seasonal variation in the sediment transport model improved the accuracy of suspended concentration predictions by about 10%. Shortage of field data covering bedform measurements under both neap and spring stages prevent direct verifications of this seasonal phenomenon.

The sediment transport model indicates high sensitivity with respect to parameters concerning the properties of cohesive materials. Sediment erosion rate, critical erosion shear stress, critical deposition shear stress and settling velocity show high relevance to predictions of suspended sediment concentrations in the Dithmarschen Bight. The sensitivity of the model due to variations of non-cohesive sediment properties is relatively small given the low proportion of sandy materials in suspension.

The calibration process of the sediment transport model revealed a non-stationary behavior of several physical parameters along the neap-spring cycle. This can also be explained through an erosion-deposition cycle that runs parallel to the neap-spring cycle. While deposition increases from spring to neap, erosion does from neap to spring. During depositional periods the amount of fresh mud material on the seabed is increased and the concentration of suspended material is reduced. This fact is reversed during the erosional period. As a logical consequence of this deposition-erosion cycle some properties of cohesive materials such as mud content, critical

shear stress (erosion-deposition), sediment erosion rate, and settling velocity show a non-stationary behavior.

The validation of the sediment transport model proves its robustness. The model performance was tested under three different conditions at different stages within the neap-spring cycle. The discrepancies between observed and predicted suspended sediment concentration in terms of RMAE values ranged from 48 to 53%. As RMAE values between 50 and 100% are excellent considering this type of variable, the reliability of the sediment model is verified. Furthermore, it highlights the consistency of the sediment model by the limited discrepancies of RMAE values (mostly lower than 50%) obtained under the different forcing conditions. The latter validates the model's applicability in a wider range of circumstances. The consistency of the model results and their close agreement with observations under different scenarios is mostly due to the implementation of non-stationary input parameters such as the roughness size and the cohesive materials' properties (i.e. mud content, critical erosion shear stress, critical deposition shear stress, sediment erosion rate coefficient, and settling velocity).

The construction of the sediment transport model involved several stages in which a spatial and temporal refinement of the input data, the inclusion of cohesive sediment dynamics and the restriction of sediment supply (i.e. areas where the EHL is exposed) have been considered to improve the performance of the model. Based on the discrepancies between observed and modelled suspended sediment concentrations, it can be deduced that: a) The model accuracy was improved by about 50%; b) The inclusion of cohesive materials into the model might claim the largest contribution from the total improvement of about 25%. Its effect is most pronounced during slack waters since the fine material can remain longer in suspension and better reproduce the observed background concentrations; c) The second largest accuracy contribution of about 15% is due to the implementation of the methodology in determining the bed roughness (indicated in chapter IV); d) The restriction of sediment supply over areas where the EHL is exposed contributed to the remaining 10% of the improvement in model accuracy; e) The accuracy improvement in the sediment model due to the grain size variation across the study area was negligible. This poor contribution can be basically attributed to the low fraction of sand material in suspension. Nevertheless, it might become relevant in the definition of the bed load and in considering the morphological developments on medium- and large-temporal scale simulations. The grain size map for the Dithmarschen Bight (Fig. 3.29) shows relatively large particles over the sand banks. Therefore, a reduction in erosional effects over the wave-exposed sand banks is expected and will moderate the morphological predictions.

Suspended sediment material is made up largely of cohesive fine particles. The proportion of fine sediments in suspension varies temporally and spatially, but

usually remains within a range of 85 to 100% from the total concentration. Whereas fine sediments are spread all over the domain, sand particles are transported mostly through the main channels.

Broadly speaking, a positive net supply of sediments is observed in the eastern-most region as depicted in the cumulative curve of sediment volume crossing through the Piep section T3 (see Figs. 6.26 and 6.27). Hence, tidal flats are expected to continuously accumulate sediments during calm weather conditions. Lightweight materials transported in suspension can disperse easily from the main current or channels and partly settle over the flats during high waters. Once the material is settled; its chance of being re-entrained and drained back during the ebb phase is lower, given the small velocities along the tidal flats. The opposite tends to happen to heavier, non-cohesive particles transported as bed load, producing a negative net supply.

The Suederpiep channel is responsible for most of the suspended sediment entering and leaving the study area. It can be estimated at approximately 80% of the total. This proportion can be even higher when only non-cohesive particles are considered. The remaining 20% moves along the Norderpiep and tidal flats.

The bed load is a very small fraction of the total sand load. Through Norderpiep about 2.5% of the total sand load is bed load. This fraction is less across Suederpiep and Piep, where it can be estimated at about 1.25%. The latter results can be drastically reduced if both cohesive and non-cohesive materials are accounted for in the total load.

Finally, the sediment model performance was improved substantially after including the dynamics of cohesive sediments and through the spatial and temporal refinement of several physical parameters. Implementing all these factors into the model improved its accuracy by about 50% and produced an excellent agreement between observed and predicted suspended concentrations through the neap-spring cycle. Extensive field measurements obtained mostly from the PROMORPH research project were fundamental in the development of methodologies and strategies for predicting grain sizes, bedform dimensions and sediment concentrations. This confirms the relevance of field data in the development of process-based models. It can, therefore, be said that further improvements in measurement techniques and an extension of surveys into unexplored areas will surely contribute to additional advances of the sediment transport model.

References

- Ackers, P., and W. White. 1973. Sediment transport: new approach and analysis, *Journal of the Hydraulics Division*, 99(HY11), 2041-2060.
- Allen, J.R.L. 1968. The nature and origin of bedforms hierarchies, *Sedimentology*, 10(3), 161-182.
- Allen, J.R.L. 1971. Transverse erosional marks of mud and rock: their physical basis and geological significance, *Sediment. Geol.*, 5, 167-385.
- Allen, J.R.L. 1982. *Sedimentary Structures, Their Character and Physical Basis*, Elseviers Science Publishers, Amsterdam, 589 pp.
- Amos, C.L. 1995. Siliciclastic tidal flats, In G.M.E. Perillo (ed.), *Geomorphology and Sedimentology of Estuaries, Development in Sedimentology*, Elsevier Press, Amsterdam, 53, 273-301.
- Andersen, T.J. 2001. Cohesive sediment transport in coastal lagoons with special emphasis on the biological influence on the erosion and deposition of fine-grained material, PhD. Thesis, University of Copenhagen.
- Anderson, A.G. 1953. The characteristics of sediment waves formed by flow in open channels, *Proceedings Third Midwestern Conference in Fluid Mechanics*, Minneapolis, 379-395.
- Ariathurai, C.R. 1974. A finite element model for sediment transport in estuaries, Ph.D. thesis, University of California, Davis, CA.
- Asp, N.E., J. Wilkens, K. Ricklefs, and R. Mayerle. 2001. Geology and morphodynamics of a tidal flat area of the German North Sea coast and its support to a medium-scale morphodynamic modeling, *Proceedings VIII Congresso da ABEQUA, Mariluz-Imbe*, 14-20.
- Asp, N.E. 2004. Long- to short-term morphodynamic evolution of the tidal channels and flats of the Dithmarschen Bight, German North Sea, *Berichte Forschungs- und Technologiezentrum Westküste der Universität Kiel*, 34.

- Athallah, M. 1968. Prediction of Bedforms in Erodible Channels, Ph.D. Thesis, Colorado State University, Fort Collins.
- Austen, I., T.J. Andersen, and K. Edelvang. 1999. The influence of benthic diatoms and invertebrates on the erodability of an intertidal mudflat, the Danish Wadden Sea, *Estuarine, Coastal and Shelf Science*, 49, 99-111.
- Bagnold, R.A. 1940. Beach formation by waves: some model experiments in a wave tank, *Journal of the Institute of Civil Engineers*, 15, 27-52.
- Bagnold, R.A. 1956. The flow of cohesionless grains in a fluid, *Philosophical Transactions of the Royal Society of London*, A249, 235-297.
- Bagnold, R.A. 1966. An approach to the sediment transport problem from general physics, Professional Paper U.S. Geological Survey Professional Paper, 422-J, 1-37.
- Bascom, W.N. 1951. The relationship between sand size and beach-face slope, *Trans. Am. Geophys. Union* 32, 866-874.
- Bijker, E.W. 1971. Longshore transport computations. *Journal of the Waterways, Harbors and Coastal Engineering Division*, 97(4), 687-701.
- Blondel, P., and B.J. Murton. 1997. *Handbook of Seafloor Sonar Imagery*, John Wiley & Sons, Ltd. Publishers, 314 pp.
- BMFT. 1994. Optimierung des Küstenschutzes auf Sylt – Phase II, Bundesministerium für Forschung und Technologie, Amt für Ländliche Räume, Husum, 221 pp.
- Bogardi, J. 1974. *Sediment Transport in Alluvial Streams*. Akademiai Kiado, Budapest, 825 pp.
- Booij, N., R.C. Ris, and L.H. Holthuijsen. 1999. A third generation wave model for coastal regions, Part I, Model description and validation, *Journal of Geophysical Research*, 104(C4), 7649-7666.
- Brahms, A. 1754. *Anfangsgründe der Deich und Wasserbaukunst*, vol. I, p. 105, Aurich.

- Briaud, J.L., F. Ting, H.C. Chen, S.R. Gudavalli, S. Perugu, G. Wei. 1999. SRICOS: Prediction of scour rate in cohesive soils at bridge piers, *ASCE Journal of Geotechnical Engineering*, 125, 237-246.
- Briaud, J.L., H.C. Chen, Y. Li, P. Nurtjahyo, and J. Wang. 2004. Pier and contraction scour in cohesive soils, National Cooperative Highway Research Program NCHRP, Washington, D.C., report 516, 118 pp.
- Carter, R.W.G. 1988. Coastal Environments. An Introduction to the Physical, Ecological and Cultural Systems of Coastlines, Academic Press, London, 617 pp.
- Casey, H.J. 1935. Über Geschiebebewegung, *Mitteilungen Preussischen Versuchsanstalt für Wasserbau und Schiffbau*, Berlin.
- CERC. 2002. Coastal Engineering Manual, Part III, Ch. 5, Coastal Engineering Research Centre, Department of the Army, Vicksburg, Mississippi, 67pp.
- Chan, W.Y., W.H. Wai, Y.S. Li. 2006. Critical shear stress for deposition of cohesive sediments in Mai Po, Conference of Global Chinese Scholars on Hydrodynamics, CESH, 300-305.
- Cornaglia, P. 1889. On beaches, *Accademia Nazionale dei Lincei Atti, Classe di Scienze Fisiche, Matematiche e Naturali*, 5(4), 284-304. Reproduced in translation in: J.S. Fisher and R. Dolan (Editors), 1977. Beach processes and Coastal Hydrodynamics, 39, 11-26.
- Cornish, V. 1898. On sea beaches and sand banks, *Geographical Journal*, 11, 528-559, (see also pages 628-647).
- Coulomb, C.A. 1773. *Ac. R. Sci. Mem. Math. Phys. Par Divers Savants* 7.
- Damgaard, J.S., L.C. Van Rijn, L.J. Hall, R.L. Soulsby. 2001. Intercomparison of engineering methods for sand transport, Paper CJ in Van Rijn, L.C, A.G. Davies, J. Van de Graaff, J.S. Ribberink. 2001. Sediment transport modeling in marine coastal environments, Aqua Publications, Amsterdam, 415 pp.
- Darcy, H. 1854. Sur des recherches expérimentales relatives au mouvement des eaux dans les tuyaux, *Comptes rendus des séances de l'Académie des Sciences*, 38, 1109-1121.

- Dean, R.G. 1991. Future directions in cross-shore transport modeling. Proceedings of the specialty workshop on the development and application of cross-shore sediment transport and beach profile change models. Am. Soc. Civ. Eng., Seattle, unpubl. rep.
- Du Boys, M.P. 1879. Études du régime du Rhône et l'action exercée par les eaux sur un lit à fond de graviers indéfiniment affouillable, *Annales des Ponts et Chaussées*, 5(18), 141-195.
- Eaglesong, P.S., and R.G. Dean. 1959. Wave-induced motion of bottom sediment particles, *Proceedings American Society of Civil Engineers, Journal of the Hydraulics Division*, HY10, 53-79.
- Eaglesong, P.S., and R.G. Dean. 1961. Wave-induced motion of bottom sediment particles, *Trans. Am. Soc. Civil Eng.*, 126(1), 1162-1189.
- Eaglesong, P.S., B. Glenne, and J.A. Dracup. 1963. Equilibrium characteristics of sand beaches, *Proceedings American Society of Civil Engineers, Journal of the Hydraulics Division*, 89(HY1), 35-57.
- Einstein, H.A. 1950. The bedload function for sediment transportation in open channel flows, U.S. Dept. Agric. Soil Conserv. Serv., Washington, DC., *Tech. Bull.* 1026, 71 pp.
- Engelund, F. 1965. A criterion for the occurrence of suspended load, *La Houille Blanche*, 8, 7.
- Engelund, F. 1970. Instability of erodible beds, *Journal Fluid Mechanics*, 42, 225-244.
- Escobar, C.A., and R. Mayerle. 2006. Effect of sediment sizes and bedform roughness on the predictive ability of sediment transport models, *Proceedings of the 15th Congress of APD-IAHR-ISMH, Madras*, 761-766.
- Exner, F.M. 1925. Über die Wechselwirkung zwischen Wasser und Geschiebe in Flüssen, *Sitzungsberichte der Akademie der Wissenschaften in Wien Math. Naturwiss., Abt. IIa*, 134, 165-180.
- Fick, A. 1855. Ueber diffusion, *Ann. Phys. Chem.*, 94, 59-86.

- Fish, J.P., and H.A. Carr. 1990. *Sound Underwater Images*, American Underwater Search and Survey Ltd., Cataumet, 189 pp.
- Fredsøe, J., and R. Deigaard. 1992. *Mechanics of Coastal Sediment Transport*, World Scientific, Singapore, 369 pp.
- Frijlink, H.C. 1952. Discussion of bed load movement formulae, Delft Hydraulics, Report No. X2344/LV, Delft.
- Froehle, P. and S. Kohlhase. 1995. Long-term statistical analysis of sea state within storm surges, Proceedings 4th International Conference on Coastal and Port Engineering in Developing Countries, COPEDEC IV, Rio de Janeiro.
- Gadow, S. 1970. Sedimente und Chemismus, In: Reineck, H.E. ed., *Das Watt, Ablagerungen und Lebensraum*, Frankfurt, 23-35.
- Galappatti, G., and C.B. Vreugdenhil. 1985. A depth-integrated model for suspended sediment transport, *Journal of Hydraulic Research*, 23(4), 359-377.
- Gilbert, G.K. 1914. The transportation of debris by running water, U.S. Geological Survey Professional Paper 86, 263 pp.
- Gladki, H. 1975. Discussions of determination of sand bed roughness for fixed beds, *Journal of Hydraulic Research*, 13(2), 221-222.
- Grant, W.D., and O.S. Madsen. 1982. Movable bed roughness in unsteady oscillatory flow, *Journal of Geophysical Research*, 87(C1), 469-481.
- Grass, A.J. 1970. Initial instability of fine bed sand, *Journal of the Hydraulics Division*, 96, 619-632.
- Guedes, C., R. Weisse, J.C. Carretero, and E. Alvarez. 2002. A 40 years hindcast of wind, sea level and waves in European waters, Proceedings of 21st International Conference on Offshore Mechanics and Arctic Engineering, Oslo.
- Guillén, J., Palanques, A., Puig, P., and Soriano, S. 2004. Temporal grain-size variability of marine shallow sediment: natural and man induced processes, Workshop HWK, Delmenhorst, 61-64.

- Gularte, R.C., W.E. Kelly, and V.A. Nacci. 1980. Erosion of cohesive sediments as a rate process, *Ocean Engng.*, 7, 539-551.
- Harbor, D.J. 1998. Dynamics of bedforms in the lower Mississippi River, *Journal of Sedimentary Research*, 68(5), 750-762.
- Hartsuiker, G. 1997. Deutsche Bucht and Dithmarschen Bucht, Set-up and calibration of tidal flow models, Delft Hydraulics, Report No. H1821.
- Hasselmann, S., K. Hasselmann, E. Bauer, P.A.E.M. Janssen, G.J. Komen, L. Bertotti, P. Lionello, A. Guillaume, V.C. Cardone, J.A. Greenwood, M. Reistad, L. Zambresky, and J.A. Ewing. 1988. The WAM model – A third generation ocean wave prediction model, *Journal Phys. Oceanogr.*, 18, 1775–1810.
- Hayes, M.O. 1979. Barrier island morphology as a function of tidal and wave regime, In: *Barrier Islands from the Gulf of St. Lawrence to the Gulf of Mexico*, Leatherman, S.P. (eds), Academic Press, New York, 27 pp.
- Helmholtz, H. 1888. Über atmosphärische Bewegungen, *Sitzungsbericht Königl. Preuss. Akad. Wiss. Berlin*, I 26, 647-663.
- Herschel, C. 1897. On the origin of the Chézy formula, *Journal Association of Engineering Societies*, 18, 363-368.
- Hirschhäuser, T. 1997. Numerische Simulation der Morphodynamik des Nordfriesischen Wattenmeeres, Diplomarbeit, TU Darmstadt.
- Hirschhäuser, T., P. Mewis, and U. Zanke. 1998. Determination of the initial distribution of particle size in morphodynamic modeling in tidal areas, *International Conference on Hydro-science and Engineering, ICHE*, 16 pp.
- Hjulström, F. 1939. Transportation of detritus by moving water, *Recent Marine Sediments*, Edited by P.D. Trask, Dover, New York.
- Holdaway, G.P., P.D. Thorne, D. Flatt, S.E. Jones, and D. Prandle. 1999. Comparison between ADCP and transmissometer measurements of suspended sediment concentration, *Continental Shelf Research*, 19, 421-441.

- Horn, D.P. 1991. A numerical model for shore-normal sediment size variation, Ph.D. Thesis, Univ. Oxford, 407 pp.
- Horn, D.P. 1992. A review and experimental assessment of equilibrium grain size and the ideal wave-graded profile, *Marine Geology*, 108, 161-174.
- Huang, I.T. 2006. Investigation of Sediment Dynamics Using Numerical Model in the Central Dithmarschen Bight, German North Sea Coast, Master Thesis, Coastal Research Laboratory, University of Kiel, 75 pp.
- Hwang, K.N., and A.J. Mehta. 1989. Fine sediment erodability in lake Okeechobee, Coastal and Oceanographic Engineering Department, University of Florida, Report UFL/COEL-89/019, 140 pp.
- Inglis, C.C. 1949. The behavior and control of rivers and canals, Central Waterpower Irrigation and Navigation Research Station, Poona, Research Publication 13, 79-91.
- Inman, D.L. 1949. Sorting of sediments in the light of fluid mechanics, *Journal of Sedimentary Petrology*, 19, 51-70.
- Ippen, A.T., and P.S. Eagleson. 1955. A study of sediment sorting by waves shoaling on a plane beach, U.S. Army Corps Eng., Beach Erosion Board, Tech. Memo No. 63, 83 pp.
- Jacoub, G., and B. Westrich. 2002. Numerical simulation of unsteady flow and sedimentation processes in a flood retention reservoir, 5th International Conference on Hydro-Sciences and Engineering, Warsaw, 9 pp.
- Janoo, V. 1998. Quantification of Shape, Angularity, and Surface Texture of Base Course Materials, Special Report 98-1, US Army Corps of Engineers, Cold Regions Research & Engineering Laboratory, 22 pp.
- Jerolmack, D.J., and D. Mohrig. 2005. A unified model for subaqueous bed form dynamics, *Water Resources Research*, 41 (12), W12421.
- Kamphuis, J.W. 1974. Determination of sand roughness for fixed beds, *Journal of Hydraulic Research*, 12(2), 193-203.

- Kennedy, J.F. 1961. Stationary waves and anti-dunes in alluvial channels, W.M. Keck Laboratory, California Institute of Technology, Report No. KH-R-2.
- Kennedy, J.F. 1963. The mechanics of dunes and anti-dunes in erodible-bed channels, *Journal Fluid Mechanics*, 16, 521-544.
- Kennedy, J.F. 1969. The formation of sediment ripples, dunes and anti-dunes, *Annual Reviews Fluid Mechanics*, 1, 147-168.
- Kerssens, P.J.M., A. Prins, and L.C. Van Rijn. 1979. Model for suspended sediment transport, *Journal of the Hydraulics Division, ASCE*, 105(5), 461-476.
- King, C.A.M. 1972. *Beaches and Coasts*, 2nd ed., Edward Arnold, London, 570 pp.
- Komar, P.D., and M.C. Miller. 1975. On the comparison between the threshold of sediment motion under waves and unidirectional currents with a discussion of the practical evaluation of the threshold, *Journal of Sedimentary Petrology*, 45, 362-367.
- Krone, R.B. 1962. Flume studies of the transport of sediment in the estuarial shoaling processes, Final report, Hydraulic Eng. Lab. U.S. Army Corps. of Eng., 110 pp.
- Lees, G. 1964. The measurement of particle shape and its influence in engineering materials, *British Granite and Whinstone Federation Journal*, Vol. 4, No. 2, 17-38.
- Li, Z.H., K.D. Nguyen, J.C. Brun-Cottan, and J.M. Martin. 1994. Numerical simulation of the turbidity maximum transport in the Gironde estuary, *Oceanologica acta* 17, 479-500.
- Liu, H.K. 1957. Mechanics of sediment-ripple formation, *Proceedings Am. Soc. Civil Engrs.*, *Journal of Hydraulics Division*, 83, 1-23.
- Luthardt, H. 1987. Analyse der Wassernahen Druck und Windfelder über der Nordsee aus Routinebeobachtungen, *Hamburger Geophysikalische Einzelschriften*, A83, 115 pp.
- Mahatma. 2004. The spatial and temporal patterns of erodibility on an intertidal flat in the East Frisian Wadden Sea, Germany, Ph.D. Thesis, University of Kiel, 129 pp.

- Manning, R. 1895. On the flow of water in open channels and pipes, Transactions, Institution of Civil Engineers of Ireland, Dublin, 20, 161-207.
- Mayerle, R., T. Razakafoniaina, C. Palacio, and G. Pramono. 2002. Bed forms and equivalent roughness sizes in tidal channels, Proceedings of the International Conference on Fluvial Hydraulics (River Flow 2002), IAHR, Louvain-la-Neuve, 349-357.
- Mayerle, R., G. Pramono, and C. Escobar. 2005. Dimension and roughness distribution of bed forms in tidal channels in the German Bight, *Die Küste*, 69, 229-251.
- McManus, J. 1988. Grain size determination and interpretation, In: Techniques in Sedimentology, Tucker M (ed), Oxford, Blackwell, 63-85.
- McNown, J.S. 1951. Particles in slow motion, *La Houille Blanche*, Vol.6, No. 5.
- Medina R., M.A. Losada, I.J. Losada, and C. Vidal. 1994. Temporal and spatial relationship between sediment grain size and beach profile, *Marine Geology*, 118, 195-206.
- Mehta, A.J., T.M. Parchure, J.G. Dixit, and R. Ariathurai. 1982. Resuspension potential of deposited cohesive sediment beds, In V.S. Kennedy (ed.), *Estuarine comparisons*, Academic Press, 591-609.
- Meyer-Peter, E., and R. Müller. 1948. Formulas for bed load transport, Proceedings of the second meeting of the International Association of Hydraulic Structures Research, Stockholm, 39-64.
- Miller, R.L., and J.M. Zeigler. 1958. A model relating dynamics and sediment pattern in equilibrium in the region of shoaling waves, breaker zone, and foreshore, *Journal of Geology*, 66, 417-441.
- Miller, R.L., and J.M. Zeigler. 1964. A study of sediment distribution in the zone of shoaling waves over complicated bottom topography. In: R.L. Miller (Editor), *papers in Marine Geology, Shepard Commemorative Volume*, Macmillan, New York, 133-153.
- Nielsen, P. 1983. Analytical determination of nearshore wave height variation due to refraction shoaling and friction, *Coastal Engineering*, 7, 233-251.

- Niemeyer, H.D., R. Goldenbogen, E. Schroeder, and H. Kunz. 1995. Untersuchungen zur Morphodynamik des Wattenmeers im Forschungsvorhaben WADE, *Die Küste*, 57, 65-94.
- Nieuwjaar, M., and T. Van der Kaaij. 1987. Sediment concentration and transport in case of irregular non-breaking waves with a current, Delft Tech. Univ., Civ. Eng. Dep., Delft.
- Nikuradse, J. 1933. Strömungsgesetze in Rauhen Rohren, VDI – Forschungsheft Arb. Ing. Wes., 361, 22 pp. English translation: Laws of flow in rough pipes, Tech. Memo. 1292, Natl. Adv. Comm. For Aeron., Washington D.C., 1950.
- O'Connor, B.A., and J. Nicholson. 1988. A three-dimensional model of suspended particulate sediment transport, *Coastal Engineering*, 12(2), 157-174.
- Oliver, D.R. 1961. The sedimentation of suspensions of closely sized spherical particles, *Chem. Eng. Sci.*, 15, 230-242.
- Olphen, H. 1963. *An Introduction to Clay Colloid Chemistry*, John Wiley & Sons, Ltd. Publishers, 301 pp.
- Palacio, C., C. Winter, and R. Mayerle. 2001. Set up of a hydrodynamic model for the Meldorf Bight, *Proceedings of the World Water and Environmental Resources Congress*, ASCE/EWRI, Orlando.
- Palacio, C.A. 2002. Metodología para la validación de modelos hidrodinámicos utilizando amplia información de campo: Aplicación a la bahía Meldorf en la costa del mar del norte Alemán, Ph.D. Thesis, Universidad Nacional de Colombia, Medellín, 181 pp.
- Partheniades, E. 1965. Erosion and deposition of cohesive soils. *Journal Hydraulics Div.*, ASCE 91(HY1), 105-139.
- Poerbandono. 2003. Sediment Transport Measurements and Modelling in the Meldorf Bight Tidal Channels, German North Sea Coast, Ph.D. Thesis, University of Kiel, 151 pp.
- Poerbandono and R. Mayerle. 2005. Composition and dynamics of sediments in tidal channels of the German North Sea coast, *Die Küste*, 69, 63-91.

- Powers, M.C. 1953. A new roundness scale for sedimentary particles, *Journal of Sedimentary Research*, 23(2), 117-119.
- Pramono, G.H. 2005. The Study of Bedforms and Equivalent Roughness Sizes in the Central Dithmarschen Bight, Ph.D. Thesis, University of Kiel, 136 pp.
- Prandtl, L. 1952. *Essentials of Fluid Dynamics*, Hafner Publishing Co., New York, 50 pp.
- Raudkivi, A.J. 1976. *Loose Boundary Hydraulics*, 2nd ed., Pergamon, New York, 397 pp.
- Raudkivi, A.J. 1988. The roughness height under waves, *Journal of Hydraulic Research*, 26(5), 569-584.
- Razakafoniaina, N.T. 2001. Assessment of the equivalent bed roughness size in tidal channels on the basis of numerical model simulation and Side Scan Sonar observations, Master Thesis, Coastal Research Laboratory, University of Kiel, 84 pp.
- Reimers, H.C. 2003. Sedimentverteilung und Benthosverbreitung in den Watten der Dithmarscher Bucht als Indikator für morphodynamische Veränderungen, Abschlußbericht zum Forschungsvorhaben Sedimorph im GKSS Hochschulprogramm, 18.
- Reineck, H.E., and I.B. Singh. 1980. *Depositional Sedimentary Environments*, Springer-Verlag, Berlin, 549 pp.
- Richardson, J.F., and W.N. Zaki. 1954. Sedimentation and fluidization: Part I, *Trans. Inst. Chem. Engrs.*, 32, 35-53.
- Ricklefs, K., and N.E. Asp. 2005. Geology and morphodynamics of a tidal flat area along the German North Sea coast, *Die Küste*, 69, 93-127.
- Riethmüller, R., M. Heineke, H. Kuehl, and R. Keuker-Rüdiger. 2000. Chlorophyll a concentration as an index of sediment surface stabilisation by microphytobenthos, *Continental Shelf Research*, 20, 1351-1372.

- Ris, R.C., N. Booij, and L.H. Holthuijsen. 1999. A third generation wave model for coastal regions, Part II, verification, *Journal of Geophysical Research*, 104(c4), 7667-7682.
- Roelvink, J.A., and G.K.F.M. Van Banning. 1994. Design and development of DELFT3D and application to coastal morphodynamics, in: Verwey, Minns, Babovic, and Maksimovic (eds), *Hydroinformatics' 94*, Balkema, Rotterdam.
- Rouse, H. 1937. Modern conceptions of the mechanics of fluid turbulence, *Transactions of the American Society of Civil Engineers*, 102, 463-543.
- Rouse, H. 1947. *Elementary Mechanics of Fluids*, John Wiley and Sons, New York, 376 pp.
- Sanford, L.P., and J.P. Halka. 1993. Assessing the paradigm of mutually exclusive erosion and deposition of mud, with examples from upper Chesapeake Bay, *Marine Geology*, 114, 37-57.
- Sanford, L.P., and J.P.Y. Maa. 2001. A unified erosion formulation for fine sediments, *Marine Geology*, 179, 9-23.
- SCCWRP. 1994. Sediment grain size: Interlaboratory Intercalibration Experiment, Southern California Coastal Water Research Project, Sediment Grain Size Intercalibration Committee, Westminster, Tech. Rep. 276.
- Schiller, L. and A. Naumann. 1933. Über die grundlegenden Berechnungen bei der Schwerkraftaufbereitung, *Zeitschrift des Vereines Deutscher Ingenieure* 77 (12), 318-320.
- Shields, A. 1936. Anwendung der Aehnlichkeitsmechanik und der Turbulenzforschung auf die Geschiebebewegung, *Mitteilungen Preussischen Versuchsanstalt für Wasserbau und Schiffbau*, 26, 1-26. In: W.P. Ott and J.C. van Uchelen (translators), U.S. Dep. of Agric. Soil Conser. Serv. Coop. Lab., California, Inst. of Technol., Pasadena, 36 pp.
- Simons, D.B., and E.V. Richardson. 1966. Resistance to flow in alluvial channels, U.S. Geological Survey Professional Paper, 422-J.
- Soulsby, R.L. 1998. *Dynamics of Marine Sands: A Manual for Practical Applications*, Thomas Telford Publ., London, 250 pp.

- Stokes, G.G. 1851. On the effect of the internal friction on fluids on the motion of pendulums, *Trans. Camb. Phil. Soc.*, 9, 8-106.
- Straub, L.G. 1940. Approaches to the study of mechanics of bed movement, *Iowa State University Studies, Engineering Bulletin* 20, 1940.
- Thorn, M.F.C. 1982. Physical processes of siltation in tidal channels, *Proceedings Hydraulic Modelling in Maritime Engineering, ICE, London*, 47-55.
- Tison, L.J. 1949. Origine des Ondes de Sable et des Bancs de Sable sous l'Action des Courants, *Proceedings 3rd Congress I.A.H.R.*, Report II-13, 1-15.
- Tison, L.J. 1953. Recherches sur la tension limite d'entrainement des materiaux constitutifs du lit, *Proceedings of the Minnesota International Hydraulics Convention, IAHR, Delft*, 21-35.
- Tolhurst, T.J., K.S. Black, S.A. Shayler, S. Mather, I. Black, K. Baker, and D.M. Paterson. 1999. Measuring the in situ erosion shear stress of intertidal sediments with the cohesive strength meter (CSM), *Estuarine, Coastal and Shelf Science*, 49, 281-294.
- U.S. Interagency Committee on Water Resources, Subcommittee on Sedimentation. 1957. Some Fundamentals of Particle-size Analysis, Report 12 of A Study of Methods Used in Measurement and Analysis of Sediment Loads in Streams, Federal Interagency Sedimentation Project, Corps of Engineers, Vicksburg, 55 pp.
- Uthus, L., I. Hoff, and I. Horvli. 2005. Evaluation of grain shape characterization methods for unbound aggregates, 7th International Conference on the Bearing Capacity of Roads, Railways and Aircrafts, Trondheim.
- Van den Berg, J.H., and A. Van Gelder. 1989. Scour and fill sequences in flows over very fine sand and silt, *Proc. 4th Int. Conf. on Fluvial Sedimentology, Barcelona*.
- Van der Mark, C.F., A. Blom, S.J.M.H. Hulscher, S.F. Leclair, and D. Mohrig. 2005. On modeling the variability of bedform dimensions, *Proceedings River, Coastal and Estuarine Morphodynamics, IAHR*, 831-841.
- Van Ledden, M., Z.B. Wang, H. Winterwerp, H. De Vriend. 2006. Modelling sand-mud morphodynamics in the Friesche Zeegat, *Ocean Dynamics*, 56, 248-265.

- Van Olphen, H. 1963. *An Introduction to Clay Colloid Chemistry*, John Wiley & Sons, New York.
- Van Rijn, L.C. 1984a. Sediment transport, Part I: Bed load transport, *Journal of Hydraulic Engineering*, 110(10), 1431-1456.
- Van Rijn, L.C. 1984b. Sediment transport, Part II: Suspended load transport, *Journal of Hydraulic Engineering*, 110(11), 1613-1641.
- Van Rijn, L.C. 1984c. Sediment transport, Part III: Bed forms and alluvial roughness, *Journal of Hydraulic Engineering*, 110(12), 1733-1754.
- Van Rijn, L.C. 1989. *Handbook of Sediment Transport by Currents and Waves*, Report H461, Delft Hydraulics, Delft.
- Van Rijn, L.C. 1993. *Principles of Sediment Transport in Rivers, Estuaries and Coastal Seas*, Aqua Publications, Amsterdam, 584 pp.
- Van Rijn, L.C. 2000. *General view on sand transport by currents and waves*, Delft Hydraulics, Report Z2899.20-Z2099.30-Z2824.30, Delft.
- Van Rijn, L.C., A.G. Davies, J. Van de Graaff, and J.S. Ribberink. 2001. *Sediment Transport Modelling in Marine Coastal Environments*, Aqua Publications, Amsterdam, 415 pp.
- Vela-Diez, S. 2001. *Sediment Mapping of the Tidal Flat Channels off Buesum*, Master Thesis, Coastal Research Laboratory, University of Kiel, 91pp.
- Velikanov, M.A. 1936. Formation of sand ripples on the stream bottom, *Int. Assoc. Scientific Hydrology, Commission de Potamologie, Sec. 3, Report 13*, 17 pp.
- Verboom, G.K., J.G. De Ronde, and R.P. Van Dijk. 1992. A fine grid tidal flow and storm surge model of the North Sea, *Continental Shelf Research*, 12, 213-233.
- Wadell, H. 1932. Volume, shape and roundness of rock particles, *Journal of Geology*, 40, 443-451.
- Wang, X., and X. Ke. 1997. Grain-size characteristics of the extant tidal flat sediments along the Jiangsu coast, China, *Sedimentary Geology*, 112, 105-122.

- Wikramanayake, P.N. 1993. Velocity profiles and suspended sediment transport in wave-current flows, Ph.D. Thesis, Massachusetts Institute of Technology, 285 pp.
- Wilkens, J. 2004. Medium Scale Morphodynamics of the Central Dithmarschen Bight, Ph.D. Thesis, University of Kiel, 181 pp.
- Winkelmolen, A.M. 1971. Rollability, a functional shape property of sand grains, *Journal of Sedimentary Petrology*, Vol. 41, No. 3, 703-714.
- Winter, C. 2003. Validation of the CSM-GBM nesting, Determination of open sea boundary conditions for small scale coastal models, Coastal Research Laboratory, University of Kiel, Report No. 04-03.
- Winter, C., and R. Mayerle. 2003. Calibration and validation of a sediment transport model with extensive data-sets for a tidal channel system in the German Wadden Sea, *Coastal Sediments Conference*, 18-23.
- Winter, C., Poerbandono, H. Hoyme, and R. Mayerle. 2005. Modelling of suspended sediment dynamics in tidal channels of the German Bight, *Die Küste*, 69, 253-278.
- Winterwerp, J.C., J.M. Cornelisse and C. Kuijper. 1991. A laboratory study on the behavior of mud from the Western Scheldt under tidal conditions, In *Nearshore and estuarine cohesive sediment transport, workshop*, St. Petersburg, Florida, 295-313.
- Winterwerp, J.C. 2003. On the deposition flux of cohesive sediment, In: Maa JPY (ed.), *Book of abstracts 7th International Conference on Nearshore and Estuarine Cohesive Sediment Transport Processes*, Virginia, United States.
- WL | Delft Hydraulics. 2003/2006. *Delft3D-FLOW, Simulation of multi-dimensional hydrodynamic flows and transport phenomena, including sediments*, User Manual, Delft.
- Wren, D.G., B.D. Barkdoll, R.A. Kuhnle, and R.W. Derrow. 2000. Field techniques for suspended sediment measurement, *Journal of Hydraulic Engineering*, 126(2), 97-104.
- Yalin, M.S. 1964. Geometrical properties of sand waves, *Journal of the Hydraulics Division*, 90(HY5), 105-119.

-
- Yalin, M.S. 1972. *Mechanics of Sediment Transport*, Pergamon Press, Oxford, 290 pp.
- Yang, C.T. 1973. Incipient motion and sediment transport, *Journal of the Hydraulics Division*, 99(HY10), 1679-1704.
- Zanke, U. 1995. Sachstandsbericht zur Entwicklung eines numerischen Modells mit beweglicher Sohle, Teil 1: Sohle aus gleichförmigem Sediment. Teil 2: Sohle aus ungleichförmigem Sediment, internal report, TU Darmstadt.
- Zingg, T. 1935. Beiträge zur Schotteranalyse, *Schweizerische Mineralogische und Petrologische Mitteilungen*, 15, 39-140.
- Znamenskaya, N.S. 1969. Hydraulic criteria for streams with the movable bed. Translated from *Trudy Gos Hidrol Inst-Ta*, No. 173, 43-48. *Soviet Hydrology, Selected Papers*, No. 5, 452-455.

Erklärung

Hiermit erkläre ich, dass die Abhandlung – abgesehen von der Beratung durch meine akademischen Lehrer, nach Inhalt und Form meine eigene Arbeit ist. Diese Arbeit hat an keiner anderen Stelle im Rahmen eines Prüfungsverfahrens vorgelegen. Außerdem erkläre ich, dass dies mein erster Promotionsversuch ist.

Kiel, den 30. Mai 2007

Carlos Alejandro Escobar Sierra

Curriculum Vitae

Personal data

Name Carlos Alejandro Escobar Sierra
Nationality Colombian
Place of birth Medellín, Colombia
Date of birth 26 October 1971
Sex Male
Address Alsenstrasse 19, 24118 Kiel, Germany
Phone +49-431-8803730
E-mail cescobar@corelab.uni-kiel.de

Education

1996- 2000 Master of Science in Aprovechamiento de Recursos Hidraulicos at Escuela de Minas, Universidad Nacional de Colombia, Medellín
1989- 1995 Bachelor of Civil Enginnering at Escuela de Minas, Universidad Nacional de Colombia, Medellín
1982- 1988 High school at Liceo Municipal Concejo de Medellín, Colombia
1978- 1982 Elementary school at Colegio San Jose de Calasanz, Medellín, Colombia

Working experience

2003- 2007 Research co-worker at the Coastal Research Laboratory, Christian Albrechts University of Kiel, Germany
1999- 2003 Assistant Professor at Universidad Eafit, Hydraulic Department, Medellín, Colombia
1999- 1999 Lecturer at Universidad Cooperativa de Colombia, Hydraulic Department, Medellín, Colombia
1994- 1999 Civil engineer staff at Integral S.A, Departamento de Presas Hidráulicas, Medellín, Colombia
1994- 1994 Research assistant of the hydraulic laboratory at Universidad Nacional de Colombia, Medellín

